UNIVERSITY OF CALIFORNIA,
IRVINE

Study of Methods for Microfabrication of Fused Silica Planar CVGs and Direct Angle Measurements

DISSERTATION

submitted in partial satisfaction of the requirements
for the degree of

DOCTOR OF PHILOSOPHY

in Mechanical and Aerospace Engineering

by

Daryosh Vatanparvar

Dissertation Committee:
Professor Andrei M. Shkel, Chair
Professor Tryphon T. Georgiou
Professor Lorenzo Valdevit

2022

DEDICATION

This dissertation is dedicated to my dear parents Nastaran and Abbas and my role model of a brother, Korosh.

Contents

List of Figures

List of Tables

ACKNOWLEDGMENTS

First of all, I would like to express my deepest gratitude and appreciation to my advisor Professor Andrei M. Shkel for providing this opportunity and his continuous support and guidance through my Ph.D. studies. Besides my advisor, I would like to thank my dissertation committee, Professor Tryphon T. Georgiou and Professor Lorenzo Valdevit, for taking the time to review this dissertation and provide insightful comments.

Next, I would like to thank my current and former lab mates at UCI Microsystems Lab, Dr. Alexandra Efimovskaya, Dr. Radwan M. Noor, Dr. Mohammad H. Asadian Ardakani, Dr. Sina Askari, Dr. Yusheng Wang, Yu-wei Lin, Danmeng Wang, Chi-Shih Jao, Austin Parrish, and Eudald Sangenis for the stimulating discussions and insightful suggestions. In addition, I would like to thank UCI Integrated Nano-Research Facility (INRF) staff, Jake Hes, Dr. Mo Kebaili, Dr. Chuang-Yuan Lee, and Richard Chang for their help and valuable suggestions on fabrication aspects of the project.

I would like to acknowledge the funding provided by Defense Advance Research Projects Agency (DARPA), the U.S. Navy, Office of Naval Research (ONR), and National Institution of Standards and Technology (NIST), without which this work would not have been possible. Specifically, this work was supported in part by ONR under contract No. N00014-19-1-2338, DARPA under grant No. N66001-16-1-4021, and the US department of commerce, NIST under contract No. 70NANB17H192.

Last but not least, I would like to thank my family, my parents, and my brother, for their continuous support and encouragement throughout my education. Also, I would like to thank my dear friends who accompanied me in this journey with their irreplaceable emotional support.

VITA

Daryosh Vatanparvar

EDUCATION

Doctor of Philosophy in Mechanical and Aerospace Engineering **2022**
University of California, Irvine *Irvine, CA, USA*

Master of Science in Mechanical and Aerospace Engineering **2019**
University of California, Irvine *Irvine, CA, USA*

Bachelor of Science in Mechanical Engineering **2016**
Sharif University of Technology *Tehran, Iran*

RESEARCH EXPERIENCE

Graduate Student Researcher **2016–2022**
University of California, Irvine *Irvine, California, USA*

Undergraduate Student Researcher **2014–2016**
Sharif University of Technology *Tehran, Iran*

TEACHING EXPERIENCE

Teaching Assistant - Mechanical Vibrations **2021–2022**
University of California, Irvine *Irvine, California, USA*

Teaching Assistant - Mechanical Vibrations **2018–2019**
University of California, Irvine *Irvine, California, USA*

Teaching Assistant - Mechanical Vibrations **2017–2018**
University of California, Irvine *Irvine, California, USA*

REFEREED JOURNAL PUBLICATIONS

Direct Angle Measurement Using Dynamically-Amplified Gyroscopes — **2022**
IEEE Sensors Journal

On Correlation of Anisoelasticity, Angular Gain, and Temperature in Whole-Angle CVGs — **2022**
IEEE Sensors Journal

Fabrication of Planar Fused Silica Resonant Micro-Devices on Silicon Substrates — **Under review**
IEEE/ASME Journal of MEMS

REFEREED CONFERENCE PUBLICATIONS

Temperature Sensitivity of Angular Gain in Micro Rate-Integrating Gyroscopes (MRIG) — **Jan. 2022**
IEEE MEMS

Digital Manufacturing of Resonance MEMS from a Single-Layer Fused Silica Material — **Jan. 2022**
IEEE MEMS

Fabrication Process and Structural Characterization of Fused Silica-on-Silicon Toroidal Ring Gyroscope — **Oct. 2021**
IEEE SENSORS

Identification of Gain Mismatches in Control Electronics of Rate Integrating CVGs — **Mar. 2021**
IEEE INERTIAL

Instabilities Due to Electrostatic Tuning of Frequency-Split in Coriolis Vibratory Gyroscopes — **Oct. 2020**
IEEE SENSORS

Effect of Electrostatic Nonlinearity on Force-to-Rebalance Mode of Operation in CVG — **Sept. 2020**
DGON

Quadrature-Induced Noise in Coriolis Vibratory Gyroscopes — **Mar. 2020**
IEEE INERTIAL

Characterization of Scale Factor Nonlinearities in Coriolis Vibratory Gyroscopes — **Apr. 2019**
IEEE INERTIAL

Effect of Fabrication Imperfections on Energy Loss Through Mechanical Mode Coupling in MEMS **Mar. 2018**
IEEE INERTIAL

Patent Disclosures

Laser Micromachining of MEMS Resonators from Bulk of Optically Transparent Material **Oct. 2021**
UC Case No. 2022-732-1

ABSTRACT OF THE DISSERTATION

Study of Methods for Microfabrication of Fused Silica Planar CVGs and Direct Angle Measurements

By

Daryosh Vatanparvar

Doctor of Philosophy in Mechanical and Aerospace Engineering

University of California, Irvine, 2022

Professor Andrei M. Shkel, Chair

This Ph.D. dissertation focuses on developing microfabrication processes to realize planar Fused Silica (FS) Micro-Electro-Mechanical System (MEMS) technology for the implementation of Micro-Rate-Integrating Gyroscopes (MRIG). Additionally, it includes a study on identifying error sources in Coriolis Vibratory Gyroscopes (CVG) with Whole-Angle (WA) mode of operation. The FS planar MRIG is envisioned to provide navigational-grade noise performance, unprecedented dynamic range, and thermal stability at the Size, Weight, Power, and Cost (SWaP-C) factor of today's commercially-available silicon micro-scale gyroscopes.

As part of this work, we developed the Fused silica-On-Silicon (FOS) process for batch fabrication of resonators from low-loss amorphous FS material based on conventional microfabrication techniques. As the core step of the fabrication process for plasma etching of FS, we identified optimal parameters to achieve a 7:1 aspect ratio of etching with near-vertical sidewalls. For demonstration, a Toroidal Ring Gyroscope (TRG) architecture was fabricated through the developed process. With the metal-coated FS-TRG devices, we demonstrated resonator functionality and measured a quality factor on the order of 539,000 and a frequency split in the operational modes as low as 7 Hz. We also introduced a digital manufacturing process, which utilizes Femtosecond Laser-Induced Chemical Etching (FLICE) to fabricate

stand-alone FS MEMS vibratory structures for the first time. Through process optimization, we demonstrated that FLICE is an enabling technology for patterning micro-channels with an aspect ratio of 55:1 and higher, ideal for fabricating MEMS resonators with ultrahigh capacitive transduction. By employing FLICE as part of a 3-step process, we fabricated Disk Resonator Gyroscopes (DRG) from a single-layer FS material. We demonstrated resonator functionality and measured the frequency split as low as 54.7 Hz and the quality factor as high as 614,000. To the best of our knowledge, the quality factors demonstrated as part of this dissertation are the highest quality factors reported for a planar FS resonator in the kilohertz frequency range.

We developed a mathematical electro-mechanical model of WA operation, through which we simulated and characterized the effect of mechanical imperfections of the structure and imperfections in the WA control electronics on precession of oscillations. We demonstrated that mechanical imperfections in MRIG, including anisodamping and anisoelasticity, limit the resolution of angle measurements by introducing angle-dependent bias errors and angular drift. Imperfections in the control electronics, including phase errors, asymmetries in motion actuation and detection gains, were shown to adversely affect the outcome of the WA control loops and cause interference on the precession. We verified the simulation results experimentally by implementing the WA control with an FPGA/DSP-based platform and applying it to a planar silicon MRIG as the testbed.

Finally, we identified a mismatch in MRIG's Temperature Coefficients of Frequency (TCF) as the primary mechanism causing Angular Gain Temperature Sensitivity (AGTS) and angular drift in the WA mode of operation. We provided mitigation strategies to significantly reduce AGTS, despite the TCF-mismatch in the mechanical sensing element. We demonstrated angular gain stability better than 223 ppb (equivalent to a rate-bias-stability better than 0.2 deg/hr), which would be critical for high accuracy angle measurements in prolonged operations.

Chapter 1

Introduction

This chapter presents motivation of the research, including an overview, background, and problem statement. This is followed by a literature review of prior work on Micro-Rate-Integrating Gyroscopes (MRIG) concept, control architectures for Whole-Angle (WA) mode of operation, and microfabrication processes for planar fused silica resonators. Then, the objectives of the research are formulated, and the outline of the dissertation concludes this introductory chapter.

1.1 Motivation

In a strap-down Inertial Navigation System (INS), the spatial orientation of the Inertial Measurement Unit (IMU) is required to project the acceleration measured in the body frame onto the navigation frame and compensate for gravitational contribution to the spatial acceleration measurements, [119]. A Rate Gyroscope (RG) is typically used for indirect orientation measurement through time-integration of the angular rate output. Due to measurement errors in RG, such as noise, bias offsets, thermally induced instabilities, integration of the

angular rate output would result in an angle estimation error that grows over time. As a result of errors in angle estimation, the gravitational interference cannot be compensated; the uncompensated gravitational acceleration gets integrated, and the position error grows with the duration of navigation. The importance of using low noise gyroscopes (i.e., high-performance navigational-grade gyroscopes) in an INS is indisputable. On the other hand, in the numerical time-integration process, one would face challenges with the limited sampling rate of angular rate measurements and numerical errors in the integration of discrete data points. A mitigation strategy to these challenges is to use a high-performance gyroscope, which directly measures the rotation angle, a "Rate-Integrating Gyroscope" (RIG).

Among different gyroscope mechanizations, Coriolis Vibratory Gyroscopes (CVG) can be instrumented to measure the rotation angle directly. CVGs can be divided into two broad categories based on the gyroscope's mechanical element [70]. In Class I gyroscopes, the mechanical element is designed with identical operational frequencies ($\Delta\omega$ of 0 Hz), and Class II gyroscopes are designed intentionally to be asymmetric with non-identical operational frequencies ($\Delta\omega \gg 0$ Hz). Class I or mode-matched CVG can be instrumented for angular rate measurement in the Force-to-Rebalance (FRB) mode of operation and direct angle measurement in the Whole-Angle mode of operation [70]. In these configurations, a mode-matched gyroscope provides a higher angular rate sensitivity and a mechanically unlimited dynamic range.

The challenge in reaching these desirable characteristics is to achieve excellent symmetry in the mechanical gyroscope structure. In reality, geometrical asymmetries, introduced in the fabrication process, and anisotropic mechanical properties of the structural material result in considerable anisoelasticity (i.e., the frequency split). Due to a relatively poor tolerance in microfabrication and the crystalline orientation-dependent properties of conventionally used silicon material, anisoelasticity of micro-scale gyroscopes has been observed to be a more significant challenge compared to their macro-scale counterparts. While in the

navigational-grade macro-scale gyroscopes, post-fabrication trimming is commonly used to reach mHz-level structural symmetry [96], in micro-scale and batch fabrication scenarios, this task is quite challenging. Therefore, to utilize Coriolis vibratory-based Micro-Rate-Integrating Gyroscopes (MRIG) for direct angle measurement, it is essential to understand how the asymmetries in the mechanical structure affect the angle measurements. It is also critical to realize that the control electronics used in WA operation play an essential role in providing high-resolution angle measurements. Understanding the requirements for achieving high-precision angle measurements, with respect to the limitations of realizing ideal MRIG, motivates the development of mathematical models to study the mechanical and electrical error sources and the corresponding angle error characteristics.

Besides structural symmetry, another requirement for achieving high-performance gyroscopes in mode-matched operation is to have low damping (τ^{-1}) and damping asymmetry ($\Delta(1/\tau)$) in the mechanical sensing element. High quality factor vibratory MEMS devices benefit different applications, including signal processing, timing, and inertial applications [136]. For example, timing devices rely heavily on high quality factors for low close-to-carrier phase noise and low energy consumption [135]. Whereas devices such as high-performance RIG and mode-matched rate gyroscopes rely heavily on long energy decay time constant and high quality factors [57, 61]. Current MEMS fabrication techniques are limited to using Single-Crystal Silicon (SCS) as the structural material. SCS has relatively high coefficient of thermal expansion (CTE of 3 ppm/°C [79]) and consequently high Thermo-Elastic Damping (TED) [65]. Fused Silica (FS) material, on the other hand, has an exceptionally low thermal expansion coefficient (CTE of 0.5 ppm/°C [95]), chemical inertness, optical transparency, and isotropic mechanical properties. These characteristics make FS a favorable candidate to substitute the conventional SCS as the structural material of micro-resonators. Macro-scale FS resonators, such as the Hemispherical and milli-Hemispherical Resonator Gyroscope (HRG), are examples demonstrating quality factors over 25 million [96, 120]. A substitution of SCS with FS material has the potential to realize high quality factor micro-scale resonators

with unmatched structural symmetry and packaging capabilities for ultra-high-performance Micro-Opto-Electro-Mechanical Systems (MOEMS), [74].

The state-of-the-art macro-scale HRG, [96, 120], and Precision Shell Integrating (PSI) gyroscope, [23], are examples that have proven the potential of FS as the structural material by delivering the highest noise performance among Coriolis vibratory gyroscopes. This motivates the investigation and development of planar fused silica resonant MEMS technology for different applications, including inertial. The planar fused silica resonant microstructures enable reaching high structural symmetry, minimal energy losses, and low-cost batch fabrication potential.

1.2 Background

The principle of operation of a Coriolis Vibratory Gyroscope (CVG) is based on rotation-induced Coriolis forces measured by a resonator vibrating in a 2-dimensional space (i.e., plane). The mechanical element of a CVG consists of a series of lumped masses that vibrate with a translational motion or distributed continuous masses, such as concentric rings, disks, and shells, which utilize flexural standing waves. In both structural categories, a 2-Degree of Freedom (2DoF) lumped mass-spring-damper system can be used to represent the CVG, shown in Fig. 1.1, and the equation of motion governing the mechanical element can be written as

$$\begin{bmatrix} \ddot{x} \\ \ddot{y} \end{bmatrix} + Z \begin{bmatrix} \dot{x} \\ \dot{y} \end{bmatrix} + K \begin{bmatrix} x \\ y \end{bmatrix} = \begin{bmatrix} F_x \\ F_y \end{bmatrix}, \tag{1.1}$$

where the variables x, y, F_x, and F_y denote the displacement and control forces along the reference X and Y axes. The Z and K matrices include the coefficients of damping, elasticity,

and the Coriolis forces, [70], as

$$Z = \begin{bmatrix} \frac{2}{\tau} + \Delta(\frac{1}{\tau})\cos 2\theta_\tau & \Delta(\frac{1}{\tau})\sin 2\theta_\tau - 2\kappa\Omega \\ \Delta(\frac{1}{\tau})\sin 2\theta_\tau + 2\kappa\Omega & \frac{2}{\tau} - \Delta(\frac{1}{\tau})\cos 2\theta_\tau \end{bmatrix}$$

$$K = \begin{bmatrix} \omega^2 - \omega\Delta\omega\cos 2\theta_\omega & -\omega\Delta\omega\sin 2\theta_\omega \\ -\omega\Delta\omega\sin 2\theta_\omega & \omega^2 + \omega\Delta\omega\cos 2\theta_\omega \end{bmatrix} \tag{1.2}$$

where κ and Ω denote the mechanical angular gain (Bryan's coefficient [14]) and the input angular rate. Definitions of the average resonant frequency ω, frequency split $\Delta\omega$, average damping coefficient $1/\tau$, damping difference $\Delta(1/\tau)$, and misalignment angles (θ_ω and θ_τ) can be found in Fig. 1.1.

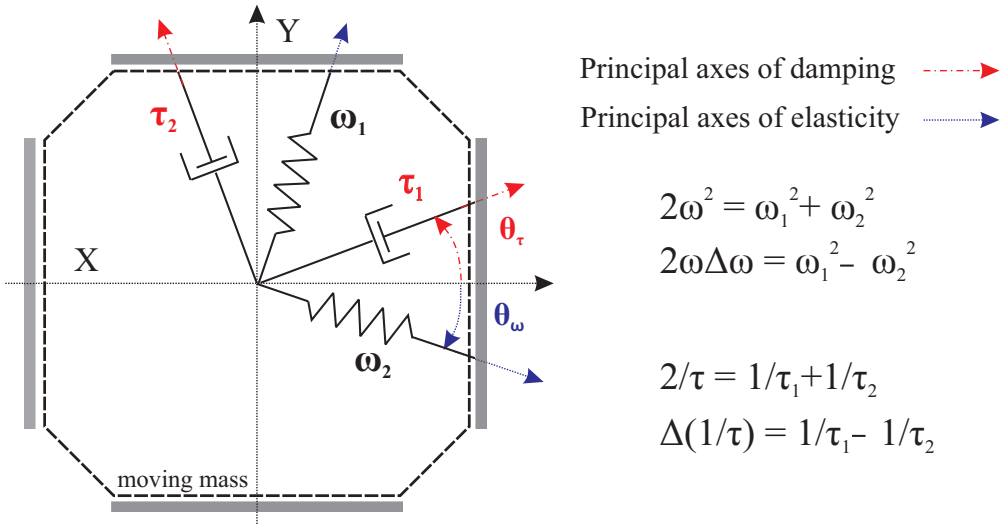

Figure 1.1: A lumped mass-spring-damper representation of a Coriolis vibratory gyroscope. The XY axes represent the non-inertial reference frame attached to casing of the sensing element aligned with the direction of actuation and detection. Principal axes of damping, principal axes of elasticity, and their orientation with respect to the reference axes are illustrated.

1.2.1 Angular Rate Measurement

In the angular rate mode of operation, we excite the drive mode using an external force (F_x) to have a vibration along the X-axis (Fig. 1.1); in the presence of rotation, the secondary mode gets excited as a result of the Coriolis coupling forces and the mass vibrates along the Y-axis as well. The case in which the secondary mode freely responds to the Coriolis forces and the amplitude of vibration along the Y-axis is used to measure the input angular rate is referred to as the open-loop angular rate mode of operation. The mechanical scale factor in this mode of operation is derived as, [70],

$$SF = -\frac{\kappa f_{x0}}{2\omega_x}\left(\sqrt{\frac{1}{\tau_x^2} + (\omega_x - \omega_{fx})^2}\right)^{-1}\left(\sqrt{\frac{1}{\tau_y^2} + (\omega_y - \omega_{fx})^2}\right)^{-1}, \quad [m/deg/s] \tag{1.3}$$

where the magnitude of the drive force and the drive frequency are denoted by f_{x0} and ω_{fx} in units of [N] and [rad/s], respectively. The demodulated response of the open-loop angular rate gyroscope (i.e., the amplitude of vibration in the secondary mode) can be represented as

$$Output = SF \times (\Omega + B) + v_{NER} \tag{1.4}$$

where the bias offset due to anisodamping is denoted by B, and the Noise-Equivalent Angular Rate (v_{NER}) is used to represent the mechanical and electrical noise sources affecting the measurements. It is evident that the mechanical SF needs to be maximized to improve sensor performance with respect to various noise sources that corrupt the angular rate measurement. Based on Eq. (1.3), this can be achieved by matching the actuation frequency, the drive mode resonant frequency, and the sense mode resonant frequency (i.e., $\omega_{fx} = \omega_x = \omega_y$).

Once the frequencies are matched (i.e., achieving a frequency split lower than the mechanical bandwidth of the sense mode), the system's damping must be reduced to improve the noise

performance further. For a given drive frequency, this is equivalent to increasing the energy decay time constants (τ_x and τ_y).

Based on Eq. (1.4), the bias due to anisodamping ($\Delta(1/\tau)$) would offset the angular rate measurements by

$$B = -\frac{1}{2\kappa}\Delta(\frac{1}{\tau})\sin 2\theta_\tau \tag{1.5}$$

The bias in angular rate measurements is indistinguishable from the physical input angular rate (Ω). To minimize bias, we need to reduce anisodamping, precisely the difference in the reciprocal of the energy decay time constants $\Delta(\frac{1}{\tau})$. It is worth mentioning that bias offsets can be identified during an initial calibration procedure by rotating a gyroscope in clockwise and counter-clockwise directions with the same angular velocity. However, since anisodamping changes during operation, due to temperature variations, bias drifts are inevitable. Nevertheless, a gyroscope with a high quality factor and energy decay time constant would provide lower anisodamping and lower anisodamping variations, which would improve the bias offset and bias stability [20].

A mode-matched high quality factor gyroscope instrumented for open-loop angular rate measurement would yield a limited mechanical bandwidth (proportional to $\Delta\omega/Q$) and impractically long response time. Therefore, it is essential to apply a feedback control to the secondary mode to suppress the rotation-induced vibration along the Y-axis and enhance the bandwidth, [70, 126]. In this configuration, which is referred to as the closed-loop angular rate mode or the Force-to-ReBalance (FRB) mode, the magnitude of the control force along the sense axis is used to measure the input angular rate. It should be noted that the previously mentioned requirements to achieve high noise performance and improved thermal stability apply to the FRB mode of operation as well [57].

1.2.2 Angle Measurement

As previously discussed, mode-matched Coriolis Vibratory Gyroscopes (CVG) can be utilized for angular rate and direct angle measurements [110]. To instrument a CVG for direct angle measurement, a Whole-Angle (WA) control architecture needs to be employed [70]. In the WA mode of operation, the mechanical resonator functions as an angular rate-integrating sensor that can theoretically measure rotations with no limit on the angular velocity. A CVG in the WA mode operates based on the precession of the oscillation pattern in a non-inertial frame in the presence of rotation, illustrated in Fig. 1.2 (a) and (c). In the ideal case, the measured pattern angle (θ) would be equal in magnitude to the amount of rotation applied to the sensing element but with a negative sign. In an inertial frame, this would be observed as an oscillation pattern that is stationary in orientation independent of the input rotation, illustrated in Fig. 1.2(b).

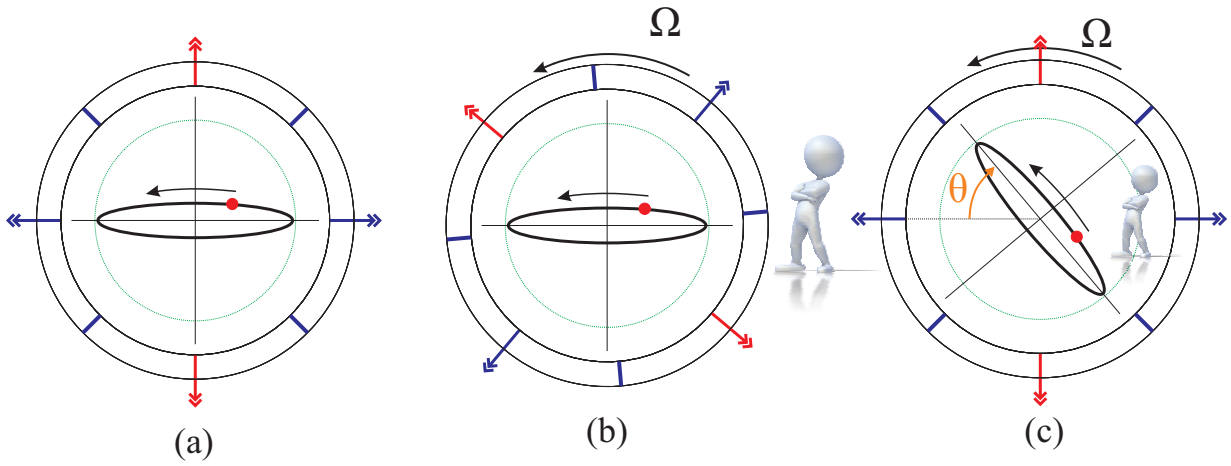

Figure 1.2: Principle of rate-integrating mode of operation, (a) oscillation pattern when there is no rotation applied to the gyroscope, (b) oscillation pattern in the presence of rotation observed in an inertial coordinate frame, (c) oscillation pattern in the presence of rotation observed in a non-inertial rotating coordinate frame (fixed to the gyroscope frame). Precession of the oscillation pattern (θ) in the gyroscope rotating frame gives a direct angle measurement of the input rotation.

The rate-integrating mechanism was first demonstrated using an oscillating pendulum by Foucault [30], by which he confirmed the rotation of the earth. Years after that, Bryan

provided a theoretical foundation demonstrating that the same principle can be applied to cylindrical or bell-shaped resonators, [14]. Currently, the most successful implementation of a Coriolis vibratory-based RIG is the sonic vibrating bell gyroscope [68], later known as the Hemispherical Resonator Gyroscope (HRG) [122].

In theory, a CVG in the WA mode of operation provides the benefits above by directly measuring the spatial orientation. However, in practice, the complexity of WA control and the requirements imposed on the mechanical resonator and control electronics are much more vast than gyroscope operation for angular rate measurements. Hence, the WA mode of operation is mainly implemented with macro-scale HRG devices, and the angular rate mode of operation is implemented with today's consumer-grade, tactical grade, and near-navigational grade MEMS gyroscopes.

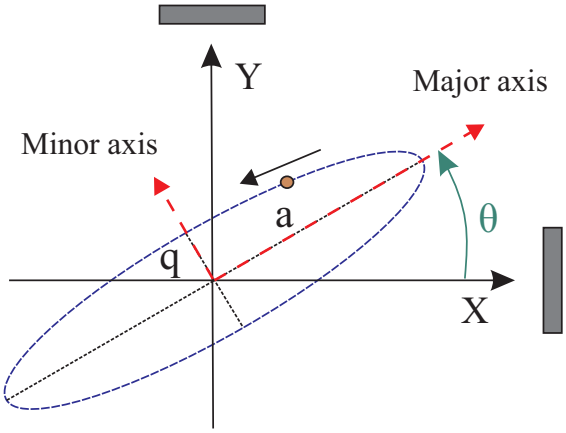

Figure 1.3: Schematics illustrating the elliptical trajectory of oscillation along X and Y axes in a Coriolis vibratory gyroscope. The orientation of the oscillation pattern amplitude of vibration along the semi-major and semi-minor axes of the elliptical trajectory are shown.

Mathematical models have been reported by Zhuravlev [143], Friedland [31], and Lynch [70] as a foundation for studying the mechanical sources of error in WA mode of operation. Based on Lynch and Firedland's model, in the WA mode of operation, the oscillation trajectory in the non-inertial reference frame takes an orbital shape, illustrated in Fig. 1.3. The vibration

along the X and Y axes can be represented in a general form through the following equations.

$$\begin{aligned} x(t) &= a\cos\theta cos(\omega t+\phi) - q\sin\theta sin(\omega t+\phi), \\ y(t) &= a\sin\theta cos(\omega t+\phi) + q\cos\theta sin(\omega t+\phi), \end{aligned} \tag{1.6}$$

where a and q denote the vibration amplitude along the major and minor axes of the elliptical pattern, illustrated in Fig. 1.3. The undesired oscillation along the semi-minor axis of the elliptical orbit is referred to as the oscillation component in-quadrature with the reference phase or "quadrature," in short, [70]. In Eq. (1.6), parameters ω and ϕ represent the average oscillation frequency and phase of oscillation, respectively. In Lynch's analytical framework on evolution of pendulum variables, precession is governed by the following equation [70]

$$\begin{aligned} \dot{\theta} = -\kappa\Omega + \frac{1}{2}\Delta(\frac{1}{\tau})\sin 2(\theta-\theta_\tau)\frac{E}{\sqrt{E^2-Q^2}} + \frac{1}{2}\Delta\omega\cos 2(\theta-\theta_\omega)\frac{Q}{\sqrt{E^2-Q^2}} \\ -\frac{a}{2\omega\sqrt{E^2-Q^2}}(f_{q_s}\cos\delta\phi - f_{q_c}\sin\delta\phi) + \frac{q}{2\omega\sqrt{E^2-Q^2}}f_{a_s}\sin\delta\phi, \end{aligned} \tag{1.7}$$

where θ is used to denote the angle of precession and variables E and Q represent the energy and quadrature in the system, which correlate to the shape of the orbital trajectory through the following equations

$$\begin{cases} E = a^2 + q^2 \\ Q = 2aq \end{cases} \tag{1.8}$$

In an ideal CVG, the gyroscope has perfect symmetry in both elasticity and damping (i.e., $\Delta\omega = 0$ and $\Delta\frac{1}{\tau} = 0$) and the phase of oscillation is perfectly tracked and used as a reference for signal modulation and demodulation (i.e., $\delta\phi = 0$). In this case, the ideal gyroscope in WA operation acts as a rate-integrator and the precession is equal to

$$\dot{\theta} = -\kappa\Omega \tag{1.9}$$

In reality, however, mechanical imperfections, including anisoelasticity and anisodamping, affect precession, shown in Eq. (1.7). Therefore, an error is inevitable between the actual input rotation ($\int \Omega dt$) and the angle measurement based on precession ($-\theta/\kappa$).

In summary, high quality factor, damping symmetry, and stiffness symmetry are the critical characteristics to improve the performance in MEMS rate and rate-integrating gyroscopes. These are the optimization parameters that will be discussed in this thesis.

1.2.3 Anisoelasticity

As previously mentioned, due to imperfections in microfabrication, having the perfect structural symmetry is not possible. In practical implementations, electrostatic frequency tuning is used to reduce the higher resonant frequency and match it with the lower resonant frequency, [28]. Electrostatic frequency tuning requires an ultra-stable DC power supply to generate large DC voltages. Implementing DC power supplies using Integrated Circuits (IC) is challenging due to power consumption limitations and the need to integrate sizable high power handling transistors. On the other hand, electrostatic forces cause bias instabilities, scale factor nonlinearities, and additional vibration sensitivity in the gyroscope [69,125,128]. Therefore, to improve the noise performance of gyroscopes, it is essential to minimize the need for electrostatic tuning and reserve it for fine-tuning to reach a sub-Hz frequency split. Hence, the fabrication of MRIG with near-to-perfect structural symmetry is crucial and an unsolved challenge.

In developing highly symmetric MEMS gyroscopes, factors associated with the fabrication process, such as etch non-uniformity, alignment errors, high surface roughness, and granularity of deposited thin films, are part of the problem which must be addressed. On the other hand, since the conventionally used Single-Crystal Silicon (SCS) material exhibits crystalline-orientation dependent mechanical properties [45], even an ideal fabrication pro-

cess would not yield a symmetric gyroscope with identical resonant frequencies. To reach the required level of structural symmetry, tight control of the fabrication process and using non-crystalline structural materials are necessary.

1.2.4 Energy Dissipation Mechanisms

The potential and kinetic energy of a resonator are reduced with each oscillation due to different dissipation mechanisms, which include but are not limited to Anchor Loss (AL), Thermo-Elastic Damping (TED), Surface Losses (SL), Air Damping (AD), Mode Coupling (MC), etc. The total dissipation is formulated as a summation of damping due to each mechanism

$$\frac{1}{Q} = \frac{1}{Q_{AL}} + \frac{1}{Q_{TED}} + \frac{1}{Q_{AD}} + \frac{1}{Q_{SL}} + \frac{1}{Q_{MC}} + ... \tag{1.10}$$

It is noted that the total quality factor of a resonator would be determined by the mechanism causing the highest energy dissipation (i.e., the mechanism with the lowest quality factor limit) [6]. Hence, identifying the mechanism which imposes an upper limit for quality factor helps to optimize the design, fabrication, or packaging process to improve the quality factor. For example, vacuum sealing of devices at sub-μTorr pressures would effectively eliminate the energy loss due to squeeze film damping (air damping) in the resonator [5]. Furthermore, specific design considerations on the positioning of the anchors or the use of dynamically balanced design architectures would avoid wave propagation and energy loss through the anchors [83]. Examples of dynamically balanced modes are "wine-glass vibration modes" in the disk, ring, and shell resonators. In lumped mass designs, anti-phase-driven multi-mass implementations minimize energy loss through the substrate, [24, 105, 124]. Furthermore, a proper suspension element design would provide a sufficient frequency separation between the operational modes and spurious modes and would minimize energy loss through mode coupling [127].

Thermo-Elastic Damping (TED)

Thermo-Elastic Damping (TED) is an interstice energy loss mechanism that is mainly dependent on the structural material of the resonator. The process of thermo-elastic damping is described in detail by Lifshitz in [65]. Acoustic modes such as normal vibration modes in resonators experience damping due to their non-linear interaction with a surrounding bath of thermally-excited elastic modes or phonons. Suppose the relaxation rate of the phonon distribution to a local Bose-Einstein distribution is much faster than the frequency of the acoustic mode. In that case, one has a well-defined temperature field, and there is no need to treat the thermal phonons as individual excitation. This regime of operation is referred to as the regime with diffusive thermal phonons, and the energy loss due to the interaction in this regime is called thermo-elastic damping. If the relaxation rate was comparable to the frequency of the acoustic mode, the energy loss is referred to as the Akhiezer energy loss, [60].

Our study and analysis for gyroscopes are focused on resonators with frequencies below 0.5 MHz; therefore, TED is an effective and dominant dissipation mechanism, not the Akhiezer energy loss. In TED, relaxation of vibration in a deformed solid happens through an irreversible flow of heat driven by local temperature gradients that form with the strain field in the resonator. The coupling of the temperature gradients and the strain field is dependent on the Thermal Expansion Coefficient (TEC) α. Therefore, using a material with a low TEC would reduce the TED. Without going into details of deriving the TED equation, the exact solution which can be used to estimate the TED quality factor in a thin beam is

$$Q^{-1} = \frac{E\alpha^2 T_0}{C_p}\left(\frac{6}{\xi^2} - \frac{6}{\xi^3}\frac{sinh\xi + sin\xi}{cosh\xi + cos\xi}\right) \tag{1.11}$$

where ξ is defined as,

$$\xi = b\sqrt{\omega_0/(2\chi)} \tag{1.12}$$

where ω, E, α, T_0, and C_p, b and χ are the vibration frequency, Young's modulus, coefficient of thermal expansion, temperature, heat capacity, width of the beam, and thermal diffusivity of the solid, respectively.

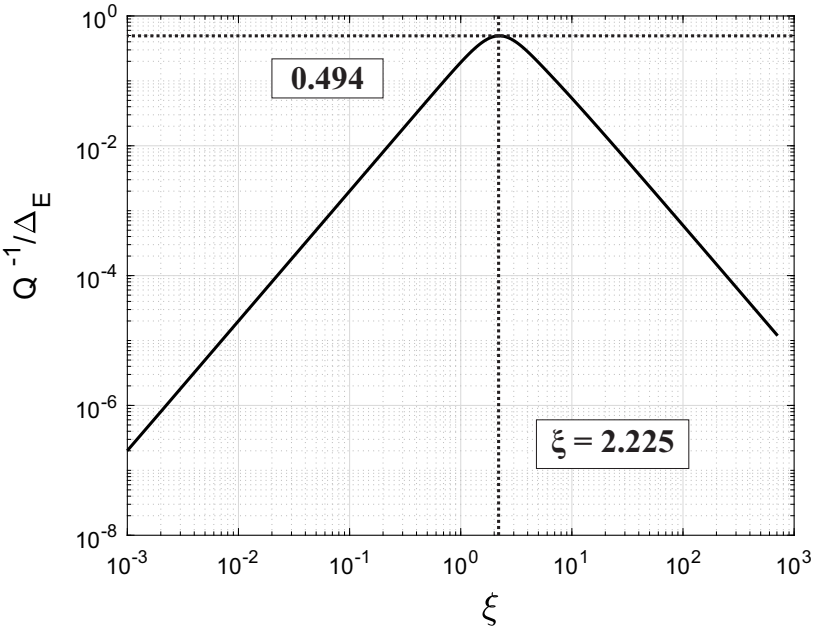

Figure 1.4: Shown is the Q^{-1}/Δ_E as a function of the dimensionless parameter ξ.

By defining the relaxation length as $\Delta_E = E\alpha^2 T_0/C_p$, the inverse quality factor per relaxation length (Q^{-1}/Δ_E) as a function of the dimensionless parameter ξ can be calculated, shown in Fig. 1.4. The first conclusion to be drawn from this universal behavior is that the peak value of thermo-elastic damping, given approximately by $0.494\Delta_E$, is independent of the dimensions of the beam. It only depends on temperature through the thermodynamic properties E, α, and C of the material.

As it is shown in Eq. (1.11), the TED quality factor is inversely proportional to α^2. Hence, the reduction of the expansion coefficient would reduce dissipation. In [95], Roy et al. reported materials that have the lowest thermal expansion coefficients, which include oxides such as SiO_2 and TiO_2. As we estimated in Table 1.1, the relaxation strength of SiO_2 is two orders of magnitude lower than SCS. Therefore, the TED quality factor limit achieved in SiO_2 across different frequencies is at least 564k, while for SCS, it is around 10k. Due to

Material	Young's Modulus	TEC	Heat Capacitance	Density	Thermal Diffusivity	Relaxation Strength
Silicon	165 GPa	2.6e-6 C^{-1}	0.71 J/g K	2329.6 $\frac{kg}{m^3}$	$0.8cm^2/s$	2e-4
Fused Silica	72 GPa	0.52e-6 C^{-1}	0.74 J/g K	2202 $\frac{kg}{m^3}$	$0.008cm^2/s$	3.6e-6
Nickel	205 GPa	13e-6 C^{-1}	0.440 J/g K	8908 $\frac{kg}{m^3}$	$0.27cm^2/s$	2.7e-3

Table 1.1: Estimated relaxation strength of single-crystal silicon, fused silica, and nickel material.

the compatibility of SiO_2 with most MEMS processes and its five-times lower thermo-elastic coupling, it is preferred to be used to fabricate MEMS resonators.

1.3 Literature Review

In this section, we review prior art and prior research on technology development of high precision MRIG. We first review plasma etching and fabrication of planar resonators from fused silica as the structural material, followed by applications of Femtosecond Laser-Induced Chemical Etching (FLICE) in microfabrication processes. Finally, different implementations of Whole-Angle (WA) control architecture for Rate-Integrating Gyroscopes (RIG) are conferred.

1.3.1 Planar Fused Silica Resonator Fabrication

Despite fused silica's many desirable properties, micromachining of Fused Silica (FS) structures has remained a challenge. The development of micro-scale FS resonators has been pursued from two directions. The first direction was aspired by moving towards miniaturizing the state-of-the-art Hemispherical Resonator Gyroscope (HRG) [7, 23]. Due to the relative

dimensions of the structure and the nature of their fabrication process, we refer to them as 3-Dimensional (3D) FS resonators. The second direction adheres closely to the integrated circuits (IC) micromachining techniques and the conventional silicon MEMS technology to realize planar or 2-Dimensional (2D) FS resonators.

Due to considerable overlap with the established IC manufacturing techniques, mass production and batch fabrication of 2D FS micro-resonators is currently believed to be realized at a lower cost and complexity than the 3D micro-resonators. It is also anticipated that the single-chip planar multi-sensor integration may serve as a more compact solution for different applications, such as Positioning, Navigation, and Timing (PNT). This dissertation focuses on the development of planar FS micro-resonators. In the following, we review prior efforts to fabricate planar FS structures, process tuning, and results on high aspect ratio etching of the material through plasma etching and Femtosecond Laser-Induced Chemical Etching (FLICE).

Fused Silica Plasma Etching

In [80], Osipov et al. reported a fabrication process for deep plasma-chemical etching of single-crystal quartz plates in a SF_6/O_2 gas mixture. The Taguchi matrix technique was used to rank basic technological parameters, and their influence on the etch rate was used to optimize the plasma-chemical etching process. The parameters that were found to play a critical part in the etching process were the bias voltage applied to the substrate holder, output power of the high-frequency generator, oxygen flow rate, and position of the substrate holder relative to the lower edge of the discharge chamber. They performed a control experiment on through wafer etching of windows with large linear dimensions (3 mm x 10 mm) in a single-crystal quartz plate (z-cut) with a thickness of 369 μm.

Jiaxing et al. presented a multi-scale numerical method coupled with the reactor, sheath,

and trench model to simulate dry etching of SiO_2 in inductively coupled C_4F_8 plasma, [114]. In their simulation, they decided on ion and neutral particle densities in the reactor. Then the ion energy and angular distributions (IEDs and IADs) were obtained in the sheath model with the sheath boundary conditions provided. They primarily focused on the effects of the discharge parameters on the etching results. They found that the discharge parameters, including discharge pressure, radio-frequency (rf) power, gas mixture ratios, bias voltage, and frequency, have synergistic effects on IEDs and IADs on the etched material surface, thus further affecting the trench profiles evolution.

Li et al. in [63], investigated the effect of adding Ar, Ne, and He noble gases to C_4F_8 inductively coupled plasmas for SiO_2 etching. The systematic variation of their ionization potentials, metastable energy levels, and mass of the dominant ion in C_4F_8 containing a high percentage of the noble gas provided them with means to evaluate the relative importance of gas-phase and surface processes in the etching of SiO_2 . The group observed that Ar addition gives rise to the largest ion current density and He to the smallest ion current density for given experimental conditions. Ion energy distributions of all ions are displaced to lower energies for C_4F_8/Ar discharges as compared with C_4F_8/Ne or C_4F_8/He plasmas. They observed that upon RF biasing of the substrates, the ion energies required for etching to take place are lowest for C_4F_8/Ar discharges, followed by C_4F_8/He and C_4F_8/Ne discharges.

In [3], Akashi et al. from Hitachi reported on plasma etching of grooves in borosilicate glass and their optimization for profile control. Plasma etching was carried out using an anodically bonded silicon wafer as an etching mask. They improved the sidewall angle by removing excessively thick polymer film produced by carbon-fluoride etching gases during etching. Two fabrication processes were experimentally compared for effective removal of the film. In the first method, they used plasma etching with the addition of argon to the etching gases. In the second method, plasma etching and subsequent ultrasonic cleaning in DI water were alternately carried out. They reported on fabrication of grooves with a

maximum sidewall angle of 85° independent of its opening width.

At the University of California, Irvine (UCI), Ahmed et al. demonstrated results on plasma etching of Fused Silica (FS) and Borosilicate glass (BSG), [1]. In their experiments, they utilized a ULVAC NLD 570 etcher and a gas mixture of C_3F_8 and Ar. This work demonstrated etched features as deep as 100 μm with wall angles within 3 degrees deviation. In [1], four different masks were explored for etching SiO_2, including nickel, amorphous silicon, bonded silicon, and photoresist. An aspect ratio independent etching, 8:1 selectivity, more vertical wall angle, low defect, and less roughness were observed when using an amorphous silicon mask. It was concluded that the KMPR photoresist is cost-effective and suitable for shallow etching. In the case of using bonded silicon mask, the process required complicated bonding and involved yield issues related to bonding; however, it showed no mask re-deposition issues. The precision deep etching of small features (below 20 μm) was a challenge with the bonded bulk silicon mask. It was concluded that nickel metal is a preferred masking material for capacitive MEMS resonators due to its high selectivity when etching deep features with aspect ratios around 7:1 for FS and 8:1 for BSG. Results on sidewall roughness improvement of BSG based on post-fabrication annealing reducing the roughness from 900 nm to 85 nm were also reported in [1].

For micro-fluidic devices, Kolari et al. reported results on Reactive Ion Etching (RIE) of glass (PyrexTM and fused silica) substrates with cavities deeper than 100 μm. They used silicon wafers as the etch mask, which were patterned by silicon DRIE, and showed that 100 μm deep and nearly vertical structures could be etched into the glass, [58]. In this work, they compared different masking materials for their application and feature sizes. The silicon shadow mask was used without practical thickness limitations with an etching selectivity of 4:1 to both vertical and lateral directions. However, it was observed that a full-thickness (400 μm) silicon wafer was not suitable for features with less than 200 μm width due to the high initial aspect ratio.

The most recent result on RIE process optimization was reported in [84], [86], [85]. Pedersen et al. developed an Inductively-Coupled Plasma (ICP) process to etch anisotropic features into fused silica. Etching very deep features (e.g., more than 100 microns) into fused silica with nearly vertical sidewalls was demonstrated using the optimized recipes from their developed model. The group reported an etch rate on the order of 500 nm/min and sidewall angles of 89.1 degrees. As reference geometries, they were etching concentric rings with gap sizes on the order of 25 μm (an aspect ratio of 4:1). In their work, an ULVAC NLD-6000 with a gas mixture of C_3F_8 and O_2 was used for etching and the nickel material was their choice of masking.

Fused Silica Resonant MEMS Implementation

Jung et al. demonstrated a silicon/quartz bonding and quartz deep RIE (DRIE) process to fabricate micro-mechanical quartz resonator structures, [54]. They reported on thick quartz micro-structures (around 50 μm) fabricated by deep RIE of quartz with a gas mixture of C_4F_8 and He. In addition, a simple fused-quartz freestanding cantilever structures were fabricated and presented. The bonded silicon wafer was used as an etch mask layer and as a substrate for quartz structures. They did not present any quantitative measurements on the fabricated structures.

Hwang et al. reported a similar process to fabricate electrostatically-actuated, in-plane micromechanical resonators made from fused quartz. Their proposed method enabled a wafer-level fabrication of fused quartz resonators readily mounted on the silicon substrate, which is advantageous over the conventional fabrication method of quartz crystal resonators. Using the proposed process, they fabricated 40-μm-thick laterally-driven fused quartz cantilever resonators. They reported Q-values of the metal-coated fused quartz cantilevers on the order of 21,700 to 48,900 according to the length of cantilevers. However, considerable stress and a shape distortion caused by the corrosion of the silicon mask layer during the

quartz DRIE process were reported to be the issue with the process, [52].

Song et al., in [111], presented results on the fabrication of fused-quartz micromechanical resonators using quartz-on-quartz structure. Plasma-assisted bonding technique was applied to fabricate a homogeneous quartz-on-quartz (QoQ) wafer instead of a Silicon-on-Quartz (SoQ) wafer to reduce the residual stress after bonding. An electroplated nickel mask was used to minimize the corrosion of the etch mask. A 27-kHz capacitively transduced double-ended tuning fork fused-quartz resonator oscillator was successfully fabricated using the developed process; a Quality factor of 68k was reported.

Chang et al. at HRL reported on two deep reactive ion etching processes developed to miniaturize quartz resonators for wireless communication applications, [21]. The first process used an SF_6 based chemistry with high bias voltage for high-rate thinning of quartz while maintaining mirror-like surface smoothness. The second process used CF_4-based chemistry to produce high-aspect-ratio, micron-size quartz structures with an etch depth on the order of 12 μm. Both processes were intended to make possible ultra-small, integrated Ultra-High-Frequency (UHF) quartz filters.

Cao et al. reported characterization results of deep reactive ion etching of fused silica with three different masking materials: Single-Crystal Silicon (SCS), negative photoresist KMPR and SU-8, [18]. They observed that KMPR and SU-8 showed higher mask selectivity and were easier to integrate and remove than silicon. Using a KMPR mask, a high aspect ratio (8:1) etch with a 6 μm mask opening was obtained. SU-8 masks also achieved high aspect ratios of 4.5:1 for 20 μm wide trenches, with mask selectivity of 2:1. However, the polymeric masks caused greater FS sidewall roughness. Using SCS mask, etch depths were limited by severe mask faceting and Aspect Ratio Dependent Etching (ARDE), which effectively eliminated the possibility of using thick masks to obtain deep etches. For 4-hr DRIE on a 20 μm wide trench, their achieved etch depth was 86 μm, with no observed etch stop. They obtained etch depths of above 250 μm for wide mask openings with a 100 μm SU-8 mask and 8-hr

DRIE. However, they observed that the SU-8 mask faceted during DRIE. For both SU-8 and KMPR, rough FS sidewalls were obtained. For all masks, they measured etch rates of 0.2-0.5 μm/min. In [19], they used the FS DRIE technology for fabrication of a compact, multi-layer, vertically-stacked fused silica microsystems. They reported a measured quality factor of 33.2k at the resonant frequency of 90.7 kHz.

Khan et al. reported a fabrication process through which an FS device layer and an FS substrate layer were bonded through metal-to-metal compression bonding, [56]. The metal layer was used as both the bonding material and sacrificial layer for releasing the structure after plasma etching of the device layer. They demonstrated the functionality of a 42kHz ring resonator at atmospheric pressures through Laser Doppler Vibrometer (LDV) measurements and magnetic actuation.

The only fully operational prototype of planar FS gyroscope has been developed and demonstrated by Boeing and Jet Propulsion Laboratory (JPL), [20]. Challoner et at. reported a quality factor of 130k with an operational Disk Resonator Gyroscope (DRG) at the resonant frequency of 15.9 kHz. The noise performance of their device was reported with a Bias Instability (BI) of 0.8 deg/hr and Angle Random Walk (ARW) of 0.023 deg/$\sqrt{hr}$. Details of the fabrication process and etched feature sizes were not reported. However, the same group described a general fabrication process of an all Fused Silica wafer-level vacuum-sealed DRG in a patent, [59].

Femtosecond Laser-Induced Chemical Etching (FLICE)

FLICE has been an enabling technology for patterning 3-dimensional micro-structures from optically transparent material, such as fused silica. Prior works were mainly on applications of FLICE in the fabrication of micro-fluidics and micro-optics and are reviewed next.

Butkute et al. demonstrated fluidic and micromechanical structures which were fabricated

using a single fabrication step and combined the possibility for free movement and surface roughness with sub-1 μm Root Mean Square (RMS), [15]. They patterned thin glass features in micro-fluidic channels, which moved freely by applying compressed air through the inlets. They also demonstrated the possibility to pattern fused silica micro-gears that can freely move with respect to each other.

Bellouard et al. have demonstrated the integration of micro-mechanical elements and optical waveguides in a monolithic fused silica platform [11]. The waveguides were used to probe the displacement of a moving platform whose motion was precisely guided by double-compound flexure kinematics. Although they focused on a specific device, the concept applies to various sensors where optical waves can be used as the signal source and information carrier.

The fabrication of curved micro-components by FLICE is typically challenging since nanoplanes fail to form a path for the etchant to penetrate along. In [94], Ross et al. demonstrated that varying the laser polarization orientation dynamically to ensure that the polarization remains orthogonal to the translational direction enables highly selective and isotropic etching of non-planar surfaces.

Stankevic et al., [112], reported a method of inscribing micro-channels in fused silica by using the line-array writing. They demonstrated the formation of channels with a rectangular cross-section of different sizes. They reported that the size of the rectangular cross-section could be controlled by adjusting laser pulse energy and dimension of the lines array. The micro-channels were inscribed in the fused silica substrate using linear and circular polarization. They demonstrated that etching selectivity for the polarization perpendicular to the writing speed was higher than that for parallel polarization but similar compared to the case of circular polarization.

In [53], Jonusauskas reported a hybrid subtractive–additive-welding fs-laser fabrication technique to produce a mechanically robust functional microfluidic system capable of sorting

different sized (1 and 10 μm) microparticles. This was enabled by utilizing a widely tunable (in power and repetition rate) Yb:KGW amplified fs-laser system. They demonstrated that a combination of subtractive and additive laser fabrication technologies could create complex functional Lab-On-Chip systems.

In [46], Hu et al. reported the fabrication of an all-glass microchip with built-in microlenses using FLICE. The microlenses and microchannels prepared by a single FLICE operation exhibited good robustness, stability, and optical performance. Using an innovative tuning method, they demonstrated the capability to change the refractive index through the medium in the optofluidic channel.

Gottmann et al. reported the highest selectivity of up to 1400 for the FLICE of quartz glass in hot KOH, [34]. Interestingly, they showed that 1 ps laser radiation results in higher selectivity and longer processing windows than shorter femtosecond laser radiation. In the picosecond range, they demonstrated that using a repetition rate of 750 kHz, the higher writing velocity of 200 mm/s results in an improved selectivity. Thus, the processing precision is better than obtained using 50 mm/s writing velocity. It is a unique observation that faster laser writing results in improved precision. They used high-speed FLICE to drill 200 μm holes in 1-mm-thick quartz glass, and the scaling of the FLICE process was demonstrated with a 3 m/s writing velocity and a 10 ps laser radiation in only 9 ms (50 holes per second).

Li et al. reported a polarization-insensitive selective etching in fused silica based on picosecond laser irradiation [64]. They showed that the picosecond laser irradiation can produce interconnected nanocracks that are preferentially oriented along the laser scan direction. The revealed characteristic was used for fabricating microfluidic channels along different directions to achieve high etching rates insensitive to the writing laser polarization state.

In [134], Wang et al. used temporally shaped femtosecond laser Bessel-beam–assisted chemical etching for microchannel fabrication in fused silica. Compared with the conventional

single pulse, the etching depth was enhanced by a factor of 13 when the temporally shaped Bessel beam was used. They demonstrated that the shape of the microchannels could be regulated by adjusting parameters, such as laser energy, pulse delay, and pulse number. Based on the results, they envisioned high-throughput and high-aspect-ratio microchannel fabrication in fused silica for potential application in microfluidics.

1.3.2 Instrumentation of WA Gyroscopes

This section reviews literature on the instrumentation of Rate-Integrating Gyroscopes (RIG) for direct angle, or Whole Angle (WA) measurements. We discuss prior work on implementation of WA control, studies on error sources in WA operation, and control strategies for compensating mechanical imperfections.

Open-Loop and Closed-Loop WA Control

Prikhodko et al. reported in [90], direct angle measurement using a Quad Mass Gyroscope (QMG) [124] MRIG architecture in an open-loop configuration; an above 60 dB improvement in bandwidth was reported through the WA operation in mode-matched condition compared to the open-loop angular rate mode. In [121], Trusov et al. reported direct angle measurement through the closed-loop WA control proposed by Lynch, [70], using the non-axisymmetric QMG. They used carouseling to identify anisoelasticity and anisodamping in the MRIG. Askari et al. implemented the open-loop and closed-loop WA control on a 2M quality factor QMG and reported experimentally measured angular error during precession [8]. They experimentally confirmed that in the open-loop WA operation, quadrature is inversely proportional to the input angular rate and that angle-dependent errors reduce with the input angular rate. In [9], Askari et al. reported experimental results on variation of frequency split and angular gain due to temperature variations; they proposed a correc-

tion approach of angular gain based on the measured frequency mismatch during gyroscope operation.

Senkal et al. reported results on the implementation of parametric drive for energy control in the WA control [103]. The parametric drive for energy control has been primarily used in WA control of HRG as reported by [96]. Senkal implemented the parametric drive with a silicon Toroidal Ring Gyroscope (TRG) using a star-shaped electrode. They confirmed that parametric pumping can bypass the errors associated with finding the orientation of the standing wave, time delay in the calculation, and x-y drive and sense gain drift. They demonstrated 14x improvement in scale factor stability compared to conventional x-y drive and better than 20 ppm scale factor stability without any compensation or temperature stabilization. In [102], Senkal et al. reported experimental results on the instrumentation of a Dual Foucault Pendulum (DFP) for direct angle measurement. Rate integrating operation of the gyroscope was experimentally demonstrated via FPGA-based closed-loop control. An angular gain factor of 0.8 and scale factor variation of 22 ppm RMS was measured over 2 hours of rate integrating operation.

In-run Compensation of Mechanical Imperfections

Taher-Tehrani et al. reported experimental results on the identification of anisodamping in an MRIG and applying a compensation force along the minor-axis in-quadrature with the phase of oscillation to reduce the effect of anisodamping on precession [115]. They also applied virtual carouseling to overcome the angle-locking effect due to the remaining anisodamping. By applying the compensation force, the rate threshold was effectively reduced to 3 °/s, 12 times lower than the original value. Through self-precession (carouseling), a consistent scale factor and a 1 °/s rate measurement capability below the gyroscope's original rate threshold was demonstrated. They used a silicon Disk Resonator Gyroscope (DRG) as the device under test. Similar results were reported by Hu et al. in [47]; they used variations of

the energy control output to identify damping mismatch in the gyroscope.

Hu et al. proposed using an Extended Kalman Filter for estimation of anisoelasticity and anisodamping for feed-forward compensation [48]. In this work, an offline EKF was utilized to estimate system parameters based on the slow varying averaged dynamic model; numeric simulation was used to validate the proposed algorithms. Offline application of the EKF with experimental gyroscope operation data also showed consistent results. Estimated damping parameters from the EKF were used in a DSP-based real-time WA control system to set the correct amount of feedback to compensate for the non-proportional damping in the gyroscope. They demonstrated angular drift reduction from 10 °/s to 1 °/s.

Zhang et al. proposed using adaptive compensators to suppress the effects of anisoelasticity and anisodamping on quadrature and angular precession [141]. In their control architecture, the adaptive compensators run together with PI feedback controllers and compute feed-forward action to compensate for the mismatches in elasticity and damping. Each compensator consisted of an estimator, which ran a recursive least square algorithm to estimate gyroscope parameters, and a compensator took the estimated parameters and computed the compensation action. They presented simulation results showing that the proposed adaptive control scheme effectively compensates for the residual quadrature and gyro's unwanted angular precession. In [38], Guo et al. experimentally demonstrated the adaptive controller with a Hemispherical Resonator Gyroscope (HRG). They used virtual carouseling as a self-precession method to speed up the convergence process in the adaptive algorithm. They demonstrated a reduction in the angle-dependent drift from 0.0316 s^{-1} to 0.0051 s^{-1} and the HRG's angular rate threshold was reduced to under 0.005 s^{-1}.

In [35], Gregory et al. proposed a modified control architecture based on Lynch's model and Zhubanov's results [142]. The control loop in their implementation dynamically determined and compensated for anisodamping and anisoelasticity by creating a force on the gyroscope to oppose the apparent force due to damping mismatch on precession and quadrature, re-

spectively. Through simulation results, they demonstrated that residual quadrature and the effect of anisodamping and anisoelasticity can be reduced and the drift in the gyroscope decreased by more than two orders of magnitude. Cho et al. presented experimental results on implementing the control with a Single Crystal-Silicon Cylindrical Rate-Integrating Gyro (CING), [22], and they demonstrated a 2-times reduction in angle-dependent bias errors.

Prikhodko et al. reported analytical results on the effect of anisodamping on precession, [87]. To simplify the mathematics, they neglected the effect of anisoelasticity and derived a closed-form expression for precession. They demonstrated that with an input angular rate below $(\Delta(1/\tau)/2\kappa)$, the orientation does not precess. Based on the mathematical model, they hypothesized that one could overcome the angle-locking limitation at small input angular rates through self-precession. They provided numerical simulation results validating their hypothesis. Experimental results on virtual rotation of an MRIG for overcoming angle-locking were later reported by Pridkhodko in [89]. As part of the WA operation with virtual carouseling, they implemented the dynamic mismatch control proposed by Gregory to compensate for the effect of anisodamping and anisoelasticity on precession. With these settings, they demonstrated angular rate measurements lower than 0.1 °/s, orders of magnitude below the rate threshold.

Compensation of Non-linear Effects

Nitzan et al. proposed an auxiliary feedback control that would go along with the conventional WA control to reduce the amplitude-frequency coupling during precession [77]. In their approach, the biasing voltage along the X and Y axes were regulated as a function of the pattern angle to maintain a low frequency split despite variations in the vibration amplitude. They showed preliminary results on reduced variation of the resonant frequency during precession. They used a silicon DRG as a testbed.

In [49], Hu et al. developed a mathematical model to study the effect of nonlinearity in capacitive detection and electrostatically induced Duffing nonlinearity on precession. Through the averaged motion equations of the non-linear RIG, they demonstrated that stiffness nonlinearities result in 4θ harmonics in the quadrature control and resonance frequency tracking; damping nonlinearity causes a 4θ harmonic drift error. They introduced and applied an algorithm to reduce the nonlinearity in capacitive detection to a silicon DRG. Through this approach, they demonstrated that an angular rate drift error less than 0.2 $^\circ$/s can be achieved.

1.4 Research Objective

To sum up, high quality factor mode-matched Coriolis vibratory gyroscopes provide significantly higher sensitivity to angular rates and can be instrumented for direct angle measurement. Driven by the superior mechanical properties of fused silica over single-crystal silicon, there has been an interest in fabricating MEMS resonators from fused silica material since the 90s for timing and inertial sensing applications, [137]. A compelling improvement in the performance of macro-scale Hemispherical Resonator Gyroscopes (HRG), which was achieved by using fused silica instead of aluminum as the structural material [96], has amplified this interest. While, in theory, the use of fused silica material promises an improved TED limit compared to silicon, fabrication processes need to be developed and optimized to manufacture stand-alone fused silica resonators and reach the TED limit of pristine fused silica material, respectively.

In this thesis, we explore two fabrication processes to realize planar fused silica resonators. In one process, the fabrication is based on lithography, wafer bonding, plasma etching, and electroplating for low-cost batch manufacturing of high quality factor resonators. The second fabrication process explores utilizing the Femtosecond Laser-Induced Chemical Etching

(FLICE) technique to fabricate planar resonators from a single-layer of fused silica material. For both processes, we perform optimization to meet the geometrical requirements for the realization of high precision MRIG. We demonstrate the feasibility of the process, functioning prototypes, and complete structural characterization.

In the Whole-Angle (WA) mode of operation, MRIGs can be instrumented to operate in a higher dynamic range for angular rate measurements and provides the capability to identify imperfections in the MRIG. While the requirements for high accuracy direct angle measurement are known to be dependent on anisodamping and anisoelasticity of the mechanical structure, the adverse effects of these mechanical imperfections and imperfections in the WA control electronics on the accuracy of angle measurements are not fully understood. More importantly, mechanical characteristics of MRIG change during operation primarily due to thermal effects. This thesis studies the error sources in the WA mode of operation and the effect of temperature fluctuations on the angle error characteristics.

1.5 Dissertation Outline

In Chapter 2, we discuss our results on developing a process for fabrication of micro-scale planar resonators from fused silica material. The process is designed based on lithography, wafer bonding, electroplating, wet etching, and plasma etching, for realization and batch fabrication of micro-scale fused silica resonators. The process's feasibility is demonstrated by implementing fused silica Toroidal Ring Gyroscope (TRG) MRIG prototypes. The device functionality and structural characterization results are presented, including the frequency split and quality factor.

Chapter 3 explores a novel and non-conventional approach for fabricating resonant MEMS from optically transparent material, such as fused silica, using Ultrafast-Laser-Induced Chem-

ical Etching (ULICE). Process optimization results on a Femtosecond Laser-Induced Chemical Etching (FLICE)-based process are discussed to fabricate planar fused silica MEMS resonators for the first time. We demonstrate the process by fabricating Disk Resonator Gyroscope (DRG) MRIG prototypes; experimental results on resonator functionality of the fabricated devices and the structural characteristics are presented.

In Chapter 4, we study the effect of uncompensated anisoelasticity on precession and the corresponding errors in direct angle measurements. Through analytical equations and numerical simulation results, we first investigate the effectiveness of a conventionally used PI quadrature controller and the correlation of residual quadrature to system and control parameters. Furthermore, we demonstrate the effect of residual quadrature on the precession of angle and characterize the corresponding angle errors. Experimental data with a Dual Foucault Pendulum (DFP) MRIG is presented to validate the simulation results.

In Chapter 5, we study the mechanism behind Angular Gain Temperature Sensitivity (AGTS) and identify strategies to minimize it. Experimental results on thermal characteristics of the DFP gyroscope are presented, which we use to explain the correlation between the Temperature Coefficient of Frequency Split (TCFS) and AGTS. Strategies for improving angular gain stability are discussed and experimentally demonstrated. We implement a Dynamic Quadrature Controller (DQC) with the MRIG and demonstrate a significant reduction in AGTS to below 11 ppm for WA operation in temperatures ranging from 15 ℃ to 45 ℃.

In Chapter 6, we study the effect of imperfections in the detection and control electronics on precession in WA mode of operation. We develop a mathematical model to capture both the mechanical sources of error and error sources associated with the electronics. Using the model, we demonstrate that due to imperfections in electronics, the effectiveness of WA control loops is compromised, and as a result, the control forces interfere with the free precession of the oscillation pattern. Based on our findings, a methodology is proposed through which we can decouple mechanical error sources from electrical error sources for

identification and compensation of the detection and actuation gain mismatches. We apply the proposed method to the DFP gyroscope and demonstrate improvements in the resolution of angle measurements.

In Chapter 7, we develop a reduced-order model for higher degree-of-freedom gyroscope architectures, such as the Dynamically-Amplified Gyroscope (DAG). We compare DAG to conventional single-mass gyroscopes through the reduced-order model and examine the application of established gyroscope control architectures to DAG. We demonstrate that the established feedback controls for CVG can be applied to a higher-DoF DAG architecture. We verify this conjecture by adapting the conventional closed-loop WA control and implementing it with a DAG. We experimentally demonstrated direct angle measurement for the first time based on the precession of oscillation pattern using a DAG. Characterization results on the angular gain, anisoelasticity, and anisodamping of the DAG are reported.

Finally, the thesis is concluded in Chapter 8 with a summary of results and future research directions.

Chapter 2

Fabrication Based on Plasma Etching Technology

2.1 Introduction

In this chapter, we discuss our results on developing a process for fabricating micro-scale planar resonators from fused silica material. This process is designed based on lithography, wafer bonding, electroplating, wet etching, and plasma etching for realization and batch fabrication of micro-scale fused silica resonators. The process's feasibility is demonstrated by implementing fused silica Toroidal Ring Gyroscope (TRG) prototypes. The device functionality and structural characterization results are presented, including the frequency split and quality factor.

This chapter is organized as follows. In Section 2.2, we present results on optimization of an FS plasma etching recipe to provide fast and high-aspect-ratio etching. In Section 2.3, we discuss the process flow and the respective trade-offs for different 2D FS micro-resonator fabrication methods along with our results and the challenges of developing a

Fused silica-On-Silicon (FOS) fabrication process. In Section 2.4, we analyze the Toroidal Ring Gyroscope (TRG) design and examine Finite Element Analysis (FEA) predictions of the resonant frequency and TED quality factor limit of FS-TRG. In Section 2.5, structural characterization results of the FS-TRG implemented through the FOS process are presented, including a study of the effect of metal coating on the quality factor of FS-TRGs. A summary of our results and conclusions are found in Section 2.6.

2.2 Plasma Etching of Fused Silica

Fabrication of planar Fused Silica (FS) micro-resonant devices can be performed through different processes, [21, 52, 54, 56, 59, 111]. Across all reported processes, plasma etching of the FS device layer is regarded as an important and challenging step. FS's plasma etching is typically performed using high-density plasma generated using fluorocarbons. The chemical reaction includes deposition of a polymer layer using passivating neutrals and bombardment of the layer with high energy ion fluxes, which result in a layer-by-layer removal of the FS material. In a single step of etching, the fluorocarbon plasma provides both the passivation layer and the ions involved in the sputtering mechanism [140].

In this technique, features are patterned in the material as defined by a mask. For plasma etching of FS, different masking materials have been explored, including metals, such as aluminum and nickel; semiconductors, such as bulk or amorphous silicon; or polymers, such as SU8 or KMPR photoresists [1, 2, 18, 58]. It has been reported that due to high selectivity and low cost, nickel is considered to be a desirable material for masking [1, 18]. In our study, we utilized nickel metal mask for high aspect-ratio plasma etching of FS.

An ideal FS plasma etching process would provide a high etch rate and yield high aspect ratio features with vertical sidewalls, smooth surfaces, and no etch defects. As reported

in [140], a fast etch rate and minimum tapering can be achieved through balanced neutral passivation, ion-assisted desorption, and sputtering. To find an optimized plasma etching recipe, we designed an experiment to evaluate the effects of different process parameters on etch rate, etch profile, and etch quality.

2.2.1 Design of Experiment

For plasma etching of FS, we utilized an SPTS APS PM system. The SPTS system operates based on a high-power Inductively Coupled Plasma (ICP) technology to generate high density and uniform plasma at low process pressure (4 mTorr). The system is comprised of two independent 13.56 MHz Radio Frequency (RF) induction power generators: an antenna power generator that controls the generation of high-density plasma and a platen power that controls the self-biased electrical field. In our setup, C_4F_8 was used as the precursor; O_2 and Ar were used as the buffer gases to stabilize plasma, balance polymer accumulation, and enhance the sputtering effect, [62, 133]. In our SPTS system, 4-inch wafers were held down using an electrostatic chuck while the temperature was controlled using a back-side pressurized helium gas. The temperature of the helium gas was regulated through an auxiliary chiller system.

As part of the plasma etching process optimization, 500 μm thick FS samples were utilized. Samples were prepared according to procedures and process optimization detailed in [42], where thick, vertical, and smooth photoresist mold was reported as a critical factor contributing to anisotropic etching. In brief, 7 μm nickel hard mask was electroplated with patterns defined through a chemically-enhanced AZ-12xT positive photoresist mold. Wafers were diced into 10 mm × 10 mm samples using DISCO DAD3220 dicing saw. The test samples were mounted using Santovac oil on an SCS handle wafer, after which die-level etching was performed. In our experiments, we designed rectangular features with a length size of

Table 2.1: Summary of process parameters in five sets of experiments.

Parameters/ Experiment	C_4F_8 flow rate (sccm)	Temperature (C)	Ar flow rate (sccm)	Antenna power (W)	Bias power (W)
1	65	40	75	1750	100 200 300 400
2				1250 1500 1750 2000	300
3			0 25 50 75 100	1500	
4		-5 10 25 40	50		
5	55 65 75	40			

500 μm and a width size ranging from 20 μm to 500 μm. A Scanning Electron Microscope (SEM) cross-section image of an etched test sample is shown in Fig. 2.1.

Table 2.1 outlines the design of experiments with their respective parameters. Five sets of experiments were conducted, varying five process parameters: bias (platen) power, antenna power, Ar flow rate, temperature, and C_4F_8 flow rate. Chamber pressure was kept at 4 mTorr and O_2 flow rate was set at 15 sccm for all experiments. Samples were etched for a total of 240 minutes (four hours). Every 60 minutes of etching was followed by 30 minutes "O_2 + Ar" plasma cleaning for conditioning of the chamber and to avoid polymer build-up.

Evaluations were performed through SEM images obtained with FEI Quanta 3D Field Emission Gun (FEG). Etched samples were removed of the metal mask, cleaned, and diced to

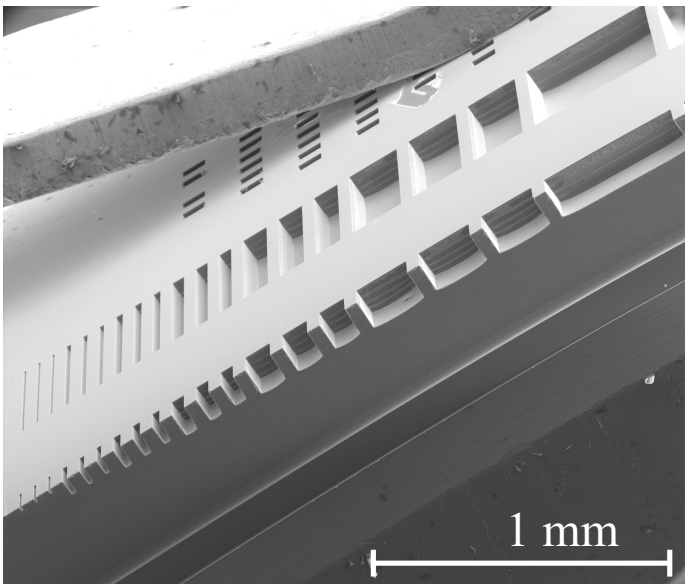

Figure 2.1: SEM cross-section image of a test sample used in the plasma etching process optimization.

obtain cross-sections. SEM evaluations allowed for measurements of the depth of etching, the etch rate, sidewall angles, and for obvious monitoring of etching defects, such as trench widening, microtrenching, faceting, tapering, and sidewall roughness.

Etch rates were estimated based on the features' depth from the top surface down to the center of the bottom trench. In the case of microtrenching, excessive etching at regions closest to the sidewall was thus disregarded in measurements. Etch defects were identified based on their characteristics.

2.2.2 Optimization of Process Parameters

Platen power

RF self-biasing power ranging from 100 W to 400 W was investigated in 100 W increments. Other etch parameters were kept constant within the set of experiments, with antenna power at 1750 W, the temperature of 40 °C, Ar and C_4F_8 flow rates at 75 sccm and 65 sccm,

respectively.

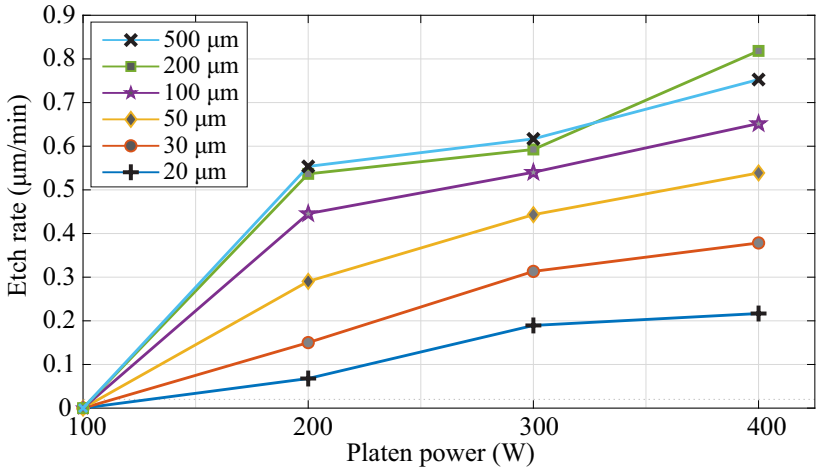

Figure 2.2: Effect of platen power on etch rate of rectangular channels as a function of the channel width size. A monotonic increase in etch rate was observed among all channel sizes.

An increase in etch rate was observed with increasing platen power. A higher platen power increases the acceleration of ions bombarded vertically to the substrate, which intensifies both the physical etching and ion-assisted chemical etching [67, 140]. Figure 2.2 summarizes the improvement in etch rate at higher platen power for different channel sizes.

We believe that for a platen power on the order of 100 W and below, the fluorocarbon polymer deposition rate was higher than its removal rate. Hence, due to insufficient ion energy, no etching occurred [99, 140]. In general, etching occurs when the sputtering of polymer exceeds its deposition, and the etch rate continues to increase as the ion energy increases, assuming there is sufficient passivation.

High bias power encouraged anisotropic etching as ions are accelerated vertically to the substrate. In Fig. 2.3, the progression of the etched profile is shown as bias power was increased above the threshold bias of 200 W; tapering of the sidewalls was reduced at higher platen power. Due to a higher sputtering, the enhanced etch rate and improved sidewall angle at high bias power come with a cost of high consumption rate of the metal mask and a reduction of mask selectivity. On the other hand, charging of the nickel layer causes a

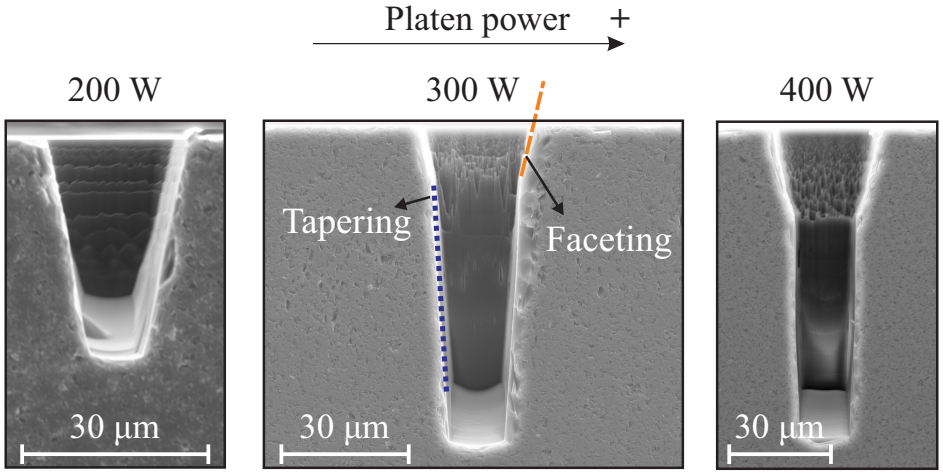

Figure 2.3: Progression of etch profile with increasing bias power for feature size of 30 µm. Sidewall angle (i.e., tapering) improved to be near vertical for high bias power. However, higher consumption of the nickel mask and reduced selectivity were observed at higher platen power, as evident in escalated faceting, compromising both sidewall angle and dimension concordance.

nonuniform erosion of the nickel mask, especially at the corners, leading to faceting. Thus, once nickel is completely consumed, unprotected regions underneath are subsequently etched, resulting in faceting and trench widening of etched FS features [32, 50]. In our study, an average of 2.4 µm enlargement of the opening was measured across all feature sizes for each 100 W increment in bias power. As the metal mask is consumed, a consistent amount of FS substrate is exposed, irrespective of the feature size. One possible workaround to maintain a high etch rate while defining vertical and high aspect ratio features is to deposit a thicker hard mask that is preserved through the whole etching process [50].

Therefore, while high platen power was found to be highly desirable, the lower mask selectivity, faceting, and Critical Dimension (CD) loss are the major issues. As a result, we resorted to a bias power of 300 W.

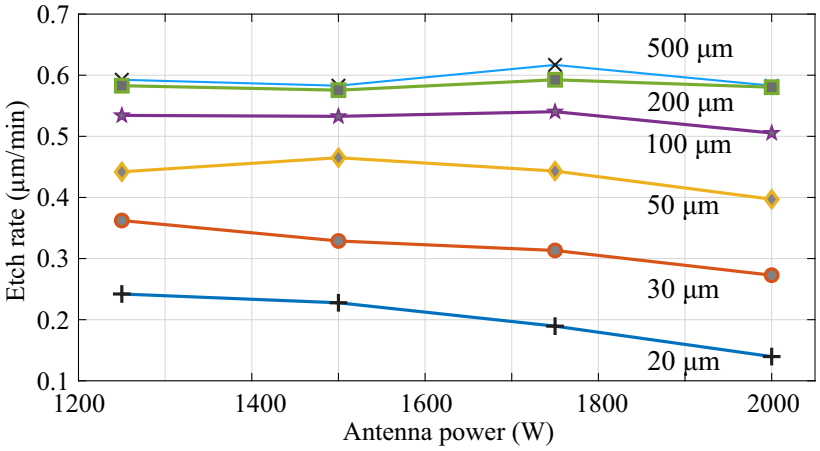

Figure 2.4: Effect of antenna power on etch rate. Etch rate decreased with increasing antenna power due to energy loss from self-collision of high-density ions.

Antenna power

In the second experiment, four levels of RF antenna power were investigated: 1250 W, 1500 W, 1750 W, and 2000 W. Increasing antenna power was expected to improve etch rate due to an increased plasma density. However, we observed a decrease in the etch rate with increasing antenna power, specifically for rectangular channels with a width size lower than 200 μm with the most significant decrease at 2000 W antenna power (Figure 2.4). A decrease in the etch rate with high antenna power has been previously reported [37, 55]. When ion density is more than its optimum value, energy is lost to self-collision between plasma particles before reaching the substrate, reducing the number of active ions. Not only that, at high antenna power of 2000 W, microtrenching was observed for features with dimensions ≤ 30 μm, possibly due to the formation of a charged layer deflecting the paths of traveling ions [97].

At antenna power of 2000 W where microtrenching was observed, Fig. 2.5, sidewall angle was compromised, whereas for antenna powers below 2000 W, manipulating antenna power had minimal effect on etched sidewall angle, similar to findings reported by [2]. Specifically, deviations of sidewall angle were within 2% for antenna power ranging from 1250 W to

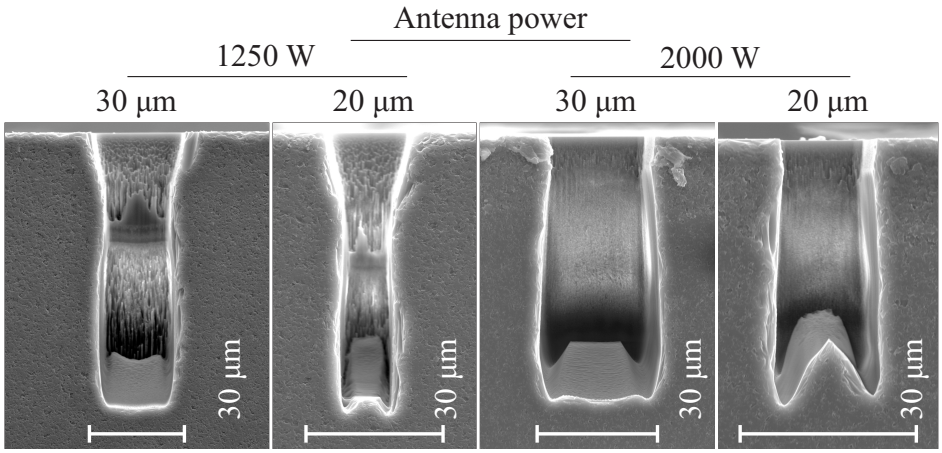

Figure 2.5: Progression of etch profile with an increase of antenna power for feature sizes of 20 µm and 30 µm. Surface smoothness improved at higher antenna power. At 2000 W antenna power, microtrenching negatively affected the etch profile.

1750 W. As shown in Fig. 2.5, etched surfaces were slightly rougher at antenna power of 1250 W and comparably smooth at higher antenna power. We, therefore, identified antenna power of 1500 W to be optimal to take advantage of both the slightly higher etch rate and smooth surfaces.

Argon flow rate

Argon (Ar) gas is typically added to the gas mixture to reduce the passivating neutral to ion flux ratio important for the control of etch profiles [140]. Also, Argon's high mass density has the benefit of reducing micro masking, a potential effect attributed to the use of a metal mask in FS plasma etching [72].

The Ar flow rate was manipulated in the experiment while keeping C_4F_8 flow constant at 65 sccm. Ar addition of 0, 25, 50, 75, and 100 sccm were investigated.

Maximum etch rate was achieved with an Ar flow rate of 0 sccm. Etch rate of FS initially reduced with an Ar flow rate of 25 sccm, followed by an n-shaped graph where etch rate gradually recovered when the Ar flow rate up to 75 sccm and later decreased with further

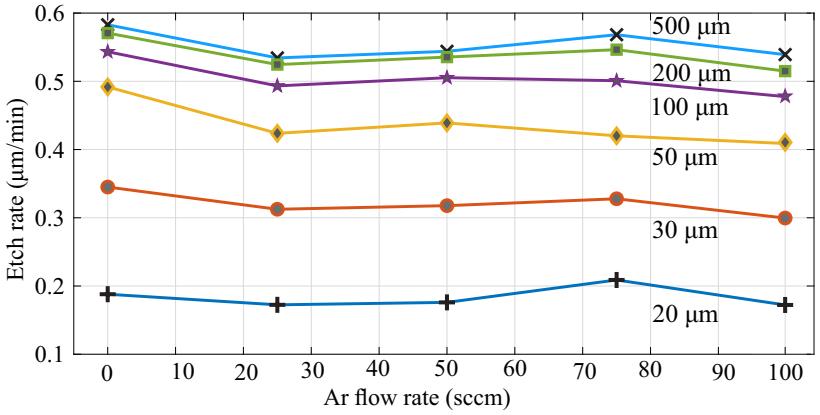

Figure 2.6: Effect of Ar addition on etch rate. A reduction in etch rate was initially observed, followed by a slight recovery of etch rate up to Ar flow rate of 75 sccm and another decrease in etch rate with flow rate exceeding 75 sccm.

addition of Ar. Figure 2.6 illustrates the relationship. The initial reduction of etch rate when Ar flow rate increased from 0 sccm to 25 sccm could be due to an increased fluorocarbon film deposition rate [62]. Thicker fluorocarbon film also resulted in a smoother sidewall, after which sidewall roughness degraded gradually (Fig. 2.7). We believe that when excessive Ar was introduced at 100 sccm (additive ratio of 1.53), the neutral passivation and the ion-assisted chemical etching were compromised. In turn, physical etching became the dominating etch mechanism, resulting in a lower etch rate and rough etched surfaces [1]. Figure 2.7 shows sidewall roughness for etching without Ar, with 25 sccm, and 100 sccm Ar flow rates.

Sidewall angles improved from a tapered profile to near-vertical with increased Ar flow rate, with the highest average of 92.6° obtained at Ar flow rate of 75 sccm. Further addition beyond this point reversed the effect for features with dimensions below 200 µm to form a tapered sidewall. Figure 2.8 shows the progression of sidewall angle with an increase of Ar flow rate.

The initial addition of Ar (25 sccm) decreased etch rate but offered slightly improved sidewall angle and best sidewall smoothness. Further increase in Ar flow rate up to 75 sccm resulted in an increased etch rate and near-vertical sidewall angle but slightly degraded etch surface

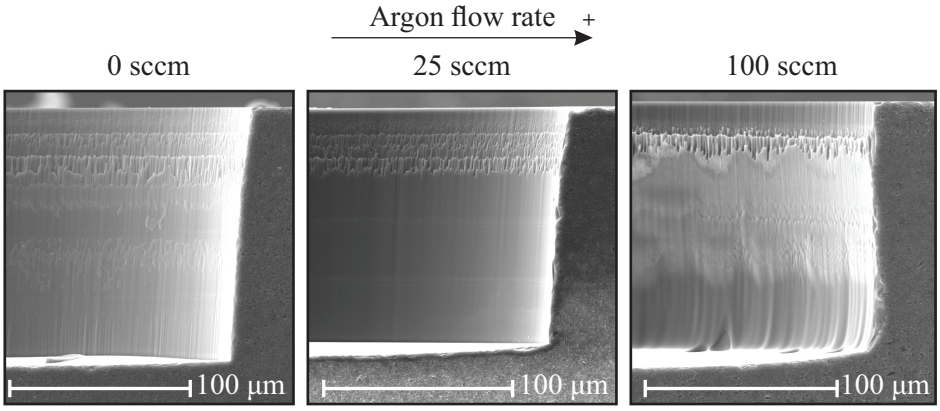

Figure 2.7: Sidewall roughness comparison between no Ar addition, Ar flow rate of 25 sccm, and Ar flow rate of 100 sccm. Sidewall roughness improved going from 0 sccm to 25 sccm flow rate but gradually degraded with higher Ar flow rates. At 100 sccm, physical sputtering became the dominating etching mechanism, roughening the surface.

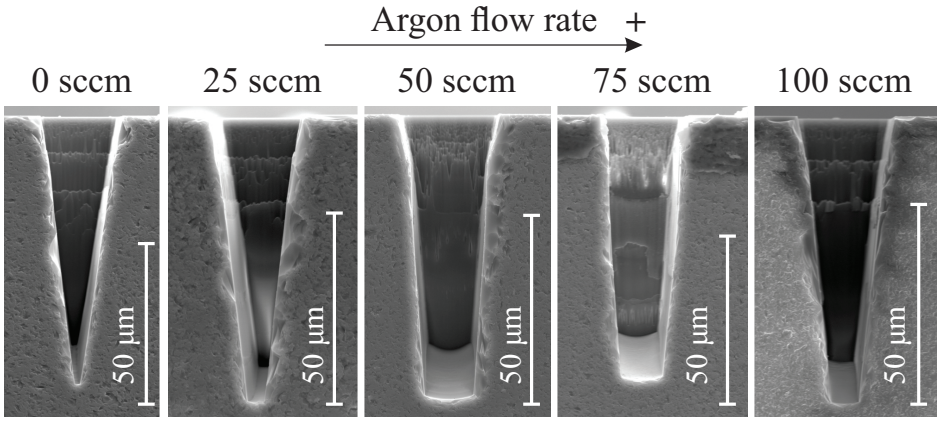

Figure 2.8: Sidewall angle progression in 30 µm channels with increase of Ar flow rate. Sidewall angle changed from tapered to near-vertical with an increase of Ar flow rate up to 75 sccm. Further increase in flow rate degraded sidewall angle.

roughness. Finally, etching with excessive Ar addition resulted in undesirable etch qualities of reduced etch rate, rough surface, and degraded sidewall angle. Thus, an Ar flow rate of 50 sccm was found to provide an optimal surface smoothness and near-vertical sidewalls.

Temperature and C_4F_8 flow rate

Platen temperatures of -5, 10, 25, and 40°C were compared. Higher temperature enhances the chemical etching process, and at the same time, it accelerates the removal of etching

byproducts, leading to a higher etch rate [66, 116]. As expected, etch rate increased with increasing temperature. The average etch rate across different dimensions as a function of temperature is shown in Fig. 2.9(a). No significant difference in sidewall angle was observed in this study. Therefore, the platen temperature of 40°C was regarded as the best parameter.

We investigated C_4F_8 flow rates of 55, 65, and 75 sccm, corresponding to oxygen to fluorocarbon ratios of 22%, 23%, and 27%, respectively. We observed an increase in etch rate with a C_4F_8 flow rate up to 65 sccm, with reduction observed when the flow rate was further increased to 75 sccm, Fig. 2.9(b). We believe that the initial enhancement of the etching process may be attributed to an increase in free radicals when the etch gas flow rate increases. However, high flow rate reduced etch rate possibly due to the high-density plasma and energy loss due to self-collision.

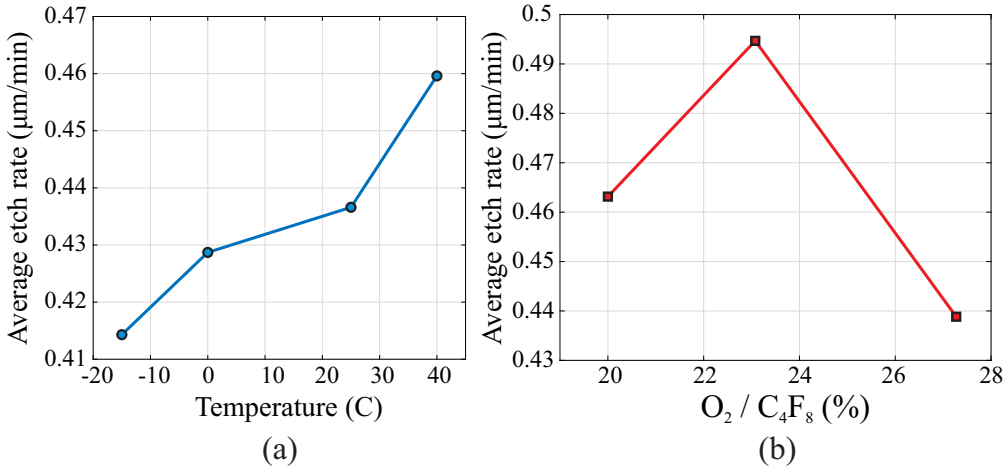

Figure 2.9: (a) Average etch rate across all feature sizes as a function of the platen temperature. Etch rate increased with increasing platen temperature as chemical etching process enhanced. The Effect of manipulating C_4F_8 flow rate on the average etch rate across all feature sizes is shown in (b). An initial increase followed by a decrease in etch rate was observed.

Surface roughness improved gradually with increasing C_4F_8 flow rate, with 75 sccm offering the best surface smoothness, possibly related to the deposited polymer layer at high C_4F_8 flow rate. Nonetheless, the sidewall angle was slightly tapered at 75 sccm C_4F_8 as the polymer layer impeded vertical etching. 65 sccm C_4F_8 flow rate was optimal, providing a

Table 2.2: Optimized fused silica plasma etching process parameters.

Parameter	Value
Pressure	4 mT
Platen power	300W
Antenna power	1500W
Temperature	40 ^{o}C
O_2 flow rate	15 sccm
Ar flow rate	50 sccm
C_4F_8 flow rate	65 sccm

high etch rate and smooth and near-vertical sidewalls.

With a goal of achieving a high etch rate, near-vertical sidewalls, and low surface roughness, optimized parameters for the FS plasma etching recipe were identified and are summarized in Table 2.2.

2.3 Micro-Resonant Device Fabrication Process

2.3.1 Considerations of Substrates and Processes

For fabrication of 2D FS micro-resonators, three approaches are commonly used and are discussed in this section.

In the first approach, an FS or an SCS substrate with pre-etched cavities is bonded to the FS device layer using plasma-assisted wafer bonding techniques. The device layer is etched after bonding using a high-density plasma source. Once the etch is completed, the resonator would be free to vibrate above the pre-etched cavities. In the case of using an FS substrate, the cavities are typically defined through wet etching, [111]; for an SCS substrate, cavities

are defined using Reactive Ion Etching (RIE), [36].

In the second approach, an FS device layer and an FS substrate layer are bonded through metal-to-metal compression bonding, [56], as opposed to the plasma bonding in the previously described approach. The metal layer is used as both the bonding material and sacrificial layer for releasing the structure after plasma etching of the device layer.

In the third approach, reported in [52], an FS device layer is bonded to an SCS substrate. The device layer is patterned using plasma etching, and the structure is released in the last step through isotropic etching of silicon material underneath the resonator.

We identified the respective trade-offs for each of the fabrication methods described. One of the main challenges for the pre-etched cavity approach (first approach) relates to the TEC mismatch between different layers. The structures experience a high temperature during plasma etching, especially when an FS substrate is used. Due to the TEC mismatch between the masking, device, and substrate, the FS device layer goes through high thermo-mechanical stress. Once the device layer is partially released, the TEC mismatch would cause deformations in the device layer, adversely affecting the etch profile.

Furthermore, after plasma etching, since the structure is released, it is fragile and prone to breakage in subsequent processing steps, reducing the yield. The second approach requires additional complex fabrication steps to define the bonding/sacrificial metal layers and planarize the metal posts for bonding the device and substrate layers. More importantly, in both the first and second processes, aligning the plasma etching mask to the cavities and the metal posts, which are defined in previous steps, is challenging.

In the third approach, since the device layer is fully bonded to the silicon substrate until the last release step, a higher yield is expected. On the other hand, due to the higher thermal conductivity of SCS substrate, an optimum cooling of the wafer during the plasma etching process can be achieved. Furthermore, no alignment is required as the FS-defined features

serve as release holes for etching the silicon substrate layer in the subsequent steps. Due to the advantages mentioned above, we focused on developing a process to fabricate planar fused silica resonators with silicon substrates (third approach) and demonstrated the process through fabrication of Fused Silica Toroidal Ring Gyroscopes (FS-TRG).

2.3.2 Fused silica-On-Silicon (FOS) Fabrication Process

We leveraged the optimized FS plasma etching recipe as part of a Fused silica-On-Silicon (FOS) process for high-yield fabrication of 2D FS micro-resonant devices. The proposed fabrication process is illustrated in Fig. 2.10.

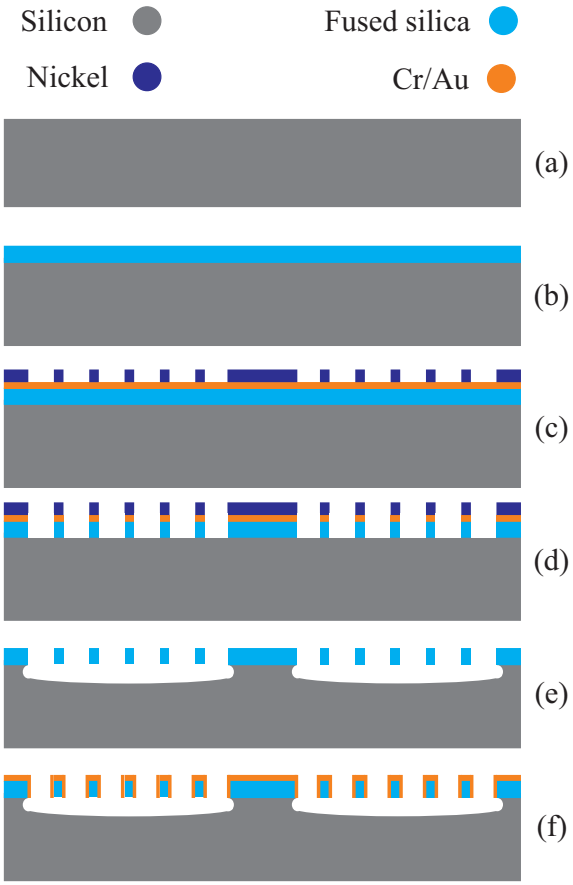

Figure 2.10: Schematics of the Fused silica-on-Silicon (FOS) fabrication process.

Initially, a 4-inch 500 µm thick SCS substrate wafer was bonded to a 100 µm thick FS wafer

through plasma-activated fusion bonding, as illustrated in step (b). For bonding, the wafers were immersed in an RCA-1 solution ($NH_4OH : H_2O_2 : H_2O = 1 : 1 : 5$) at 75 to 80 °C followed by rinsing with DI water and blow drying using nitrogen air. Using Plasma-Therm Reactive Ion Etching (RIE) system, the wafers were exposed to O_2 plasma for 150 seconds to increase the initial bonding strength. In the plasma treatment, we used an O_2 flow rate of 24 sccm, process pressure of 90 mTorr, and antenna power of 25 W. After surface activation, the wafers were rinsed with DI water and blow-dried with nitrogen. Subsequently, the wafers were manually brought into contact and were annealed on a hot plate for 8 hours at 200 °C. The annealing temperature was chosen to provide high bonding strength while avoiding wafer breakage due to a significant TCF mismatch between SCS and FS. The temperature was increased to 200 °C with a ramp rate of 30 °C/hour to provide enough time for thermal relaxation and partial stress release for both the SCS and FS layers.

In step (c), using electron-beam Physical Vapor Deposition (PVD), 10 nm chromium and 100 nm gold thin-film layers were deposited onto the FS device layer. The chromium layer served as an adhesion layer, and the gold layer was used as the seed layer for nickel electroplating. The chemically amplified AZ-12xT positive photoresist was used to create 15 μm thick molds for nickel plating. An HT-2 Ready-to-Use (RTU) nickel plating solution by Techni was used for electroplating 11 μm nickel on top of the gold layer with a deposition rate of 50 nm/min. After electroplating, the photoresist was removed by acetone, and the nickel layer was used for masking during the plasma etching step.

We determined that due to the TEC mismatch of the nickel layer and FS device layer, adhesion of the electroplated nickel layer to the gold layer was crucial to avoid nickel delamination during the plasma etching process. After the photoresist developing step, we performed photoresist descumming on the gold layer and surface conditioning by wafer dipping in diluted sulfuric acid (volume concentration of 5%) to enhance adhesion.

In step (d), the FOS wafer-stack was etched using UCI's SPTS APS PM oxide etching

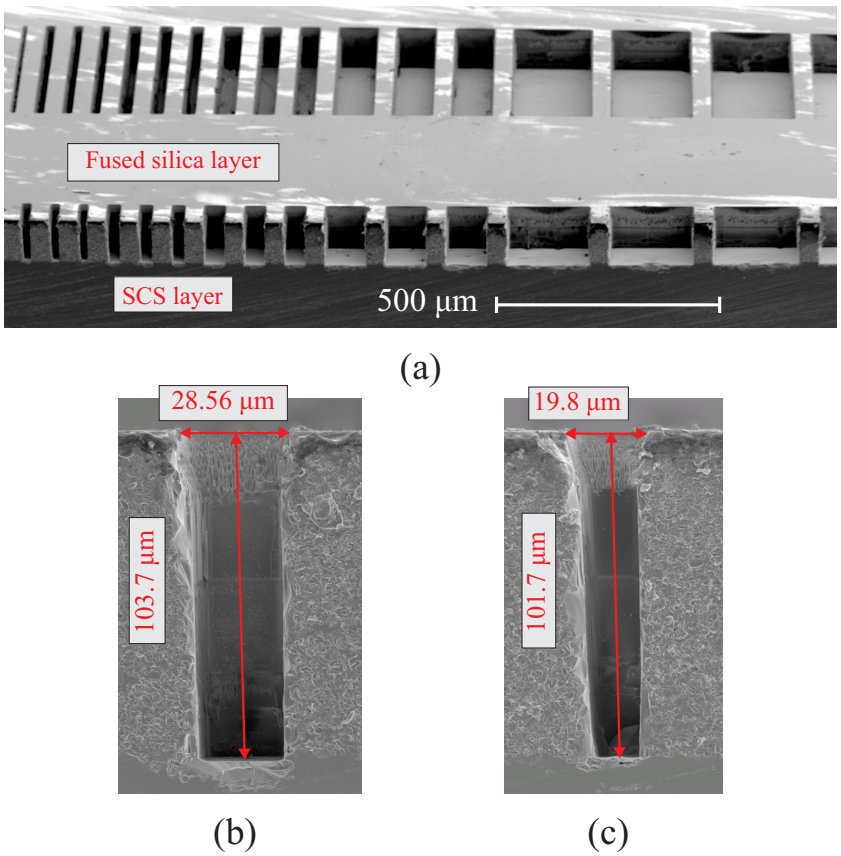

Figure 2.11: SEM images of a FOS test structure prior to release. In (a), a fully etched fused silica layer with rectangular channels of different opening sizes, ranging from 20 µm to 500 µm, is demonstrated. Cross-section images (b) and (c) demonstrate etched features with 3.3:1 and 5:1 aspect ratios and near-vertical sidewalls. The average etch rate was estimated to be on the order of 0.46 µm/minute.

system. The etching was performed with the optimized parameters reported in Section 2.2. Despite a mismatch in TEC of SCS and FS, due to the helium backside cooling mechanism along with a relatively high thermal conductivity of the SCS substrate, both a die-level and a wafer-level plasma etching of FOS structures were determined to be feasible. After plasma etching, the nickel mask and Cr/Au layers were removed through wet etching. Using SEM, cross-section images of the FOS test structures were used for characterization, as shown in Fig. 2.11. In the FOS process, the SCS substrate acted as an etch-stop. Therefore, Aspect Ratio Dependent Etching (ARDE) was avoided (Fig. 2.11(a)). We demonstrated 100 µm deep etched channels with aspect-ratios of 3.3:1 and 5:1, shown in Fig. 2.11 (b) and (c).

In step (e), the FOS structures were released by utilizing gaseous XeF_2 to etch the silicon substrate layer isotropically. At low pressures (10 mTorr), the XeF_2 crystal turns into a gas phase and enters the trenches defined on the FS device layer, isotropically etching the SCS substrate layer, illustrated in Fig. 2.12(a). We characterized the silicon etching process by defining a trench in the FS layer and etching the structure for 20 pulses, each for 60 seconds at a pressure of 3 Torr. A cross-section SEM of the structure, shown in Fig. 2.12(b), was used to characterize the etch rate and etch profile. The etch rate was estimated to be on the order of 5.2 microns-per-pulse, and it was used to determine the time required for full-release of resonant devices.

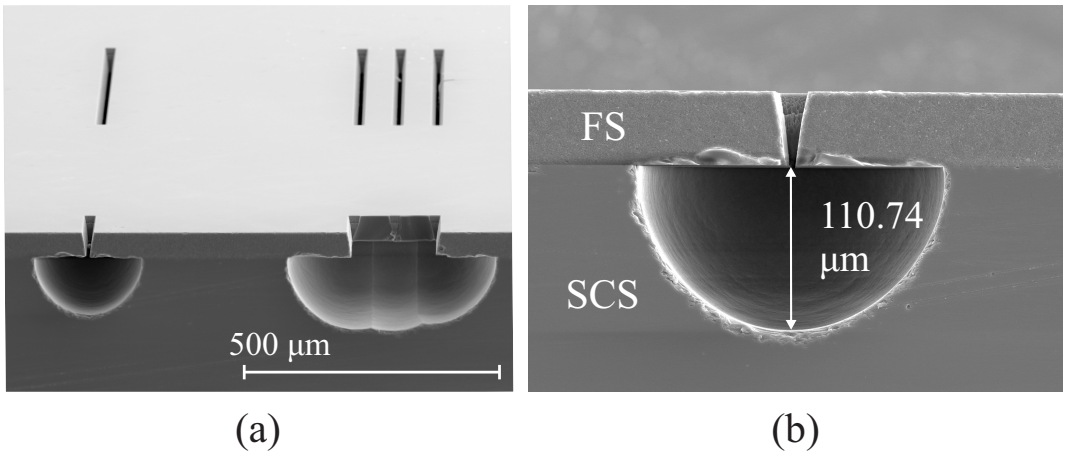

Figure 2.12: SEM cross-section images of FOS test structures etched using XeF_2 for 20 pulses. The isotropic etch profile for single-trench and triple-trench features defined in the fused silica layer is illustrated in (a). The isotropic etch rate for a single-trench opening was estimated to be on the order of 5.2 microns-per-pulse shown in (b).

In step (f), piranha cleaning was used to remove polymers left from the plasma etching process and residues from the metal etching agents. We did not observe stiction issues during piranha cleaning after the releasing process for a capacitive gap size on the order of 25 μm and a minimum resonant frequency of 10 kHz. The cleaning was followed by a metal coating of the FS structure to provide conductivity for electrostatic actuation and detection.

2.4 Toroidal Ring Gyroscope Design

To demonstrate the FOS process, we implemented a Fused Silica Toroidal Ring Gyroscope (FS-TRG) resonator. The TRG design architecture consists of concentric rings, which serve as both the inertial mass and suspension elements of the resonator, [101, 104]. The rings are connected through spokes and anchored at the outer ring, as shown in Fig. 2.13.

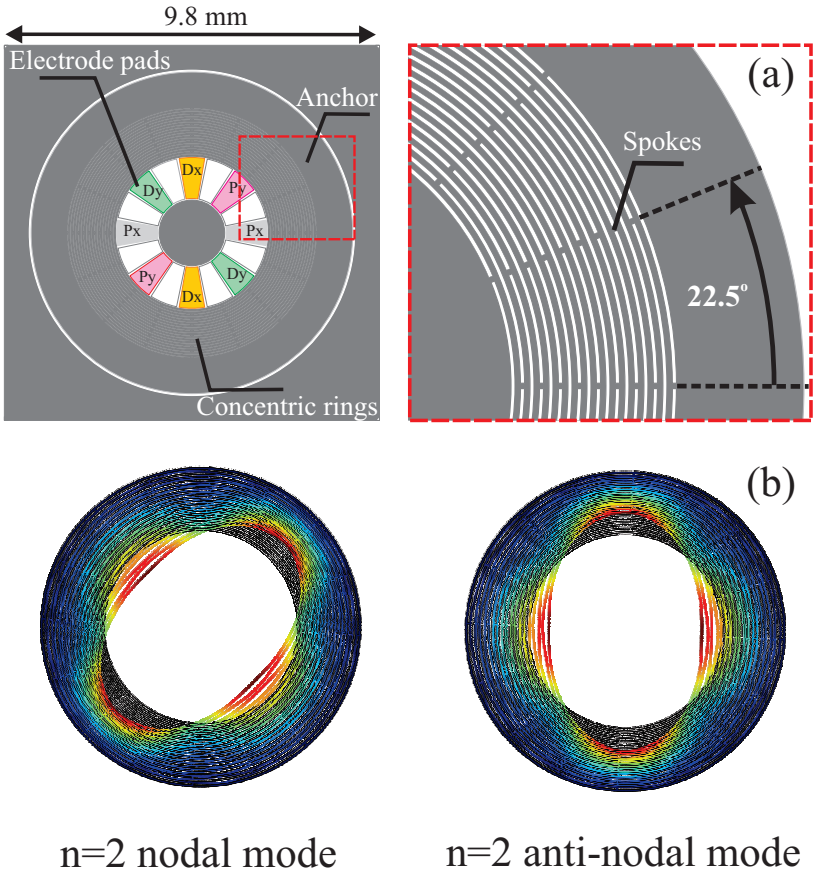

Figure 2.13: The design of the TRG used for demonstration of the FOS process is shown in (a). The modal deformations of n=2 wineglass modes are illustrated in (b).

The TRG was designed to operate in the n=2 wineglass modes (Fig. 2.13(b)). Based on the balanced dynamics of the wineglass modes along with the isotropic mechanical properties of FS, the energy loss through anchors of the FS-TRG was anticipated to be minimal. Sixteen electrode pads were designed, facing the innermost ring for electrostatic actuation, detection, and frequency tuning.

In the TRG design, 18 rings with a width size of 40 μm and a gap size of 30 μm were used. To minimize quality factor degradation through mode coupling, we selected the number of rings, anchor size, and ring width to achieve a minimum frequency separation of 2 kHz between the operational n=2 wineglass modes and the parasitic modes, [127].

Through Finite Element Analysis (FEA) using COMSOL multiphysics software, the resonant frequency and TED quality factor of the FS-TRG were calculated to be on the order of 10.35 kHz and 3.6 M, respectively. In Table 2.3, by comparing simulation results for single-crystal silicon and fused silica as the structural material, we illustrate the benefit of using fused silica to achieve a higher TED quality factor limit.

Table 2.3: FEA simulation results on TED quality factor and resonant frequency of TRG design architecture.

Parameters/material	Fused silica	Silicon
TED quality factor	3.6M	32k
Resonant frequency	10.35 kHz	15.46 kHz
Parasitic separation	2.36 kHz	3.28 kHz

2.5 Device Characterization Results

In this section, we present results on the fabrication of FS-TRG using the FOS process and the experimental data of structural characteristics, including the frequency split and quality factor.

2.5.1 Fabrication

To reduce the duration of FS device layer etching, the FS-TRG structures were etched with a platen power of 400 W. As a result, we were able to etch the 100 μm FS layer in less than 170

minutes (an etch rate of 0.59 μm/minute). SEM images of an FS-TRG fabricated through the FOS process are shown in Fig. 2.14, taken prior to the releasing step. The concentric rings and the electrode pads are demonstrated in Fig. 2.14(a). A cross-section image of the concentric rings is shown in Fig. 2.14(b), annotated with dimensions and bonding interface between the FS device layer and SCS substrate layer.

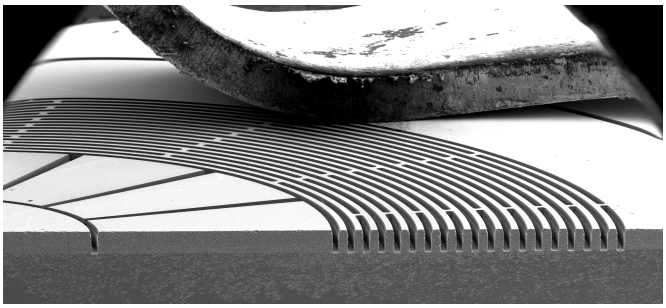

(a)

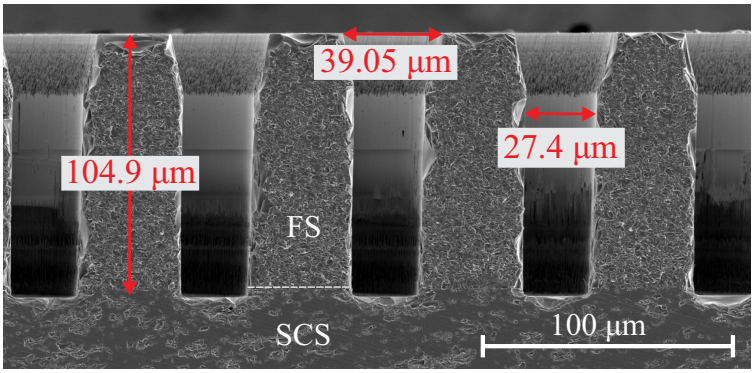

(b)

Figure 2.14: SEM images show the FS-TRG cross-section, (a), and a close-up cross-section of the concentric rings, (b). A complete plasma etching of the 100 μm thick FS device layer with near-vertical sidewalls is demonstrated. Due to a lower selectivity at higher platen power, faceting and surface-roughness are evident on the top portion of features.

Through different experiments, we determined that ten 60-second cycles of XeF_2 etching were enough to fully release a single FS-TRG structure. During the releasing step, we utilized optical images (top view) to confirm a full-release of the FS-TRG structure, shown in Fig. 2.15(a). Due to a nonuniform etch rate of SCS, the releasing step was carried out on individual die level. Notably, we observed that the etch rate of SCS would reduce with an increase in the number of devices to be released simultaneously, possibly as a result of the

loading effect.

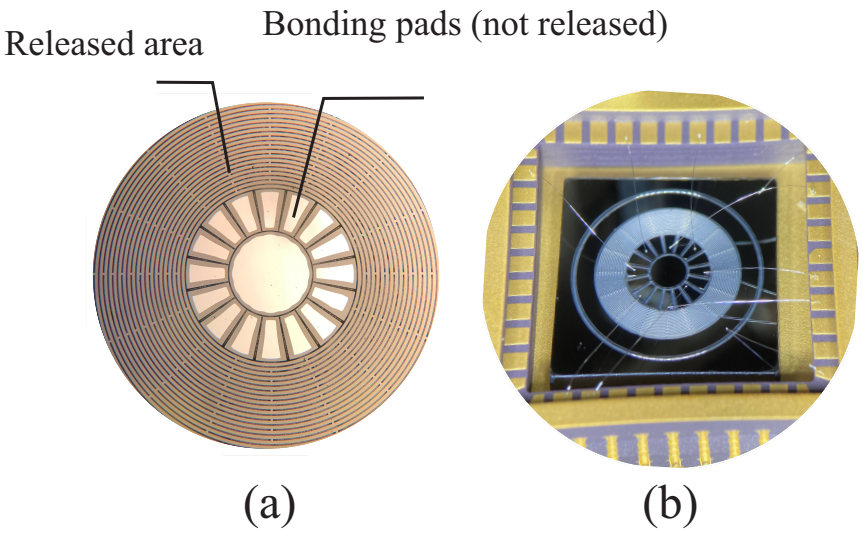

Figure 2.15: An optical image (top view) was utilized to determine a full-release of the FS-TRG structure shown in (a). An image of the released FS-TRG wire bonded to a chip carrier is shown in (b).

2.5.2 Structural Characterization

After releasing, the FS-TRG structures were uniformly coated with a 5 nm thick chromium layer using Denton DC sputtering system. The devices were temporarily attached and wire bonded to a chip carrier for electrostatic actuation and detection, Fig. 2.15(b). The FS-TRG devices were tested in a vacuum chamber at a pressure below 30 μTorr.

Using a Zurich HF2Li lock-in amplifier, the Device Under Test (DUT) was excited using a combination of DC and AC voltages applied to the drive electrodes. At the same time, the displacement of the inner ring was measured both electrostatically and using Laser Doppler Vibrometer (LDV). A side-by-side comparison was performed between the frequency response measured using the LDV and the simulated natural frequencies to identify different modes, shown in Fig. 2.16. Considering the Critical-Dimension (CD) loss in lithography and etching, which caused a deviation between the design and the actual ring width (shown in Fig. 2.14), the measured resonant frequencies were in good agreement with the FEA results.

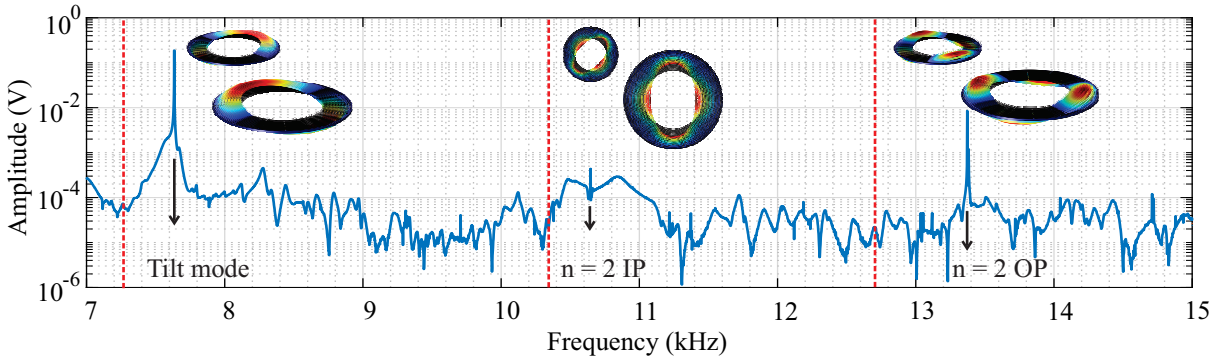

Figure 2.16: Frequency response of an FS-TRG device. The experimental measurement is shown using a continuous line, and the dashed lines mark the simulated natural frequencies for the in-plane n=2 wineglass modes, the tilt, and the n=2 out-of-plane modes. Considering the CD loss in plasma etching, the measured resonant frequencies are in good agreement with the simulation results demonstrating a mode separation above 2 kHz.

By utilizing the frequency response and ring down response, we characterized the frequency split and quality factor of two FS-TRG devices in their n=2 wineglass modes, summarized in Table 2.4. Based on an electrostatically measured frequency response shown in Fig. 2.17, we measured a frequency split as low as 8 Hz and quality factor as high as 539k in the FS-TRG devices. To the best of our knowledge, these results demonstrate the highest quality factor measured in metal-coated planar FS micro-resonators in the kilohertz frequency range.

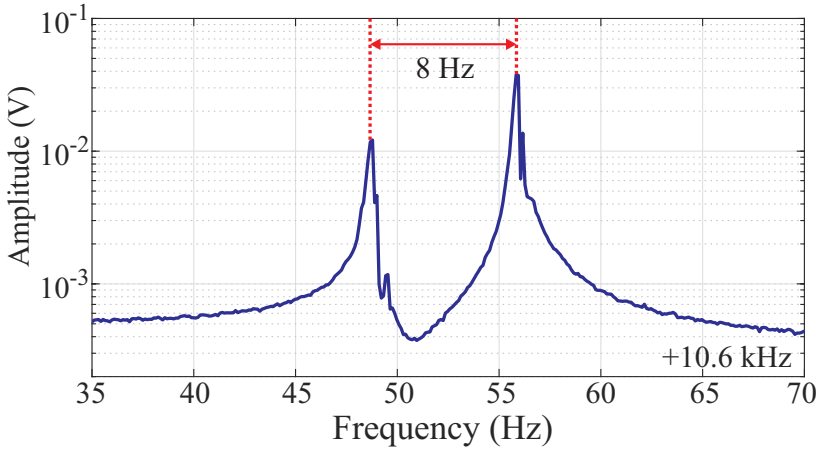

Figure 2.17: Frequency response of TRG #2 measured through electrostatic actuation and detection. An as-fabricated frequency split as small as 8 Hz was measured, which is an indication of acceptable process control and uniformity of etch rate.

Table 2.4: Experimental characterization results of two FS-TRG.

Parameters	TRG #1	TRG #2
Resonant frequency 1	10.453 kHz	10.648 kHz
Resonant frequency 2	10.466 kHz	10.656 kHz
Frequency split	13 Hz	8 Hz
Quality factor 1	539k	488k
Quality factor 2	511k	436k

2.5.3 Quality Factor Study

As noted from the simulated TED quality factor of FS-TRG structure (Table 2.3), we anticipated that other energy dissipation mechanisms were affecting the quality factor of the device. Based on results in [75], we hypothesized that metal coating was potentially reducing the quality factor of the TRG.

To characterize the effect of metal coating on quality factor, we coated an FS-TRG device with different thicknesses of chromium varying from 5 nm to 30 nm. Before depositing a thicker chromium layer, we removed the previously deposited metal layer through wet etching. The device was then cleaned using piranha solution and dehydrated for 4 hours at 120 $^{\circ}C$. We measured the quality factor of both n=2 in-plane and out-of-plane wineglass modes in each experiment. The measured quality factors as a function of metal thickness are shown in Fig. 2.18.

By increasing the thickness of the metal layer, we observed an increase in sensitivity of capacitive detection. However, as shown in Fig 2.18, by increasing the thickness from 5 to 30 nm, a quality factor reduction of more than 50% was observed for all four modes. After reaching a metal thickness of 5 nm, we repeated the experiment by removing the chromium layer and depositing a 30 nm chromium layer. We observed acceptable repeatability in the experimental results, which confirmed the negative effect of metal coating on quality factor of FS-TRGs. The quality factor degradation in the out-of-plane modes was more drastic

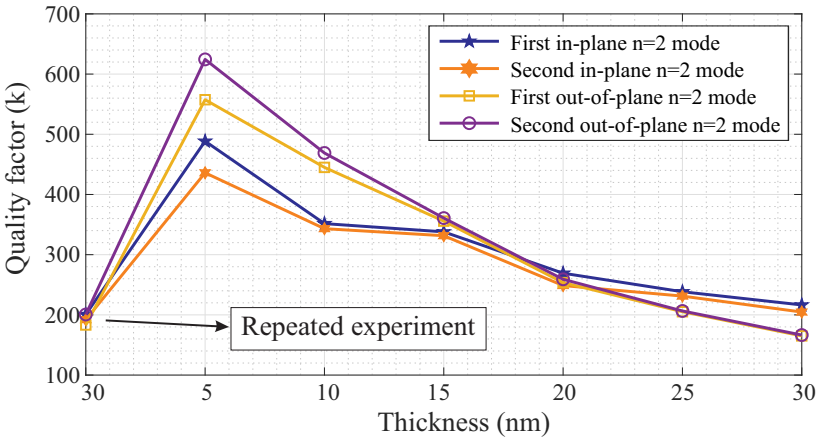

Figure 2.18: Experimental data demonstrating the effect of metal coating on quality factor of wineglass n=2 in-plane and out-of-plane modes of the FS-TRG. As shown, by increasing the metal thickness from 5 to 30 nm, a quality factor reduction of more than 50% in all modes was observed.

than the in-plane modes, possibly due to the thickness distribution of the metal layer on the top surface and sidewalls and the difference in modal deformations.

2.6 Conclusion

In this chapter, we presented a study on developing a fabrication process for planar fused silica micro-resonant devices. For demonstration, a Toroidal Ring Gyroscope (TRG) was fabricated through the developed process. We demonstrated results on plasma etching recipe optimization and structural realization of TRG with a 100 μm thick device layer. We experimentally demonstrated a successful electrostatic actuation and detection for the operation of the FS-TRG. While a relatively high roughness on the sidewalls due to the plasma etching process was observed, we measured a quality factor on the order of 539k, and a frequency split as low as 7 Hz for the FS-TRG with a 5 nm thick metal coating. To the best of our knowledge, in this work, we demonstrated the highest quality factor planar micro-resonant devices fabricated from fused silica through plasma etching with operational frequencies in the kilohertz range.

Based on structural characterization results, a high correlation between quality factor and thickness of the metal coating was noted, indicating that metal coating of 2D FS resonators is a major source of energy dissipation that needs to be mitigated.

Chapter 3

Fabrication Based on Ultrafast-Laser-Induced Chemical Etching (ULICE)

3.1 Introduction

In the previous chapter, we presented results on adopting conventional micromachining processes to fabricate resonant MEMS from fused silica material. Fabrication of fused silica resonators through plasma etching is a complex process, which includes wafer bonding, multiple lithography steps, metal coating, electroplating, metal etching, etc. More importantly, due to the chemical inertness of fused silica material, plasma etching is a slow process and yields a limited Aspect-Ratio (AR), typically below 10:1. The heat generated during plasma etching produces a large amount of stress due to the Thermal Expansion Coefficient (TEC) mismatch between different layers.

To overcome these limitations, we explored a novel and non-conventional approach for fab-

ricating resonant MEMS from optically transparent material, such as fused silica, using Ultrafast-Laser-Induced Chemical Etching (ULICE). In this chapter, we discuss our results on developing a Femtosecond Laser-Induced Chemical Etching (FLICE)-based process for fabrication of planar fused silica MEMS resonators for the first time. We demonstrate the process by fabricating Disk Resonator Gyroscope (DRG) prototypes; experimental results on the functionality of the fabricated devices and the structural characteristics are presented.

This chapter is organized as follows. In Section 3.2, we introduce the FLICE technique and review its advantages as compared to conventional laser micromachining processes. Section 3.3 presents our results on optimization of the laser marking parameters to achieve fast and high-aspect-ratio etching through FLICE. In Section 3.4, we discuss a laser-based manufacturing process fabricating resonant MEMS from a single-layer fused silica material. In the same section, results on the fabrication of DRG prototypes are presented to demonstrate the process; furthermore, structural characterization results of the fabricated devices are included. A summary of our results and conclusions are found in Section 3.5.

3.2 FLICE

Sub-bandgap laser light emitted with short pulses results in non-linear photoionization when focused tightly within a dielectric material, [113]. Using a femtosecond laser with ultrashort pulses, the absorption of optical energy induces a variety of highly localized modifications to the material's structure while leaving the surrounding material largely unaffected.

Depending on the pulse duration and the pulse energy, the laser modification can manifest itself in several ways, [43]. At higher pulse energies, micro-explosions are created within the laser's focus, destructively melting and modifying the material, [33, 106]. This type of modification is commonly referred to as Type III modification (i.e., laser ablation). In type

II modification, using mid-range pulse energies, nano-gratings with a sub-wavelength period are created, increasing the material's chemical etching rate by orders of magnitude. The femtosecond laser-induced selectivity, around 1000:1, is leveraged for patterning 3-dimensional structures from different glass materials, [10, 16, 39, 41]. The etching side of this two-step process is a matter of submerging the irradiated material in a bath of aqueous HF or KOH solutions, depending on how accurate or rapid we wish to etch the material.

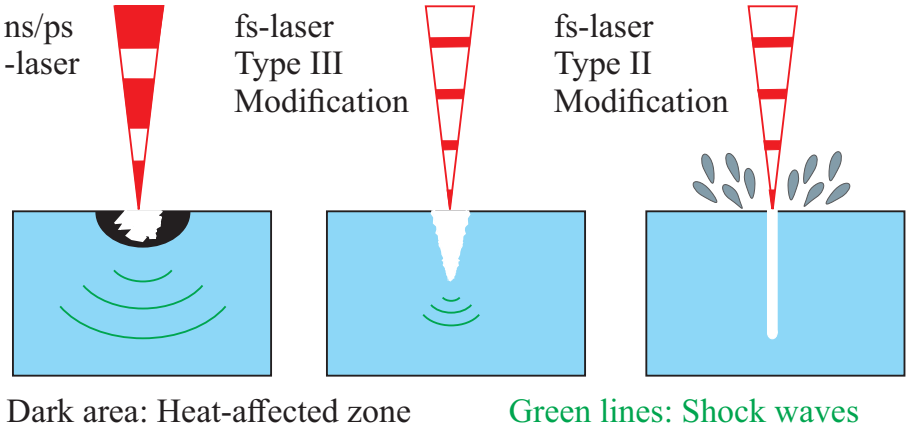

Figure 3.1: A comparison between using ns/ps lasers, fs-laser type II, and fs-laser type III micromachining of fused silica material.

For ultrafast lasers, energy deposition occurs on a timescale that is short compared to atomic relaxation processes. As a result, the Heat-Affected Zone (HAZ) in the material is minimized, [100]. Also, at lower pulse energies required for the type II modification, we avoid generating shock waves which potentially result in micro-cracks in the material. Since the material modification is confined to the laser focal volume, laser inscribing can be performed deep within a transparent substrate. As compared to picosecond laser-induced modification, a femtosecond laser provides an ultra-high-resolution of etching primarily determined by the pulse energy and the size and shape of the laser focus (plasma zone), [25].

Therefore, translating the material through the laser focus in three dimensions allows for arbitrarily shaped channels, planes, or volumes to be inscribed. The applications of FLICE in fabrication of glass micro-components such as micro-optics, microfluidics, micromechanics,

and lab-on-chip devices are reviewed in [16].

In the following, we report our results on optimization and implementation of FLICE for fabricating Fused Silica (FS) vibratory MEMS.

3.2.1 Laser System Configuration

Standard components of a femtosecond laser micro-machining system are a femtosecond laser source, an Acousto-Optic Modulator (AOM), galvanometer scanners, linear stages, Computerized Numerical Controlled (CNC) type motion controllers, a polarizer, and an objective lens. Our work focused on optimizing the multi-component system for a fast throughout wafer-level fabrication process with high repeatability.

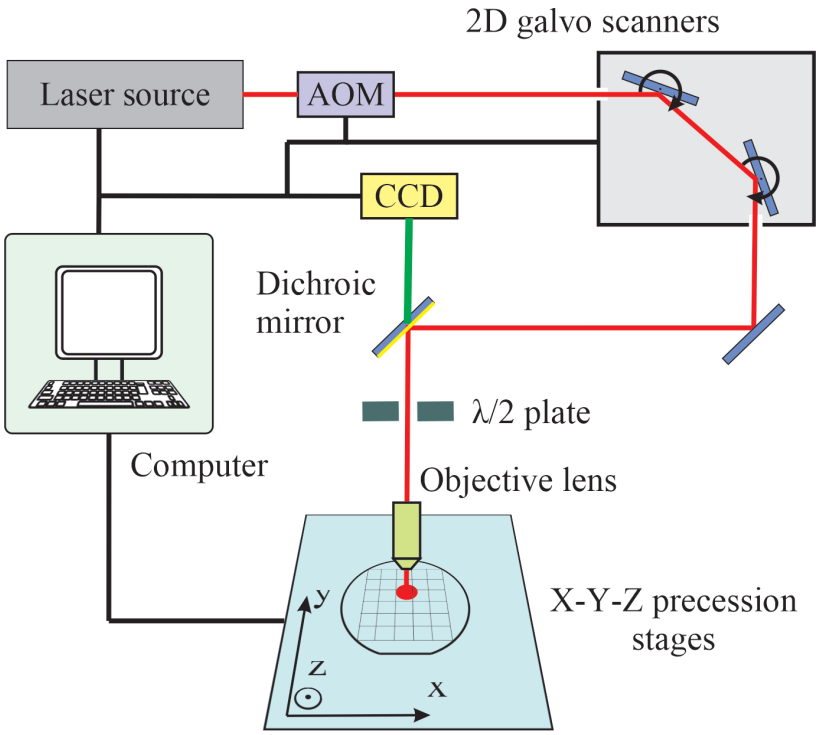

Figure 3.2: Schematics of UCI's FS laser station used for the FLICE process.

As the core part of the system, the femtosecond laser source generates ultra-short laser pulses

at a high repetition rate. Due to its unmatched flexibility, we integrated a Light Conversion Carbide laser source with UCI's FS laser station, which generates laser pulses at 1030nm wavelength with energies up to 83 µJ (5W in power) in a single-shot or with a repetition rate up to 1MHz. The pulse duration is adjustable and can be set to 290 fs – 20 ps values. The AOM module adjusts pulse amplitude (pulse energy), depending on the working material and the intended type of modification. A Mitutoyo 50X magnification lens (NA=0.42) was used to focus the collimated beam deep in the bulk of the transparent material.

The Femtosecond Laser-Induced Chemical Etching (FLICE) process requires the positioning of the working sample, very precisely and at high speed, over a considerable distance along the X and Y axes. The configuration used in UCI's femtosecond laser station employs an XY translation stage and a galvanometer (galvo) dual-axis scanner. Translation stages can provide long movement, but they typically have large inertial loads, therefore, low operational speeds. Galvo scanners provide rotary motors that drive small mirrors for the deflection of the laser beam. The inertial load in these scanners is typically small, providing high-speed movement. Through the Infinite Field of View (IFOV) module, a single controller is utilized to operate these two disparate actuators, i.e., slow long-stroke actuator (stage) and fast short-stroke actuator (scanner). When they are mechanically configured in series, they provide long (a travel distance of up to 6 inches) and fast movement (a speed of up to 30 mm/s) with ultra-high resolution and accuracy. Along with the XY translation stages, a Z-axis motorized stage is used to focus the laser in the bulk of the material and modify it at different depths.

In the configuration, which is shown in Fig. 3.2, a rotary motor with a half-wave plate is used to linearly polarize the laser beam and maintain the polarization perpendicular to the direction of writing to achieve the highest selectivity in etching, [44, 112, 117]. An objective lens is used to tightly focus the collimated beam on the surface or in the bulk of the material. The Charge-Coupled Device (CCD) camera and the dichroic mirror provide an in-axis live vision of the process sample through the objective lens.

When configured for the FLICE process, the system produces a final beam spot size of approximately 3 μm, filtered using a 4-F optical system. It will utilize the 2-axis scanner and the 3-axis cartesian motion package for producing the required raster motion. The two motion components will work in concert through IFOV software to create a seamless blend of scanner and linear axis motion required by the process.

3.3 Process Optimization

Since laser-based manufacturing is performed in series, optimization of the process parameters is required to achieve high throughput manufacturing. Optimization was performed with three main goals:(a) to increase the selectivity of wet etching, (b) to increase the laser marking speed, and (c) to achieve optimal surface quality.

For fabrication of MEMS resonators, a higher selectivity is correlated with the etch profile and the maximum achievable AR of etching; increasing the laser marking speed would allow us to perform wafer-level fabrication in a short process time. Last but not least, we need to choose optimal process parameters to reduce surface roughness and other defects in microstructures patterned using FLICE. Among the process parameters which must be optimized are pulse energy, pulse width, repetition rate, marking speed, and beam shaping [138].

3.3.1 1D Channel Patterning and Optimization

The FS laser station was configured to output a tightly focused Gaussian laser beam. Inscribing and wet etching of 1-Dimensional (1D) channels in the bulk of fused silica material, illustrated in Fig. 3.3(a), is commonly used to optimize the parameters of the FLICE process [27]. In our experiment, we inscribed 30 mm long straight lines, with different laser parameters, 100-microns deep below the surface of FS samples. The samples were mechan-

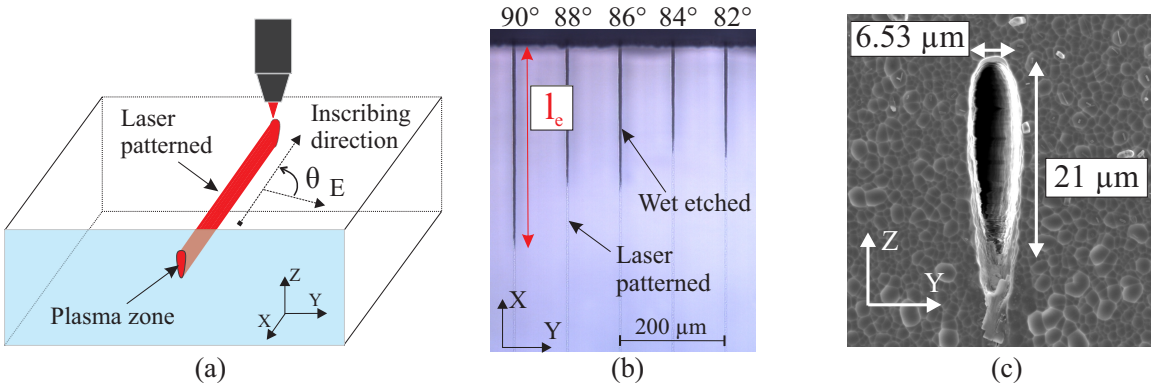

Figure 3.3: (a) Schematics of a 1D laser inscription. Laser parameter optimization was performed based on the measured etch rate of 1D channels. (b) An optical image of wet etched 1D channels patterned using FLICE at different polarization angles (top view). (c) Cross-section SEM image of an etched 1D channel inscribed inside of the material.

ically diced so that the entrance of the channels was exposed to 8M KOH solution at 85°C during the wet etching step. After 1 hour of wet etching, due to the birefringence effect, the etched channels appeared darker as compared to the laser-modified but non-etched areas, shown in Fig. 3.3(b). A cross-section Scanning Electron Microscope (SEM) image of 1D channels after wet etching is shown in Fig. 3.3(c). By measuring the length of the wet-etched channels (l_e), we investigated the optimum parameters for the FLICE process. The effect of polarization, pulse energy, and marking speed is discussed in the following.

Polarization

It has been reported that a linearly polarized laser beam with an orientation perpendicular to the direction of inscription provides the highest selectivity in FLICE [27, 112]. We investigated this by laser inscribing and wet etching of multiple 1D channels along the X-axis and setting the orientation of polarization (θ) at different values using the servo-controlled half-wave plate.

As illustrated in Fig. 3.4, we observed a high correlation between polarization and etch rate. These results confirmed that the polarization of the laser must be kept perpendicular to the

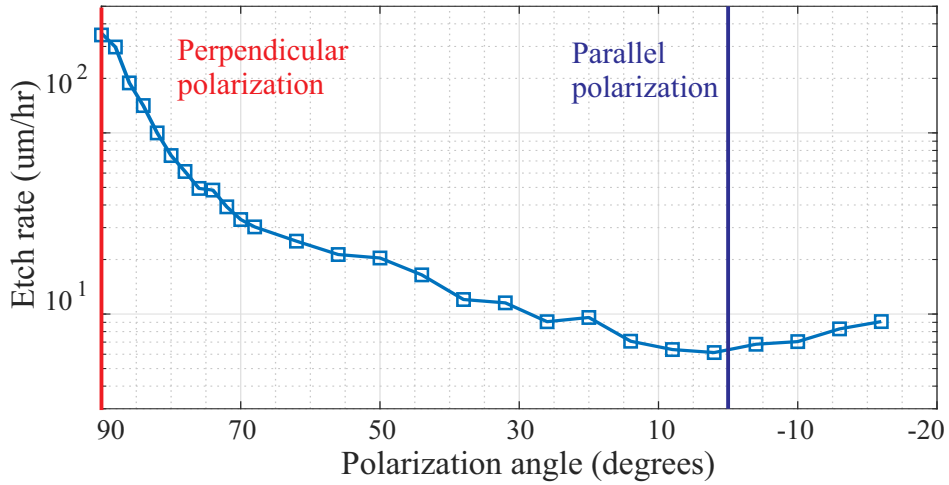

Figure 3.4: Measured etch rate of 1-dimensional channels patterned using FLICE at different polarization angles annotated as θ in Fig. 2(a).

marking direction to achieve the highest selectivity in the FLICE process. This observation is partly explained by the fact that nano-gratings are formed perpendicular to the polarization direction in type-II modification. By having self-aligned nano-gratings along the marking direction, the wet etching process is facilitated and the etch rate increases.

For laser patterning of MEMS resonators, especially gyroscopes, it is vital to have a high and consistent etch rate at different areas. Therefore, we implemented a function through which the servo-controlled polarizer dynamically adjusts polarization based on the direction of travel. To achieve a perpendicular polarization, we set the half-wave plate orientation based on the travel angle, demonstrated in Fig. 3.5, and a PID controller was utilized to reach the angle set point in a timely manner. We were enabled to pattern circular and other complex shapes through the dynamic polarizer.

Pulse Energy and Marking Speed

For a repetition rate of 125 kHz, 250 kHz, 500 kHz, 750 kHz, and 1 MHz, the etch rate was characterized for pulse energies ranging from 0.5 µJ to 4 µJ and marking speeds from 0.1 mm/s to 20 mm/s. Our results for a repetition rate of 250 kHz and 500 kHz are shown in

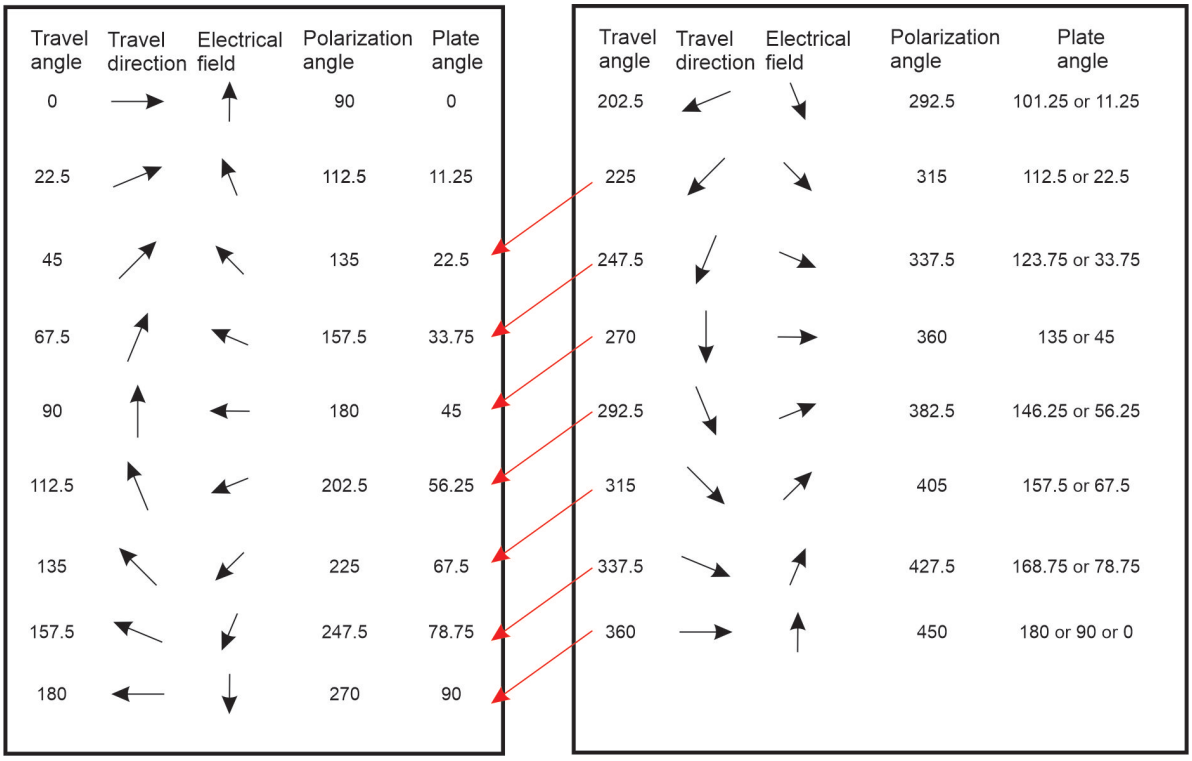

Figure 3.5: Set values for orientation of the half-wave plate as a function of the travel angle (i.e., the direction of travel).

Fig. 3.6(a) and (b).

Generally, we measured the highest etch rate (selectivity) at moderate pulse energies at low marking speeds. At higher marking speeds, we observed a significant drop in etch rate due to an insufficient effective number of pulses per area [92]. We observed lower etch rates at high pulse energies and high repetition rates, possibly due to the accumulation of heat in the material causing molten and re-solidified features (i.e., Type-III modification).

Using 8M KOH as the etching agent, we determined that for a pulse duration of 360 fs, pulse energy of 2 μJ yielded the highest etch rate on the order of 325 μm/hr at a relatively high marking speed of 5 mm/s. Based on the etch rate of pristine FS in 8M KOH solution at 85 °C, which is around 0.38 μm/hr, we achieved a selectivity on the order of 855:1 using the FLICE process. We believe that by researching a broader range of parameters, specifically by exploring a higher pulse duration, we can further optimize the process and achieve similar

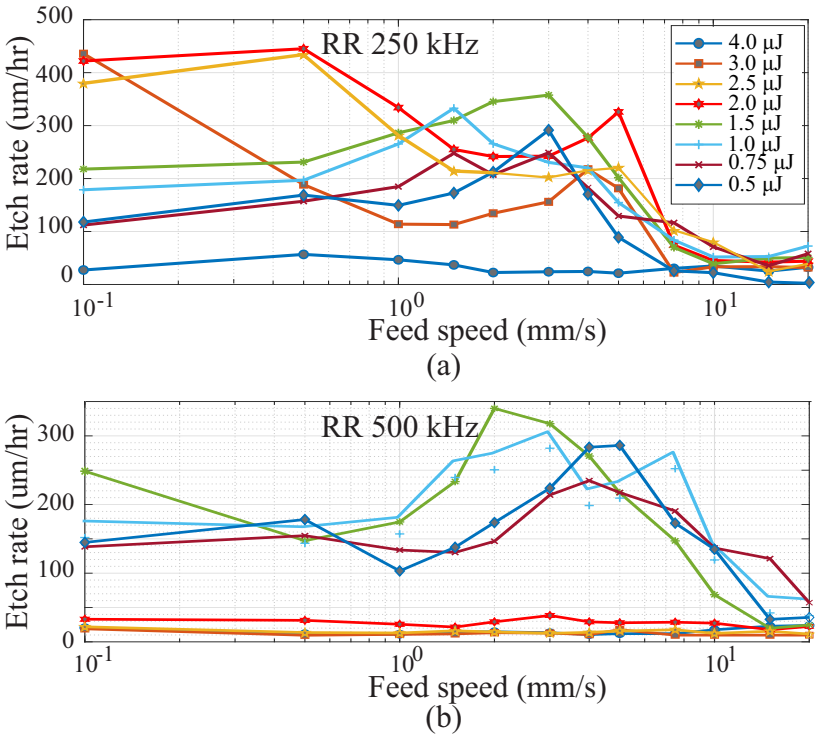

Figure 3.6: Measured etch rate for 1D channels patterned using the FLICE process at different pulse energies and marking speeds for a repetition rate of 250 kHz (a) and 500 kHz (b).

selectivity at an order of magnitude higher marking speeds [41].

Repetition Rate

At marking speeds above 5 mm/s, the repetition rate must be increased accordingly to achieve the same fluence (i.e., the effective number of pulses per area). We compared the maximum possible etch rate of 1D patterning for a given marking speed as a function of the repetition rate. Preliminary results, which we obtained using UCI's femtosecond laser system, are shown in Fig. 3.7. As demonstrated, for a marking speed of 10 mm/s, as the repetition rate was increased, the selective etch rate was observed to increase. However, we did not observe the same behavior for marking speeds of 15 mm/s and 20 mm/s.

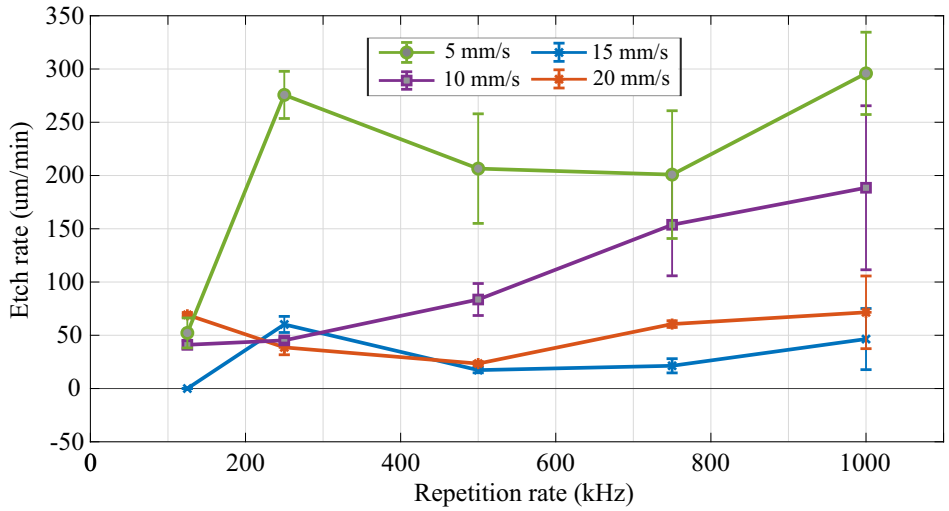

Figure 3.7: The maximum etch rate measured for a given marking speed, at different pulse energies, is illustrated as a function of the repetition rate.

Size of Laser-Modified Region

As previously mentioned, the size of the laser-modified region (i.e., the plasma zone) depends on the laser focal volume and the marking parameters, including the pulse energy and marking speed, [73]. To achieve smaller gaps and increase patterning resolution, we studied the effect of laser parameters on the size of the laser-modified region. The effect of marking speed on the laser-modified region is illustrated in Fig. 3.8. As shown, the laser-modified region size was largely unaffected by the marking speed and the effective number of pulses per area.

Based on the results in Fig. 3.7, we concluded that the highest etch rate was achieved at a marking speed of 5 mm/s. The etch rate at different pulse energies for a marking speed of 5 mm/s is shown in Fig. 3.9. For pulse energies between 0.5 μJ and 2.5 μJ, the etch rate was observed to be sufficiently higher with a value above 200 μm/hr; therefore, for this range of pulse energies, we studied the effect on the size of the laser-modified region.

The results are shown in Fig. 3.10. Based on the results, we concluded that we could regulate the length and width of the laser-modified region by adjusting the pulse energy, achieving a

variety of gaps and depths through a single-line laser patterning and wet etching.

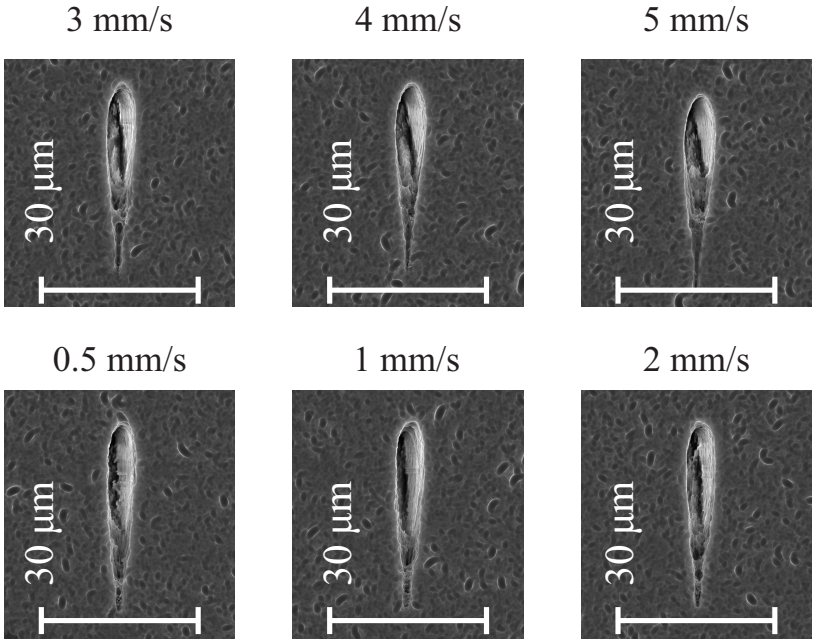

Figure 3.8: SEM cross-section images of 1D channels patterned with a pulse energy of 2 µJ at different marking speeds.

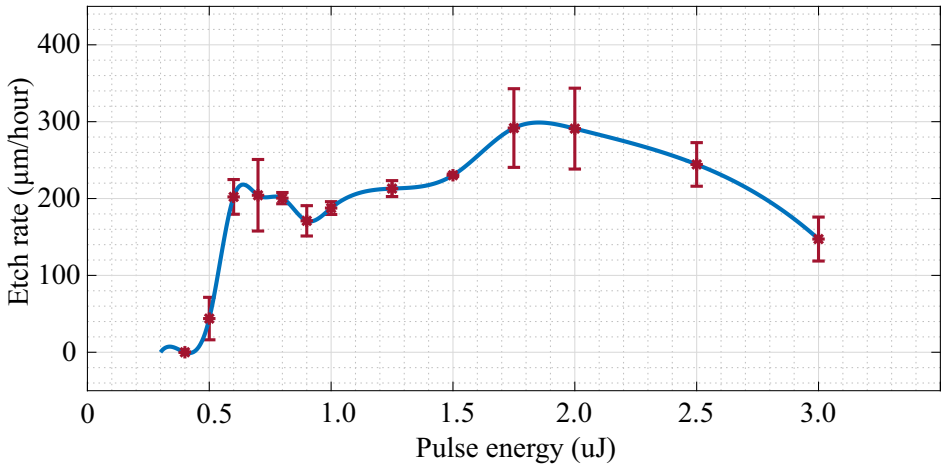

Figure 3.9: Measured etch rate at different pulse energies for a marking speed of 5 mm/s.

Another critical factor that affects the size of the laser-modified region is the beam waist diameter (i.e., beam focal volume). We conjectured that couple-of-microns and sub-micron openings could be realized by utilizing a higher Numerical Aperture (NA) lens and using a laser beam with a lower wavelength (515 nm or 257 nm).

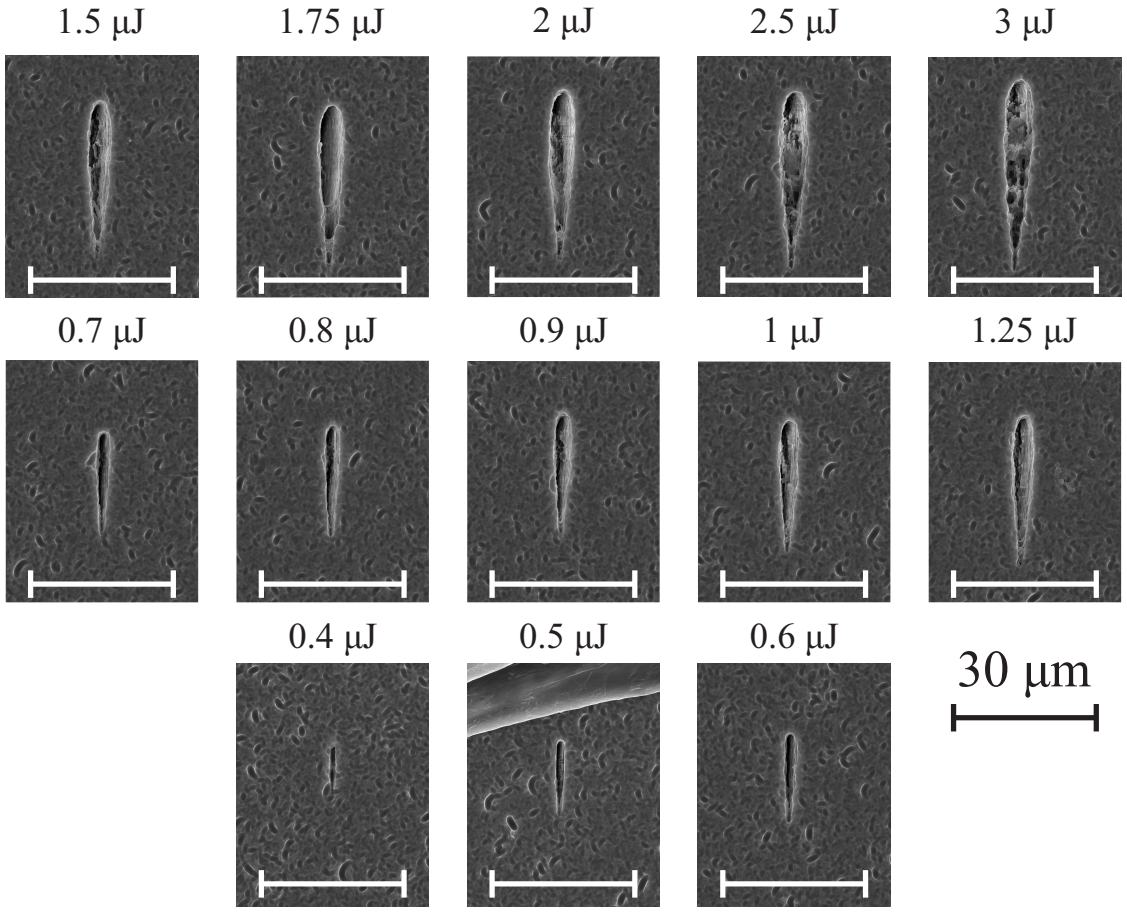

Figure 3.10: SEM cross-section images of 1D channels patterned at a marking speed of 5 mm/s and pulse energies ranging from 0.4-3 µJ.

3.3.2 2D and 3D Patterning

To pattern 2-Dimensional (2D) and 3-Dimensional (3D) features, 1D channels need to be stacked along the Y and Z axes to form a matrix and patterned through a raster motion. For the previously optimized laser parameters, the surface quality and etch rate of 2D and 3D patterns would depend on the density of the 1D lines. Here, we provide results on optimizing the etch rate and etch quality of 2D and 3D features based on the distance of two consecutive 1D patterns (i.e., the step size of patterning).

Patterning 2D Planes

As illustrated in Fig. 3.11(a), 2D planes can be patterned by inscribing 1D channels along the X-axis at different depths (i.e., different Z-positions). High AR 2D channels can be implemented in micro-scale resonators to define capacitive electrodes, suspension elements, etc.

We patterned 1D channels at different Z-positions with different Z-step sizes in an experiment. A repetition rate of 250 kHz, pulse energy of 2 μJ, and marking speed of 5 mm/s were used for patterning. Based on the results shown in Fig. 3.11(b), we observed that to achieve a higher etch rate in patterning 2D planes, the overlap between two consecutive patterns needs to be maximized by setting the Z-step size to 1 μm. As reported in [27], reducing the Z-step size would also help reduce the roughness on the sidewalls. We inscribed 300-microns-deep 2D planes in FS with a Z-step size of 1 μm and channels with an AR as high as 55:1 were demonstrated (Fig. 3.11(b))). We believe that what is demonstrated here is not the limit of the FLICE, and features with a higher AR can be achieved through the same process.

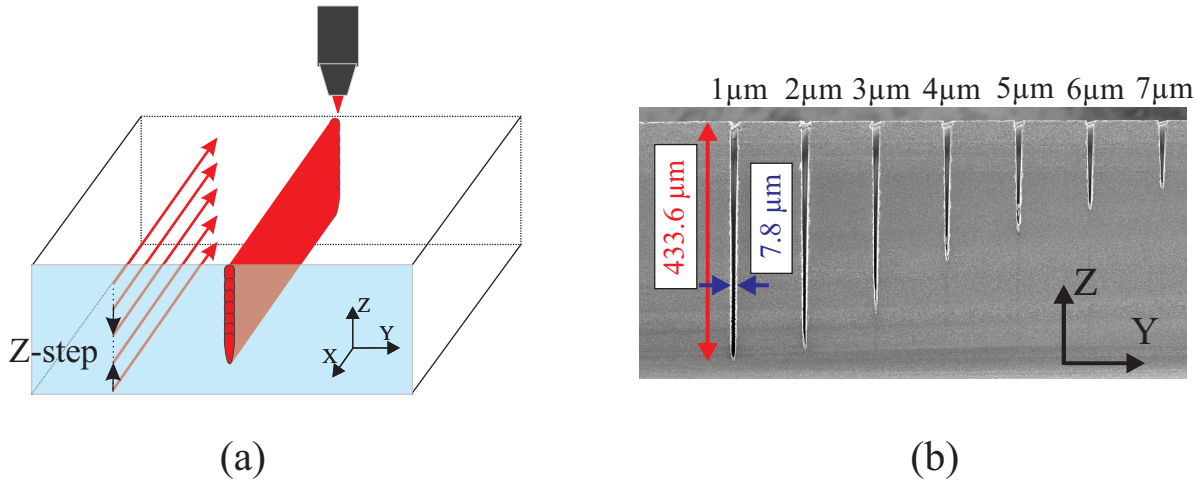

Figure 3.11: (a) Fabrication of 2D planes using the FLICE process by inscribing lines at different Z-positions. (b) Effect of the Z-step size on etch rate is illustrated.

Minimum Gap Size

In an experiment, we patterned 2D planes with a depth size of 75 µm and a Z-step size of 1 µm using pulse energies ranging from 0.4 µJ to 1.5 µJ. We investigated the minimum gap size achievable through 2D laser patterning. The SEM images are shown in Fig. 3.12.

Similar to results on 1D patterning, we confirmed that reducing the pulse energy provides smaller gaps, which is ideal for achieving higher capacitive transduction for electrostatic actuation, detection, and frequency tuning. In the case of etch rate, we observed that the etch rate of 2D planes reduces at higher pulse energies. By comparing this observation with results in Fig. 3.9, we see that the optimum pulse energy is not necessarily the same for 1D and 2D patterning. For wet etching of 1D patterns, the wet etchant enters the channels from the side and removes material along the direction of inscription. In 2D patterning, however, the etchant enters from the top surface, perpendicular to the direction of inscription. This could explain the discrepancy between the two results.

We also observed that the etch defects at the corner of the etched features were reduced in size at lower pulse energies. We believe that these defects were caused by glass debris

obstructing the laser beam. During 1D patterning close to the top surface, the material gets ablated, and in turn, glass particles are generated, which distort the laser beam in the following steps of patterning.

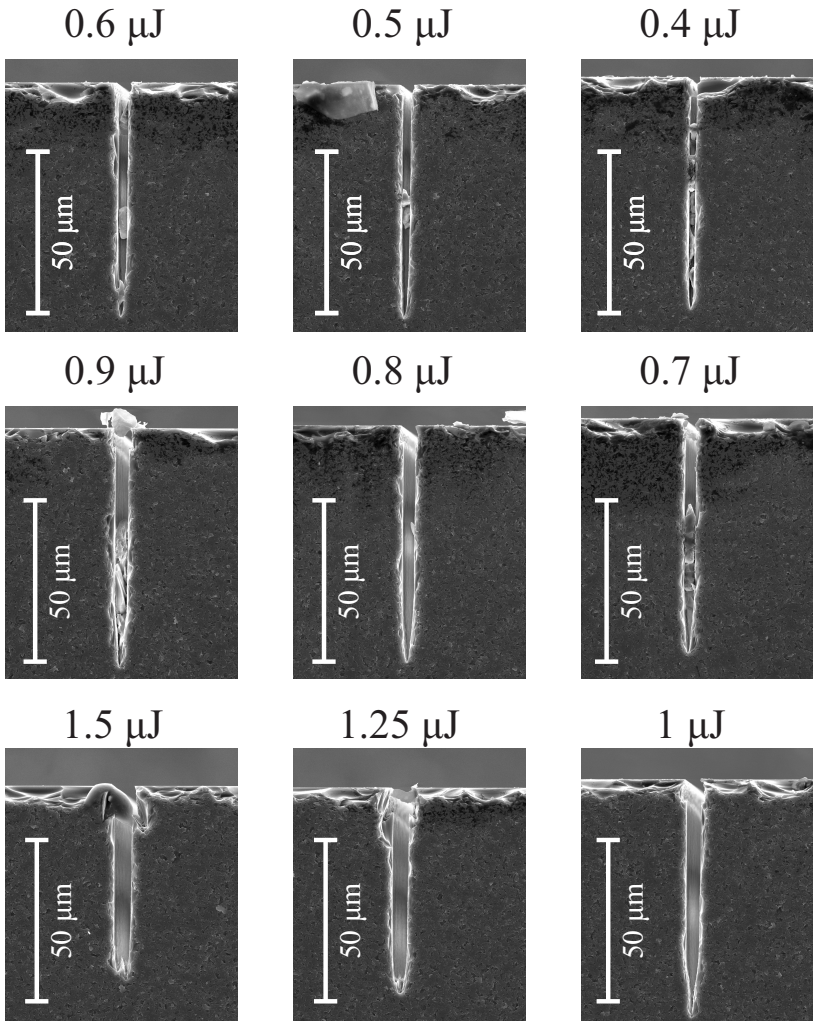

Figure 3.12: SEM cross-section images of 2D channels patterned at a marking speed of 5 mm/s and pulse energies ranging from 0.4-1.5 µJ.

Patterning 3D Features

In MEMS structures, it is beneficial to have the capability to pattern channels with different gap sizes. As an example, in parallel plate architecture, electrode fingers are arranged sequentially with smaller and larger gaps to create a net electrostatic force in an intended direction. To implement larger gaps than what is achieved by a single 2D plane, we explored patterning 3D features by stacking 2D planes. The same idea can be extended beyond patterning simple 3D channels and realizing arbitrary 3D geometries using FLICE.

For patterning 3D, we stacked 2D planes along the Y-axis and patterned them sequentially from the bottom to the top surface, illustrated in Fig. 3.13. Similar to 2D planes, for patterning 3D features, the step size along the Y-axis determines the etch quality and etch rate. Here, we present results on finding the optimum Y-step size to pattern 3D features using FLICE.

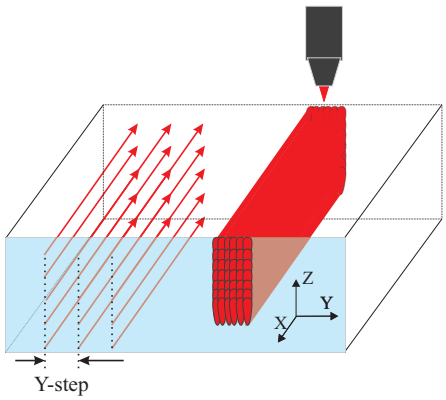

Figure 3.13: Illustration of patterning 3D features through stacking 2D planes along the Y-axis. We studied the effect of the Y-step size on the etch rate and etch quality.

In the experiment, 50-µm wide and 100-µm deep channels were patterned by stacking 2D planes along the Y-axis with Y-step sizes ranging from 1 µm to 10 µm. For patterning, we used a repetition rate of 250 kHz, marking speed of 5 mm/s, and pulse energy of 2 µJ, and for the 2D planes, we used a Z-step size of 1 µm. SEM images of the 3D channels and the cross-sections images are shown in Fig. 3.14(a) and (b), respectively.

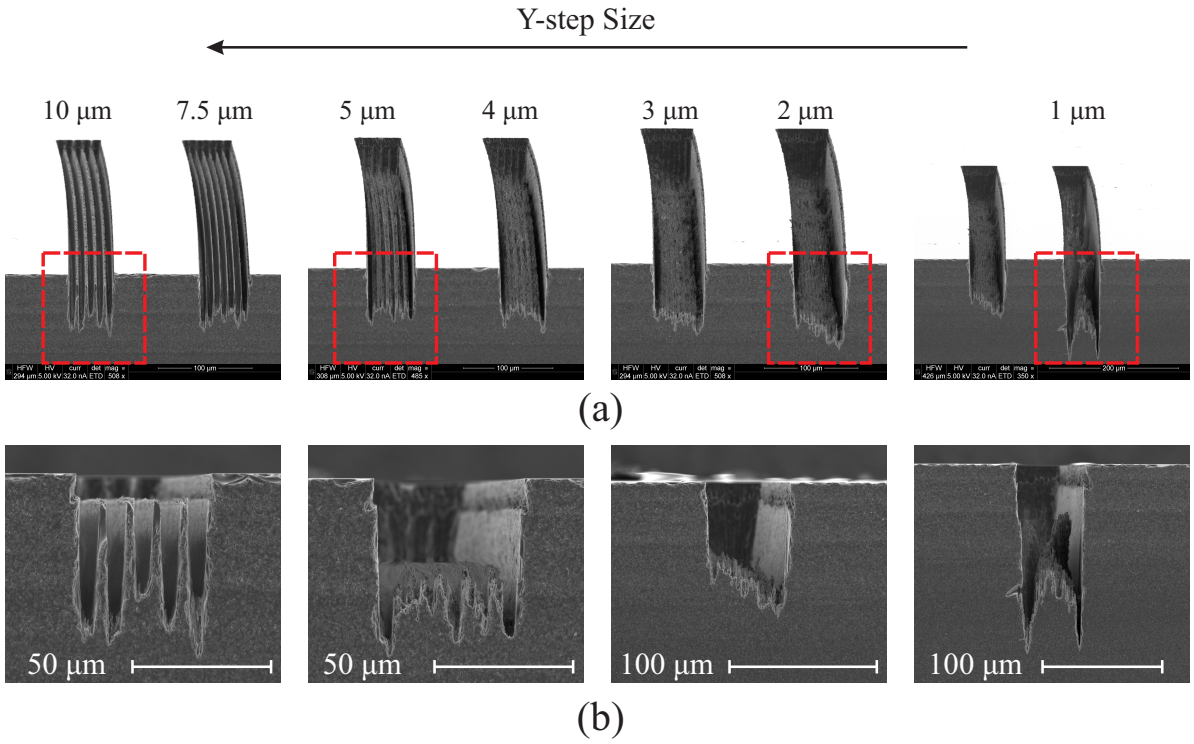

Figure 3.14: Effect of the Y-step size on etch rate and etch quality of 3D channels wet etched using KOH. SEM images of 3D channels with different Y-step sizes are shown in (a) and the cross-section images are shown in (b).

As demonstrated, the etch profile of a 3D channel degrades at higher Y-step sizes due to an insufficient overlap between two consecutive 2D planes. At higher overlaps, a Y-step size of 1 µm, we observed a higher etch rate and micro-trenching-like defects. Based on the results in [10], this type of defect can be minimized by reducing the pulse energy. Alternatively, we explored using 15% HydroFluoric (HF) solution, instead of KOH, for wet etching of the laser-patterned samples. For the same laser patterning parameters and duration of wet etching, we repeated the experiment and the results are shown in Fig. 3.15.

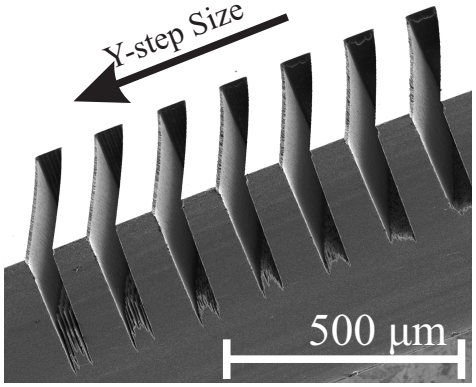

(a)

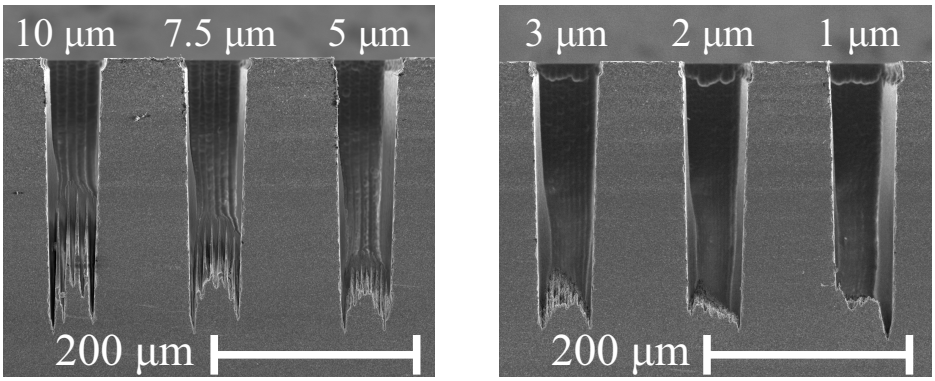

(b)

Figure 3.15: Effect of the Y-step size on etch rate and etch quality of 3D channels wet etched using HF. SEM images of 3D channels with different Y-step sizes are shown in (a), and the cross-section images are shown in (b).

It is shown that by using a more rigorous etching agent, such as HF acid, for wet etching of laser-patterned samples, a twice higher and consistent etch rate can be achieved, independent of the Y-step size. Nevertheless, a Y-step size on the order of 1 µm must be used to achieve a smoother surface on the bottom and the wall in the back.

As previously mentioned, a similar raster scanning and inscription can be used to pattern arbitrary 3D geometries. We implemented patterns shown in Fig. 3.16(a) to create square-shaped and circular features through FLICE, and the results are shown Fig. 3.16(b).

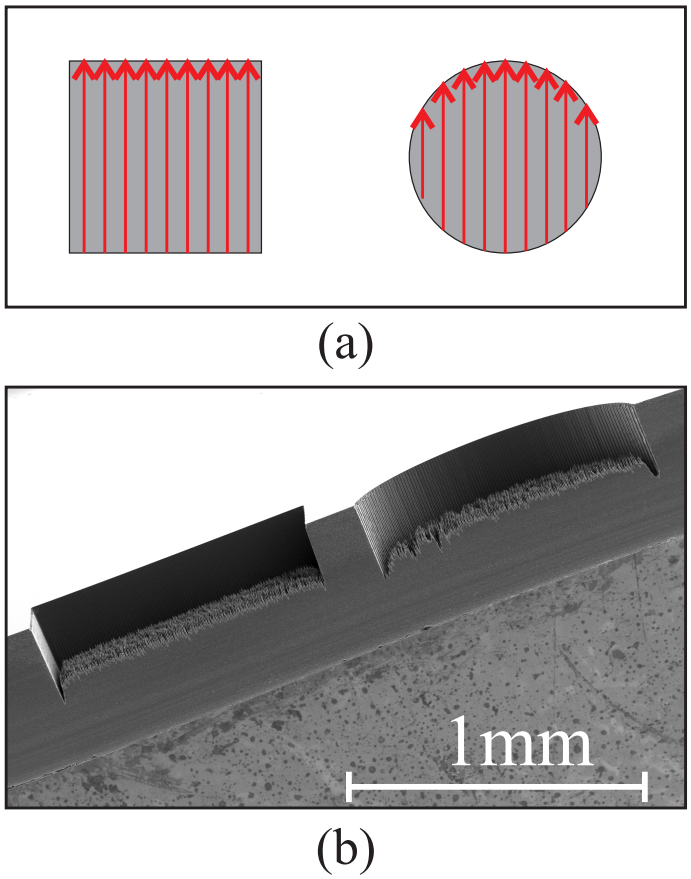

Figure 3.16: Patterning square-shaped and circular features through FLICE.

Surface Roughness

Surface roughness is a key requirement for both mechanical resonators and optical components. For mechanical resonators, quality factor degradation through surface losses can be prevented by achieving smooth surfaces (< 100nm in roughness). Surface roughness Improvements through optimization of laser inscription parameters have been reported in [15, 27].

In general, sidewalls' surface roughness can be improved by maintaining a perpendicular polarization, reducing the pulse energy, increasing the effective number of pulses per area, and stacking lines with high overlaps along the Z-direction (with respect to the length of the laser-modified region). Preliminary measurements of surface roughness on sidewalls of fused silica structures patterned through the FLICE are illustrated through SEM images

and stylus profilometer measurements in Fig. 3.17.

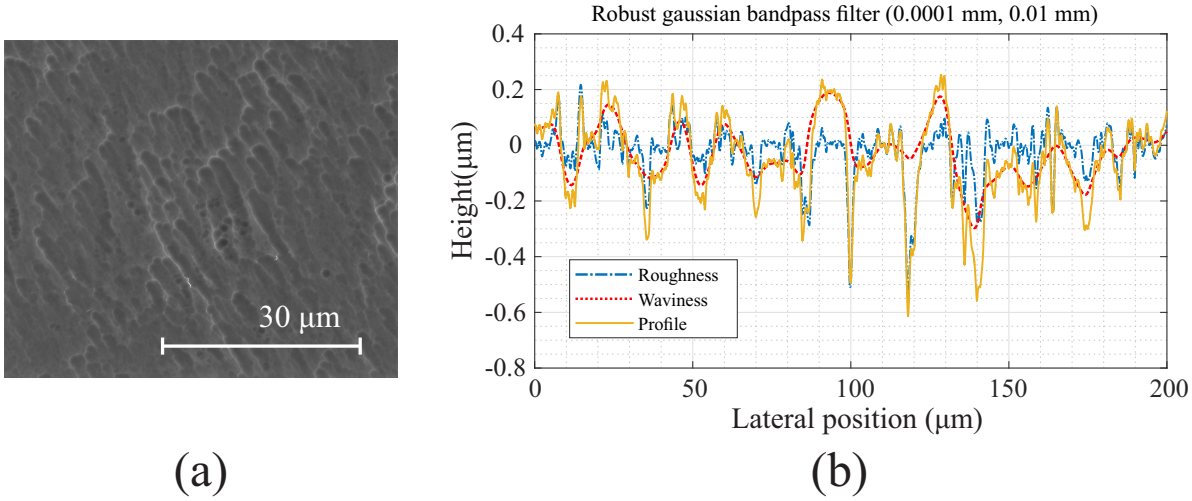

Figure 3.17: (a) SEM image of sidewalls of fused silica features fabricated using FLICE. (b) Contact measurements on height variation, which was utilized to estimate the roughness of laser-patterned features.

Based on the measurements, we estimated a roughness on the order of 50 nm for a pulse energy of 0.8 µJ, marking speed of 5 mm/s, and z-steps of 1 micron. Through further optimization, we believe that we can reach an as-fabricated roughness below 50 nm. Post-processing techniques for surface treatments, such as high-temperature annealing [40, 98] and selective reflow of fused silica using CO_2 lasers [108, 138], are promising for reaching sub-nanometer roughness in laser-patterned fused silica structures.

3.4 Resonator Fabrication

3.4.1 Process

We employed FLICE as part of a 3-steps process for the fabrication of stand-alone micro-resonators, illustrated in Fig. 3.18. In the first step, the femtosecond laser is tightly focused in the bulk of FS to inscribe a cavity and the resonator from bottom to top. The resonator includes the electrodes, proof-mass, suspension elements, anchors, etc. In the second step,

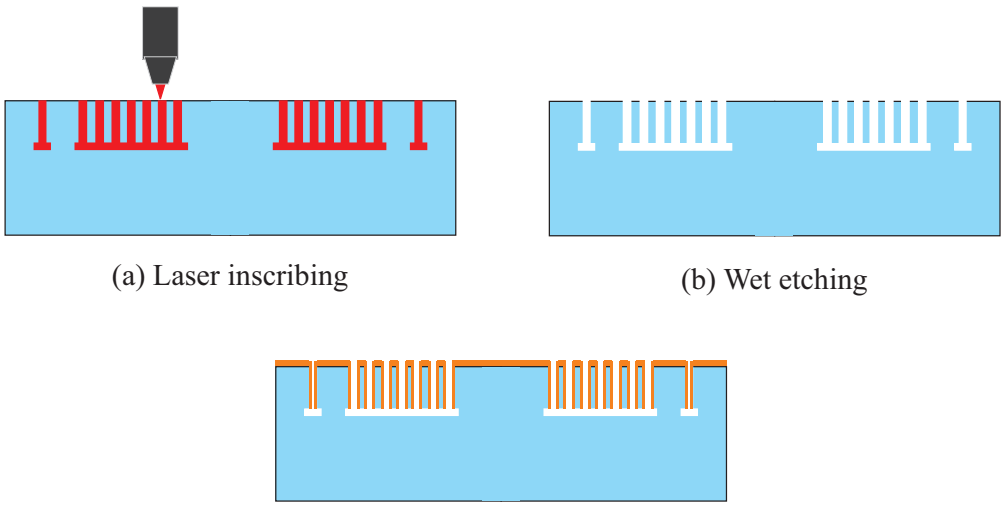

Figure 3.18: The proposed 3-steps process for fabrication of fused silica resonators from a single-layer fused silica material. This process benefits from a homogeneous integration of the device and handle layers and eliminates the need for wafer bonding.

the structure is submerged in an aqueous KOH solution to selectively etch the modified material, precisely defining and releasing the resonator. In step three, a thin layer of metal is uniformly deposited on the structure through sputter coating to achieve the conductivity required for electrostatic actuation and detection.

In this process, suspension elements and electrode gaps are defined by patterning 2D planes across the thickness of the material. As a result, the gap size is determined by the width of the laser-modified region. For patterning anti-gaps, 2D planes must be stacked to achieve larger openings. For complex geometries, since the direction of travel changes at different zones, the dynamic polarizer must achieve perpendicular polarization throughout the process. The cavity is patterned as a horizontal 2D plane below the structure. The length of the laser-modified region determines the cavity gap size. In the wet etching process, the solution enters the structure from the top surface, and once the device layer is defined, the cavity is etched away, releasing the structure.

As illustrated in Fig. 3.18, the proposed process uses a single-layer fused silica material for

a homogeneous co-definition of the device layer and substrate layer. As a result, thermal stress in the fabricated structure is significantly reduced.

3.4.2 Disk Resonator Gyroscope (DRG) Design

To demonstrate the feasibility of the process, a 25 mm^2 Disk Resonator Gyroscope (DRG) structure [20] was fabricated using the proposed process with a design shown in Fig. 3.19(a). The DRG consists of concentric rings anchored at the most-inner ring, and the deformation is measured using electrodes facing the outer ring.

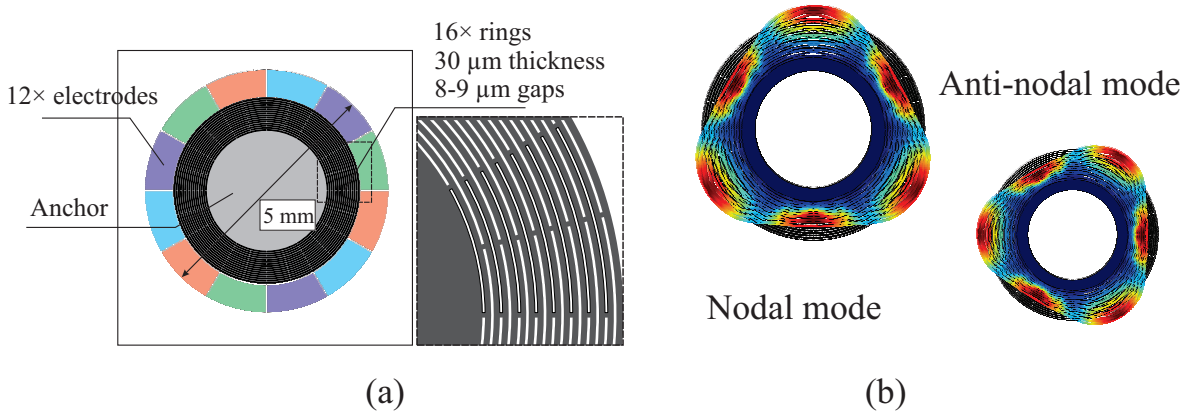

Figure 3.19: (a) The DRG was designed to operate in the n=3 wineglass modes. The concentric rings were connected in series through spokes with 30-degrees angle separation. (b) The modal deformation of the DRG in n=3 wineglass modes is illustrated.

This particular DRG was designed to operate in the n=3 wineglass modes. The modal deformation of the DRG in n=3 wineglass modes is shown in Fig. 3.19(b). The Thermo-Elastic Damping (TED) quality factor and natural frequency of the DRG were simulated using COMSOL multiphysics on the order of 20M and 109 kHz, respectively. Based on simulation results, we determined that the TED quality factor limit of this design for the case of using Single-Crystal Silicon (SCS) as the structural material was on the order of 11k, 2000 times lower than the case of using FS as the structural material.

3.4.3 FLICE of DRG Structure

Device Layer

As an initial step, we used FLICE to pattern the device layer of the DRG, including the rings and electrodes. For patterning, we used a pulse duration of 360 fs, a repetition rate of 250 kHz, pulse energy of 0.8 μJ, a marking speed of 5 mm/s; an 8M KOH solution was used to wet etch the laser-patterned structures.

Inscription of the design of the DRG (Fig. 3.19(a)) was performed at -100 μm Z-position and repeated at different Z-positions reaching the top surface with a Z-step size of 1 μm. After laser patterning, the structure was submerged in KOH solution for 2 hours to etch away the laser-modified regions. After wet etching, the structure was mechanically diced, and the cross-section SEM images are shown in Fig. 3.20.

As illustrated, we patterned the DRG's device layer through FLICE and demonstrated a capacitive gap size on the order of 7.3 μm (averaged value) and a depth size on the order of 175.29 μm; the aspect ratio was estimated to be on the order of 20:1, and the tapering angle was below 1°.

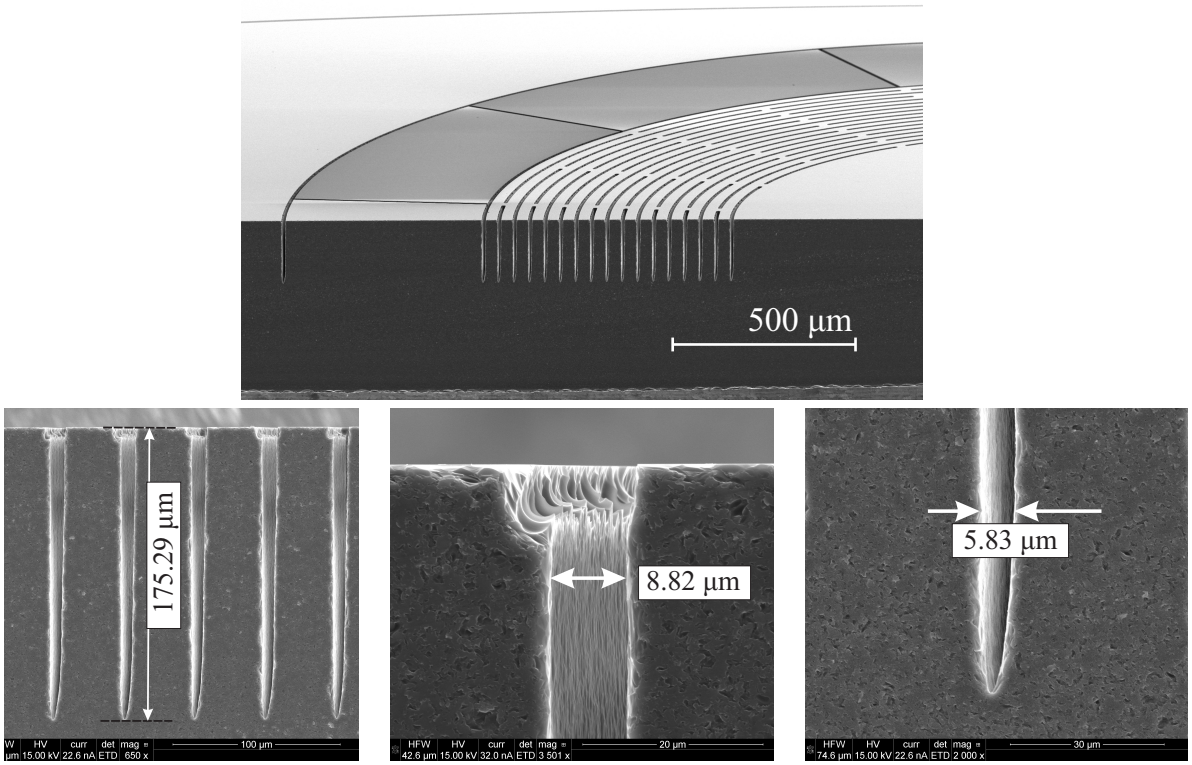

Figure 3.20: SEM images of the device layer of a DRG fabricated from fused silica through the FLICE process.

Full Resonator Structure

To realize a micro-scale resonator, we inscribed the DRG structure and the corresponding release cavity in FS, followed by 2 hours of wet etching in KOH solution. In this experiment, we used pulse energy on the order of 2 µJ.

Optical and SEM images were utilized to make sure that the cavity was etched during the wet etching process and that the resonator was fully released, shown in Fig. 3.21(a) and (b), respectively. As illustrated, we were able to successfully fabricate and release an FS-DRG, with a device-layer thickness of 113 µm and gap size of 9.6 µm (11.8:1 AR).

The DRG was sputter-coated with a 15 nm chromium/gold layer (1:2 ratio) using the DENTON AC sputter coater for electrostatic characterization. The sputtering system was designed to deposit metal with a 60° inclination angle on samples mounted on a planar rotating

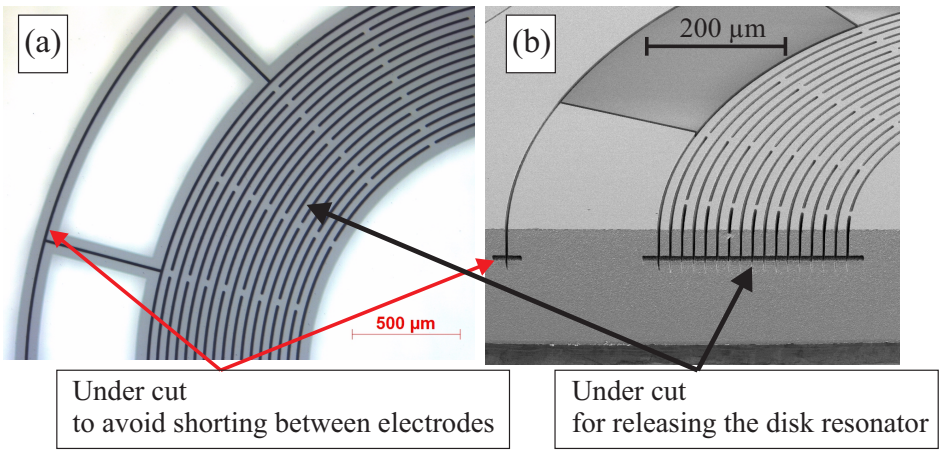

Figure 3.21: In step two of the fabrication process, an optical image was utilized to check for full release of the structures, shown in (a). SEM cross-section image of a fully released FS-DRG patterned using the FLICE process is shown in (b).

stage. The deposition rate was set to a value on the order of 0.5 Å/s.

3.4.4 Device Functionality and Characterization Results

To electrically access the electrodes, we mounted and wire-bonded the DRG devices to a chip carrier, as shown in Fig. 3.22(a). A combination of DC and AC voltages was applied to dedicated electrodes to generate electrostatic forces for actuation of the DRG; the motional current generated due to gap variations was converted to voltage using transimpedance amplifiers and used to measure the displacement.

The DRG devices and the front-end electronics were put in a vacuum chamber, and the frequency response (Fig. 3.22(b)) and ringdown response were measured in 30 µtorr vacuum to demonstrate the functionality of the device and characterize the frequency split and quality factor of the resonator.

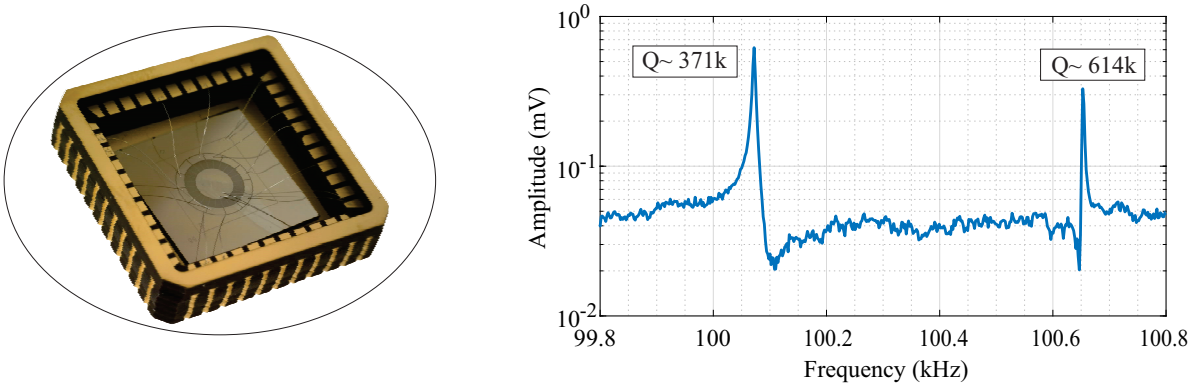

(a) (b)

Figure 3.22: Frequency response of the FS-DRG measured through electrostatic actuation and detection. The measured frequency split and quality factor are summarized in Table 3.1.

Table 3.1: Characterization results on two FS-DRG fabricated through the FLICE.

Parameters	**DRG#1**	**DRG#2**
Resonant frequency1 (kHz)	100.075	100.135
Resonant frequency2 (kHz)	100.655	100.365
Frequency split (Hz)	580	230
Quality factor 1	371k	437k
Quality factor 2	614k	534k

The initial results are included in Table 3.1 and revealed a frequency split on the order 230 Hz and 580 Hz and a quality factor as high as 614k. Notably, the measured quality factor for the metal-coated DRG was 5-times higher than the quality factor reported for plasma etched FS-DRGs [20]. Through more investigation, we found out that the polarizer was not working correctly in the first fabrication run. The polarization was not perpendicular to the direction of travel at specific orientations. We hypothesized that the DRG devices were not etched uniformly as a result of this issue, and in turn, the symmetry was negatively affected.

In a second fabrication run, the algorithm of the dynamic polarizer was corrected, and two DRG devices were patterned. In the fabrication second run, to achieve a higher Signal-to-Noise Ratio (SNR) for electrostatic detection, we coated the devices with 60 nm of chromium and gold layers (1:5 ratio). The results are summarized in Table 3.2. The frequency response of DRG#3 is shown in Fig. 3.23 demonstrating a frequency split on the order of 54.7 Hz. The

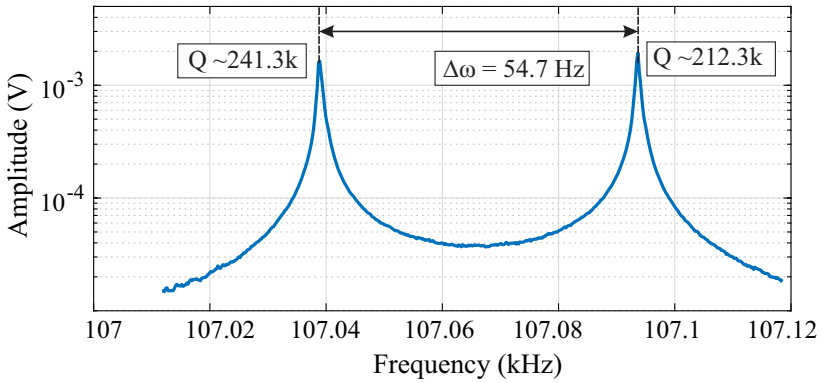

Figure 3.23: Frequency response of DRG#3, demonstrating a frequency split on the order of 54.7 Hz.

lower quality factor measured with the DRGs from the second fabrication run is attributed to a 4-times thicker metal coating.

Table 3.2: Characterization results on DRGs from the second fabrication run.

Parameters	**DRG#3**	**DRG#4**
Resonant frequency1 (kHz)	107.093	106.788
Resonant frequency2 (kHz)	107.038	106.893
Frequency split (Hz)	54.7	105
Quality factor 1	241.3k	222.3k
Quality factor 2	212.3k	296.3k

3.5 Conclusion

For the first time, we demonstrated a FLICE-like fabrication process for manufacturing stand-alone fused silica MEMS vibratory structures. Through patterning 1D channels, optimum laser parameters were found to maximize the laser-induced selectivity. Furthermore, step sizes were optimized to improve the surface quality and etch rate for patterning 2D and 3D features using FLICE. Through the process optimization, we demonstrated that with a femtosecond laser-induced etching selectivity on the order of 855:1, rectangular channels with an aspect ratio on the order of 55:1 and higher could be realized ideal for fabrication of capacitive MEMS resonators.

We introduced a 3-steps process utilizing FLICE to fabricate resonant MEMS devices. FS-DRGs were fabricated through the introduced process, and initial results on structural characterization were reported. We demonstrated resonator functionality in the fabricated devices through electrostatic actuation and detection. A frequency split as low as 54.7 Hz and a quality factor as high 614k were demonstrated, which notably exceeds that of plasma etch fused silica DRGs reported in [20].

Chapter 4

Effect of Anisoelasticity on Precession in Whole-Angle Operation

4.1 Introduction

In an ideal case, a fully symmetric Coriolis Vibratory Gyroscope (CVG) with identical resonant frequencies is required for Whole-Angle (WA) mode of operation. In reality, geometrical asymmetries introduced in the fabrication process and anisotropic mechanical properties of the structural material result in anisoelasticity (i.e., the frequency split). This chapter studies the effect of uncompensated anisoelasticity on precession and the corresponding errors in direct angle measurements.

This chapter is organized as follows. Through analytical equations and numerical simulation results, discussed in Section 4.2, we first investigate the effectiveness of the PI quadrature controller, as well as the correlation of residual quadrature to system parameters and control parameters. Furthermore, we demonstrate the effect of residual quadrature on precession of angle and characterize the corresponding angle errors. In Section 4.3, experimental data

with a Micro-Electro-Mechanical (MEM) Dual Foucault Pendulum (DFP) gyroscope, [105], is presented to validate the simulation results. A summary of our results and conclusions are found in Section 4.4.

4.2 Quadrature in WA Operation

In the open-loop WA mode of operation, in which no feedback control loops are utilized, it has been reported that due to anisoelasticity, the oscillation pattern deviates from an ideal straight line and becomes a semi-elliptical orbit illustrated in Fig. 4.1, [8, 81]. The elliptical trajectory is a result of an off-resonance excitation of the operational modes during rotation through the Coriolis forces. The vibration in the non-inertial reference frame, along the X and Y axes, can be represented in a general form through the following equations

$$\begin{aligned} x(t) &= a\cos\theta\cos(\omega t+\phi) - q\sin\theta\sin(\omega t+\phi), \\ y(t) &= a\sin\theta\cos(\omega t+\phi) + q\cos\theta\sin(\omega t+\phi), \end{aligned} \tag{4.1}$$

where a and q denote the vibration amplitude along the major and minor axes of the elliptical pattern, respectively. In the case of open-loop WA operation, the amount of ellipticity (q) depends on the relative orientation of the oscillation pattern with respect to the orientation of the principal axes of elasticity, [81].

The undesired oscillation along the semi-minor axis of the elliptical orbit is referred to as the oscillation component in-quadrature with the reference phase or "quadrature," in short, [70]. In Eq. (4.1), parameters ω and ϕ represent the average oscillation frequency and phase of oscillation, respectively.

To operate a CVG in the closed-loop WA mode of operation, Friedland [51] and Lynch [70] have proposed similar feedback control architectures to compensate for energy dissipation

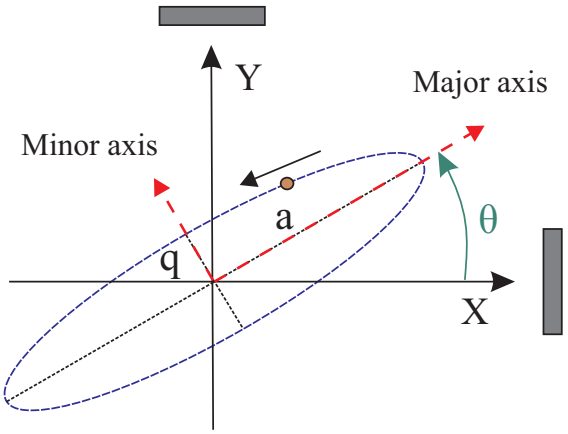

Figure 4.1: Schematics illustrating the elliptical trajectory of oscillation along X and Y axes in a Coriolis vibratory gyroscope. The orientation of the oscillation pattern, amplitude of vibration along the semi-major and semi-minor axes of the elliptical trajectory are shown.

and anisoelasticity of the gyroscope. The proposed feedback controls were designed based on a reduced-order model of CVGs, developed through the method of averaging and utilizing the slow-varying parameters of the CVG system, [12, 78]. In the closed-loop WA control architecture, which is widely adopted by the community, [8, 9, 35, 87, 89, 115, 123], a Proportional-Integral (PI) feedback controller is utilized to reduce the quadrature (Q) in the system, thus compensating for the effect of anisoelasticity on precession. However, in literature, for example, [9, 87, 115], different observations have been reported on effectiveness of the PI quadrature-control on reduction of quadrature. Here, we investigate the effectiveness of the PI quadrature controller in WA mode of operation and the angle measurement errors due to an uncompensated quadrature.

Based on the reduced-order model of a CVG operating in the WA mode, reported by Lynch in [70], assuming that quadrature is small as compared to the oscillation along the major axis of the orbital trajectory (i.e., $q << a$), the rate of precession can be calculated as

$$\dot{\theta} = -\kappa\Omega + \frac{1}{2}\Delta(\frac{1}{\tau})\sin 2(\theta - \theta_\tau) + \frac{1}{2}\Delta\omega\cos 2(\theta - \theta_\omega)\frac{Q}{E}, \tag{4.2}$$

where κ is the structural angular gain (Bryan's factor, [14]) and Ω represents the input

angular rate. Parameters $\Delta(\frac{1}{\tau})$, $\Delta\omega$, θ_τ, and θ_ω denote anisodamping, anisoelasticity, and the corresponding mismatch-angle in the principal axes of damping and elasticity, respectively. In Eq. (4.2), variables E and Q, in units of $[V^2]$, represent the energy and quadrature in the system, which correlate to the shape of the orbital trajectory through the following equations

$$\begin{cases} E = a^2 + q^2 \\ Q = 2aq \end{cases} \tag{4.3}$$

In the WA closed-loop control architecture proposed by Lynch in [70], measurements of vibration in the non-inertial coordinate frame "attached" to the CVG, defined by the X and Y axes, are used to estimate the quadrature in the system (Q). The estimated quadrature is then used as the input of a PI controller to calculate the quadrature control voltage as

$$v_{q_c} = -K_p[Q + K_i \int_0^t Q dt'], \tag{4.4}$$

where K_p and K_i denote the proportional and integral coefficients of the PI controller for quadrature compensation.

To suppress quadrature without interfering with the Coriolis-induced precession of angle, the quadrature control voltage (v_{q_c}) is modulated at the phase of oscillation and then applied as a force along the minor axis of the elliptical pattern, [31, 70, 143], illustrated in Fig. 4.1. To achieve this, based on the instantaneous orientation of the oscillation pattern (θ), the quadrature control voltage is projected along the X and Y axes through a coordinate transformation and then applied as electrostatic forces to the vibratory system. As a result of the coordinate transformation, the resultant of the quadrature-control force-vectors applied along the X and Y axes would be aligned with the minor axis of the elliptical trajectory. In

this case, the following equation describes the evolution of quadrature in the gyroscope, [70]

$$\dot{Q} = -\frac{2}{\tau}Q - u_\omega + \frac{\sqrt{E}}{\omega}G_A G_D v_{q_c}, \tag{4.5}$$

where τ, u_ω, and v_{q_c} represent the average energy decay time constant, perturbation due to anisoelasticity, and quadrature control voltage. In Eq. (4.5), coefficients G_D and G_A denote the electro-mechanical conversion gains for position to readout voltages and control voltages to electrostatic forces, respectively. As reported in [70], for a CVG with linear elasticity, the perturbation due to anisoelasticity takes the following form

$$u_\omega = \Delta\omega \sin 2(\theta - \theta_\omega)E, \tag{4.6}$$

A block diagram of the reduced-order mathematical model for WA mode of operation, including the PI quadrature control, is illustrated in Fig. 4.2. Two different analyses are provided in this thesis to study the effect of anisoelasticity on quadrature and the corresponding effects on precession. We used Eq. (4.2), (4.4)-(4.6) as the starting point of our numerical and analytical studies.

As previously mentioned, in the closed-loop WA mode of operation, a separate feedback control loop is used to sustain the energy in the system. The energy-control architecture in the WA mode of operation is far from the focus of this study and will not be discussed; we assumed that the energy in the system was perfectly sustained. Therefore, in the following derivations, the variable E was substituted with a constant value of E_0 (i.e., the set-point of the energy-control loop).

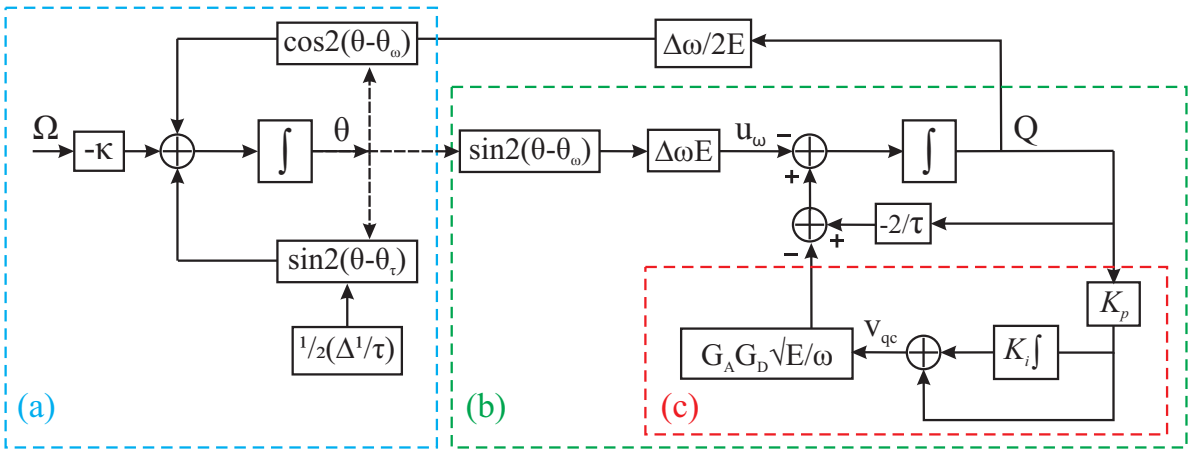

Figure 4.2: Block diagram illustration of WA operation reduced-order model. Effect of physical rotation (Ω), anisodamping ($\Delta(1/\tau)$), and anisoelasticity ($\Delta\omega$) on precession of angle (θ) is illustrated in (a). The effect of anisoelasticity on quadrature (Q) and the nonlinear coupling to the pattern angle is illustrated in (b). The PI feedback control, which is utilized for suppression of quadrature, is illustrated (c).

4.2.1 Quadrature Control and Residual Quadrature

Equations (4.2) and (4.5) are nonlinear differential equations which are coupled through variables Q and θ. To derive an analytical solution for quadrature, we make an assumption that the first term on the right-hand side of Eq. (4.2), which describes the effect of physical rotation on precession, is an order of magnitude higher as compared to the terms describing the effect of anisodamping, $(\frac{1}{2}\Delta(\frac{1}{\tau}))$, and anisoelasticity, $(\frac{1}{2}\Delta\omega\frac{Q}{E})$, on precession. With this assumption, we can approximate the angle of precession to the first-order as

$$\theta \approx -\kappa\Omega t, \tag{4.7}$$

where, for the case of anisodamping in CVG, this approximation can be verified using analytical equations reported in [87]. Through this approximation, the perturbation due to anisoelasticity (u_ω), defined in Eq. (4.6), can be regarded as a harmonic sinusoidal term with a frequency equal to $2\kappa\Omega$. Consequently, Eq. (4.5) becomes a linear differential equation, independent of θ.

Based on Eq. (4.5), with quadrature (Q) as the state-variable and the anisoelasticity perturbation (u_ω), we concluded that in the WA operation, anisoelasticity results in a harmonic response in quadrature. Using Eq. (4.4)-(4.7), we derived the following expression for quadrature in the Laplace domain

$$Q(s) = -\frac{\Delta\omega E_0}{s + \frac{2}{\tau} + G_A G_D K_p \frac{\sqrt{E_0}}{\omega}(1 + K_i/s)} \tag{4.8}$$

As a case study, a set of parameters were chosen based on typical characteristics of a MEM gyroscope, summarized in Table 4.1, and were used for simulation of quadrature. Using the transfer function in Eq. (4.8), the magnitude of $Q(s)$ (i.e., the amplitude of variation in quadrature) as a function of the input angular rate ($s = 4\kappa\Omega\pi j$) was calculated, and the results are shown in Fig. 4.3.

Table 4.1: Parameters used for calculations and numerical simulation.

Parameters	Values	Parameters	Values
E_0	$2.5 \times 10^{-3}\ V^2$	K_p	$8k$
κ	0.76	K_i	40
τ	21.95 s	ω	15000.1 Hz
$\Delta(1/\tau)$	4.1 mHz	$\Delta\omega$	200 mHz
θ_τ	3°	θ_ω	10°
$G_A G_D$	$1e5$	Ω	constant

It is demonstrated that by not utilizing a quadrature-control loop (i.e., $K_p = 0$), through precession, the quadrature changes harmonically with a relatively large amplitude, shown using a red dashed line in Fig. 4.3. In this case, for input angular rates below ~40 Degrees-per-Second (DPS), we determined that the effect of anisoelasticity on precession exceeds that of physical rotation (i.e., $\Delta\omega Q_{pk}/2E_0 > \kappa\Omega$, where Q_{pk} is used to denote the amplitude of variation in quadrature), which contradicts our initial assumption. Therefore, in this case study, our first-order approximation for the angle of precession, in Eq. (4.7), holds only for an input angular rate above 40 DPS. In fact, for the case of applying a relatively small

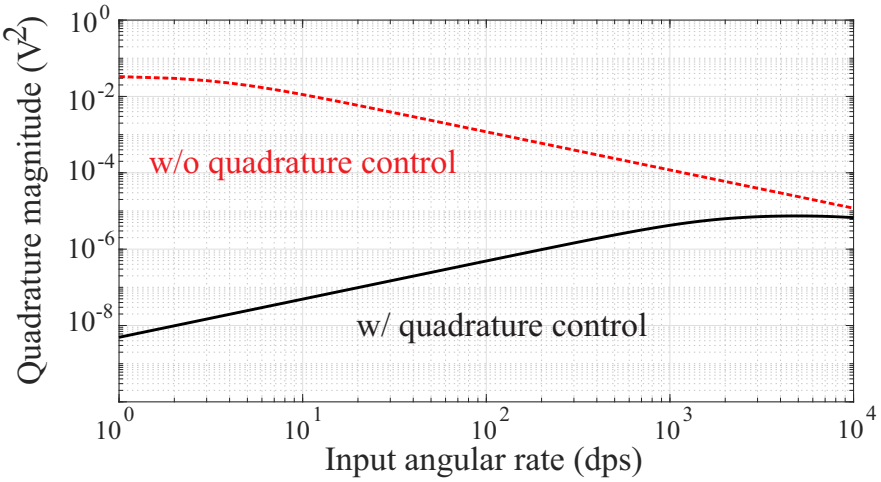

Figure 4.3: Magnitude of quadrature in WA CVG calculated as a function of the input angular rate using the transfer function in Eq. (4.8). The contribution of a PI-based quadrature feedback control to suppression of quadrature is demonstrated.

input angular rate, the oscillation pattern would not precess due to the large quadrature as reported in [81].

In the case of applying an input angular rate above the anisoelasticity limit (a value around 40 DPS in this case study), the oscillation pattern precesses, the first-order approximation in Eq. (4.7) holds, and the quadrature can be estimated using Eq. (4.8), as illustrated in Fig. 4.3. In the latter case, it is shown that the amount of quadrature is inversely proportional to the input angular rate, which has been experimentally observed and reported in [8].

In the case of utilizing the quadrature-control loop (i.e., $K_p \neq 0$), quadrature is suppressed by several orders of magnitude, shown using a continuous black line in Fig. 4.3. We determined that since we are dealing with a time-varying perturbation in the system (u_ω), the PI quadrature controller cannot fully eliminate quadrature. The residual quadrature was observed to be proportional to the input angular rate. Since the effect of anisoelasticity on precession becomes smaller, at the same scale as the input angular rate, we concluded that in the absence of anisodamping and by applying the PI quadrature control, the WA gyroscope would precess at input angular rates well below 40 DPS. Nevertheless, the residual quadrature would affect precession, as shown in Eq. (4.2).

It is worth mentioning that in theory, quadrature can be suppressed using a PI feedback architecture independent of the magnitude of anisoelasticity, as long as the assumptions of the averaged reduced-order model are not overlooked. In practice, however, since the quadrature compensation voltage (v_{q_c}) is proportional to the frequency split, noted from equations (4.4) and (4.8), the output voltage range of control electronics and power consumption specifications set an upper limit for the allowable anisoelasticity.

In the next section, we study the effect of residual quadrature on precession in the WA mode of operation and the corresponding errors in direct angle measurement.

4.2.2 Effect of Residual Quadrature on Precession

Due to a complex form of the two coupled non-linear differential equations (4.2) and (4.5), we utilized numerical simulation to study the effect of residual quadrature on precession. For simulation, Eq. (4.2) and (4.5) were solved numerically in their original form using a linear solver with a constant time-step of 1e-4 s, and the evolution of angle (θ) was simulated for different input angular rates.

Assuming a constant input angular rate, based on fractional analysis [78, 87], the precession of angle would consist of a time-linear variation due to the physical rotation and a summation of even-ordered harmonics represented as

$$\theta = \theta_{Rot} + \sum_{q=1}^{\infty} \theta_{b_q} \sin(2q(\theta_{Rot} - \phi_q)), \tag{4.9}$$

where the harmonic errors are conventionally referred to as Angle-Dependent Bias (ADB), [89, 115], and the precession due to physical rotation has the following form

$$\theta_{Rot} = -\kappa_e \Omega t, \tag{4.10}$$

where κ_e and θ_{b_q} denote the Effective Angular Gain (EAG) and the amplitude of ADB for different harmonics.

We numerically simulated the angle of precession for three cases: (a) accounting for anisodamping, (b) accounting for anisoelasticity, and (c) accounting for both of these imperfections. The simulated angle of precession (θ) was used to characterize the change in angular gain ($\delta\kappa = \kappa_e - \kappa$) and the ADB for the first two harmonics. The simulation results are shown in Fig. 4.4.

Anisodamping

In Fig. 4.4, we illustrate that anisodamping in a CVG results in ADB errors with 2θ, 4θ, ... dependencies, along with a reduction of the angular gain. The reduction of the angular gain ($\delta\kappa$) and the 2θ dependent ADB were observed to reduce quadratically and linearly at higher input angular rates, respectively. These results match with the analytical results reported in [87]. The 4θ dependent ADB was observed to reduce quadratically at higher input angular rates, as shown in Fig. 4.4(c).

Through simulation results, we also confirmed that at an input angular rate below $\Delta(\frac{1}{\tau})/2\kappa$, the WA CVG would not precess. For parameters summarized in Table 4.1, the anisodamping threshold of precession was estimated to be on the order of 0.17 DPS.

Anisoelasticity

For the case of having anisoelasticity along with a PI quadrature-control loop, the 2θ dependent ADB error was observed to be negligible, but a reduction in angular gain and a 4θ dependent angle error were characterized.

In Eq. (4.2), since the quadrature value (Q) changes with a 2θ angle dependency, the

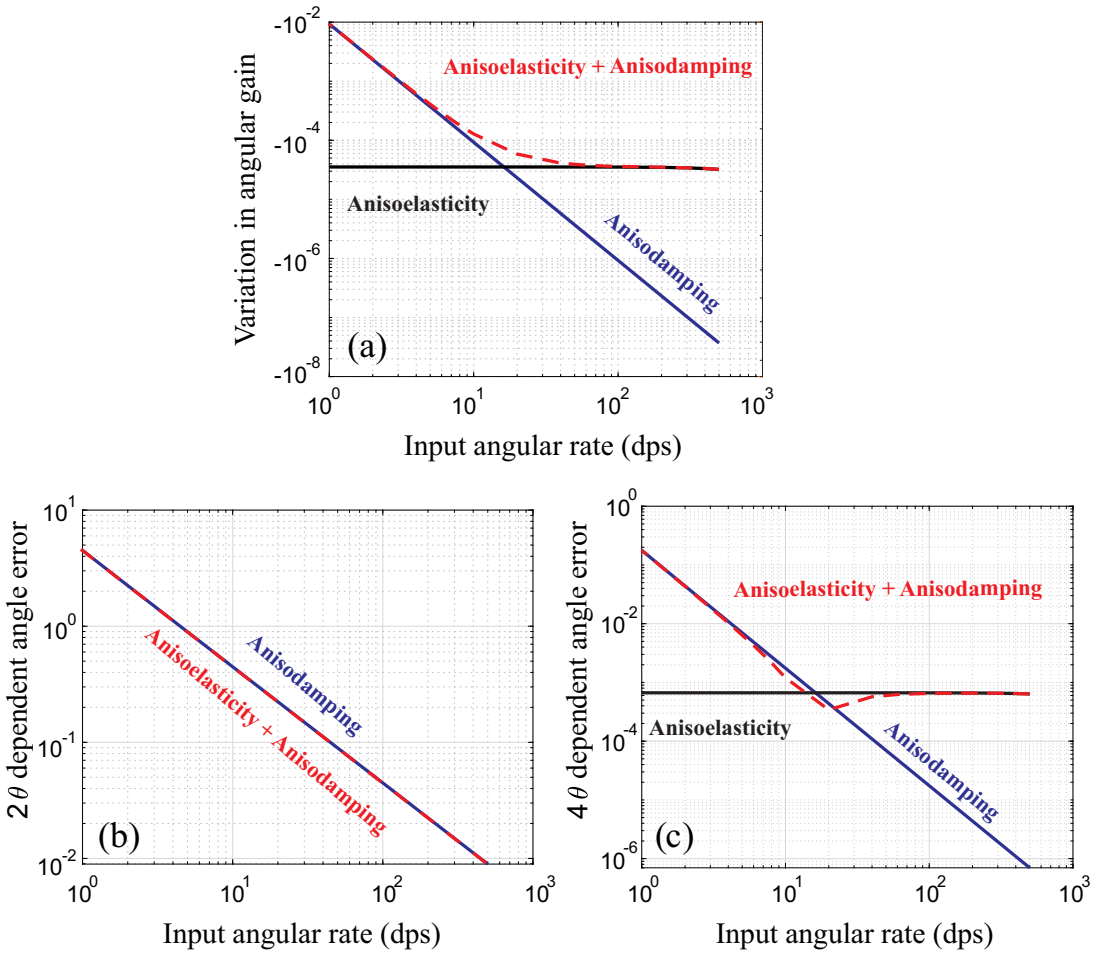

Figure 4.4: Simulation results illustrating the effect of anisodamping and anisoelasticity in CVG on precession. Reduction of angular gain ($\delta\kappa$) as a function of the input angular rate is illustrated in (a). The 2θ and 4θ dependent angle bias errors are shown for different values of input angular rate in (b) and (c), respectively. We observed that while the effect of anisodamping on precession diminishes at high input angular rates, the effect of anisoelasticity on precession was observed to be consistent and independent of the input angular rate.

ADB error due to anisoelasticity would be modulated at 4θ, 8θ, and higher-order dependencies. Furthermore, since quadrature (Q) increases linearly with the input angular rate, as illustrated in Fig. 4.3, the reduction in the angular gain and the ADBs were observed to be consistent at different input angular rates in the frequency range below the closed-loop bandwidth of the quadrature control loop. Based on simulation results, we also confirmed that anisoelasticity would not cause an angle-locking effect in the CVG, assuming that a quadrature-control loop is utilized.

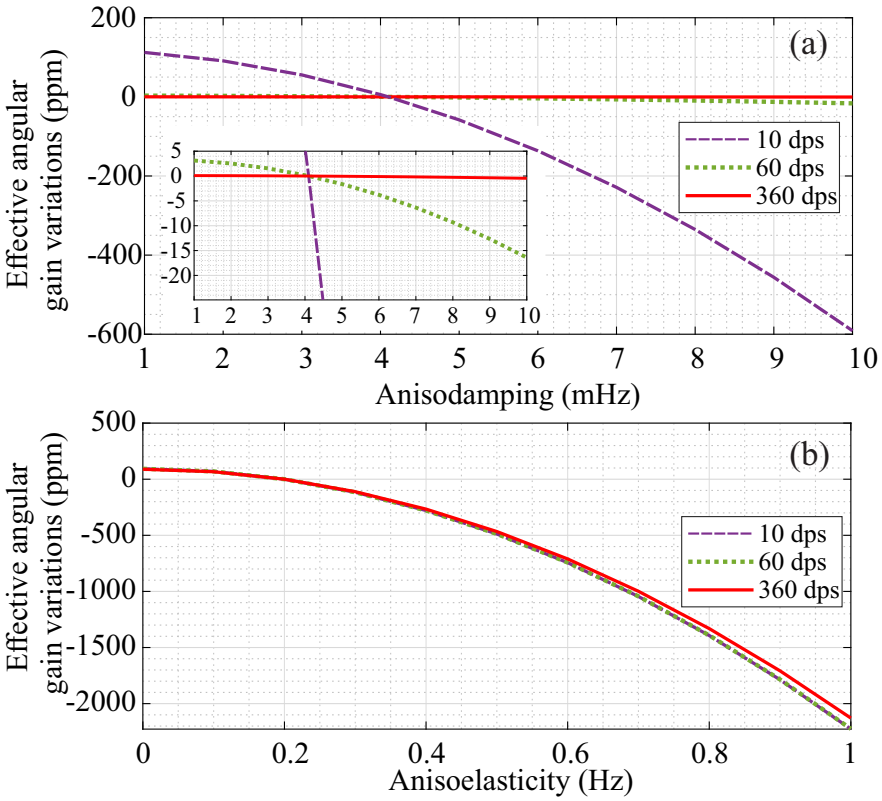

Figure 4.5: Simulation results on the effect of anisodamping and anisoelasticity variation on EAG for different input angular rates shown in (a) and (b), correspondingly. As demonstrated, at high input angular rates, sensitivity of EAG to variations of anisodamping is reduced significantly. In the case of a variation in anisoelasticity, the effect on EAG is shown to be independent of the input angular rate.

Anisodamping + Anisoelasticity

In the third case, we accounted for both the anisodamping and anisoelasticity of the CVG. Depending on the dominance of each mechanism at a given input angular rate, we observed a combination of ADB errors and angular gain reduction due to anisodamping and anisoelasticity. At a low input angular rate, anisodamping was observed to mainly affect the precession, causing a reduction in the angular gain and the ADB errors. At higher input angular rates, the effect of anisodamping was observed to diminish and anisoelasticity was determined to mainly affect the precession.

4.2.3 Variation of Angle Error Characteristics

During WA operation, anisoelasticity and anisodamping of the mechanical resonator could potentially change. Temperature fluctuations, environmental vibration, and g-sensitivity are among the mechanisms that can cause the aforementioned variations in anisoelasticity and anisodamping, and in turn, cause a drift in the angle error characteristics.

From equations (4.9) and (4.10), it is apparent that variation of the EAG (κ_e) results in an unbounded angular drift, proportional to the instantaneous angular rate input, that grows over the duration of operation. A variation of the ADB, on the other hand, would only affect the resolution of angle measurements, an error that is bounded and independent of the duration of gyroscope operation. For prolonged gyroscope operation, the stability of EAG is of the highest importance.

Through numerical simulation, we modeled the drift of EAG due to variations of anisoelasticity and anisodamping for different input angular rates. In the simulation, we accounted for both the anisodamping and anisoelasticity of the gyroscope, and the variation in EAG was estimated with respect to the nominal EAG calculated based on parameters in Table 4.1.

As illustrated in Fig. 4.5(a), we determined that EAG decreases for a higher amount of anisodamping in the gyroscope. More importantly, the sensitivity of EAG to variations of anisodamping was observed to depend on the input angular rate. By applying a constant rotation with 360 DPS angular velocity to the CVG, angular gain variation was estimated to be less 1 ppm for anisodamping variations from 1 to 10 mHz (inset of Fig. 4.5(a)). In the case of having a variation in anisoelasticity, the change in EAG was observed to be independent of the input angular rate (Fig. 4.5(b)).

These observations are consistent with the simulation results shown in Fig. 4.4(a), which confirm that anisodamping and variations of anisodamping have orders of magnitude smaller effect on EAG, as compared to anisoelasticity and variations in anisoelasticity, at higher input angular rates. It should also be noted that the sensitivity of EAG to anisoelasticity variations, which is evaluated based on the slope of EAG variation versus anisoelasticity in Fig. 4.5(b), is the lowest when the gyroscope is operated in a mode-matched condition (i.e., $\Delta\omega \approx 0$).

The quadrature control gain (K_p) also affects the sensitivity of EAG to anisoelasticity, which will be discussed in the next section using experimental results.

4.3 Experimental results

In this section, a set of experiments were designed to verify the simulation results obtained by the numerical model of CVGs operating in the WA mode. Using the experimental results, we aimed to validate the effect of anisoelasticity and residual quadrature on precession.

4.3.1 Device Under Test (DUT)

The Dual Foucault Pendulum (DFP) gyroscope [105], with a design architecture shown in Fig. 4.6, was used as the device under test. The axisymmetrical DFP gyroscope design architecture consisted of inner and outer masses that moved in an anti-phase motion along the X and Y axes. This particular DFP device with a footprint less than 4 mm^2 was fabricated with a 40 μm-thick device layer. The nominal operational frequency and quality factor of the DFP were measured on the order of 15 kHz and 1.1 M, respectively. Details on design parameters and fabrication process of the DFP gyroscope can be found in [4].

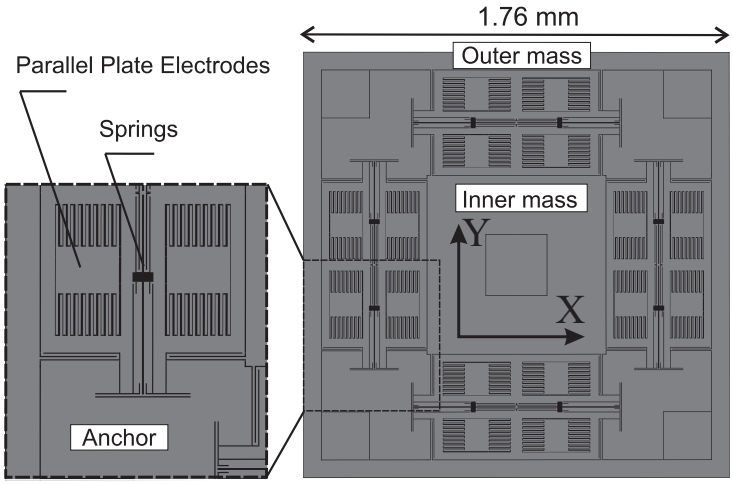

Figure 4.6: Design of the DFP gyroscope, which was used for experimental validation of the modeling results. As shown, parallel plate electrodes were used for motion actuation, detection, and electrostatic frequency tuning.

The closed-loop WA control, as described in [70], was implemented with a Zurich HF2Li lock-in amplifier using the Real-Time Kit (RTK) module, [8]. Using the method reported in [129], gain-mismatches in the detection and control electronics along the X and Y axes were identified and compensated. The device was characterized on an Ideal Aerosmith 1291BR rate-table, and the local temperature-variation around the Leadless Chip Carrier (LCC)-packaged DFP was controlled to within ±10 mK.

4.3.2 Verification of Numerical Model of WA Operation

We characterized the angle error of the DFP gyroscope in the WA mode of operation. The experimental data were compared to simulation results to verify the numerical model used for the WA mode of operation. The device parameters, including the anisodamping, anisoelasticity, mechanical angular gain, and the actuation-detection gain, were characterized and used for the simulation of gyroscope response.

Variation of the actuation frequency as a function of pattern angle was utilized to characterize anisoelasticity, [120, 123]. In the experiment, the DFP gyroscope was physically rotated at

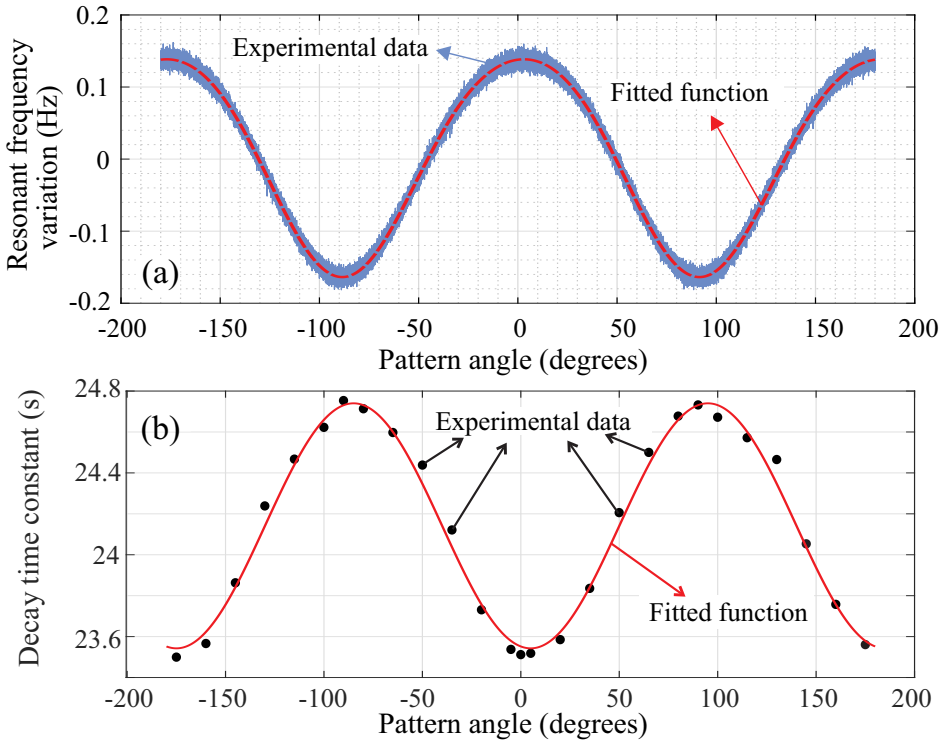

Figure 4.7: In (a), experimental data is shown on the variation of the resonant frequency as a function of pattern angle, which was utilized to characterize anisoelasticity of the DFP gyroscope. Anisodamping was characterized using the energy decay time constant at various pattern angles as shown in (b). The gyroscope parameters characterized for the DFP are summarized in Table 4.2.

an input angular rate of 10 DPS. Variation of the actuation frequency, tracked using the Phase-Locked Loop (PLL), was measured and the data is shown in Fig. 4.7(a). By fitting a 2θ dependent cosine function, the frequency split and the orientation of the principal axes of elasticity were estimated equal to $\Delta\omega$ = 302 mHz and θ_ω = 2.01°, respectively. To reach the characterized frequency split for this experiment from an as-fabricated frequency split of 114 Hz, we set the DC biasing voltages along the X and Y axes to 8.3 V and 3.035 V, respectively.

To characterize anisodamping of the DFP gyroscope, the energy decay time constant was estimated while the oscillation pattern was oriented to angles ranging from -175° to 175° with 15° increments. As shown in Fig. 4.7 (b), by fitting a cosine function to the experimental data, the average energy decay time constant τ, anisodamping $\Delta(\frac{1}{\tau})$, and the orientation of

the principal axes of damping θ_τ were estimated to be on the order of 24.14 s, 2.05 mHz, and 5.03°, respectively.

The actuation-detection gain ($G_A G_D$) was estimated based on the amplitude of vibration, the excitation voltage, and the energy decay time constant. Gyroscope parameters and control parameters of the DFP gyroscope, as summarized in Table 4.2, were used for numerical simulation.

Table 4.2: Summary of experimentally derived gyroscope parameters of the DFP used for numerical simulation.

Parameters	Values	Parameters	Values
E_0	$4 \times 10^{-4}\ V^2$	K_p	200
κ	0.76304	K_i	40
τ	24.14 s	ω	15016 Hz
$\Delta(1/\tau)$	2.05 mHz	$\Delta\omega$	302 mHz
θ_τ	5.03°	θ_ω	2.01°
$G_A G_D$	$4.269E5$	Ω	$constant$

Using Eq. (4.8), the magnitude of quadrature as a function of the input angular rate (Ω) was calculated and compared to the experimental results. As shown in Fig. 4.8(a), for the case of setting the proportional gain (K_p) to 200, we obtained a closed-loop bandwidth around 4.2 Hz for the quadrature-control loop. In frequency range lower than the bandwidth, as the input angular rate was increased, we observed that the magnitude of quadrature increased proportionally, in agreement with the analytical results.

Similar to the procedure discussed in Section 4.2, the angle of precession was simulated using gyroscope parameters summarized in Table 4.2, and both anisoelasticity and anisodamping were accounted for. The Angle-Dependent Bias (ADB) and the Effective Angular Gain (EAG) for different input angular rates were estimated based on the simulated precession and were compared to the experimentally characterized angle error of the DFP gyroscope. As shown in Fig. 4.8(b-d), a good agreement between the simulation results and experimental

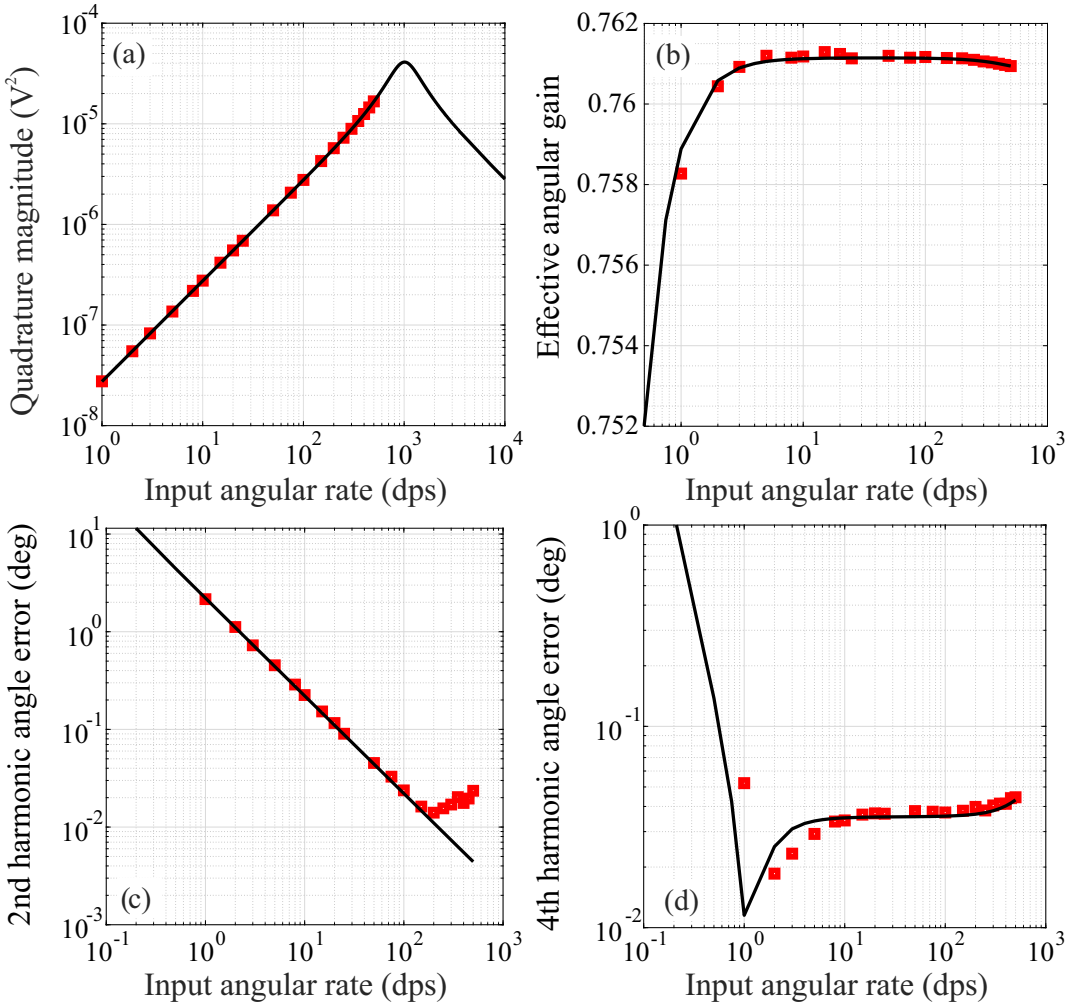

Figure 4.8: Simulation results based on the reduced-order WA model, shown using continuous lines, were compared to the experimentally obtained data of the DFP gyroscope, and good agreement between the two was observed. The magnitude of quadrature, the EAG, the 2θ, and the 4θ dependent angle errors are shown as a function of the input angular rate in (a)-(d), correspondingly.

data was observed verifying the numerical model of the WA mode of operation.

As illustrated in Fig. 4.8(b), due to anisodamping, a drastic reduction in the effective angular gain at low input angular rates was observed. At higher input angular rates, the effect of anisodamping on EAG diminishes, and anisoelasticity was observed to mainly cause a reduction in the EAG. At input angular rates above 200 DPS, the frequency of perturbation due to anisoelasticity became closer to the closed-loop bandwidth of the quadrature controller. As a result, the magnitude of quadrature increased in a non-linear fashion, as compared to

the input angular rate, and the EAG reduced.

As previously discussed, the 2θ dependent angle error in WA mode of operation is caused by anisodamping in the CVG. For the DFP gyroscope, the 2θ dependent angle error was characterized and the results are shown in Fig. 4.8(c). The ADB was observed to reduce linearly as the input angular rate was increased, in agreement with the simulation results. At input angular rates above 200 DPS, however, the ADB was observed to increase with the input angular rate. This observation can be explained by the fact that the biasing voltages used for electrostatic tuning of frequency split resulted in an amplitude-frequency coupling, [126, 128], and a 4θ dependent variation in the elasticity, [49], which was not accounted for in Eq. (4.5). Based on Eq. (4.2) and (4.5), a Duffing nonlinearity, due to the electrostatic forces, results in a 4θ dependent variation in quadrature and consequently a 2θ dependent angle error, similar to anisodamping. The 2θ dependent angle error caused by nonlinearity in elasticity correlates to the magnitude of quadrature and increases at input angular rates close to the closed-loop bandwidth of the quadrature controller, which explains the increase of the 2θ-ADB error at input angular rates above 200 DPS.

For the 4θ dependent angle error shown in Fig. 4.8(d), a good agreement between the simulation results and experimental data was observed. At low input angular rates, anisodamping, and at higher input angular rates, anisoelasticity and the corresponding residual quadrature were determined as the major sources of 4θ-ADB in the DFP gyroscope.

4.3.3 Correlation of Frequency Split and EAG

Based on Eq. (4.2) and (4.8), it is noted that frequency split and the quadrature-control parameters determine the effect of anisoelasticity on precession. In this section, we experimentally studied the effect of frequency split ($\Delta\omega$) and control parameters on the residual quadrature and the EAG.

In a series of experiments, by changing the DC biasing voltage applied along the X and Y axes of the DFP, the frequency split was modified, [28]. The frequency split in each experiment was estimated based on variations in the actuation frequency as a function of the pattern angle, as illustrated in Fig. 4.7(a).

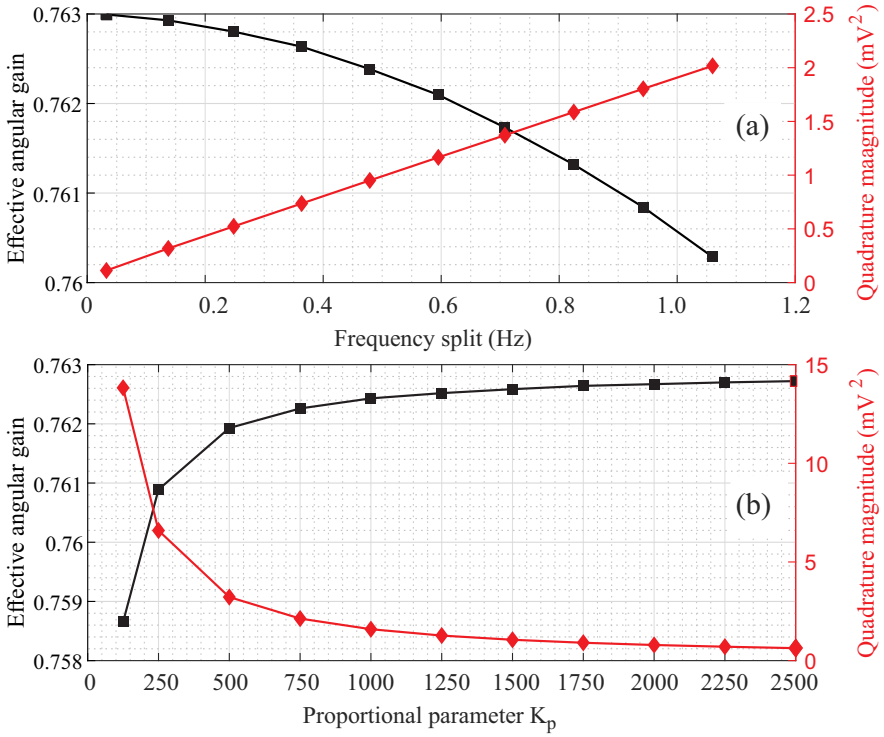

Figure 4.9: Experimental results illustrating the correlation between frequency split, residual quadrature, and effective angular gain. In (a) and (b), it is shown that reducing the frequency split (anisoelasticity) and utilizing a higher proportional gain for the quadrature controller result in a smaller residual quadrature in the gyroscope and minimize the reduction of EAG.

For different values of frequency split, the EAG and the magnitude of quadrature were characterized and the results are shown in Fig. 4.9(a). A linear relation between the frequency split and the residual quadrature is observed, which matches with the analytical expression in Eq. (4.8). It is also shown that at a higher frequency split and correspondingly at a higher residual quadrature, the EAG reduces. Based on this observation, we confirmed that by using a Proportional-Integral (PI) quadrature feedback control, the quadrature in the system cannot be fully eliminated and that the residual quadrature would affect precession.

Based on Eq. (4.8), we anticipated that increasing the proportional controller gain (K_p)

would reduce the residual quadrature and minimize the effect of anisoelasticity on the EAG and the ADBs. This was experimentally confirmed by characterizing the EAG and the residual quadrature at different K_p coefficients. In these experiments, an input angular rate of 200 DPS was applied to the CVG and the results are shown in Fig. 4.9 (b). It should be noted that for different proportional coefficients, although the closed-loop bandwidth was higher than the frequency of perturbation due to anisoelasticity (u_ω), the residual quadrature was inevitable.

Based on these results, we concluded that by reducing anisoelasticity through electrostatic frequency tuning and utilizing a quadrature-control loop with a high proportional coefficient, the effect of anisoelasticity on precession is minimized, and consequently, the EAG is maximized.

On the other hand, as shown in Fig. 4.10, we observed that by utilizing a higher proportional control gain for suppressing quadrature, the sensitivity of EAG to variations of frequency split was reduced. This observation will be important for our discussion in the next chapter when we study the correlation between EAG and the temperature of operation.

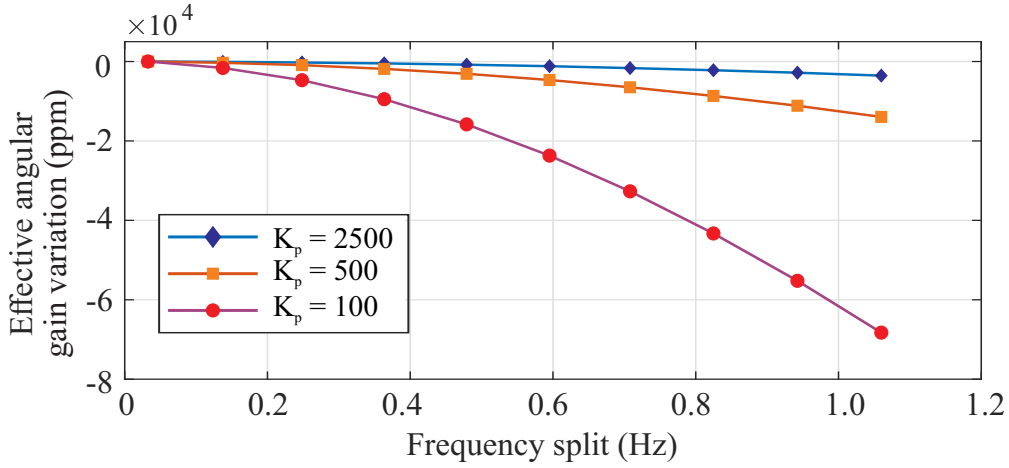

Figure 4.10: Experimental results illustrating the correlation between frequency split and the reduction in EAG for different control parameters. As shown, increasing the proportional control gain would minimize the sensitivity of EAG to frequency split.

4.4 Conclusion

In this chapter, we presented our study on the effect of anisoelasticity on the precession of angle in the WA mode of operation. Using analytical and numerical simulation results, we demonstrated that by adopting a proportional-integral control as the quadrature feedback loop, the magnitude of quadrature (i.e., ellipticity) is reduced by several orders of magnitude. However, we determined that quadrature cannot be fully eliminated through a PI feedback control, and the residual quadrature was shown to increase with the input angular rate.

We demonstrated that residual quadrature, similar to anisodamping, reduces the angular gain and introduces angle-dependent bias errors. In contrast to anisodamping, the effect of anisoelasticity on precession, including the angle-dependent bias error, was shown to be consistent at different input angular rates. Our results suggest that the errors introduced by an uncompensated quadrature degrade the resolution of angle measurements. The effect of mode-matching and quadrature-control parameters on residual quadrature was studied and experimentally verified. Mode-matching through electrostatic frequency tuning and employing a high-gain quadrature control was shown to reduce the angle errors significantly.

Chapter 5

Correlation of Angular Gain and Temperature

5.1 Introduction

In the previous chapter, through experimental data and simulation results, we demonstrated that mechanical imperfections, such as anisoelasticity and anisodamping, affect the angle measurements by reducing the Effective Angular Gain (EAG) and introducing Angle-Dependent Bias (ADB) errors. The ADB and EAG were characterized as systematic angle errors at different input angular rates. Temperature fluctuation during operation is a major source causing drift in anisodamping and anisoelasticity of gyroscopes. Here, we study the mechanism behind Angular Gain Temperature Sensitivity (AGTS) and identify strategies to minimize it.

This chapter is organized as follows. Experimental results on thermal characteristics of the DFP gyroscope are presented in Section 5.2, which we use to explain the correlation between the Temperature Coefficient of Frequency Split (TCFS) and AGTS. In the same

section, strategies for improving angular gain stability are discussed and experimentally demonstrated. In Section 5.3, we introduce the Dynamic Quadrature Controller (DQC), which fully eliminates quadrature during precession and significantly reduces AGTS. A summary of our results and conclusions are found in Section 5.4.

5.2 TCF Mismatch and Angular Gain Temperature Sensitivity

In Chapter 4, it was demonstrated that variations in anisoelasticity and anisodamping affect the angle error characteristics, including the EAG. Based on the angle error characteristics, it was demonstrated that a gyroscope operating in the WA mode provides a better angle resolution at high input angular rates. Therefore, the WA mode of operation is typically used in applications in which a relatively high input angular rate is measured, or the method of Virtual Carouseling (VC) is utilized to virtually rotate the oscillation pattern. By using VC, one can offset the rate of precession and overcome the angle errors at low angular rate inputs, [89].

We also discussed that at a high input angular rate a variation in anisoelasticity has several orders of magnitude higher contribution to the drift of EAG. Therefore, in this chapter, we focused on the correlation of EAG, anisoelasticity, and temperature for an operation in which a high input angular rate is applied to the sensing element through physical or virtual electrostatic means.

5.2.1 TCF Mismatch Characterization

To study the correlation between EAG and temperature, we first characterized the anisoelasticity of the DFP gyroscope at different temperatures. To perform this characterization, we attached a Thermo-Electric Cooling (TEC) element to the lid of the LCC-packaged DFP gyroscope to locally heat or cool the device, and an AD-592 temperature sensor was attached to the backside of the LCC package for continuous temperature measurements. Using a Thorlab TED-4015 temperature controller, we were able to control the temperature of the LCC package at different set-points with a variation within ±10 mK.

As an initialization step, at 27 ℃ temperature, the frequency split ($\Delta\omega$) of the DFP gyroscope was electrostatically reduced to 20.3 mHz. Due to an uncompensated cross-coupling in elasticity between the X and Y modes, we were unable to reduce the frequency split further below this value, [88]. To reduce the frequency split to 20.3 mHz, biasing voltages of 8.3 V and 3.009 V were applied along the X and Y axes, respectively.

After electrostatic frequency tuning, the DFP gyroscope was physically rotated at an input angular rate of 50 Degrees-Per-Second (DPS) and variation of the actuation frequency as a function of pattern angle was utilized to characterize the average resonant frequency and anisoelasticity of the DFP. The experiment was repeated for different temperatures, ranging from 17 ℃ to 45 ℃ with 2 ℃ increments. After reaching 45 ℃, the temperature was reduced to 17 ℃, and the same experiment was repeated two more times. The data points and error bars are used to show the average value and the standard deviation of our measurements.

The average resonant frequency (ω) as a function of temperature is shown in Fig. 5.1 (a). Based on a linear function fitted to the data, the Temperature Coefficient of Frequency (TCF) of the DFP gyroscope was estimated to be on the order of 390 mHz/℃ or equivalently 26 ppm/℃. The residual error in fitting, shown in Fig. 5.1 (b), illustrates that for a wide range of temperatures, the average resonant frequency does not change linearly with

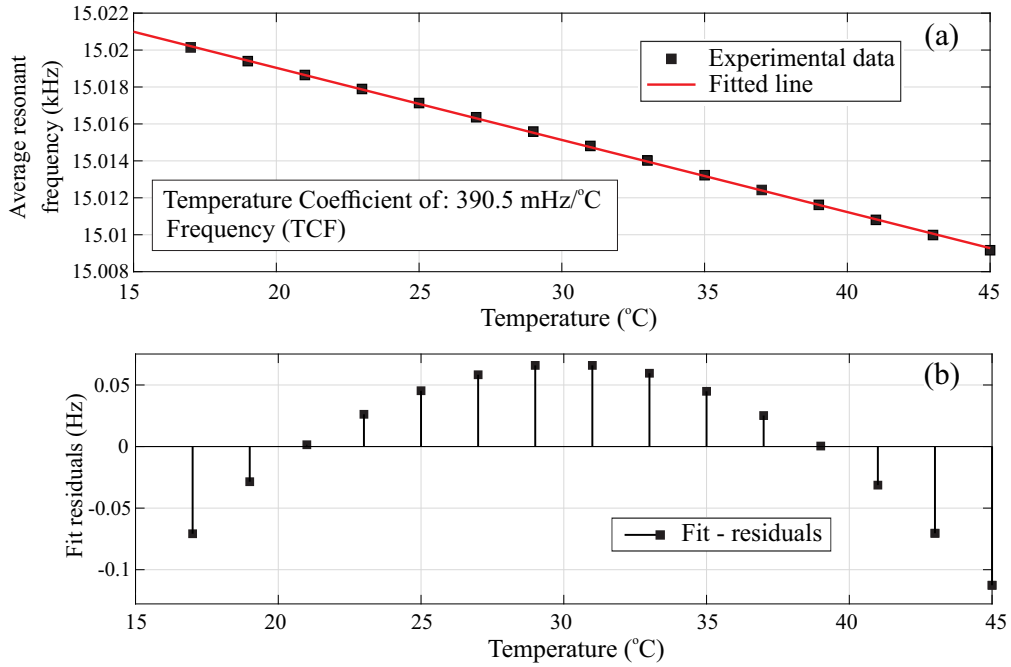

Figure 5.1: The average resonant frequency of the DFP gyroscope at different temperatures of operation. In (a), a linear function was fitted to the data and a TCF of 390.5 mHz/°C was estimated. In (b), the residual error of fitting a linear function is shown, which illustrates that for a wide range of temperatures, a linear function would not accurately capture the frequency-temperature correlation.

temperature, which is in agreement with results in [76].

In the same experiments, as the oscillation pattern was precessing, the peak-to-peak variation of the actuation frequency was measured to estimate the frequency split ($\Delta\omega$) at different temperatures, shown in Fig. 5.2. For the DFP gyroscope under test, the Temperature Coefficient of Frequency Split (TCFS) was estimated to be on the order of 9.06 mHz/°C. These results indicate a TCF mismatch on the order of 603 ppb, potentially caused by stresses of die-attachment and packaging [71] and the crystalline orientation-dependent TCF of silicon material, [76, 109].

The results shown in Fig. 5.2 demonstrated that due to the mismatch in TCF in the two degenerate modes of the DFP, a variation in temperature affects the frequency split of the gyroscope.

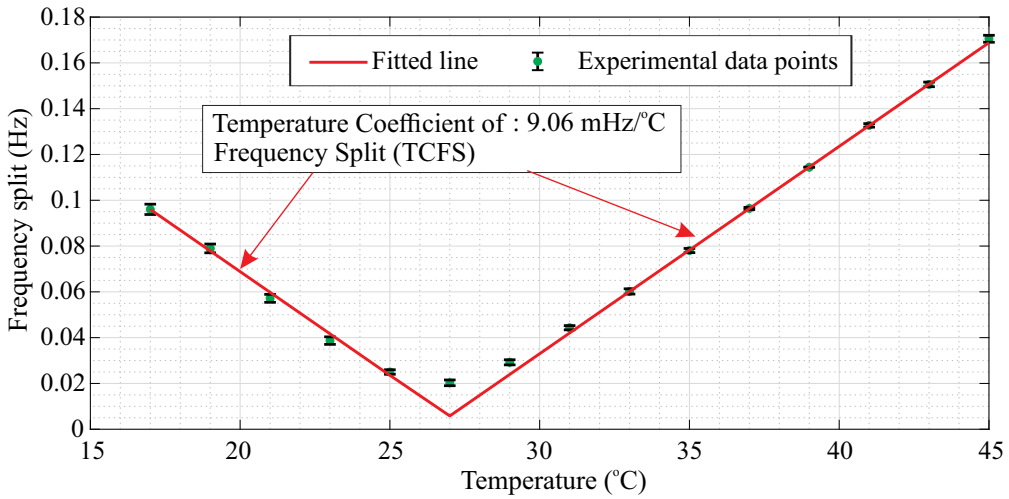

Figure 5.2: Based on variation of the actuation frequency through precession, the frequency split ($\Delta\omega$) of the DFP was characterized at different temperatures and the results are shown. We illustrate as the operation temperature deviates from 27 °C, the frequency split increases with a TCFS of 9.06 mHz/°C.

5.2.2 Angular Gain Temperature Sensitivity

Based on the results in previous chapter, we hypothesized that an increase in the frequency split due to temperature variations would reduce the EAG in the WA mode of operation and cause a drift in direct angle measurements.

To experimentally confirm this, we applied a constant rotation to the DFP gyroscope with an angular rate of 360 DPS, and the temperature of the LCC-package was increased from 17 °C to 45 °C. Once the temperature was stabilized, the precession of angle was recorded for 5 minutes and the EAG was characterized. Variations of EAG as a function of temperature for different proportional control gains (parameter of the quadrature-control loop) are illustrated in Fig. 5.3.

The results illustrate that at temperatures below or above 27 °C, due to an increase in the frequency split, the quadrature in the gyroscope also increases. The increase in the quadrature and frequency split would result in a higher ADB and a reduction of EAG. It is also demonstrated that by utilizing a quadrature controller with a higher proportional coefficient,

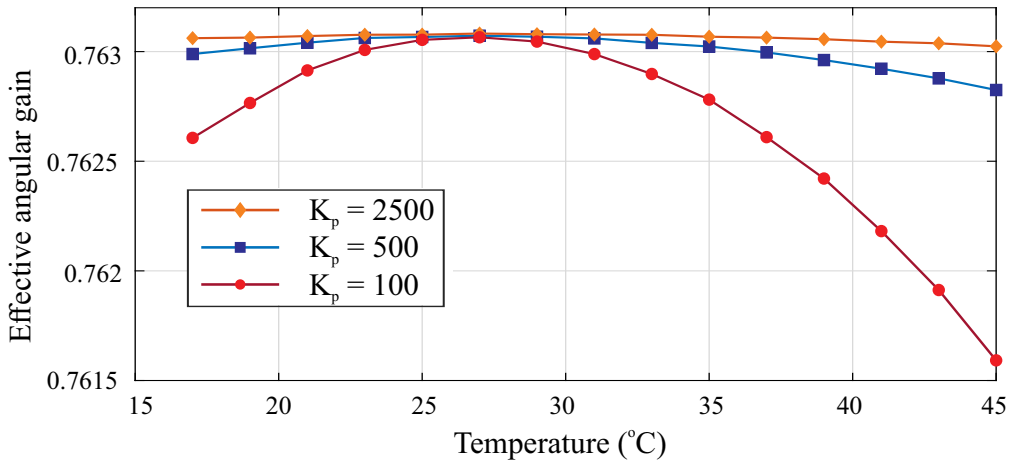

Figure 5.3: EAG of the DFP gyroscope was characterized at different temperatures for different quadrature control settings. As illustrated, the EAG changes with the temperature, a trend which is correlated with the amount of frequency split at different temperatures, shown in Fig. 5.2. It is also demonstrated that the sensitivity of EAG to frequency split can be reduced by increasing the proportional control gain (K_p).

despite of the relatively large TCFS of the DFP gyroscope, the increase in quadrature due to temperature variations was minimized, and correspondingly the sensitivity of EAG to frequency split and temperature variations was reduced. These results are in agreement with the experimental results in the previous chapter on the effect of frequency split on EAG.

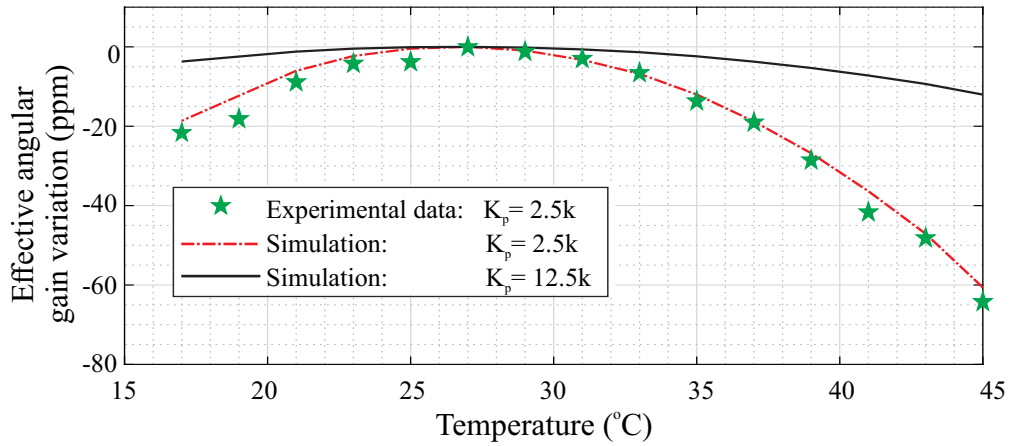

Figure 5.4: A comparison between the simulation results and experimental data for variation of the EAG (in ppm) as a function of temperature is illustrated. The results indicate that for a TCFS of 603 ppb, by using a proportional control gain of 50 we would experience a variation less than 62 ppm for the EAG, in good agreement with the simulation results.

Using the reduced-order WA model, presented in the previous chapter, the variation of the

EAG as a function of temperature was simulated using the TCFS coefficient of the DFP and the frequency split measured at 27 ℃. The variations of the EAG (in ppm with respect to the EAG at 27 ℃) are shown in Fig. 5.4, and a good agreement between simulation results and experimental data is demonstrated. It is also illustrated that by utilizing a 5x higher proportional gain, K_p = 12.5k, the variations of the EAG can be reduced to less than 10 ppm for operation at temperatures ranging from 15 ℃ to 45 ℃. An increase of the proportional gain would require an increase of low-pass filters' bandwidth and higher control voltages, possibly increasing the angle noise characteristic and the power consumption, correspondingly.

5.2.3 Improving The Angular Gain Stability

In Chapter 4, using simulation results, we demonstrated that by carouseling a Rate-Integrating Gyroscope (RIG), the effect of anisodamping and anisodamping variations on EAG can be significantly reduced. In this chapter, we experimentally confirmed that the dependency of EAG to temperature, at a relatively high input angular rate through anisoelasticity, can be minimized through electrostatic frequency tuning and utilizing a high-gain quadrature-control loop. We expected that a combination of minimizing the Angular Gain Temperature Sensitivity (AGTS) and temperature control would appreciably reduce the drift of angular gain in the WA mode of operation.

To experimentally demonstrated this, we characterized the stability of EAG in WA mode of operation. In our experiment, the DFP gyroscope was electrostatically mode-matched ($\Delta\omega$ = 20.3 mHz), and the quadrature control gain (K_p) was set to 2500. The gyroscope was physically rotated at a constant angular rate of $\mathbf{\Omega}$=360 DPS for 24 hours. For the duration of this experiment, the temperature of the device was stabilized using the temperature controller to within ±10 mK. The precession due to the physical rotation was subtracted from the angle output and the estimated angle error is shown in Fig. 5.5(a).

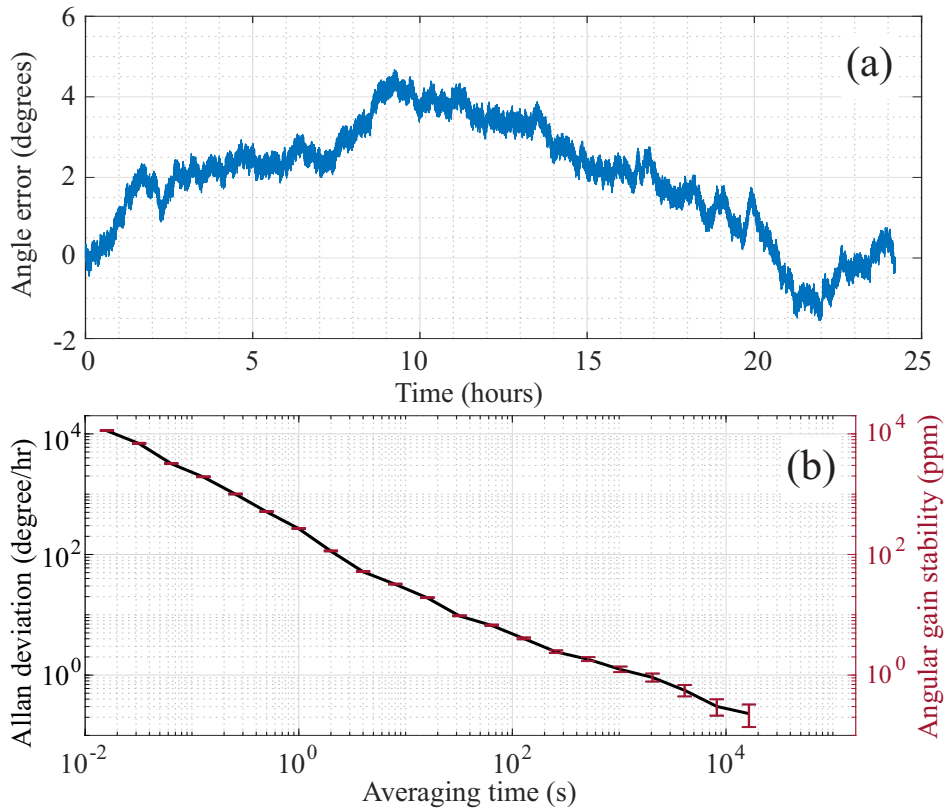

Figure 5.5: An input angular rate of 360 DPS was applied to the DFP WA gyroscope and the angular drift is shown in (a). In (b), the Allan deviation of the measured angular rate (numerical time-derivative of the measured angle) is shown demonstrating an in-run bias instability below 0.2 deg/hr and sub-ppm angular gain stability.

For 24 hours of gyroscope operation, the angle drift was observed to be less than 4.2 degrees. A time-derivative of the WA output was used to obtain angular rate measurements. The Allan variance analysis was utilized to estimate the stability in angular rate measurements and the corresponding angular gain stability, shown in Fig. 5.5(b).

Based on the reported results, we demonstrated that the DFP gyroscope provided a stability better than 0.23 deg/hr in angular rate measurements. As shown in Fig. 5.5(b), for the 24-hours long experiment, we did not observe a Rate Random Walk (RRW) noise in the gyroscope output. We believe that while the proposed methods, which included mode-matching, carouseling, incorporating a high-gain quadrature control, and temperature stabilization, could minimize angular gain variation to a great extent, they cannot fully elim-

inate it. Therefore, we expected ppb-level variations of angular gain over a long duration of operation. To reach the instability point in the Allan variance plot, Fig. 5.5(b), gyroscope output recording for more than a week was required. At 1700 Hz sampling rate, the data would have been computationally too expensive to process. In our implementation, to reduce the sampling rate, the demodulation low-pass filters' cutoff frequency and the controllers' closed-loop bandwidth must be reduced accordingly. As a result, the gyroscope measurement bandwidth would reduce. Nevertheless, we were able to demonstrate angular gain stability better than 230 ppb using the DFP MEM gyroscope, realizing high-accuracy direct angle measurements for prolonged WA operation.

5.3 Dynamic Quadrature Controller (DQC)

In the previous section, we demonstrated that Angular Gain Temperature-Sensitivity (AGTS) is coupled to the effectiveness of the quadrature feedback controller implemented to compensate for anisoelasticity. In the case of using a proportional-integral controller, it was shown that the effectiveness of the controller in reducing quadrature and AGTS could be improved through employing a higher control gain.

In this section, we implement a Dynamic Quadrature Controller (DQC), which can fully eliminate quadrature during precession. We investigate the improvement in AGTS through the DQC.

5.3.1 Quadrature Control

We previously demonstrated that anisoelasticity results in the ellipticity of the oscillation pattern (i.e., quadrature), shown in Fig. 5.6, which in turn reduces the Angular Gain (AG). Assuming that anisoelasticity is constant, the Effective Angular Gain (EAG), denoted by κ_e,

can be characterized and used to estimate the input angle of rotation. However, anisoelasticity variations during the operation of a Micro Rate-Integrating Gyroscope (MRIG) would change the EAG and cause angular drifts in measurements.

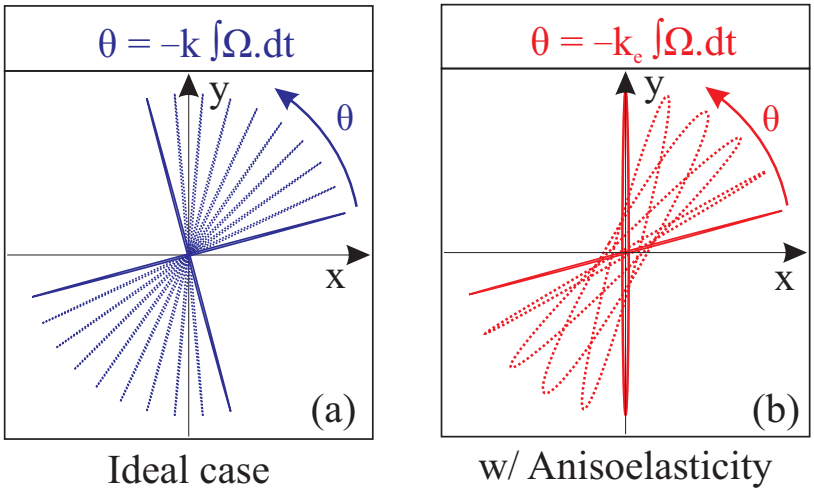

Figure 5.6: Evolution of oscillation pattern in MRIG in the presence of rotation. Anisoelasticity in micro-fabricated gyroscopes results in the ellipticity of the oscillation pattern that reduces the angular gain (i.e., $\kappa > \kappa_e$).

A mismatch in the Temperature Coefficient of Frequency (TCF) of the operational modes was shown to be the primary mechanism causing anisoelasticity variations during operation. Although a feedback controller is often utilized in the WA control architecture to compensate for ellipticity, Angular Gain Temperature Sensitivity (AGTS) becomes inevitable if ellipticity is not fully compensated. In the following, we compare the Dynamic Quadrature Controller (DQC) to the conventional Proportional-Integral (PI) controller and investigate the improvements in AGTS.

Control Architecture

Based on a reduced-order model of MRIG reported in [70], the following differential equation describes the effect of anisoelasticity on precession at a high input angular rate:

$$\dot{\theta} \approx \ -\kappa\Omega + \frac{1}{2}\Delta\omega Q E \cos 2(\theta - \theta_\omega), \tag{5.1}$$

where parameters $\Delta\omega$, θ_ω, Q, and E denote the frequency split, misalignment in the principal axes of elasticity, quadrature, and energy in MRIG. In the WA control architecture, ellipticity in the oscillation pattern is quantified using the quadrature variable (Q). The quadrature variable is used in a feedback loop to apply quadrature compensation forces (f_{qc}) to reduce ellipticity. The following differential equation describes the evolution of quadrature in the presence of anisoelasticity

$$\dot{Q} \approx -2\frac{Q}{\tau} + u_\omega + \frac{\sqrt{E}}{\omega} f_{qc}, \tag{5.2}$$

where anisoelasticity is considered as a perturbation in the form of

$$u_\omega = -\Delta\omega E \sin 2(\theta - \theta_\omega), \tag{5.3}$$

and τ, ω, and f_{qc} denote the average energy decay time constant, the average resonant frequency, and the quadrature control force, respectively. From equations (5.2) and (5.3), it can be concluded that if quadrature control is not utilized ($f_{qc} = 0$), anisoelasticity will result in a large amount of quadrature, and in turn, affect the free precession.

Conventionally, a Proportional-Integral (PI) feedback loop is used for compensation of quadrature [70], illustrated in Fig. 2. Since during precession, anisoelasticity acts as a harmonic time-varying perturbation, Eq. (5.3), a PI controller cannot fully eliminate ellipticity. As a result of the residual quadrature, anisoelasticity affects the free precession, and the Effective Angular Gain (EAG) is reduced [130]. In this case, the anisoelasticity-induced reduction of EAG is quadratically dependent on the frequency split ($\Delta\omega$). If frequency split changes during operation due to temperature variations, so does the EAG. By applying a

quadrature control that fully eliminates quadrature ($Q = 0$), the effect of anisoelasticity on precession and the dependency between EAG and frequency split would diminish.

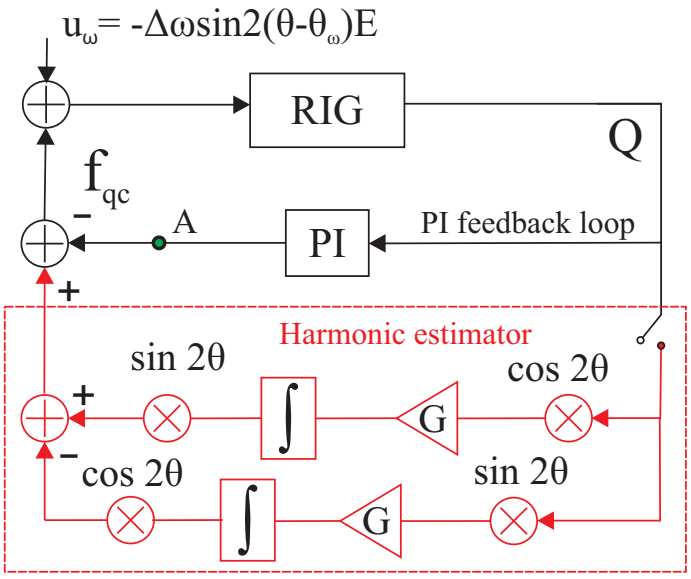

Figure 5.7: Block diagram of a Dynamic Quadrature Controller (DQC), which is comprised of a PI feedback loop and a harmonic estimator. The harmonic estimator utilizes residual quadrature (Q) to estimate and cancel the harmonic perturbation due to anisoelasticity (u_ω).

The quadrature control proposed in [35] has been reported to eliminate quadrature. As illustrated in Fig. 5.7, by utilizing a feedback loop that applies an angle-dependent compensation force along with the quadrature PI control, we can fully compensate for anisoelasticity at the source. Through a sequence of demodulation, integration, and modulation of residual quadrature based on the pattern angle (θ), the quadrature control force converges to a harmonic force with an amplitude equal to the anisoelasticity perturbation (u_ω) and a phase relation that would destructively eliminate anisoelasticity. We refer to this control architecture as a Dynamic Quadrature Controller (DQC). Mathematical background on stability and convergence of such control architecture can be found in [142].

5.3.2 Experimental Results

To demonstrate the correlation between AGTS and TCF-mismatch, we instrumented the DFP gyroscope for direct angle measurements using the WA control. For compensation of anisoelasticity, we explored two control architectures, a PI feedback loop and a DQC proposed in [70] and [35], respectively.

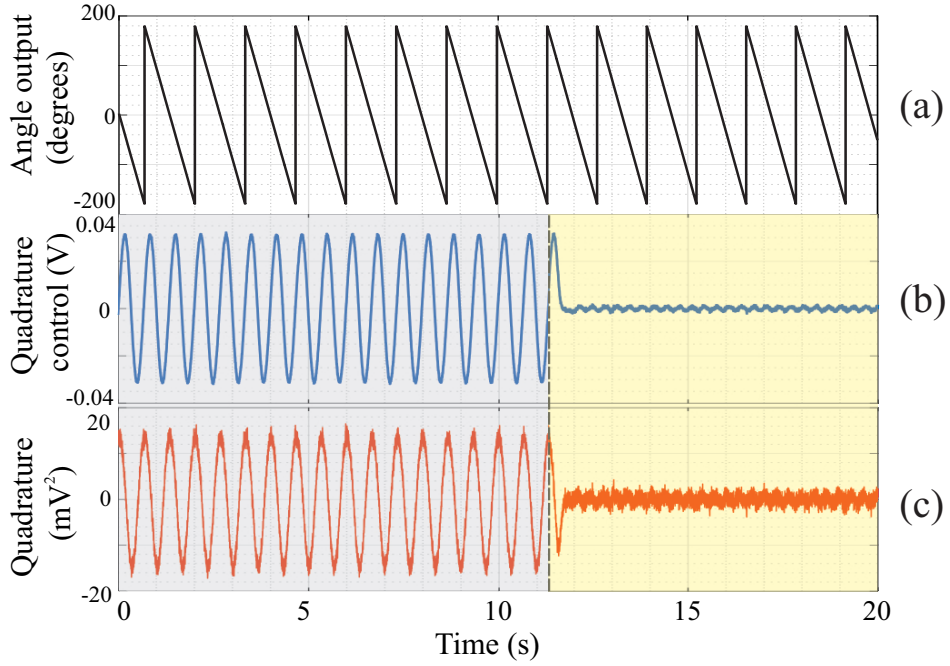

Figure 5.8: Experimental measurements of quadrature and output of the PI quadrature control are shown for two different quadrature control architectures.

The WA control was implemented using the Real-Time Kit (RTK) on a Zurich instrument HF2Li lock-in amplifier (Appendix B). By physically rotating the DFP at 360 Degrees-Per-Second (DPS), we were able to demonstrate precession, shown in Fig. 5.8(a).

Effectiveness of Quadrature Control

In this section, we experimentally compared the effectiveness of quadrature control architectures. In the experiment, the frequency split of the DFP was electrostatically reduced from

114 Hz to 302 mHz. We first applied a PI feedback loop as the quadrature control. Twelve seconds into the operation, we engaged the harmonic estimator as a part of the DQC control, Fig. 5.7. The variations of quadrature and the output of the PI feedback loop (node A in Fig. 5.7) are shown in Fig. 5.8(b) and (c).

By plotting the variation of quadrature as a function of the pattern angle (θ), we evaluated the effectiveness of the quadrature controls. As shown in Fig. 5.9, by not utilizing a quadrature control, the ellipticity (quadrature) was observed to change harmonically with a large amplitude. The PI quadrature control reduced quadrature by more than 10-times; applying the DQC could eliminate ellipticity in the WA mode of operation.

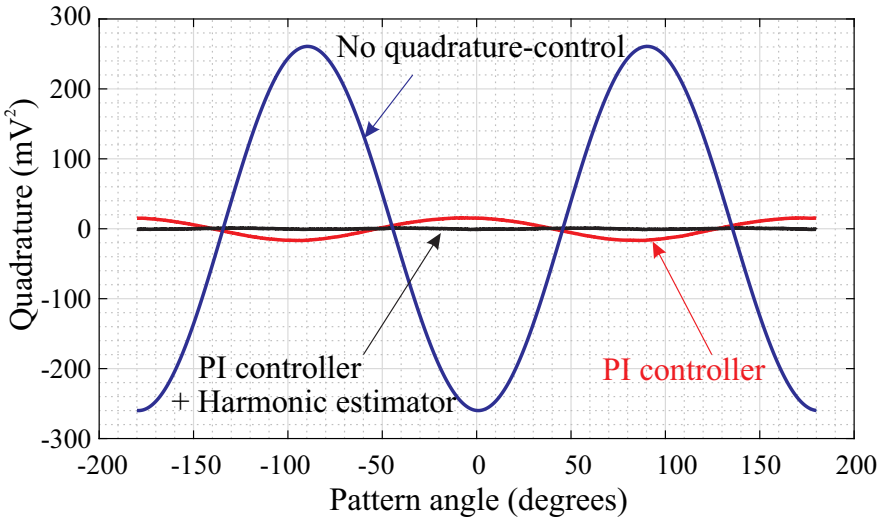

Figure 5.9: Variations of quadrature during the precession as a function of the pattern angle (θ). The effectiveness of the two control architectures for quadrature compensation is illustrated.

Similar to the conventional PI quadrature control, the output of the harmonic estimator is applied in phase with the reference oscillation phase. Therefore, the controller output does not interfere with precession [143].

Angular Gain Temperature Sensitivity

To demonstrate the improvement in Angular Gain Temperature Sensitivity (AGTS), the EAG was characterized at different temperatures, shown in Fig. 5.10. The correlation between frequency-split (Fig. 5.2) and EAG variations can be noted. By utilizing the harmonic estimator along with the PI controller, a 63-times reduction in AGTS was obtained, as illustrated in Fig. 5.10. The improvement was attributed to the effectiveness of the DQC architecture that fully eliminated ellipticity.

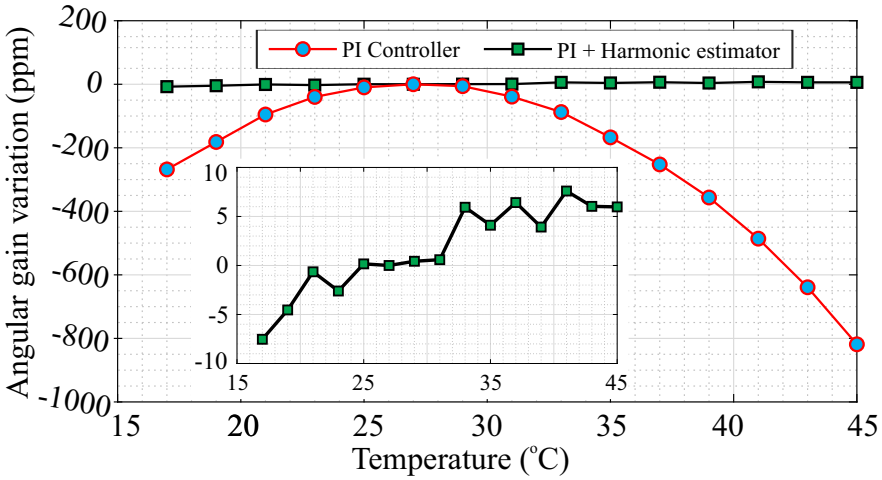

Figure 5.10: Experimental data on variations of angular gain as a function of temperature. It is demonstrated that by utilizing the DQC, the AGTS was reduced by 63-times.

In theory, since the DQC eliminates quadrature, an AGTS due to a TCF mismatch is expected to be fully compensated. The remaining AGTS observed in the inset of Fig. 5.10 is believed to have been caused by an unwanted interference of the energy control and quadrature control forces on precession.

Angular Gain Stability

We tested the improvement in the accuracy of direct angle measurements and angular gain stability. The DFP gyroscope was rotated at 360 DPS for 10 hours, and the temperature

around the LCC was changed with a profile shown in Fig. 5.11(a). Based on the EAG at 27 °C, the time-linear variation in angle was subtracted from the output of the gyroscope, and the angular drift was plotted as a function of time in Fig. 5.11(b).

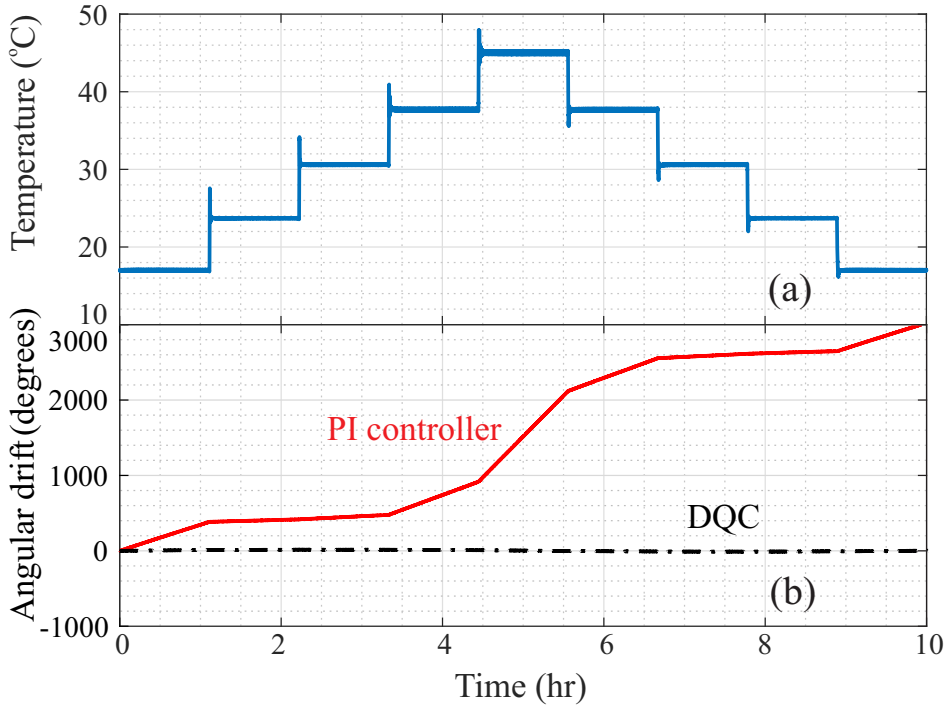

Figure 5.11: Angular drift of the DFP gyroscope rotated at 360 DPS and introduced to dynamic temperature changes, with a profile shown in (a), is demonstrated in (b).

As demonstrated in Fig. 5.11(b), in the case of using a PI quadrature control after 10 hours of operation, the angular drift was on the order of 3000 degrees. The slope of angular drift in each interval corresponded to variation of the EAG demonstrated in Fig. 5.11(b). By repeating the same experiment and applying the DQC, we could reduce the angular drift to less than 25 degrees, a 120-times improvement.

To characterize the stability of EAG, we numerically calculated the time-derivative of the measured angle and applied the Allan variance characterization method. As illustrated in Fig. 5.12, we achieved 10-times improvement in EAG stability for operation during dynamic temperature changes from 17 °C to 45 °C by applying the DQC.

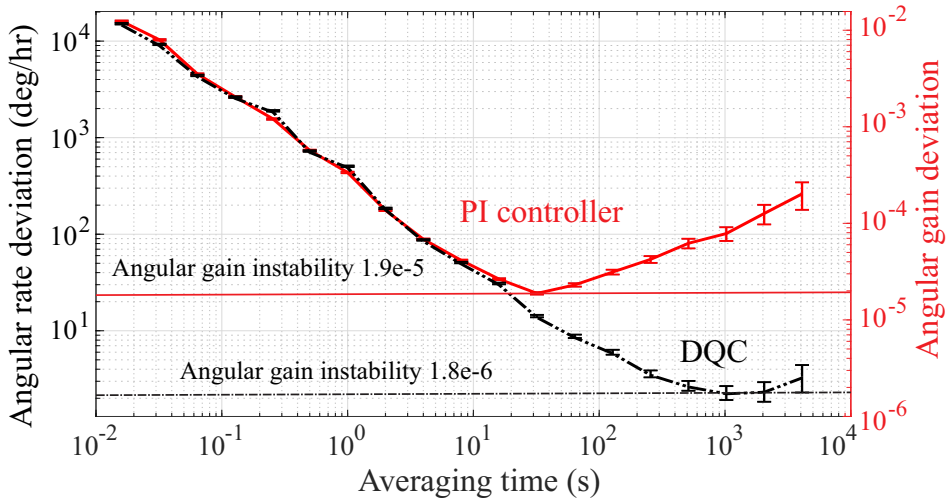

Figure 5.12: Allan variance of time-derivative of angle output. The results characterize the stability of effective angular gain in operation through dynamic temperature fluctuations.

5.4 Conclusion

This chapter explained the correlation between the temperature of operation and effective angular gain in the WA mode of operation through experimental results. We experimentally confirmed that a TCF mismatch in the mechanical sensors is the main mechanism that leads to Angular Gain Temperature Sensitivity (AGTS) at relatively high input angular rates. We demonstrated that AGTS is also dependent on the effectiveness of the quadrature control, which is utilized to reduce ellipticity and compensate for anisoelasticity. In the case of using a Proportional-Integral (PI) quadrature control, we demonstrated that through mode-matching and utilizing a high-gain quadrature control, AGTS could be reduced by several orders of magnitude. By implementing these methods with the DFP MRIG along with temperature stabilization, we demonstrated angular gain stability better than 230 ppb.

Furthermore, we explored using a harmonic estimator and a PI feedback loop as the quadrature control (i.e., the DQC) and demonstrated its potential to eliminate quadrature during precession. For the DFP gyroscope, with a TCF-mismatch on the order of 603 ppb/°C, the angular gain variation was measured to be on the order of 820 ppm for temperatures ranging

from 17 °C to 45 °C. The DQC reduced AGTS by 63-times, down to 13 ppm. Despite a TCF-mismatch in the sensing element, our results provided a mitigation strategy to achieve increased angular gain stability in MRIG. The reduction in AGTS enabled us to measure sub-degree-per-hour angular rates at ambient temperature and angular rates on the order of 2.1 deg/hr when operating in an environment with dynamic temperature variations without the need of an active temperature stabilizer.

Chapter 6

Effect of Imperfections in Control Electronics on Whole-Angle Operation

6.1 Introduction

This chapter studies the effect of imperfections in detection and control electronics on precession in the Whole-Angle (WA) mode of operation. We developed a mathematical model to capture both the mechanical sources of error and error sources associated with the electronics. Using the model, we demonstrated that due to imperfections in electronics, the effectiveness of WA control loops is compromised. As a result, the control forces interfere with the free precession of the oscillation pattern. Based on our findings, a methodology was proposed through which we were able to decouple mechanical error sources from electrical error sources for identification and compensation of the detection and actuation gain mismatches.

In Section 6.2, we introduce an electro-mechanical model for numerical simulation of RIG. We study the effect of imperfections coming from control and detection electronics on WA operation using the model. The simulation results are explained using Lynch's analytical framework on the evolution of pendulum variables. In Section 6.3, a methodology is proposed for the identification and compensation of gain asymmetries in the detection and control electronics. We apply the proposed method to a Dual Foucault Pendulum (DFP) gyroscope and demonstrate the improvements in the resolution of angle measurements. A summary of our results and conclusions are found in Section 6.4.

6.2 Mathematical Model

A lumped mass-spring-damper representation of a Coriolis Vibratory Gyroscope (CVG) is shown in Fig. 6.1. The following differential equation governs the dynamics of a CVG

$$\begin{bmatrix} \ddot{q}_1 \\ \ddot{q}_2 \end{bmatrix} + Z \begin{bmatrix} \dot{q}_1 \\ \dot{q}_2 \end{bmatrix} + K \begin{bmatrix} q_1 \\ q_2 \end{bmatrix} = \begin{bmatrix} F_1 \\ F_2 \end{bmatrix}, \tag{6.1}$$

where the variables q_1, q_2, F_1, and F_2 denote the displacement and control forces along the reference X and Y axes. The Z and K matrices include the coefficients of damping, elasticity, and the Coriolis forces

$$Z = \begin{bmatrix} \frac{2}{\tau} + \Delta(\frac{1}{\tau}) \cos 2\theta_\tau & \Delta(\frac{1}{\tau}) \sin 2\theta_\tau - 2\kappa\Omega \\ \Delta(\frac{1}{\tau}) \sin 2\theta_\tau + 2\kappa\Omega & \frac{2}{\tau} - \Delta(\frac{1}{\tau}) \cos 2\theta_\tau \end{bmatrix}$$

$$K = \begin{bmatrix} \omega^2 - \omega\Delta\omega \cos 2\theta_\omega & -\omega\Delta\omega \sin 2\theta_\omega \\ -\omega\Delta\omega \sin 2\theta_\omega & \omega^2 + \omega\Delta\omega \cos 2\theta_\omega \end{bmatrix} \tag{6.2}$$

where κ and Ω denote the mechanical angular gain and the input angular rate. Definitions of the average resonant frequency ω, frequency split $\Delta\omega$, average damping coefficient $1/\tau$, damping difference $\Delta(1/\tau)$, and misalignment angles (θ_ω and θ_τ) can be found in Fig. 6.1.

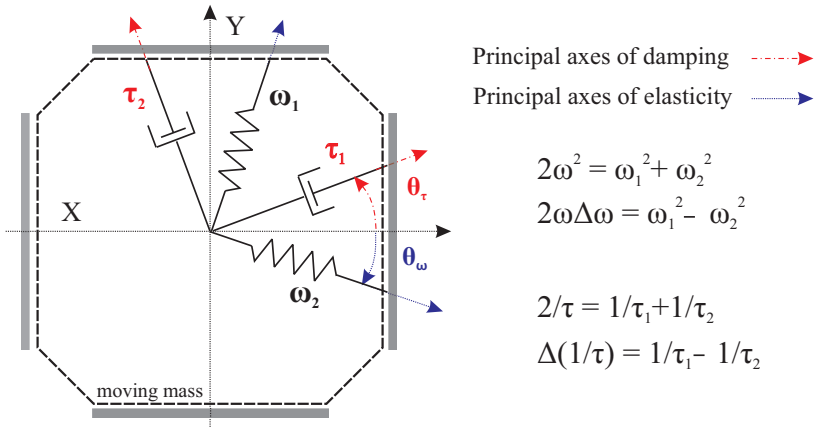

Figure 6.1: A lumped mass-spring-damper representation of a Coriolis vibratory gyroscope. The XY axes denote the non-inertial reference frame attached to the sensing element aligned with the direction of actuation and detection. Principal axes of damping, principal axes of elasticity, and their orientation with respect to the reference axes are illustrated.

The mechanical imperfections such as energy loss, anisodamping, and anisoelasticity affect the evolution of the semi-ellipsoid oscillation pattern, [31, 70, 143]. In Chapter 4, we demonstrated that the mechanical imperfections result in systematic errors in angle measurements, such as angle-dependent biases (ADB), reduced angular gain, and angle locking effect. These errors can be captured through the following representation of the angle of precession.

$$\theta = -\kappa_e \int \Omega \, dt + \theta_b, \qquad (\Omega > \Omega_{th}), \tag{6.3}$$

where θ represents the orientation of the oscillation pattern, and κ_e, Ω, Ω_{th}, and θ_b denote the effective angular gain, input angular rate, angular rate threshold, and angle bias error, respectively. The results in Chapter 4 were based on the assumption that we have ideal control electronics and that the WA control forces do not interfere with precession. This chapter studies the effect of imperfections in control electronics on angle error characteristics.

The errors in detection and control electronics stem from one or multiple parts of the elec-

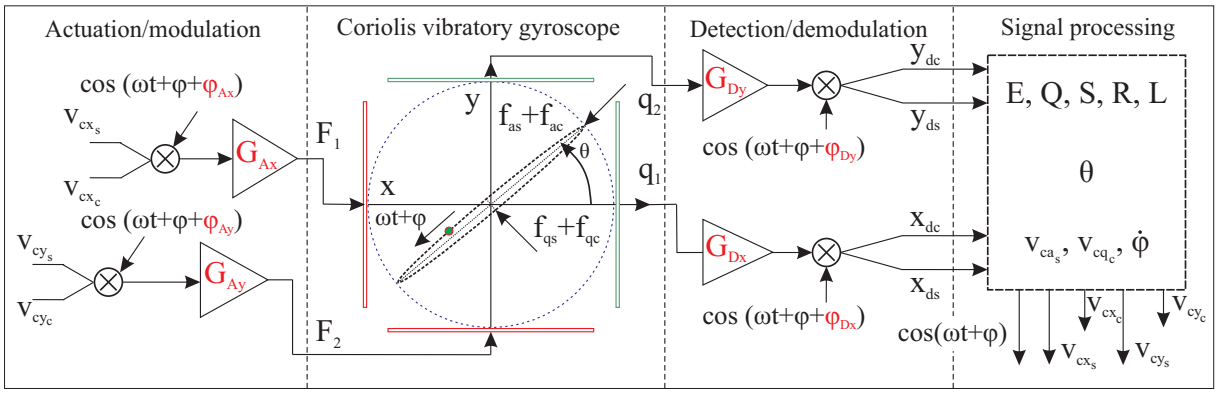

Figure 6.2: Block diagram representation of a CVG operated in the WA mode. In the actuation/modulation block, the command signals coming from the signal processing unit are modulated at the reference phase and converted to electrostatic forces along the X and Y axes using the actuation gains G_{Ax} and G_{Ay}, respectively. In the detection/demodulation block, the position of the poof-mass along the X and Y axes is converted to voltages through detection gains G_{Dx} and G_{Dy}. Then, signal demodulation is performed using the reference phase for estimating the in-phase and in-quadrature-phase components. In the signal processing unit, the demodulated signals are used to calculate pendulum variables and the control signals.

tronics, including the capacitive transduction of the resonator, front-end buffer electronics, Digital-Analog Converters (DAC), Analog-Digital Converters (ADC), Field Programmable Gate Array (FPGA), and the Digital Signal Processing (DSP) (or micro-controller unit). The combinatory effect of different sources of error can be categorized into four main groups (a) modulation phase errors, (b) demodulation phase errors, (c) mismatch in detection gains, and (d) mismatch in the actuation gains, illustrated in Fig. 6.2.

To have a representation that captures the input and output variables that are used in the actual experimental setup, we used the following as the states of the system

$$\begin{bmatrix} x \\ y \end{bmatrix} = G_D \begin{bmatrix} q_1 \\ q_2 \end{bmatrix}, \qquad \begin{bmatrix} v_x \\ v_y \end{bmatrix} = G_A^{-1} \begin{bmatrix} F_1 \\ F_2 \end{bmatrix}, \tag{6.4}$$

where G_D and G_A denote the nominal conversion gains in displacement-to-voltage and voltage-to-force-per-mass, respectively. In this representation, parameters x and y express the mass position along X and Y axes in voltages, and v_x and v_y represent the applied har-

monic voltages used for generating the electrostatic control forces. The equation of motion governing these variables are

$$\begin{bmatrix} \ddot{x} \\ \ddot{y} \end{bmatrix} + Z \begin{bmatrix} \dot{x} \\ \dot{y} \end{bmatrix} + K \begin{bmatrix} x \\ y \end{bmatrix} = G_A G_D \begin{bmatrix} v_x \\ v_y \end{bmatrix} \tag{6.5}$$

The state variables and input forces can be represented through the following coordinate transformation, which decouples the two time scales at which variables change.

$$\begin{aligned} x(t) &= x_c(t)\cos(\omega t + \phi(t)) + x_s(t)\sin(\omega t + \phi(t)) \\ y(t) &= y_c(t)\cos(\omega t + \phi(t)) + y_s(t)\sin(\omega t + \phi(t)) \\ v_x(t) &= v_{xc}(t)\cos(\omega t + \phi(t)) + v_{xs}(t)\sin(\omega t + \phi(t)) \\ v_y(t) &= v_{yc}(t)\cos(\omega t + \phi(t)) + v_{ys}(t)\sin(\omega t + \phi(t)) \end{aligned} \tag{6.6}$$

where $\omega t + \phi$ is used as the reference phase in the coordinate transformation. It is noted that estimation of variables x_c, x_s, y_c, y_s, and $\dot{\phi}$ would be enough to recover the full oscillatory response of an RIG.

As illustrated in Fig. 6.2, in the closed-loop WA control, we have measurements of the slow-varying parameters. To capture phase errors and gain mismatch in the detection electronics, we defined the following variables as detection variables (equivalent to the demodulated readouts) and are subsequently used to estimate pendulum variables.

$$\begin{aligned} \begin{bmatrix} x_{dc} \\ x_{ds} \end{bmatrix} &= R(-\phi_{Dx}) \begin{bmatrix} x_c \\ x_s \end{bmatrix} \\ \begin{bmatrix} y_{dc} \\ y_{ds} \end{bmatrix} &= G_{Dy/x} R(-\phi_{Dy}) \begin{bmatrix} y_c \\ y_s \end{bmatrix}, \end{aligned} \tag{6.7}$$

where we assumed that the previously defined nominal detection gain is equal to the detection

gain along the X-axis ($G_D = G_{Dx}$) and the ratio of the detection gain along the Y-axis to the nominal value is denoted using $G_{Dy/x}$. The matrix $\boldsymbol{R}$ represents a 2-dimensional rotation matrix, and phases ϕ_{Dx} and ϕ_{Dx} denote the phase errors in demodulation along X and Y axes, respectively.

Based on the detection variables defined in Eq. (6.7), the pendulum variables are estimated as

$$\begin{aligned} E_d &= x_{dc}^2 + x_{ds}^2 + y_{dc}^2 + y_{ds}^2 \\ Q_d &= 2(x_{dc}y_{ds} - y_{dc}x_{ds}) \\ R_d &= x_{dc}^2 + x_{ds}^2 - y_{dc}^2 - y_{ds}^2 \\ S_d &= 2(x_{dc}y_{dc} + y_{ds}x_{ds}) \\ \Im(L_d) &= 2(x_{dc}x_{ds} + y_{dc}y_{ds}) \end{aligned} \tag{6.8}$$

from which the orientation of the oscillation pattern was estimated through the following

$$\theta_d = \frac{1}{2} atan(S_d/R_d) \tag{6.9}$$

where the subscript "d" denotes that these values are estimated based on measurements, and they would be different from the actual/physical pendulum variables in the case of having errors in the detection electronics.

For WA mode, we used the conventional WA control architecture, which includes (a) energy control to maintain the amplitude along the semi-major axis of the orbital trajectory, (b) quadrature control to suppress quadrature (i.e., amplitude of vibration along the semi-minor axis) growth due to anisoelasticity, and (c) a Phase-Locked Loop (PLL) which tracks the phase of oscillation and nulls the phase difference between actuation and detection using a Numerically-Controlled Oscillator (NCO). The mathematical representation of these controllers based on the pendulum variables have been discussed in [70] and are summarized

as

$$
\begin{aligned}
v_{ca_s} &= K_E[E_d - E_0 + \frac{1}{2\tau_E}\int (E_d - E_0)\,dt] \\
v_{cq_c} &= -K_Q[Q_d - Q_0 + \frac{1}{2\tau_Q}\int (Q_d - Q_0)\,dt] \\
\dot{\phi} &= -K_{L_i}[\Im(L_d) - L_{i0} + \frac{1}{2\tau_L}\int (\Im(L_d) - L_{i0})\,dt]
\end{aligned}
\tag{6.10}
$$

where K_E, K_Q, and K_{L_i} are the proportional coefficients of the PI controllers and τ_E, τ_Q, and τ_L are the integration time constants.

In a general WA control, the control voltages defined in Eq. (6.10) are projected onto two sets of electrodes with orthogonal forcing directions along X and Y and exerted as electrostatic forces. In this approach, the vector summation of the forces along X and Y would have the appropriate direction and phase relative to the orientation of the orbital trajectory and phase of the oscillation. The control voltages along the semi-major and minor axes of the orbital trajectory are projected along X and Y axes based on the estimated orientation of the oscillation pattern θ_d as

$$
\begin{aligned}
v_{cx_c} &= -v_{cq_c}\sin(\theta_d) \\
v_{cx_s} &= +v_{ca_s}\cos(\theta_d) \\
v_{cy_c} &= +v_{cq_c}\cos(\theta_d) \\
v_{cy_s} &= +v_{ca_s}\sin(\theta_d)
\end{aligned}
\tag{6.11}
$$

These control signals would go through a similar transformation as the detection signals to

capture phase errors in modulation and actuation gain mismatch, illustrated in Fig. 6.2.

$$\begin{bmatrix} v_{x_c} \\ v_{x_s} \end{bmatrix} = R(\phi_{Ax}) \begin{bmatrix} v_{cx_c} \\ v_{cx_s} \end{bmatrix}$$
$$\begin{bmatrix} v_{y_c} \\ v_{y_s} \end{bmatrix} = G_{Ay/x} R(\phi_{Ay}) \begin{bmatrix} v_{cy_c} \\ f_{cy_s} \end{bmatrix}, \tag{6.12}$$

where the previously defined nominal actuation gain was assumed to be equal to the actuation gain along the X-axis ($G_A = G_{Ax}$) and the actuation gain ratio is denoted using $G_{Ay/x}$.

6.2.1 Effect of Non-idealities in Electronics

In this section, we utilize Lynch's analytical framework for the evolution of pendulum variables to explain the effect of imperfections in electronics on the effectiveness of WA control loops. We also use numerical simulation based on the mathematical model provided in Section 6.2 (further discussed in Appendix A) to validate our conjectures. For numerical simulation, we used MRIG parameters summarized in Table 6.1, which were characterized for the Dual Foucault Pendulum (DFP).

Table 6.1: Characterized gyroscope parameters used for numerical simulation.

Parameter	Value	Parameter	Value
ω	15016.219 Hz	K_E	2.5e3
$\Delta\omega$	0.0354 Hz	τ_E	5e-3
θ_ω	-58.82^o	K_Q	2.5e+3
τ	22.43 s	τ_Q	5e-3
$\Delta\tau$	1.169 s	K_L	2e+4
θ_τ	-1.465^o	τ_L	2.5e-5
E_0	2.5e-3 V^2	$G_A G_D$	1.01e5
Q_0 and L_{i0}	0	Mechanical angular gain	0.76307

Evolution of Pendulum Variables

In a conventional WA control architecture, the control forces can be categorized into four groups as reported in [31, 70, 143].

1. force in-quadrature to the oscillation phase along the semi-major axis of the orbital trajectory (f_{as}), which affects the energy in the system.
2. force in-quadrature to the oscillation phase along the semi-minor axis of the orbital trajectory (f_{qs}), which affects the orientation of the oscillation pattern.
3. force in-phase to the oscillation phase along the semi-major axis of the orbital trajectory (f_{ac}), which affects the actuation-detection phase relationship.
4. force in-phase to the oscillation phase along the semi-minor axis of the orbital trajectory (f_{qx}), which affects the quadrature component of oscillation.

These four categories of forces are illustrated in Fig. 6.2. Assuming for a small quadrature-to-energy ratio ($\frac{Q}{E} \ll 1$) and phase difference between the reference phase and the phase of oscillation ($\delta\phi \approx 0$), the evolution of the oscillation pattern due to these four categories of force can be modeled using

$$\begin{aligned}
\dot{E} &= -[\frac{2}{\tau} + \Delta(\frac{1}{\tau})\cos 2(\theta - \theta_\tau)]E - \frac{\sqrt{E}}{\omega} f_{a_s} \\
\dot{Q} &= -\frac{2}{\tau} Q - \Delta\omega \sin 2(\theta - \theta_\omega)E + \frac{\sqrt{E}}{\omega} f_{q_c} \\
\dot{\theta} &= -k\Omega + \frac{1}{2}\Delta(\frac{1}{\tau})\sin 2(\theta - \theta_\tau) + \Delta\omega \cos 2(\theta - \theta_\omega)\frac{Q}{E} - \frac{f_{q_s}}{2\omega\sqrt{E}} \\
\delta\dot{\phi} &= \dot{\phi} + \frac{\Delta\omega}{2}\cos 2(\theta - \theta_\omega) + \frac{1}{2}\Delta(\frac{1}{\tau})\sin 2(\theta - \theta_\tau)\frac{Q}{E} + \frac{f_{a_c}}{2\omega\sqrt{E}}
\end{aligned} \tag{6.13}$$

Assuming for ideal control electronics, the energy control force (f_{a_s}) and quadrature control force (f_{q_c}) are applied along the major and minor axes in-quadrature and in-phase to the

oscillation; therefore, control forces do not affect precession. However, as it will be discussed in the following, this statement ceases to be true in the presence of imperfections in control electronics.

Gain Mismatch in Detection Electronics

In an electrostatic motion detection circuitry, the position-to-voltage gain is a function of the nominal capacitance, capacitive gap size, carrier voltage, carrier frequency, phase delay in carrier demodulation, transimpedance gain, etc. The detection gains mismatch along the X and Y axes could stem from asymmetry in any of these parameters, except for the carrier voltage and carrier frequency. We refer to the asymmetry in the motion detection gains as the Detection Gain Mismatch (DGM, i.e., $G_{Dx} \neq G_{Dy}$).

Non-identical detection gains along the X and Y axes would result in an error in estimating the pendulum variables. For example, for the energy (E) variable, based on Eq. (6.7) and (6.8) assuming we have negligible quadrature, the estimation would be in the form of

$$E_d = E(1 + (G_{Dy/x} - 1)\sin^2(\theta)), \tag{6.14}$$

which indicates that in the presence of detection gain mismatch, the estimation of the system's actual energy (E) would have errors. The error is shown to be dependent on the orientation of the oscillation pattern and the detection gain ratio $G_{Dy/x}$. While the energy control loop would sustain the energy estimate (E_d), the actual energy would vary as a function of the pattern angle. Variations in the energy in the system would not affect the precession, Eq. (6.13); however, as a result of the DGM, the energy controller's output would not correlate to the anisodamping in the mechanical structure.

Also, an estimation of the orientation of orbital trajectory using Eq. (6.9) is based on the

assumption that detection gains along X and Y axes are identical. However, if there is a gain mismatch, we would have errors in pattern angle estimation. Assuming a negligible amount of quadrature, as compared to the energy, the orientation of the oscillation pattern based on Eq. (6.9) can be simplified as

$$\theta_d = atan2(G_{Dy/x} y_c, x_c) \tag{6.15}$$

Assuming non-identical gains along X and Y axes (i.e, $G_{Dy/x} \neq 1$), we would have an error in our estimation of the orientation of the orbital trajectory represented as

$$\theta_{error} = \theta_d - \theta, \tag{6.16}$$

where θ is the true orientation of the orbital trajectory which is obtained in the case of having identical detection gains (i.e., $G_{Dx} = G_{Dy}$). Error in the orientation estimation can be estimated as a function of the true orientation using

$$\theta_{error} = atan2(G_{Dy/x} \cdot \sin(\theta), \cos(\theta)) - \theta \tag{6.17}$$

The estimation error is illustrated in Fig. 6.3 for different ratios of detection gain mismatch ($G_{Dy/x}$). As shown, the error in the estimation of true orientation is zero along the X and Y axes and maximum in between.

The error in pattern angle estimation can be regarded as a superposition to the angle error caused by mechanical imperfections, which results in a higher ADB. On the other hand, due to an error in pattern angle estimation, we cannot apply the control forces at the correct orientation relative to the orbital trajectory.

To better explain the second issue, we refer you to Eq. (6.11). Estimating in-phase and

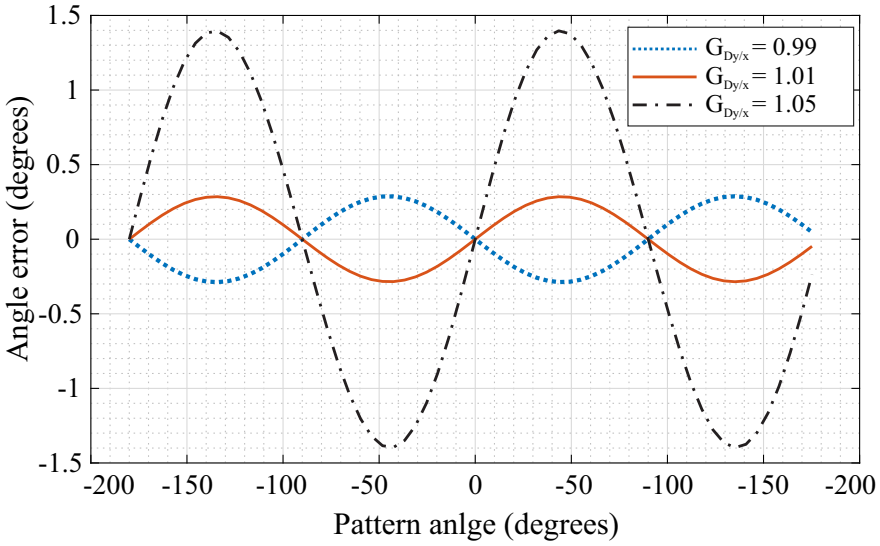

Figure 6.3: Simulated error in estimating the pattern angle for different values of detection gain ratio.

in-quadrature-phase forces along X and Y for controlling energy and quadrature requires a correct estimation of θ. Considering the error in estimating the orientation of the oscillation pattern, the forces projected on the X and Y axes based on the output of the energy and quadrature control will be in the form of

$$\begin{aligned} v_{cx_c} &= -v_{cq_c} \sin(\theta + \theta_{error}) \\ v_{cx_s} &= +v_{ca_s} \cos(\theta + \theta_{error}) \\ v_{cy_c} &= +v_{cq_c} \cos(\theta + \theta_{error}) \\ v_{cy_s} &= +v_{ca_s} \sin(\theta + \theta_{error}) \end{aligned} \tag{6.18}$$

If we project these forces back along the semi-major and minor axes of the orbital trajectory

using the true orientation of the oscillation pattern, we would have,

$$\begin{aligned} f_{a_s} &= G_A v_{ca_s} \cos(\theta_{error}) \\ f_{q_s} &= G_A v_{ca_s} \sin(\theta_{error}) \\ f_{a_c} &= G_A v_{cq_c} \sin(\theta_{error}) \\ f_{q_c} &= G_A v_{cq_c} \cos(\theta_{error}) \end{aligned} \tag{6.19}$$

as compared to the control output v_{ca_s} and v_{cq_c}, excitation forces f_{a_s}, f_{q_s}, f_{a_c}, and f_{q_c} are the actual effective forces acting along the major and minor axes of the orbital trajectory. The results indicate that due to a mismatch in detection gains, the control output of the energy controller would end up having an unwanted component along the semi-minor axis. The output of the quadrature control would have a force component along the semi-major axis in-phase and in-quadrature to the oscillation phase.

In the frame of the evolution of the pendulum, Eq. (6.13), this is equivalent to having a faulty energy controller, which affects the precession of the RIG and a quadrature controller, which affects the input-output phase relationship. It is worth mentioning that the energy control output (v_{ca_s}) is inversely proportional to the energy decay time constant (τ). Therefore, in a high quality factor gyroscope, the effect of the unwanted forcing component affecting the precession (f_{q_s}) would be negligible as compared to the direct effect of DGM on the estimation of the pattern angle, Eq. (6.17).

The simulated ADB for various detection gain ratios are shown in Fig. 6.4(a)(top). The simulation we performed was based on an input angular rate of 50 DPS and MRIG parameters summarized in Table 6.1. The simulation results demonstrated that a DGM affects ADB and effective angular gain. For the parameters, the angle error is shown to be mainly due to the direct error in pattern angle estimation, agreeing with the trend illustrated in Fig. 6.3. The variation in the energy control loop is shown in Fig. 6.4(a)(bottom), which demonstrates that DGM would affect the estimation of the mechanical energy at different

pattern angles. In turn, DGM causes an unreliable trend in energy control output which does not correlate to the anisodamping in the system.

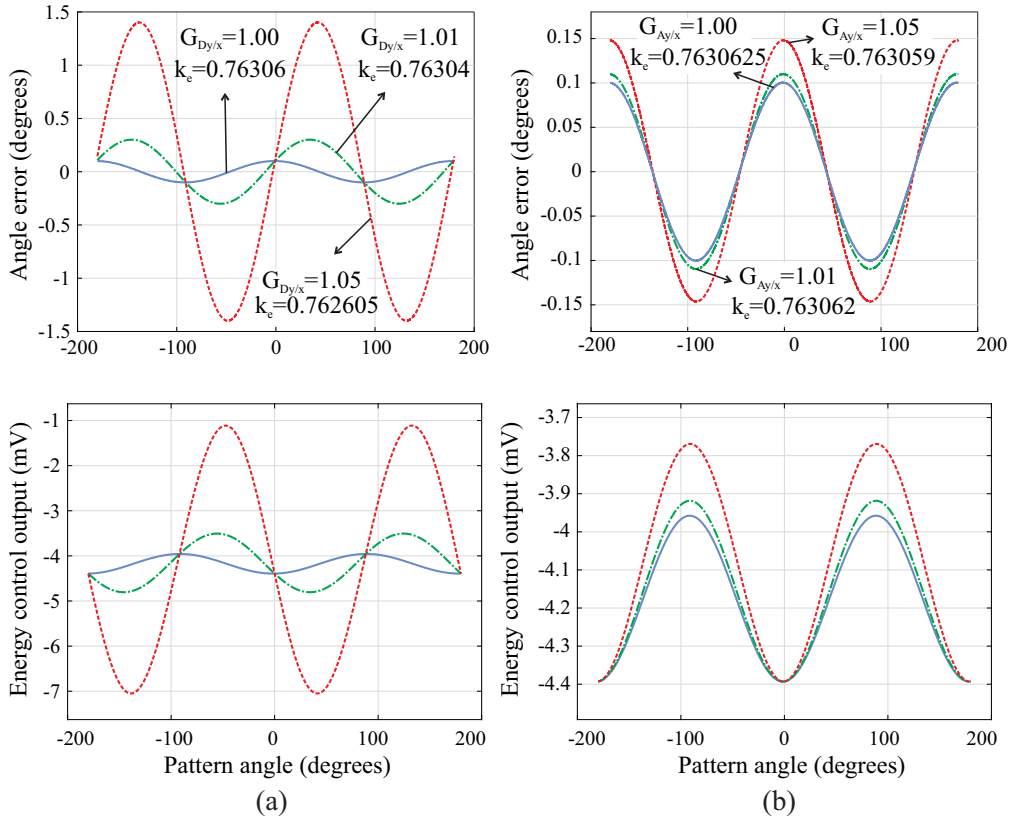

Figure 6.4: Numerical simulation results demonstrating the effect of errors in control and detection electronics on the ADB, effective angular gain, and output of energy control. Top figures and bottom figures present the simulated ADB and energy control output, respectively, for different detection gain mismatch (a) and actuation gain mismatch (b).

Actuation Electronics Gain Mismatch

A similar analysis to the DGM can be utilized to predict the effect of Actuation Gain Mismatch (AGM) on WA operation. In the presence of a mismatch in actuation gains, the force projection would not yield the correct results. Assuming a gain ratio of $G_{Ay/x}$ the

projected forces would be in the form of

$$\begin{aligned} v_{x_c} &= -v_{cq_c}\sin(\theta) \\ v_{x_s} &= +v_{ca_s}\cos(\theta) \\ v_{y_c} &= G_{Ay/x}v_{cq_c}\cos(\theta) \\ v_{y_s} &= G_{Ay/x}v_{ca_s}\sin(\theta) \end{aligned} \tag{6.20}$$

If we project the electrostatic forces due to these control voltages back along the semi-major and semi-minor axes of the orbital trajectory, we would have

$$\begin{aligned} f_{a_s} &= \frac{1}{2}G_A[(G_{Ay/x}-1)v_{ca_s}(1-\cos 2\theta) + G_{Ay/x}v_{ca_s}] \\ f_{q_s} &= \frac{1}{2}G_A(G_{Ay/x}-1)v_{ca_s}\sin 2\theta \\ f_{a_c} &= \frac{1}{2}G_A(G_{Ay/x}-1)v_{cq_c}\sin 2\theta \\ f_{q_c} &= \frac{1}{2}G_A[(G_{Ay/x}-1)v_{cq_c}(1-\cos 2\theta) + G_{Ay/x}v_{cq_c}] \end{aligned} \tag{6.21}$$

Similar to the previous case, the analytical equations indicate that the generated forces would not be correctly aligned with the orientation of the orbital trajectory. Similar to the previous case, cross-coupling between the control loops would affect the precession. Simulation results on the effect of actuation gain mismatch on the ADB and energy control output are illustrated in Fig. 6.4(b). Similar to the previous case, we confirmed that due to a high energy decay time constant in a high quality factor MRIG, the effect of a mismatch in the actuation gains on precession is minimal even for a gain ratio of 1.05 (i.e., a gain mismatch of 5%). Actuation gain mismatches are caused by asymmetries in capacitances, capacitive gap size, biasing voltages, gains of the amplifiers, etc.

Modulation Phase error

In case of having a modulation phase error in one axis relative to another, the generated forces will be correctly aligned to the orbital trajectory. However, they will not have the correct phase relative to the oscillation phase. Assuming that the actuation phase along the X-axis is taken as the reference ($\phi_{Ax} = 0$). Based on Eq. (6.12), due to a modulation phase error of ϕ_{Ay} along the Y-axis, the effective in-phase and in-quadrature phase excitation voltages along the Y-axis would be

$$\begin{aligned} v_{y_c} &= v_{cy_c}\cos(\phi_{YA}) + v_{cy_s}\sin(\phi_{YA}) \\ v_{y_s} &= v_{cy_s}\cos(\phi_{YA}) - v_{cy_c}\sin(\phi_{YA}) \end{aligned} \tag{6.22}$$

Assuming for a small phase error, the effective forces in the orbital frame would be

$$\begin{aligned} f_{a_s} &= -\frac{1}{2}G_A[v_{cq_c}\sin 2\theta\phi_{Ay} + v_{ca_s}] \\ f_{q_s} &= -\frac{1}{2}G_A v_{cq_c}(1+\cos 2\theta)\phi_{Ay} \\ f_{a_c} &= +\frac{1}{2}G_A v_{ca_s}(1-\cos 2\theta)\phi_{Ay} \\ f_{q_c} &= +\frac{1}{2}G_A[v_{ca_s}\sin 2\theta\phi_{Ay} + v_{cq_c}] \end{aligned} \tag{6.23}$$

The results indicate that due to a phase error in the modulation of control signals, the energy control output and quadrature control output would be coupled. Also, the energy control output would affect the resonant frequency, and the quadrature control loop would affect the precession. The effect of modulation phase error on angle error characteristics is shown in Fig. 6.5(a).

It is worth mentioning that in case of having an error in the modulation phase, it would be beneficial to have a low frequency split in the gyroscope ($\Delta\omega$) to reduce the quadrature controller output v_{cq_c}, and as a result, the unwanted coupling that would affect the precession

decreases.

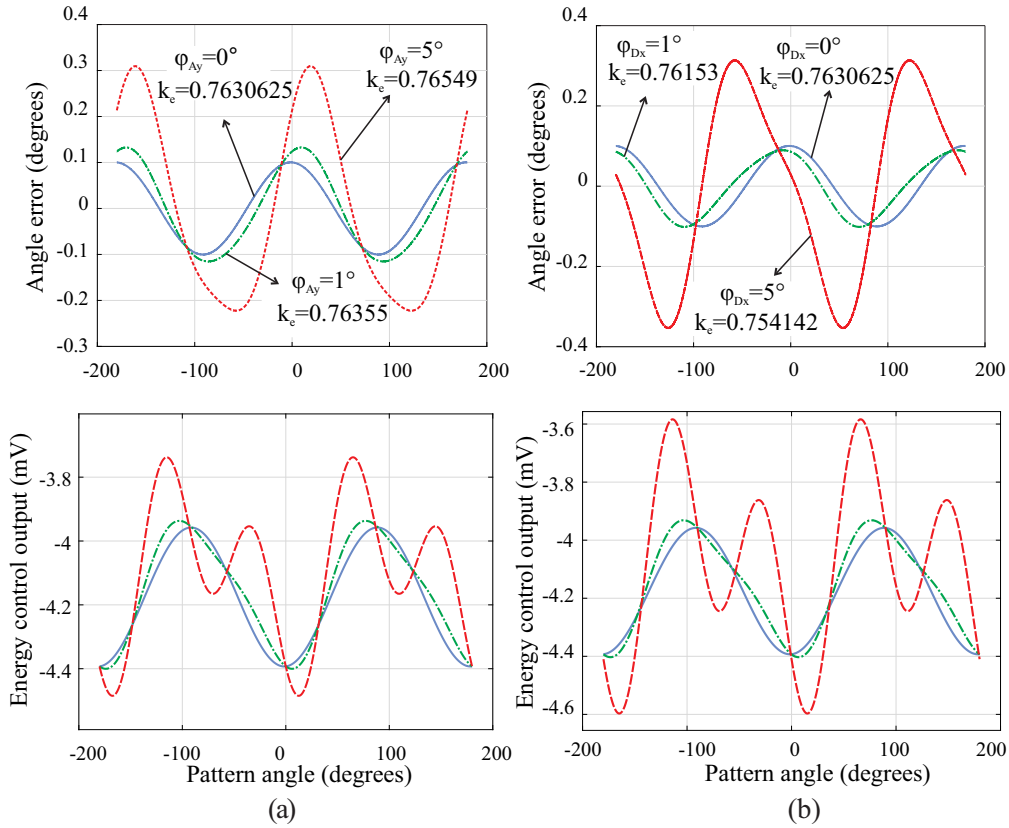

Figure 6.5: The top and bottom figures present the simulated ADB and energy control output, respectively, for different modulation phase errors (a) and demodulation phase errors (b).

Demodulation Phase error

A demodulation phase error affects our information of the slow-varying parameters and estimation of the pendulum variables. By substituting Eq. (6.7) in the definition of pendulum variables Eq. (6.8), it is noted that the pendulum variables E_d and R_d are not affected by the demodulation phase error. However, variables Q, S, and L would be affected. For example, for the quadrature (Q) pendulum variable, we have

$$Q_d = Q - 2\phi_{Dx}(x_s y_s + x_c y_c), \tag{6.24}$$

where the first term represents the actual quadrature in the system, and the second term would be the estimation error. In the quadrature control loop, the estimation of the quadrature would be zeroed using the PI controller. However, based on Eq. (6.24), the actual quadrature would have an unwanted bias equal to

$$Q = \phi_{Dx} S \tag{6.25}$$

Using the numerical model, we simulated variations of the actual quadrature in WA operation (Q) as a function of the pattern angle for different values of demodulation phase error shown in Fig. 6.6. It is demonstrated that the unwanted bias in quadrature in the presence of a demodulation phase error would be orders of magnitude larger than the ideal case ($\phi_{Dx} = 0$). The high residual quadrature adds to the error in precession based on Eq. (6.13).

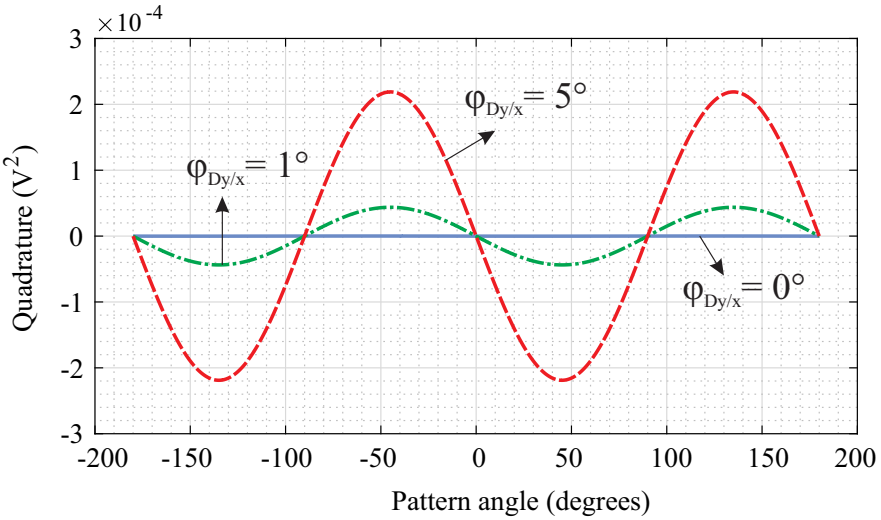

Figure 6.6: Simulation results on the actual quadrature (Q) during precession as a function of the pattern angle for different values of demodulation phase error in the detection electronics.

A similar derivation can be performed for the errors in S_d measurements as

$$S_d = (1 + \phi_{Dx}^2) S, \tag{6.26}$$

which denotes that the S measurements would be scaled by $(1+\phi_{Dx}^2)$, resulting in a pattern angle estimation error. In Fig. 6.5(b), the effects of demodulation phase error on variations in the angle bias, effective angular gain, and the output of the energy control are demonstrated. The simulation results concluded that the high quadrature residue, caused by a demodulation phase error, was the main source of the ADB.

6.3 Identification of Gain Asymmetries

In Section 6.2, we presented a detailed study on the effect of phase errors and gain asymmetries in the detection and control electronics on WA operation. In this section, we present a methodology for identifying the gain mismatches in control and detection electronics. We applied the proposed methodology to the DFP MRIG as a calibration step and presented the improvements in angle measurement resolution.

Phase errors in modulation and demodulation can be identified through the input-output phase response of the gyroscope at different actuation frequencies with respect to the natural frequencies. Identifying the mismatch in detection and actuation gains requires an observation of the vibration amplitude (in microns), which is not a trivial task. On the other hand, based on the input-output response, one can compare the product of detection and actuation gains between the X and Y axes. Here, we present a method to identify detection gain mismatch using the angle error (ADB) measured at high angular rate input. As discussed in Chapter 4, the 2θ-dependent angle error due to mechanical imperfections reduces at higher the input angular rates ($\mathbf{\Omega}$). Therefore, the measured 2-θ-dependent ADB at a high input rate correlates to the error in pattern angle estimation caused by imperfections in the electronics, dominantly by the detection gain mismatch as previously shown in Fig. 6.4(a).

Our approach of identifying the detection gain mismatch includes physically rotating the DFP gyroscope at high input rates and using the measured angle error to identify the detection gain ratio ($G_{Dy/x}$).

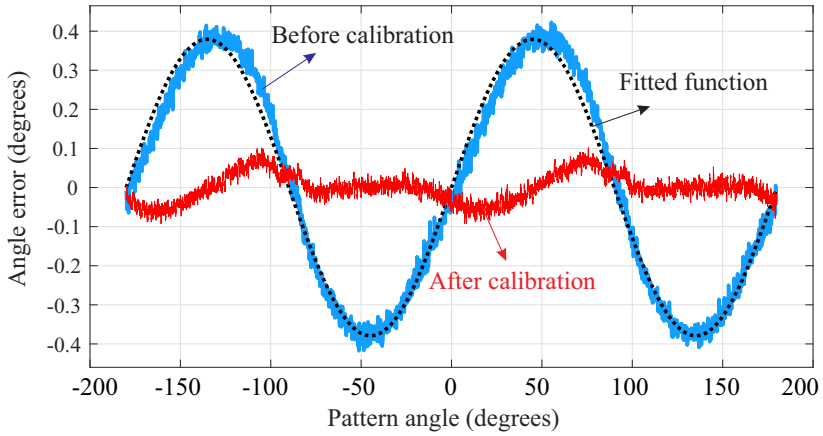

Figure 6.7: Experimentally measured angle error in DFP MRIG at an input angular rate of 500 DPS. Based on the initially measured angle error (before calibration), a detection gain ratio of 1.01332 was estimated. The measure angle error after calibration of the detection gain mismatch is shown.

In Fig. 6.7, the angle error of the DFP gyroscope at 500 DPS is shown. At an input rate of 500 DPS, the angle error of anisodamping of 0.004 Hz was estimated to be around ten millidegrees. Therefore, it can be concluded that the detection gain mismatch must have caused the measured angle error (0.8 degrees peak-to-peak). By fitting a function described in Eq. (6.17), using a non-linear least-squares method, the detection gain ratio was estimated. Based on the estimated detection gain ratio of 1.01332, G_{Dy} in Fig. 6.2 was adjusted to achieve matched detection gains along X and Y axes. The adjustment was made in the micro-controller as it was more convenient and more accurate than analog voltage scalars with limited resolution in the detection path, which would have changed the phase relation. The improvement in the measured angle error after calibration of the detection gain mismatch is presented in Fig. 6.7.

In order to identify a mismatch in the actuation gain (G_{Ax} and G_{Ay}) the output of the energy control loop was utilized. The amplitude decay rate can estimate an accurate estimation of

damping along the X and Y axes in the semi-major axis amplitude of the orbital trajectory, while a rate control loop is used to maintain the oscillation pattern at 0 and 90 angles.

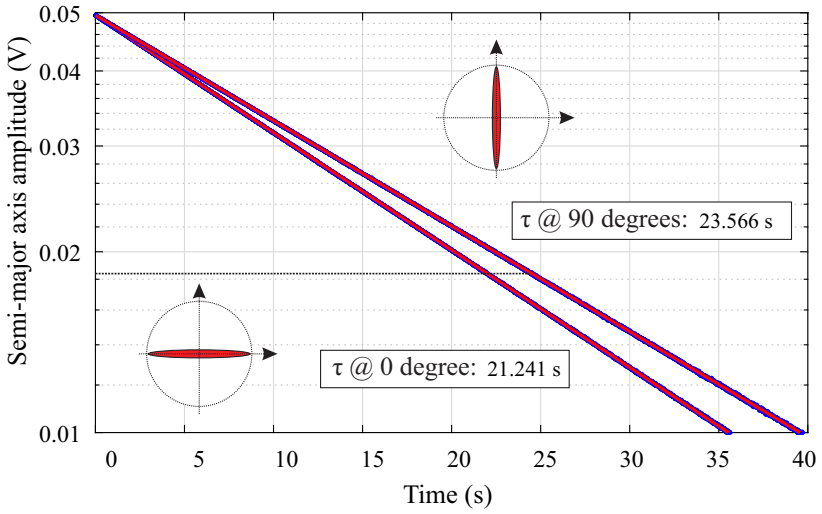

Figure 6.8: Experimental characterization of damping along X and Y axes using the energy decay rate.

The decay time constants, as estimated in Fig. 6.8, represent damping along the X and Y axes. The ratio of the time constants denotes the ratio of the forces needed to contain the oscillation amplitude at a constant value along the X and Y axes.

The energy control output at 0 and 90-degree pattern angles were measured to be 4.342 mV and 4.012 mV. Based on these values, the actuation gain ratio ($G_{Ay/x}$) was estimated to be 0.9912 and was calibrated by adjusting G_{Ay}, shown in Fig. 6.2, in the micro-controller.

6.4 Conclusion

This chapter studied the effect of imperfections in the control electronics on precession in the WA mode of operation. We developed an electro-mechanical model to simulate the response in WA operation in the presence of imperfections in both the mechanical structure and electronics. We demonstrated that phase errors in signal modulation, demodulation,

and asymmetries in the detection and actuation gains along the X and Y axes would introduce additional error to the direct angle measurements, affecting the Angle-Dependent Bias (ADB) and the Effective Angular Gain (EAG). Based on the analytical equations, we concluded that the negative effects of imperfections in control electronics are coupled to the mechanical characteristics of MRIG. For low quality factor MRIG with higher anisoelasticity, the adverse effects of employing a non-ideal control electronic are significantly higher. Using Lynch's analytical model for the evolution of the orbital trajectory, we explained the simulation results further.

A methodology for identifying gain asymmetries in detection and control electronics was presented and applied to a DFP MRIG as a testbed. We utilized the ADB error to identify and compensate for gain mismatch in the detection electronics. Subsequently, we used the energy decay time constants and energy control output to identify asymmetry in the actuation gains. A 10-times improvement in ADB error after compensation of gain asymmetries was experimentally demonstrated.

Chapter 7

Direct Angle Measurement Using Dynamically-Amplified Gyroscopes

7.1 Introduction

This chapter develops a reduced-order model for higher degree-of-freedom gyroscope architectures, such as the Dynamically-Amplified Gyroscope (DAG), [82]. We compare DAG to conventional single-mass gyroscopes through the reduced-order model and examine the application of established gyroscope control architectures to DAG.

This chapter is organized as follows. In Section 7.2, we introduce the DAG architecture and its advantages as compared to conventional single-mass devices. Section 7.3 presents the reduced-order model; we derive expressions for matrices of stiffness, damping, and the Coriolis force, and we numerically demonstrated that the reduced-order model would accurately represent the original 4-DoF system. We employ the reduced-order 2-DoF model to study and compare the 4-DoF DAG architecture to other traditional gyroscope architectures based on the single-mass-equivalent characteristics. We hypothesized that the established

feedback controls for CVGs can be applied to a higher-DoF DAG architecture. We verified this conjecture in Section 7.4 by adapting the conventional closed-loop WA control and implementing it with a DAG. Characterization results on the angular gain, anisoelasticity, and anisodamping of the DAG are reported in Section 7.4. A summary of our results and conclusions are found in Section 7.5.

7.2 Dynamically-Amplified Gyroscopes

Dynamically-Amplified Gyroscope (DAG) design architecture [82] consists of a drive mass for applying the control forces and a slave mass for vibration measurement, illustrated in Fig. 7.1. In this dual-mass system, we excite the drive mass with a small vibration amplitude, ideal for linear electrostatic actuation/control. In contrast, the slave mass is amplified at a much higher vibration amplitude to improve the Signal-to-Noise Ratio (SNR) in measurements. Wang et al., [131], have reported experimental results demonstrating the dynamic amplitude amplification mechanism in a micro-scale Coriolis Vibratory Gyroscope (CVG) and confirmed the corresponding improvements in the angular rate sensitivity. Through different design iterations, using a structurally optimized DAG device, noise performance of 0.09 deg/hr bias instability and 0.0096 deg/$\sqrt{hr}$ Angle Random Walk (ARW) have been reported, [132].

In initial demonstrations of the DAG architecture, the devices were instrumented in the open-loop angular rate mode of operation, [28, 29, 131, 132]. To overcome the limitations of the open-loop mode, we needed to control and operate the DAG in the Force-to-Re-Balance (FRB) mode (i.e., the closed-loop angular rate mode) or the Whole-Angle (WA) mode of operation (i.e., the rate-integrating mode). These control architectures, along with a mode-matched DAG, were expected to provide the highest angular rate sensitivity, increased dynamic range, and an extended full-scale operation with a highly linear scale factor, [91,126].

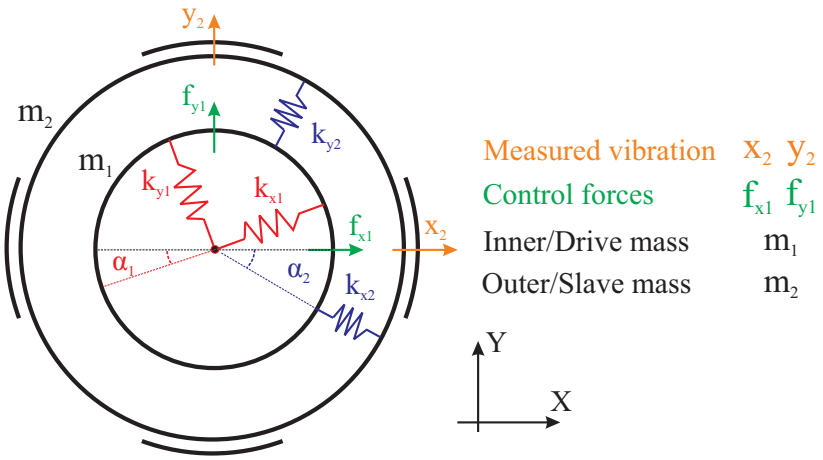

Figure 7.1: Schematics illustrating the DAG architecture [82]. The control forces are applied to the inner/drive mass and the vibration is measured on the outer/slave mass. The damping in the DAG is not illustrated here but would affect the inner and outer mass with a similar topology to elasticity.

In this thesis, we focus on instrumentation of DAG for the WA mode of operation.

The WA mode of operation for direct angle measurements has been experimentally demonstrated on different micro-scale gyroscope architectures, such as the Quad Mass Gyroscope (QMG) [8], the Disk Resonator Gyroscope (DRG) [115], and the Birdbath Resonator Gyroscope (BRG) [139]. These gyroscope architectures are mathematically modeled as a 2-DoF dynamic system, [31, 57, 70].

The DAG architecture, however, has complex dynamics, and it is conventionally modeled as a 4-Degrees of Freedom (4-DoF) dynamic system, [28]. The 4-DoF model does not provide an easy intuitive insight into the dynamics and characteristics of DAG in comparison to conventional single-mass devices, which are mathematically modeled as a 2-DoF system. In the following, through a reduced-order model, we investigate whether the established feedback controls for the angular rate or direct angle measurement, reported in [51, 70] for 2-DoF Coriolis systems, can be applied to a 4-DoF DAG.

7.3 Mathematical Model of DAG

To simulate the response of a DAG, a 4-DoF lumped mass-spring-damper model can be used as reported in [82]. The equation of motion in the matrix form is represented as

$$\ddot{q} + M^{-1}B\dot{q} + 2\Omega C\dot{q} + M^{-1}Kq = M^{-1}f, \tag{7.1}$$

where 4×4 matrices M, B, C, and K denote the mass, damping, Coriolis force, and stiffness distribution in the device and are represented as follows

$$M = \begin{bmatrix} m_1 & 0 & 0 & 0 \\ 0 & m_1 & 0 & 0 \\ 0 & 0 & m_2 & 0 \\ 0 & 0 & 0 & m_2 \end{bmatrix}, \quad B = \begin{bmatrix} b_{11} & b_{12} & b_{13} & b_{14} \\ b_{12} & b_{22} & b_{23} & b_{24} \\ b_{13} & b_{23} & b_{33} & b_{34} \\ b_{14} & b_{24} & b_{34} & b_{44} \end{bmatrix}$$

$$C = \begin{bmatrix} 0 & -\kappa_1 & 0 & 0 \\ \kappa_1 & 0 & 0 & 0 \\ 0 & 0 & 0 & -\kappa_2 \\ 0 & 0 & \kappa_2 & 0 \end{bmatrix}, \quad K = \begin{bmatrix} k_{11} & k_{12} & k_{13} & k_{14} \\ k_{12} & k_{22} & k_{23} & k_{24} \\ k_{13} & k_{23} & k_{33} & k_{34} \\ k_{14} & k_{24} & k_{34} & k_{44} \end{bmatrix} \tag{7.2}$$

An expression for the stiffness matrix (K) has been derived in [28], which was shown to be a function of stiffness distribution of concentric rings connecting the inner mass to the anchor, and the concentric rings connecting the outer mass to the inner mass, as illustrated in Fig. 7.1. We used a similar approach to derive an expression for the damping matrix (B). The displacement of the drive mass and the slave mass, and the control forces are represented

using column vectors q and f, respectively, where

$$q = \begin{bmatrix} x_1 \\ y_1 \\ x_2 \\ y_2 \end{bmatrix}, \qquad f = \begin{bmatrix} f_{x1} \\ f_{y1} \\ f_{x2} \\ f_{y2} \end{bmatrix} \tag{7.3}$$

Based on the objective of the DAG architecture, we assumed that the control forces are applied only to the drive mass (m_1) (i.e., $f_{x2} = 0$ and $f_{y2} = 0$). Based on the equation of motion (7.1), a state-space model can be developed to numerically simulate the input-output response of the DAG in both the time and frequency domains.

In this chapter, our objective is to develop a reduced-order model to gain insight into the differences in characteristics of a single-mass gyroscope and the dual-mass DAG. To develop the reduced-order model, we approximated the 4-DoF linear dynamic system using its two dominant eigenmodes, [26], which are utilized in DAG architecture. To achieve this, the stiffness-per-mass matrix ($M^{-1}K$) was written in its canonical form, [118], represented as

$$M^{-1}K = Q\Lambda Q^{-1} \tag{7.4}$$

Since the stiffness matrix (K) is symmetric and the mass matrix (M) is diagonal, matrices Q and Λ can be found consisting of eigenvectors and eigenvalues of the stiffness-per-mass matrix. The matrix Λ has the following diagonal form

$$\Lambda = \begin{bmatrix} \omega_{i1}^2 & 0 & 0 & 0 \\ 0 & \omega_{i2}^2 & 0 & 0 \\ 0 & 0 & \omega_{a1}^2 & 0 \\ 0 & 0 & 0 & \omega_{a2}^2 \end{bmatrix}, \tag{7.5}$$

where ω_{i1} and ω_{i2} denote the resonant frequencies of the in-phase modes and ω_{a1} and ω_{a2} represent the resonant frequencies of the anti-phase modes. The following coordinate transformation can be used to derive an equation of motion in its canonical form, which describes the dynamics along the principal axes of elasticity (i.e., vibration in a four-dimensional semi-decoupled modal space):

$$p = Q^{-1}q \tag{7.6}$$

Based on this coordinate transformation, the following equation of motion can be derived

$$\ddot{p} + B'\dot{p} + 2\Omega C'\dot{p} + \Lambda p = Q^{-1}M^{-1}f, \tag{7.7}$$

where the damping and Coriolis matrices in the new coordinate frame are calculated as

$$B' = Q^{-1}M^{-1}BQ, \quad C' = Q^{-1}CQ \tag{7.8}$$

In the new coordinate frame, based on the actuation frequency, a combination of the four semi-decoupled modes are excited. In a DAG architecture, the frequency separation between the in-phase and anti-phase modes is designed to be significant, in the kilohertz range, and the bandwidth of each of these modes is less than 0.1 Hz. In this case, assuming that the actuation frequency is in proximity to either of the in-phase or the anti-phase modes, the system can be simplified.

In the DAG architecture, we utilize the in-phase degenerate modes to benefit from the dynamical amplitude amplification, [82]. In this case, the actuation frequency is set at the in-phase resonant frequencies. As a result, the amplitude of vibration in the anti-phase modes becomes negligible (i.e., $p_3 \approx 0$ and $p_4 \approx 0$); therefore, the dynamics of the 4-DoF DAG can be approximated by its two degenerate in-phase modes, and the order of the model can be reduced. The dynamics of the DAG in the in-phase modes is governed by the following

equation of motion

$$\ddot{\bar{p}} + \bar{B}'\dot{\bar{p}} + 2\Omega\bar{C}'\dot{\bar{p}} + \bar{\Lambda}\bar{p} = (\bar{Q^{-1}}\bar{M^{-1}})f, \tag{7.9}$$

where the operation ($\bar{\cdot}$) takes the first two rows and the first two columns of the corresponding matrices and vectors.

Eq. (7.9) represents a reduced-order model which describes the dynamics of the DAG in its degenerate in-phase modes. Based on Eq. (7.6), we used the following transformation to go back to the original coordinate frame, which describes the motion measured on the slave mass (x_2 and y_2)

$$Q^*\bar{p} = \begin{bmatrix} x_2 \\ y_2 \end{bmatrix}, \quad Q^* = \begin{bmatrix} Q_{31} & Q_{32} \\ Q_{41} & Q_{42} \end{bmatrix} \tag{7.10}$$

Based on the transformation defined by Eq. (7.10), a reduced-order model for the DAG is derived. The dynamics of the gyroscope, in its original coordinate frame, is governed by the following equation of motion

$$\begin{bmatrix} \ddot{x_2} \\ \ddot{y_2} \end{bmatrix} + B_{eq}\begin{bmatrix} \dot{x_2} \\ \dot{y_2} \end{bmatrix} + 2\Omega C_{eq}\begin{bmatrix} \dot{x_2} \\ \dot{y_2} \end{bmatrix} + \Lambda_{eq}\begin{bmatrix} x_2 \\ y_2 \end{bmatrix} = \frac{1}{m_1}T_f\begin{bmatrix} f_{x1} \\ f_{y1} \end{bmatrix}, \tag{7.11}$$

where matrices B_{eq}, C_{eq}, and Λ_{eq} denote the single-mass-equivalent characteristics of the DAG for damping, Coriolis force, and elasticity, respectively. These matrices are calculated as

$$B_{eq} = Q^*\bar{B}'(Q^*)^{-1}, \quad C_{eq} = Q^*\bar{C}'(Q^*)^{-1}, \quad \Lambda_{eq} = Q^*\bar{\Lambda}(Q^*)^{-1} \tag{7.12}$$

In Eq. (7.11), the force transformation matrix (T_f) describes the contribution of control forces applied to the inner mass of DAG (f_{x1} and f_{x2}) as inputs of the 2-DoF reduced-order

model. The matrix T_f is defined as

$$T_f = Q^*(\bar{Q^{-1}}) \tag{7.13}$$

Based on the reduced-order model shown in Eq. (7.11), we demonstrated that the DAG can be mathematically modeled as a 2-DoF system similar to conventional single-mass gyroscopes. In the DAG reduced-order model, the variables (x_2, y_2) and (f_{x1}, f_{y1}) can be regarded as outputs and inputs of a single-mass gyroscope.

7.3.1 Accuracy of Reduced-Order Model

We determined the accuracy of the reduced-order model by comparing the frequency response of the DAG, estimated using the full model and the reduced-order model. The parameters which we used for simulation are summarized in Table 7.1.

The parameters c_{x1}, c_{y1}, β_1, c_{x2}, c_{y2}, and β_2, in Table 7.1, describe the principal axes of damping affecting the inner mass and the outer mass of the DAG, respectively. Mechanical angular gains corresponding to the inner mass and the outer mass are represented using κ_1 and κ_2. We selected the values based on Finite Element Analysis (FEA) results reported in [28], for an $8.6 \times 8.6\ mm^2$ footprint DAG with concentric rings as the suspension elements.

Based on parameters in Table 7.1, the 4×4 stiffness matrix K and damping matrix B in the original coordinate frame, as defined in (7.1), were calculated as described in [28]. Subsequently, the equivalent damping matrix B_{eq}, the equivalent elasticity matrix Λ_{eq}, and the equivalent Coriolis matrix C_{eq} of the reduced-order model were calculated as in matrix equation (7.12). The state-space representations of the full-model and the reduced-order model were used to derive input-output transfer functions and numerically calculate the amplitude response.

Table 7.1: Parameters used for numerical study of the reduced-order model accuracy.

Parameters	Values	Parameters	Values
m_1	$2\ mg$	m_2	$2\ mg$
k_{x1}	$2842.4\ N/m$	k_{x2}	$78.96\ N/m$
k_{y1}	$2847.2\ N/m$	k_{y2}	$80.54\ N/m$
α_1	-10°	α_2	5°
c_{x1}	$0.2\ \mu N.s/m$	c_{x2}	$0.2\ \mu N.s/m$
c_{y1}	$0.1\ \mu N.s/m$	c_{y2}	$0.1\ \mu N.s/m$
β_1	0°	β_2	0°
κ_1	1	κ_2	1

As shown in Fig. 7.2, we calculated the amplitude response of the slave mass (x_2/f_{x1} and y_2/f_{x1}) using the original 4-DoF and the reduced-order model. We observed a good agreement between the two results in the lower frequency range, which included the in-phase operational modes, shown in Fig. 7.2(a). As expected, at higher frequencies, close to the resonant frequency of anti-phase degenerate modes, the reduced-order model falls short in predicting the response of the system. This range of frequencies is not of interest to the DAG operation since the in-phase and anti-phase modes are significantly separated in their resonant frequencies, and the CVG control system is designed to avoid the excitation of undesirable modes. A closeup view of frequency response for the in-phase modes is shown in Fig. 7.2(b), and a good agreement between simulation results of the full model and reduced-order model is illustrated.

7.3.2 Single-Mass-Equivalent Characteristics of DAG

Based on the reduced-order model and the single-mass-equivalent characteristics of the DAG, defined in (7.12), DAGs can be compared to other gyroscope structures, which are conventionally modeled as a 2-DoF system. Based on the Q matrix, which consists of eigenvectors of the stiffness-per-mass matrix ($M^{-1}K$), the single-mass-equivalent characteristics would be a linear combination of stiffness and damping affecting the drive mass and slave mass of the

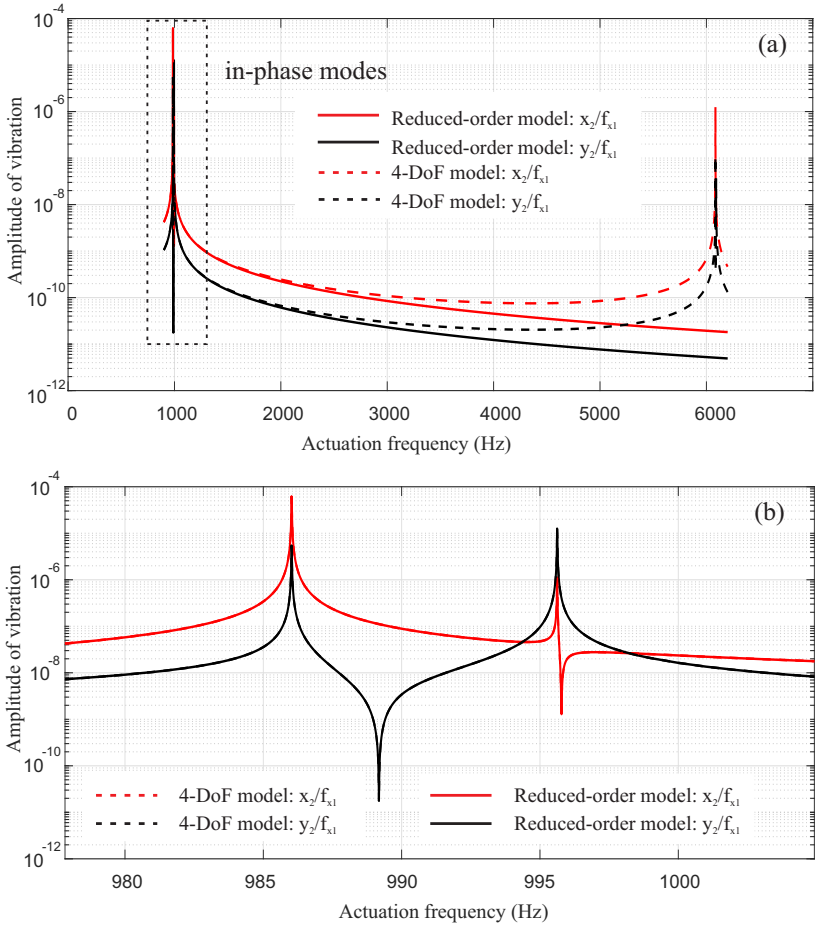

Figure 7.2: Comparison of the frequency response estimated using the full model and the reduced-order model. A closeup view of the frequency response in the frequency range around the in-phase degenerate modes is shown in (b), and a complete overlap of the results in the frequency range of interest can be observed. Dashed lines are not visible due to an overlap with continuous lines.

DAG.

As an example, we can compare the noise performance of a DAG to single-mass gyroscopes based on the reduced-order model of the DAG developed in this chapter and analytical results on CVG noise performance reported in [57]. It can be shown that in the angular rate mode of operation, a DAG would outperform a single-mass gyroscope with comparable quality factor and frequency split, if the drive amplitude of the slave mass (x_2) was designed to be higher than the drive amplitude of the single-mass gyroscope.

In this section, we utilized the DAG reduced-order model to study electrostatic mode-matching and control of DAG.

Electrostatic Compensation of Anisoelasticity

A mode-matched operation is essential for CVGs to achieve high noise performance in angular rate and rate integrating modes of operation, [57,70]. In the WA mode of operation, reduction of anisoelasticity would improve the resolution and accuracy of angle measurements, [130]. Fabrication imperfections, crystalline orientation-dependent mechanical properties of Single-Crystalline Silicon (SCS), and stresses due to packaging cause anisoelasticity in micro-scale CVGs. Electrostatic and mechanical trimming methods can be employed to reduce the anisoelasticity of DAG, [28,29]. Between these two approaches, electrostatic frequency tuning is easier to implement and provides higher resolution in frequency regulation.

Efimovskaya et al. in [28] have reported an approach, based on the 4-DoF model, to estimate the amount of anisoelasticity in a DAG and predict the tuning voltages for compensation of anisoelasticity. In that approach, based on empirical frequency response, the stiffness matrix of the device was estimated, and appropriate DC voltages were predicted and applied to tuning electrodes of both the inner and outer mass to mode-match the DAG.

Based on the reduced-order model, we report an alternative method to compensate for the frequency split and quadrature coupling of a DAG without the need to estimate system parameters. The modified stiffness-per-mass matrix of the DAG has the form of $M^{-1}(K-K_e)$,

where the electrostatically induced stiffness-per-mass is represented as

$$M^{-1}K_e = \begin{bmatrix} 0 & 0 & 0 & 0 \\ 0 & 0 & 0 & 0 \\ 0 & 0 & e_{33} & -e_{34} \\ 0 & 0 & -e_{34} & e_{44} \end{bmatrix} \tag{7.14}$$

It should be noted that as compared to the method which has been reported in [28], we rely on applying DC voltages only to the outer mass's electrodes to modify the stiffness matrix. Based on expressions reported in [28], the electrostatically induced stiffness-per-mass parameters, e_{33}, e_{44}, and e_{34}, can be adjusted independently by applying the appropriate DC voltages to tuning electrodes of the outer mass. Without loss of generality, assuming that $k_{44} > k_{33}$ in the original stiffness matrix (K), we need to find parameters e_{44} and e_{34} through which the resonant frequencies of the DAG operational modes are matched.

We utilized the single-mass-equivalent stiffness matrix of the reduced-order model to find the optimum parameters for mode-matching. The single-mass-equivalent stiffness matrix has the following form

$$\Lambda_{eq} = \begin{bmatrix} \lambda_{11} & \lambda_{12} \\ \lambda_{12} & \lambda_{22} \end{bmatrix} \tag{7.15}$$

Similar to a single-mass CVG, to reach mode-matched operation in DAG, the diagonal terms in the single-mass-equivalent stiffness matrix have to be matched (i.e., $\lambda_{11} = \lambda_{22}$) and the off-diagonal terms must be zeroed (i.e., $\lambda_{12} = 0$).

Through a numerical study, with results shown in Fig. 7.3, we demonstrated that by increasing e_{34}, the off-diagonal term ($|\lambda_{12}|$) can be reduced. Subsequently, the split between the diagonal terms ($|\lambda_{11} - \lambda_{22}|$) was reduced by adjusting the electrostatic stiffness-per-mass parameter e_{44}. The cross-coupling effect of e_{44} on the difference of the diagonal terms

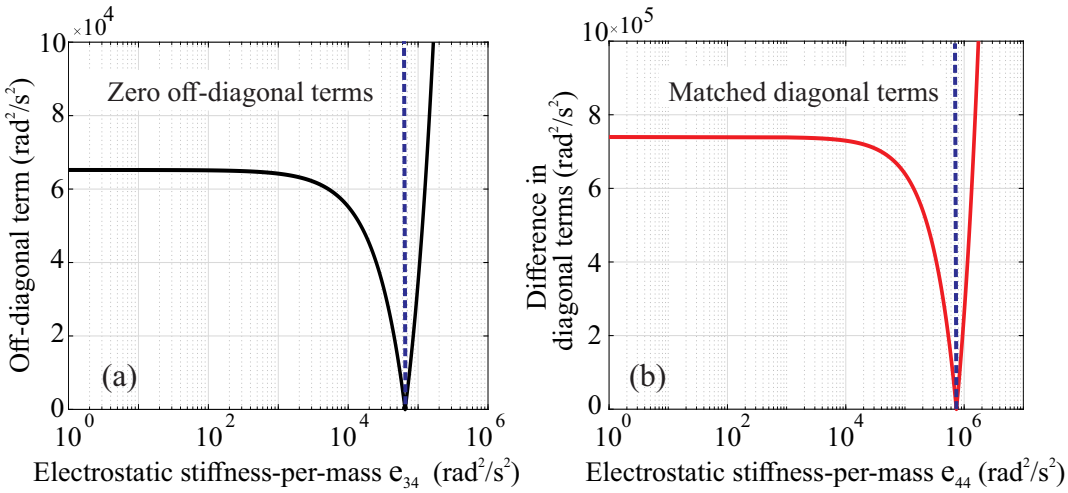

Figure 7.3: Results of a numerical study based on the reduced-order DAG model. In (a), it is illustrated that by adjusting e_{34} the off-diagonal terms of Λ_{eq} were minimized. Similarly, as illustrated in (b), parameter e_{44} was increased in increments to eliminate the split between the diagonal terms of Λ_{eq}.

was observed to be negligible. We numerically demonstrated that for a DAG with parameters summarized in Table 7.1, mode-matching was achieved by setting e_{34} and e_{44} to 65251.16 rad^2/s^2 and 740136 rad^2/s^2, respectively.

Based on the results, we demonstrated that it is sufficient to apply electrostatic softening to the slave mass of a DAG to compensate for anisoelasticity and achieve a mode-matched operation. In practice, the biasing voltages applied to the slave mass of the DAG were increased in increments until a mode-matched condition was reached, similar to what is illustrated in Fig. 7.3. During the tuning process, the Zero-Rate Output (ZRO) of the DAG was used as an indication of the remaining frequency split and quadrature coupling, [107].

Force transformation matrix

In Eq. (7.11), the force transformation matrix T_f is a non-diagonal matrix that describes the correlation between inputs of the 2-DoF reduced-order model and the forces applied to the drive mass of the DAG. As a result of having a non-diagonal force transformation matrix, a

control force applied to the drive mass along the X or Y axes would contribute as an input for both operational modes, described by the reduced-order model.

We used numerical simulation results to study the force transformation matrix and its correlation to DAG characteristics. The force transformation matrix (T_f) is calculated as

$$T_f = Q^*(\bar{Q^{-1}}) = \begin{bmatrix} Q_{31} & Q_{32} \\ Q_{41} & Q_{42} \end{bmatrix} \begin{bmatrix} Q_{11} & Q_{21} \\ Q_{12} & Q_{22} \end{bmatrix} \tag{7.16}$$

Based on Eq. (7.4), it is anticipated that the modal shape of oscillation is dependent on the distribution of mass and elasticity in the DAG, as illustrated in Fig. 7.1, and can be studied using the Q matrix. In Eq. (7.16), the first matrix correlates to the modal shape of the second mass, and the second matrix correlates to the modal shape of the first mass in the two in-phase operational modes.

Based on Eq. (7.16), we approximated the force transformation matrix as a matrix-product of a scalar matrix and a rotational matrix

$$T_f = \begin{bmatrix} G_1 & 0 \\ 0 & G_2 \end{bmatrix} \begin{bmatrix} cos(\gamma) & -sin(\gamma) \\ sin(\gamma) & cos(\gamma) \end{bmatrix} \tag{7.17}$$

To decompose the force transformation matrix, as shown in Eq. (7.17), we initially calculated

Table 7.2: Simulation results demonstrating the effect of anisoelasticity on the force transformation matrix.

Parameters	k_{x1}	k_{y1}	k_{x2}	k_{y2}	α_1	α_2	G_1	G_2	γ
Case 1	2842.4 N/m	2842.4 N/m	78.96 N/m	78.96 N/m	0	0	0.0277	0.0277	0
Case 2	2842.4 N/m	2847.2 N/m	78.96 N/m	78.96 N/m	0	0	0.0277	0.0276	0
Case 3	2842.4 N/m	2847.2 N/m	78.96 N/m	80.54 N/m	0	0	0.0277	0.0282	0
Case 4	2842.4 N/m	2847.2 N/m	78.96 N/m	80.54 N/m	0	5	0.0277	0.0282	5.0912
Case 5	2842.4 N/m	2847.2 N/m	78.96 N/m	80.54 N/m	-5	5	0.0277	0.0282	10.0912
Case 6	2842.4 N/m	2847.2 N/m	78.96 N/m	80.54 N/m	-10	5	0.0277	0.0282	15.0912

the rotational angle (γ) based on elements of the T_f matrix. Subsequently, the gains G_1 and G_2 were calculated by multiplying the force transformation matrix by inverse of the rotational matrix.

For six different cases, the force transformation matrix was calculated and decomposed, and the results are presented in Table 7.2. For an ideal case (case 1), we assumed that the principal axes of elasticity were aligned with the X and Y axes, and the elasticity along the X and Y axes were identical. For this ideal case, the force transformation matrix takes a diagonal form. The gains G_1 and G_2 were estimated to be equal and on the order of 0.0277. Based on Eq. (7.16), it can be shown that the gain factors (G_1 and G_1) are equal to the inverse of the dynamic amplification factor (i.e., the ratio of motion of the slave mass to the drive mass) estimated to be on the order of 36.03 for the parameters of case 1, shown in Table 7.2.

In cases 2 and 3, it is shown that anisoelasticity in DAG, results in a mismatch in gain factors G_1 and G_2. In cases 4-6, it is illustrated that a misalignment between the two sets of principal axes of elasticity, for the inner suspension and the outer suspension, would result in a non-diagonal force transformation matrix. The rotational angle γ was estimated to be roughly equal to the misalignment angle (i.e., $\gamma \approx \alpha_2 - \alpha_1$).

We concluded that if the principal axes of elasticity for the inner suspension and outer suspension were aligned (i.e., $\alpha_1 = \alpha_2$, in Fig. 1), the force transformation matrix becomes a diagonal matrix. In a general case, however, by identifying and accounting for the transformation in the control forces, we can apply the conventional control loops for rate and rate-integrating gyroscopes [70] to the DAG architecture.

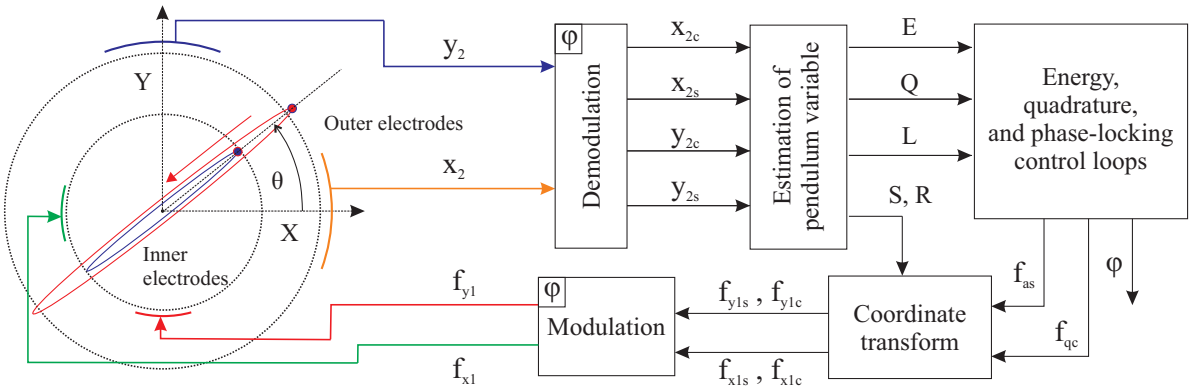

Figure 7.4: Schematics of the closed-loop WA control architecture adopted from Lynch and implemented on a DAG. Based on the DAG reduced-order model, we used the slave/outer mass displacement to estimate the pendulum variables. The pendulum variables were used to calculate the control forces, which were applied to the drive/inner mass to sustain energy and suppress quadrature.

7.4 Whole-Angle Operation

In this section, we report results on implementing the closed-loop WA control with the DAG architecture. A DAG with design parameters reported in [132] was used as the Device Under Test (DUT). In our experiments, we used a custom-designed Printed Circuit Board (PCB) to apply differential control signals to the DAG and measure the motional current through transimpedance amplifiers.

The closed-loop WA control was implemented with a Zurich HF2Li lock-in amplifier using the Real-Time Kit (RTK) module, [8]. The control loops, as described in [70], were coded and compiled on the Reduced Instruction Set Computer (RISC) microprocessor of the HF2Li instrument and executed at a rate of 2500 Hz. The WA-DAG was characterized on an Ideal Aerosmith 1270VS single-axis rate-table.

For a direct angle measurement, the closed-loop WA control architecture was adapted from [70] and implemented on the DAG, as illustrated in Fig. 7.4. Based on the DAG reduced-order model, the displacement of the slave mass along the X and Y axes (x_2 and y_2) was electrostatically measured using the parallel plate electrodes. Through synchronous de-

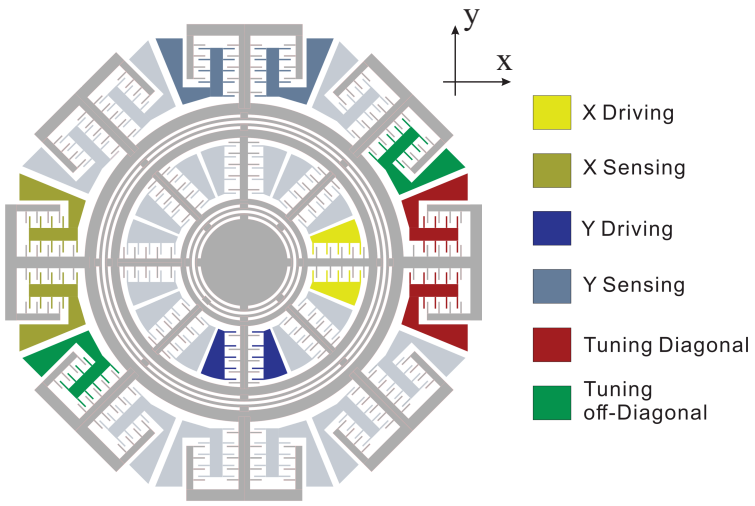

Figure 7.5: Schematics of a DAG and the electrode configuration. As shown, dedicated parallel plate electrodes were used for actuation, detection, and electrostatic tuning. To compensate for the 27 Hz as-fabricated frequency split, DC voltages of 11.383 V and 2.031 V were applied to the diagonal and off-diagonal tuning electrodes, respectively

modulation, signal components in-phase and in-quadrature with a reference phase (ϕ) were used for estimation of pendulum variables as

$$\begin{aligned} E &= x_{2c}^2 + x_{2s}^2 + y_{2c}^2 + y_{2s}^2 \\ Q &= 2(x_{2c}y_{2s} - x_{2s}y_{2c}) \\ R &= x_{2c}^2 + x_{2s}^2 - y_{2c}^2 - y_{2s}^2 \\ S &= 2(x_{2c}y_{2c} + x_{2s}y_{2s}) \\ \Im(L) &= 2(x_{2c}x_{2s} + y_{2c}y_{2s}) \end{aligned} \tag{7.18}$$

The pendulum variables provided information on the elliptical oscillation pattern. Based on the energy (E) and quadrature (Q) pendulum variables, the control forces (f_{as} and f_{qc}) were calculated and then applied along the semi-major and semi-minor axes of the ellipsoid to sustain energy and suppress quadrature, respectively, [70]. We used the orbit's instantaneous orientation (θ) to project the control forces along the X and Y axes. The control forces were then applied to the drive mass of the DAG using the drive electrodes, illustrated in Fig. 7.4.

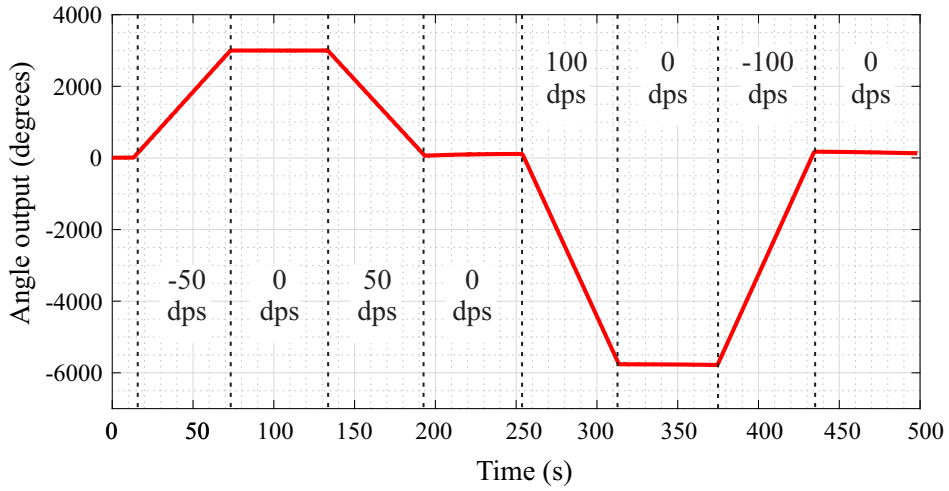

Figure 7.6: Experimental demonstration of direct angle measurements using a DAG in the WA mode of operation.

As discussed in Section 7.3, in a general case due to fabrication imperfections, the principal axes of elasticity affecting the drive mass and the slave mass would not be aligned (i.e., $\alpha_1 \neq \alpha_2$). Therefore, it is essential to estimate the rotational angle (γ) in the force transformation matrix, defined in Eq. (7.17), and include it as a part of the coordinate transformation of the control forces. As experimentally observed and reported in [28], the mismatch angle is typically less than 5 degrees. Therefore, in this initial demonstration, we assumed that the rotational angle was negligible ($\gamma \approx 0$), and the force transformation matrix was assumed to be a scalar matrix.

With an electrode configuration shown in Fig. 7.5, DC biasing voltages were applied to the outer electrodes of the DAG to compensate for anisoelasticity. As described in section 7.3, the DC voltages were manually adjusted to reduce the frequency split and quadrature coupling between the operational modes. The frequency split of the DUT was electrostatically reduced from 27 Hz to 60 mHz, by applying DC voltages of 11.383 V and 2.031 V to the diagonal and off-diagonal tuning electrodes, respectively.

As part of the WA operation, the orientation of the oscillation pattern (θ) was estimated based on the pendulum variables S and R and used as the output of the WA-DAG, [70].

Mismatches in the detection gains and actuation gains, along the X and Y axes of the DAG, were identified and compensated based on the method reported in [129]. Physical rotation was applied to the DAG in clockwise and counter-clockwise directions, and the precession of angle was measured, shown in Fig. 7.6.

As reported in [87], we can represent the output of a WA gyroscope as

$$\theta = -\kappa_e \int \Omega.dt + \theta_b, \tag{7.19}$$

where κ_e, Ω, and θ_b denote the effective angular gain, input angular rate, and angle bias error, respectively.

By applying rotation to the DAG with a constant angular rate, we characterized the effective angular gain, angle bias error, and variations in the energy and quadrature. The effective angular gain was estimated to be on the order of 0.99, close to an ideal angular gain of 1, which is predicted for this particular DAG design.

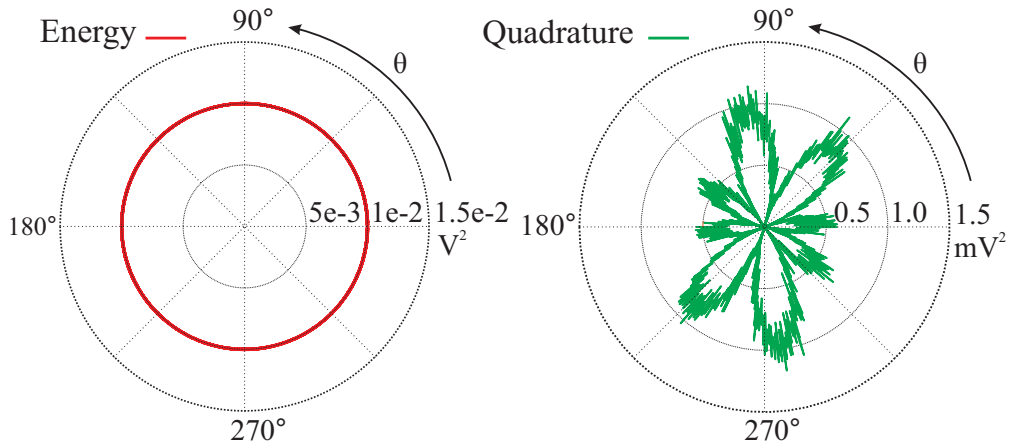

Figure 7.7: Experimental results are shown demonstrating variations in the energy and quadrature of the DAG at different pattern angles. A quadrature-to-energy ratio (Q/E) on the order of 70ppm was measured for the DAG at 40 DPS input angular rate.

Variations in the energy and quadrature through precession as a function of the pattern angle are illustrated in Fg. 7.7, using a polar coordinate system. It is illustrated that both the energy and the quadrature controllers effectively sustained the energy and suppressed the

quadrature of the DAG. For an input angular rate of 40 DPS, the magnitude of quadrature was measured to be on the order of 70 ppm, as compared to the DAG energy.

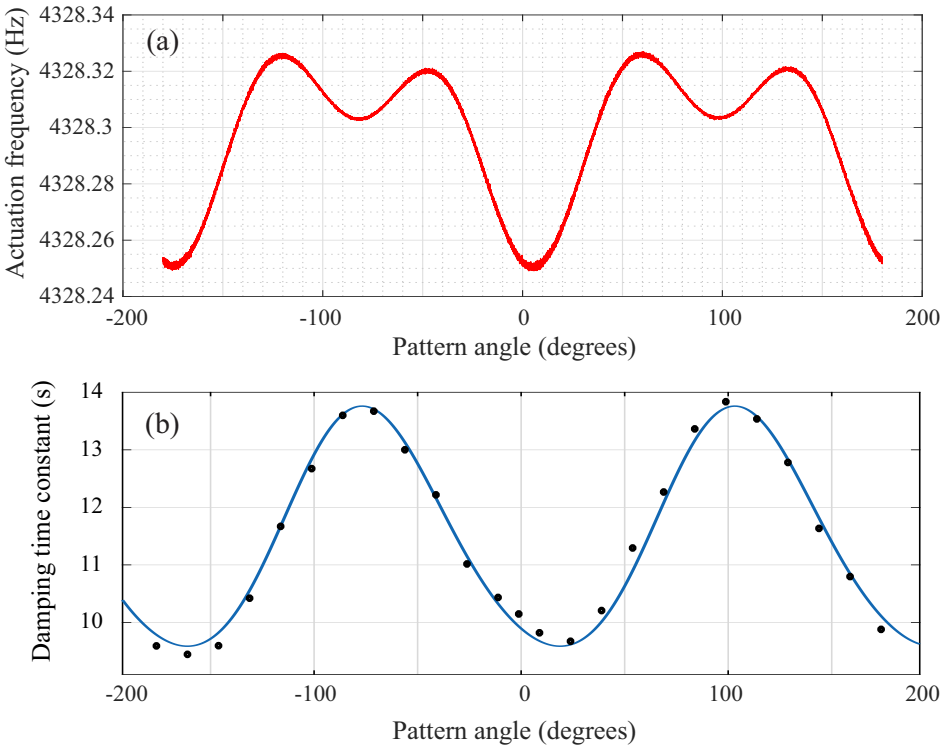

Figure 7.8: a) Variation in the actuation frequency as a function of the pattern angle was used to characterize anisoelasticity in the DAG. b) Illustration of the energy decay time constant values measured at different pattern angles to characterize anisodamping.

Variation of the actuation frequency as a function of the pattern angle is shown in Fig. 7.8(a). We estimated an average resonant frequency of 4328.29 Hz and a remaining anisoelasticity (frequency split) on the order of 60 mHz. A 4θ dependent variation in both the actuation frequency and quadrature, shown in Fig. 7.7, was observed that is attributed to non-linearity of electrostatic forces, [49].

The energy decay time constant was measured at different orientations of the oscillation pattern, illustrated in Fig. 7.8(b). Based on the data, we estimated an average decay time constant (τ) of 11.6 s and anisodamping $\Delta(1/\tau)$ on the order of 32 mHz. It should be noted that the estimated elasticity and damping characteristics would essentially describe the single-mass-equivalent characteristics of the DAG, as defined in Eq. (7.11) and (7.12).

Based on Eq. (7.19), the angle bias error was estimated by removing the linear variation in precession (i.e., $-\kappa_e \Omega t$). The angle bias error as a function of the precession angle, refereed to as the Angle-Dependent Bias (ADB) in [115], was characterized for different input angular rates, and it is shown in Fig. 7.9.

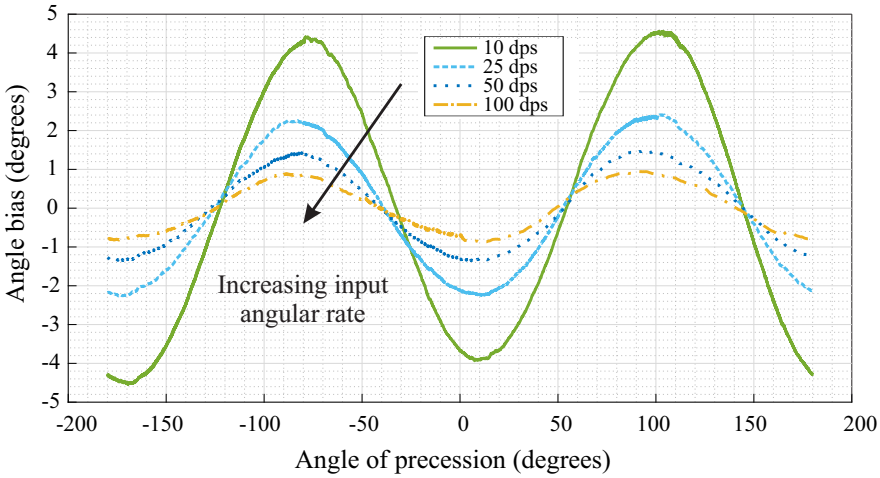

Figure 7.9: Experimental results on characterization of the ADB for input angular rates ranging from 10 DPS to 100 DPS.

The ADB was observed to reduce with the input angular rate in agreement with the analytical results in [87]. Based on the ADB expression in [87], for anisodamping of 32 mHz and an input angular rate of 10 DPS, the ADB should be on the order of 6.88 degrees pk-to-pk. However, as shown in Fig. 7.9, we measured a higher angle bias error of 8.8 degrees. We believe that a higher ADB was caused by a misalignment angle between the principal axes of elasticity affecting the drive and sense masses.

By not accounting for the rotational matrix, as defined in Eq. (7.17), there will be a misalignment angle γ between the energy control force (f_{as}) and the semi-major axis of the elliptical pattern. As a result, the energy control will interfere with the free precession and affects both the effective angular gain and the ADB, as noted in [129].

7.5 Conclusion

In this chapter, we developed a reduced-order model for DAG architecture. Using the reduced-order model, we demonstrated that the DAG can be modeled as a 2-DoF system in the frequency range of interest, close to the in-phase operational modes. Our results suggest that the DAG can be dynamically treated as a conventional single-mass gyroscope and controlled using established controllers for the rate and rate-integrating mechanization.

As an illustration, we adapted the closed-loop WA control and applied it to a DAG device. Based on the reduced-order model, we utilized the vibration measurements of the outer mass for estimation of the pendulum variables and applied the WA control forces to the inner mass. We successfully sustained the energy through this approach, and the quadrature-to-energy ratio was reduced to a value on the order of 70 ppm. The single-mass-equivalent characteristics of the DAG, including anisoelasticity, anisodamping, and effective angular gain, were experimentally characterized. Based on the initial results, anisodamping was shown to affect precession, significantly limiting the resolution of angle measurements. Nevertheless, an effective angular gain of 0.99 was characterized for the DAG, which is close to the maximum theoretical value of 1.

We analytically demonstrated that anisoelasticity and a misalignment in the principal axes of elasticity of DAG result in a non-diagonal force transformation matrix that adversely affects the free precession of vibration pattern. Even though the approach of mode reduction was demonstrated on the DAG architecture, the method is general and can be applied to other multi-degree of freedom Coriolis vibratory gyroscopes.

Chapter 8

Conclusion

This dissertation focused on development of fabrication processes allowing to use fused silica as the structural material for implementation of Micro-Rate-Integrating Gyroscope (MRIG). We demonstrated two fabrication processes, implemented the Whole-Angle (WA) control architecture and algorithms for compensation of error sources. As part of technology development, gyroscope design and process optimization were carried out to fabricate micro-scale planar fused silica gyroscopes. Two practical fabrication processes were designed for manufacturing high-quality factor planar resonators from fused silica material. In one approach, we utilized conventional lithography and plasma etching-based techniques for low-cost batch fabrication of planar fused silica MRIG. In another approach, we explored using a laser-assisted chemical etching process to fabricate fused silica resonant MEMS for the first time. We demonstrated the feasibility of employing conventional micromachining techniques as a cost-effective method for batch-fabricating MRIG with fused silica as the structural material. In the other approach, we successfully demonstrated a Femtosecond-Laser-Induced Chemical Etching (FLICE)-based process for fabricating planar micro-scale gyroscopes from a single-layer fused silica material. We demonstrated an order of magnitude higher quality factor in the fabricated fused silica prototypes compared to their silicon-made counterparts.

We confirmed the feasibility and potential of fused silica for integration as the structural material of micro-scale planar resonant devices to overcome the Thermo-Elastic Damping (TED) quality factor limit of the conventional silicon resonant devices.

Additionally, we presented a detailed study on requirements for the realization of direct angle measurements with improved thermal stability using MRIG. Toward that goal, we developed an electro-mechanical model to enable a systematic study of the effect of mechanical and electrical error sources on precession in the WA mode of operation. We verified the simulation results by implementing the WA control architecture and applying it to a silicon MRIG. We demonstrated that the thermal stability in the WA mode of operation could be improved through careful design of the control architecture. Our results confirmed that the potential of fused silica planar MEMS technology in the realization of high quality factor MRIG with sub-Hz structural symmetry is aligned with the requirements of achieving high-precision angle measurements. Finally, we demonstrated that imperfections in the WA control electronics, in addition to mechanical imperfections, can be equally influential in degrading the resolution and accuracy of angle measurements. The specific contributions of this work are summarized below.

8.1 Contributions

- We developed the Fused silica-On-Silicon (FOS) fabrication process based on conventional micromachining techniques to utilize the desirable fused silica as the structural material in planar micro-resonant devices. For demonstration, a Toroidal Ring Gyroscope (TRG) MRIG was fabricated through the developed process. We demonstrated results on plasma etching recipe optimization and structural realization of TRG with a 100 μm thick device layer. Resonator functionality was demonstrated through electrostatic actuation and detection of the FS-TRG. While a relatively high roughness on

the sidewalls due to the plasma etching process was observed, we measured a quality factor on the order of 539k for the FS-TRG with a 5 nm thick metal coating. Based on structural characterization results, we noted a high correlation between quality factor and thickness of the metal coating, indicating that metal coating of planar fused silica resonators is a major source of energy dissipation that needs to be accounted for.

- As part of this thesis, for the first time, we introduced a fabrication process utilizing Femtosecond Laser-Induced Chemical Etching (FLICE) technique for manufacturing stand-alone fused silica MEMS vibratory structures. An optimization process was reported for achieving high aspect-ratio etching of fused silica with optimal surface quality. We demonstrated that with a femtosecond laser-induced etching selectivity on the order of 855:1, rectangular channels with an aspect ratio on the order of 55:1 and higher could be realized, ideal for fabrication of capacitive MEMS resonators. We introduced a 3-step process utilizing FLICE for fabrication of resonant MEMS devices. Disk Resonator Gyroscope (DRG) MRIG prototypes were fabricated through the introduced process, and initial results on structural characterization were reported. We demonstrated resonator functionality in the fabricated devices through electrostatic actuation and detection. A frequency split as low as 54.7 Hz and a quality factor as high as 614k were demonstrated. As part of this thesis, we demonstrated the highest, to the best of our knowledge, quality factor planar micro-resonant instruments fabricated from fused silica with operational frequencies in the kilohertz range.

- We studied the effect of anisoelasticity on the precession of angle in the WA mode of operation. Using analytical and numerical simulation results, we demonstrated that by adopting a proportional-integral control as the quadrature feedback loop, the magnitude of quadrature (i.e., ellipticity) can be reduced by several orders of magnitude. However, we determined that quadrature cannot be fully eliminated during precession through a PI feedback control. We demonstrated that residual quadrature, similar

to anisodamping, reduces the angular gain and introduces angle-dependent bias errors. In contrast to anisodamping, the effect of anisoelasticity on precession, including the angle-dependent bias error, was shown to be consistent and independent of the angular input rates. Our results suggest that the errors introduced by an uncompensated quadrature degrade the resolution of angle measurements. Mode-matching through electrostatic frequency tuning and employing a high-gain quadrature control were shown to reduce the angle errors due to anisoelasticity significantly.

We explained the correlation between the temperature of operation and effective angular gain in the WA mode of operation through experimental results. In this work, virtual carouseling was implemented and utilized to characterize anisoelasticity at different operation temperatures. We experimentally confirmed that a TCF mismatch in the mechanical sensors is the primary mechanism that leads to Angular Gain Temperature Sensitivity (AGTS) at high angular rates relative to the anisodamping-induced precession. We demonstrated that AGTS is also dependent on the effectiveness of the quadrature control, which is utilized to reduce ellipticity and compensate for anisoelasticity. In the case of using a Proportional-Integral (PI) quadrature control, we demonstrated that through mode-matching and utilizing a high-gain quadrature control, AGTS could be reduced by several orders of magnitude. By applying these strategies with a Dual Foucault Pendulum MRIG along with temperature stabilization, we demonstrated angular gain stability better than 230 ppb.

Furthermore, we explored using a harmonic estimator along with a PI feedback loop as the quadrature control (i.e., the DQC) and demonstrated its potential to eliminate quadrature during precession. For the DFP gyroscope, with a TCF-mismatch on the order of 603 ppb/°C, the angular gain variation was measured to be on the order of 820 ppm for temperatures ranging from 17 °C to 45 °C. The Dynamic Quadrature Control (DQC) was observed to reduce AGTS by 63-times, down to 13 ppm. Our results demonstrated the feasibility of using micro-fabricated devices as Micro-Rate-

Integrating Gyroscopes (MRIG) and provided a mitigation strategy to increase angular gain stability, despite a TCF-mismatch in the sensing element. By reducing AGTS in the MRIG, we were able to measure sub-degree-per-hour angular rates at ambient temperature and angular rates as low as 2.1 deg/hr when operating in an environment with dynamic temperature variations without the need for an active temperature stabilizer.

- As part of this thesis, we developed an electro-mechanical model for the WA operation modality, which captures the effects of imperfections in both the mechanical structure and electronics. We demonstrated that phase errors in signal modulation, demodulation, and asymmetries in the detection and actuation gains along the X and Y axes would introduce additional angle errors, affecting the Angle-Dependent Bias (ADB) characteristics and the Effective Angular Gain (EAG). Using Lynch's analytical results on the evolution of the orbital trajectory, we explained the simulation results. A robust methodology was proposed to identify gain asymmetries in detection and control electronics. As experimentally demonstrated on the DFP MRIG, we utilized angular errors measured during precession to identify and compensate for gain mismatch in the detection electronics. Subsequently, we used energy decay time constants and energy control output to identify the asymmetry in the actuation gains. Above 10-times improvement in ADB error after compensation of gain asymmetries was experimentally demonstrated.

- Finally, we adopted the WA control architecture and applied it to a Dynamically-Amplified-Gyroscope (DAG) for direct angle measurements. As part of this study, a reduced-order model for the 4-Degrees-of-Freedom (4-DoF) DAG architecture was derived, demonstrating that the DAG can be dynamically treated as a conventional single-mass gyroscope and controlled using established controllers for the rate and rate-integrating mechanizations. Based on the reduced-order model, we utilized the vibration measurements of the outer mass for estimation of the pendulum variables and

applied the WA control forces to the inner mass. We successfully sustained the energy through this approach, and the quadrature-to-energy ratio was reduced to a value on the order of 70 ppm. Virtual carouseling was applied to the DAG, and the single-mass-equivalent characteristics, including anisoelasticity, anisodamping, and effective angular gain, were experimentally characterized. More importantly, an effective angular gain of 0.99 was experimentally demonstrated for the DAG, which is close to the maximum theoretical value of 1. We analytically demonstrated that anisoelasticity and a misalignment in the principal axes of elasticity of DAG result in a non-diagonal force transformation matrix that adversely affects the free precession of vibration pattern. We believe that, even though the approach of mode reduction was demonstrated on the DAG architecture, the method is general and can be applied to other multi-degree of freedom Coriolis vibratory gyroscopes.

8.2 Future Research Directions

- **Metal coating of planar fused silica resonators**. We believe it is essential to perform an optimization study on process parameters of thin-film deposition and the thickness of the metal layer. The goal would be to achieve a high electrostatic detection actuation gain while minimizing the quality factor degradation. This is especially important in fused silica devices with sub-ten-micron capacitive gap sizes (aspect ratio above 10:1), for which a uniform step-coating becomes challenging. Further experiments need to be conducted to characterize the quality factor of fused silica resonators without any metal coating. This is necessary to identify other mechanisms limiting the quality factor. Among the energy mechanisms to be studied are surface loss [13] and anchor loss, which could arise from fabrication imperfection-induced structural asymmetries.

- **Laser tramming of MRIG**. Towards reaching sub-Hz structural symmetry in fused silica MRIG, real-time characterization of anisoelasticity of devices along with laser-trimming of imperfections should be perused. The method of carouseling was demonstrated to be a swift and highly accurate approach for identifying frequency split and the orientation of principal axes of elasticity in an MRIG. By using Finite Element Modeling (FEM), we can use the characterized anisoelasticity to define a trimming plan to be performed using the femtosecond laser. This approach can create a closed-loop automatic process for wafer-level permanent tuning of MRIG devices. The FEM modeling can be replaced by commonly used model-driven Machine Learning (ML) methods to facilitate the search for an optimal trimming plan.

- **Stability of precession rate**. We demonstrated that Virtual Carouseling (VC) is an effective method to overcome the angular rate threshold in MRIG, originally caused by anisodamping. In our experiments, we observed that the challenge of VC implementation is in achieving an ultra-stable rate of precession. In electrostatic carouseling, the stability of the precession rate ($\dot{\theta}$) is coupled to stability of the resonant frequency, the detection gains, the actuation gains, etc. Therefore, a trade-off exists between using VC to overcome adverse effects of anisodamping and angular drift due to instability of the electrostatically induced precession. This trade-off should be further investigated.

- **Thermal drift in electronics**. Besides the thermal drifts in mechanical characteristics of MRIG, the control electronics are also affected by temperature variations. Variations in detection/actuation gains (i.e., amplitude response) and phase response of electronic circuits and components utilized in the WA operation are inevitable. Therefore, it is essential to understand the implications of thermal drift in electronics on precession. Future studies need to investigate the required stability in electronics to achieve robust operation. Also, control strategies should be developed to identify error sources associated with the control electronics during operation. This would enable a

capability for in-run compensation of these errors despite thermal drifts.

- **Whole-angle operation in the non-linear regime**. In the WA mode of operation, the noise in pick-off electronics and the noise in feedback control fundamentally limit the resolution of direct angle measurements. While increasing the amplitude of vibration can potentially improve the Signal-to-Noise Ratio (SNR), at a large amplitude of vibration, the non-linear mechanisms pose a challenge in regards to the control and operation of MRIG in the WA mode. Future research must study the limitations of WA operation in the non-linear regime.

Bibliography

[1] M. J. Ahamed, D. Senkal, A. A. Trusov, and A. M. Shkel. Study of high aspect ratio NLD plasma etching and postprocessing of fused silica and borosilicate glass. *IEEE Journal of Microelectromechanical Systems*, 24(4):790–800, 2015.

[2] T. Akashi and Y. Yoshimura. Deep reactive ion etching of borosilicate glass using an anodically bonded silicon wafer as an etching mask. *Journal of Micromechanics and Microengineering*, 16(5):1051–1056, 2006.

[3] T. Akashi and Y. Yoshimura. Profile control of a borosilicate-glass groove formed by deep reactive ion etching. *Journal of Micromechanics and Microengineering*, 18(10):105004, 2008.

[4] M. H. Asadian, S. Askari, I. B. Flader, Y. Chen, D. D. Gerrard, D. D. Shin, H.-K. Kwon, T. W. Kenny, and A. M. Shkel. High quality factor mode ordered dual foucault pendulum gyroscope. In *IEEE Sensors Conference (SENSORS)*, New Delhi, India, October 2018.

[5] M. H. Asadian, S. Askari, and A. M. Shkel. An ultrahigh vacuum packaging process demonstrating over 2 million Q-factor in MEMS vibratory gyroscopes. *IEEE Sensors Letters*, 1(6):1–4, 2017.

[6] M. H. Asadian, S. Askari, Y. Wang, and A. M. Shkel. Characterization of energy dissipation mechanisms in dual foucault pendulum gyroscopes. In *IEEE International Symposium on Inertial Sensors and Systems (INERTIAL)*, Naples, FL, USA, April 2019.

[7] M. H. Asadian, Y. Wang, and A. M. Shkel. Development of 3D fused quartz hemitoroidal shells for high-Q resonators and gyroscopes. *IEEE Journal of Microelectromechanical Systems*, 28(6):954–964, 2019.

[8] S. Askari, M. H. Asadian, and A. M. Shkel. High quality factor MEMS gyroscope with whole angle mode of operation. In *IEEE International Symposium on Inertial Sensors and Systems (INERTIAL)*, Lake Como, Italy, March 2018.

[9] S. Askari, M. H. Asadian, and A. M. Shkel. Retrospective correction of angular gain by virtual carouseling in MEMS gyroscopes. In *IEEE International Symposium on Inertial Sensors and Systems (INERTIAL)*, Naples, FL, USA, April 2019.

[10] Y. Bellouard, A. Said, M. Dugan, and P. Bado. Fabrication of high-aspect ratio, micro-fluidic channels and tunnels using femtosecond laser pulses and chemical etching. *Optics Express*, 12(10):2120–2129, 2004.

[11] Y. Bellouard, A. A. Said, and P. Bado. Integrating optics and micro-mechanics in a single substrate: a step toward monolithic integration in fused silica. *Optics Express*, 13(17):6635–6644, 2005.

[12] N. N. Bogoliubov. *Asymptotic methods in the theory of non-linear oscillations*, volume 10. CRC Press, 1961.

[13] V. B. Braginski. *Systems with small dissipation*. University of Chicago Press, 1985.

[14] G. H. Bryan. On the beats in the vibrations of a revolving cylinder or bell. In *Proceedings of the Cambridge Philosophical Society*, volume 7, 1890.

[15] A. Butkute, T. Baravykas, J. Stančikas, T. Tičkūnas, L. Jonušauskas, and V. Sirutkaitis. Optimization of selective laser etching for assembly-free 3D micromechanic fabrication. In *Laser 3D Manufacturing VIII*, volume 11677, pages 85 – 91. International Society for Optics and Photonics, 2021.

[16] A. Butkutė and L. Jonušauskas. 3D manufacturing of glass microstructures using femtosecond laser. *Micromachines*, 12(5):499, 2021.

[17] J. Cao and C. T.-C. Nguyen. Drive amplitude dependence of micromechanical resonator series motional resistance. In *International Conference on Solid-State Sensors and Actuators (TRANSDUCERS)*, Sendai, Japan, June 1999.

[18] Z. Cao, B. VanDerElzen, K. J. Owen, J. Yan, G. He, R. L. Peterson, D. Grimard, and K. Najafi. DRIE of fused silica. In *IEEE International Conference on Micro Electro Mechanical Systems (MEMS)*, Taipei, Taiwan, January 2013.

[19] Z. Cao, Y. Yuan, G. He, R. L. Peterson, and K. Najafi. Fabrication of multi-layer vertically stacked fused silica microsystems. In *The International Conference on Solid-State Sensors, Actuators and Microsystems (TRANSDUCERS)*, Barcelona, Spain, June 2013.

[20] A. D. Challoner, H. G. Howard, and J. Y. Liu. Boeing disc resonator gyroscope. In *IEEE/ION Position, Location and Navigation Symposium (PLANS)*, Monterey, CA, USA, May 2014.

[21] D. T. Chang, F. P. Stratton, R. L. Kubena, and R. J. Joyce. Optimized DRIE etching of ultra-small quartz resonators. In *IEEE International Frequency Control Symposium and PDA Exhibition Jointly with the European Frequency and Time Forum*, Tampa, FL, USA, May 2003.

[22] J. Cho, J. Gregory, and K. Najafi. High-Q, 3kHz single-crystal-silicon cylindrical rate-integrating gyro (CING). In *IEEE International Conference on Micro Electro Mechanical Systems (MEMS)*, Paris, France, February 2012.

[23] J. Y. Cho, S. Singh, J.-K. Woo, G. He, and K. Najafi. 0.00016 deg/$\sqrt{hr}$ Angle Random Walk (ARW) and 0.0014 deg/hr Bias Instability (BI) from a 5.2 MQ and 1-cm Precision Shell Integrating (PSI) gyroscope. In *IEEE International Symposium on Inertial Sensors and Systems (INERTIAL)*, Hiroshima, Japan, March 2020.

[24] S. T. Cho. Method of making a micromechanical silicon-on-glass tuning fork gyroscope, Feb. 20 1996. US Patent 5,492,596.

[25] C. Corbari, A. Champion, M. Gecevičius, M. Beresna, Y. Bellouard, and P. G. Kazansky. Femtosecond versus picosecond laser machining of nano-gratings and microchannels in silica glass. *Optics Express*, 21(4):3946–3958, 2013.

[26] E. Davison. A method for simplifying linear dynamic systems. *IEEE Transactions on automatic control*, 11(1):93–101, 1966.

[27] Y. Dogan and C. K. Madsen. Optimization of ultrafast laser parameters for 3D micromachining of fused silica. *Optics & Laser Technology*, 123:105933, 2020.

[28] A. Efimovskaya, D. Wang, Y.-W. Lin, and A. M. Shkel. Electrostatic compensation of structural imperfections in dynamically amplified dual-mass gyroscope. *Sensors and Actuators A: Physical*, 275:99–108, 2018.

[29] A. Efimovskaya, D. Wang, and A. M. Shkel. Mechanical trimming with focused ion beam for permanent tuning of MEMS dual-mass gyroscope. *Sensors and Actuators A: Physical*, 313:112189, 2020.

[30] M. Foucault. Physical demonstration of the rotation of the earth by means of the pendulum. *Journal of the Franklin Institute, of the State of Pennsylvania, for the Promotion of the Mechanic Arts; Devoted to Mechanical and Physical Science, Civil Engineering, the Arts and Manufactures, and the Recording of American and Other Patent Inventions (1828-1851)*, 21(5):350, 1851.

[31] B. Friedland and M. Hutton. Theory and error analysis of vibrating-member gyroscope. *IEEE Transactions on Automatic Control*, 23(4):545–556, 1978.

[32] T. Fukasawa, T. Hayashi, and Y. Horiike. Conelike defect in deep quartz etching employing neutral loop discharge. *Japanese Journal of Applied Physics*, 42(10R):6691, 2003.

[33] E. N. Glezer and E. Mazur. Ultrafast-laser driven micro-explosions in transparent materials. *Applied Physics Letters*, 71(7):882–884, 1997.

[34] J. Gottmann, M. Hermans, N. Repiev, and J. Ortmann. Selective laser-induced etching of 3D precision quartz glass components for microfluidic applications—up-scaling of complexity and speed. *Micromachines*, 8(4):110, 2017.

[35] J. A. Gregory, J. Cho, and K. Najafi. Novel mismatch compensation methods for rate-integrating gyroscopes. In *Proceedings of the IEEE/ION Position, Location and Navigation Symposium (PLANS)*, Myrtle Beach, SC, USA, April 2012.

[36] S. Grousset, P. Lavenus, L. Benaissa, R. Taïbi, E. Augendre, T. Signamarcheix, O. Le Traon, and S. Ballandras. Quartz-based vibrating MEMS fabricated using a wafer-bonding process with sealed cavities. In *IEEE International Frequency Control Symposium (FCS)*, Taipei, Taiwan, May 2014.

[37] R. Gunn, C. Welch, D. Stephens, and L. Deng. Comparison of etch processes for etching SiO2 dielectric films. Technical report, tech. rep., Oxford Instruments Plasma Technology, 2009.

[38] K. Guo, Y. Wu, Y. Zhang, D. Xiao, and X. Wu. Adaptive compensation of damping asymmetry in whole-angle hemispherical resonator gyroscope. *AIP Advances*, 10(10):105109, 2020.

[39] F. He, Y. Cheng, Z. Xu, Y. Liao, J. Xu, H. Sun, C. Wang, Z. Zhou, K. Sugioka, K. Midorikawa, et al. Direct fabrication of homogeneous microfluidic channels embedded in fused silica using a femtosecond laser. *Optics Letters*, 35(3):282–284, 2010.

[40] F. He, J. Lin, and Y. Cheng. Fabrication of hollow optical waveguides in fused silica by three-dimensional femtosecond laser micromachining. *Applied Physics B*, 105(2):379–384, 2011.

[41] M. Hermans, J. Gottmann, and F. Riedel. Selective, laser-induced etching of fused silica at high scan-speeds using KOH. *Journal of Laser Micro/Nanoengineering*, 9(2):126–131, 2014.

[42] D. Hii, D. Vatanparvar, and A. M. Shkel. Optimization of photoresist plating mold fabrication for metal mask patterning. *Journal of Vacuum Science & Technology B, Nanotechnology and Microelectronics: Materials, Processing, Measurement, and Phenomena*, 39(2):022601, 2021.

[43] C. Hnatovsky, R. Taylor, P. Rajeev, E. Simova, V. Bhardwaj, D. Rayner, and P. Corkum. Pulse duration dependence of femtosecond-laser-fabricated nanogratings in fused silica. *Applied Physics Letters*, 87(1):014104, 2005.

[44] C. Hnatovsky, R. Taylor, E. Simova, P. Rajeev, D. Rayner, V. Bhardwaj, and P. Corkum. Fabrication of microchannels in glass using focused femtosecond laser radiation and selective chemical etching. *Applied Physics A*, 84(1):47–61, 2006.

[45] M. A. Hopcroft, W. D. Nix, and T. W. Kenny. What is the Young's modulus of silicon? *IEEE Journal of Microelectromechanical Systems*, 19(2):229–238, 2010.

[46] Y. Hu, S. Rao, S. Wu, P. Wei, W. Qiu, D. Wu, B. Xu, J. Ni, L. Yang, J. Li, et al. All-glass 3D optofluidic microchip with built-in tunable microlens fabricated by femtosecond laser-assisted etching. *Advanced Optical Materials*, 6(9):1701299, 2018.

[47] Z. Hu and B. Gallacher. Control and damping imperfection compensation for a rate integrating MEMS gyroscope. In *DGON Inertial Sensors and Systems Symposium (ISS)*, Karlsruhe, Germany, September 2015.

[48] Z. Hu and B. Gallacher. Extended Kalman filtering based parameter estimation and drift compensation for a MEMS rate integrating gyroscope. *Sensors and Actuators A: Physical*, 250:96–105, 2016.

[49] Z. Hu and B. J. Gallacher. Effects of nonlinearity on the angular drift error of an electrostatic MEMS rate integrating gyroscope. *IEEE Sensors Journal*, 19(22):10271–10280, 2019.

[50] M. Huff and M. Pedersen. Electrical field-induced faceting of etched features using plasma etching of fused silica. *Journal of Applied Physics*, 122(2):023302, 2017.

[51] M. F. Hutton and B. Friedland. Control system for angular displacement sensor, Nov. 23 1976. US Patent 3,992,952.

[52] Y.-S. Hwang, H.-K. Jung, E.-S. Song, I.-J. Hyeon, Y.-K. Kim, and C.-W. Baek. Fabrication of electrostatically-actuated, in-plane fused quartz resonators using Silicon-On-Quartz (SOQ) bonding and quartz DRIE. In *IEEE International Conference on Micro Electro Mechanical Systems (MEMS)*, Sorrento, Italy, January 2009.

[53] L. Jonušauskas, S. Rekštyte, R. Buividas, S. Butkus, R. Gadonas, S. Juodkazis, and M. Malinauskas. Hybrid subtractive-additive-welding microfabrication for lab-on-chip applications via single amplified femtosecond laser source. *Optical Engineering*, 56(9):094108, 2017.

[54] H.-K. Jung, Y.-S. Hwang, I.-J. Hyeon, Y.-K. Kim, and C.-W. Baek. Silicon/quartz bonding and quartz deep RIE for the fabrication of quartz resonator structures. In *IEEE International Conference on Nano/Micro Engineered and Molecular Systems*, Sanya, China, January 2008.

[55] S.-T. Jung, H.-S. Song, D.-S. Kim, and H.-S. Kim. Inductively coupled plasma etching of SiO2 layers for planar lightwave circuits. *Thin Solid Films*, 341(1-2):188–191, 1999.

[56] M. J. Khan, T. Tsukamoto, M. S. Al Farisi, and S. Tanaka. Fabrication method of micromachined quartz glass resonator using sacrificial supporting structures. *Sensors and Actuators A: Physical*, 305:111922, 2020.

[57] D. Kim and R. T. M'Closkey. Spectral analysis of vibratory gyro noise. *IEEE Sensors Journal*, 13(11):4361–4374, 2013.

[58] K. Kolari, V. Saarela, and S. Franssila. Deep plasma etching of glass for fluidic devices with different mask materials. *Journal of Micromechanics and Microengineering*, 18(6):064010, 2008.

[59] R. L. Kubena and D. T. Chang. Disc resonator gyroscopes, Sept. 1 2009. US Patent 7,581,443.

[60] K. Kunal and N. R. Aluru. Akhiezer damping in nanostructures. *Physical Review B*, 84(24):245450, 2011.

[61] R. P. Leland. Mechanical-thermal noise in MEMS gyroscopes. *IEEE Sensors Journal*, 5(3):493–500, 2005.

[62] X. Li, L. Ling, X. Hua, M. Fukasawa, G. S. Oehrlein, M. Barela, and H. M. Anderson. Effects of Ar and O_2 additives on SiO_2 etching in C_4F_8-based plasmas. *Journal of Vacuum Science & Technology A: Vacuum, Surfaces, and Films*, 21(1):284–293, 2003.

[63] X. Li, L. Ling, X. Hua, G. S. Oehrlein, Y. Wang, and H. Anderson. Characteristics of C_4F_8 plasmas with Ar, Ne, and He additives for SiO_2 etching in an Inductively Coupled Plasma (ICP) reactor. *Journal of Vacuum Science & Technology A: Vacuum, Surfaces, and Films*, 21(6):1955–1963, 2003.

[64] X. Li, J. Xu, Z. Lin, J. Qi, P. Wang, W. Chu, Z. Fang, Z. Wang, Z. Chai, and Y. Cheng. Polarization-insensitive space-selective etching in fused silica induced by picosecond laser irradiation. *Applied Surface Science*, 485:188–193, 2019.

[65] R. Lifshitz and M. L. Roukes. Thermoelastic damping in micro-and nanomechanical systems. *Physical Review B*, 61(8):5600, 2000.

[66] L. Lin, X. Jing, F. Liu, W. Yin, D. Yu, and L. Cao. Deep dry etching of fused silica using C4F8/Ar inductively coupled plasmas. *Journal of Materials Science: Materials in Electronics*, 28(1):480–486, 2017.

[67] L. Lin, X. Jing, Q. Wang, F. Jiang, L. Cao, and D. Yu. Investigation of fused silica glass etching using C4F8/Ar inductively coupled plasmas for through glass via (TGV) applications. *Microsystem Technologies*, 22(1):119–127, 2016.

[68] E. J. Loper Jr and D. D. Lynch. Sonic vibrating bell gyro, June 5 1979. US Patent 4,157,041.

[69] D. D. Lynch. Vibration-induced drift in the hemispherical resonator gyro. In *Proceedings of the Annual Meeting of The Institute of Navigation*, Dayton, Ohio, June 1987.

[70] D. D. Lynch. Vibratory gyro analysis by the method of averaging. In *Proceedings of St. Petersburg Conference on Gyroscopic Technology and Navigation*, St. Petersburg, May 1995.

[71] R. Melamud, M. Hopcroft, C. Jha, B. Kim, S. Chandorkar, R. Candler, and T. W. Kenny. Effects of stress on the temperature coefficient of frequency in double clamped resonators. In *The International Conference on Solid-State Sensors, Actuators and Microsystems (TRANSDUCERS)*, Seoul, Korea (South), June 2005.

[72] T. Meyer, A. Girard, G. Le Dain, A. Rhallabi, E. Baudet, V. Nazabal, P. Němec, and C. Cardinaud. Surface composition and micromasking effect during the etching of amorphous Ge-Sb-Se thin films in SF6 and SF6/Ar plasmas. *Applied Surface Science*, 549:149192, 2021.

[73] I. Miyamoto, A. Horn, J. Gottmann, D. Wortmann, and F. Yoshino. Fusion welding of glass using femtosecond laser pulses with high-repetition rates. *Journal of Laser Micro/Nanoengineering*, 2(1):57–63, 2007.

[74] M. E. Motamedi, M. C. Wu, and K. S. Pister. Micro-opto-electro-mechanical devices and on-chip optical processing. *Optical Engineering*, 36(5):1282–1297, 1997.

[75] T. Nagourney, J. Y. Cho, A. Darvishian, B. Shiari, and K. Najafi. Effect of metal annealing on the Q-factor of metal-coated fused silica micro shell resonators. In *IEEE International Symposium on Inertial Sensors and Systems (ISISS)*, Hapuna Beach, HI, USA, March 2015.

[76] E. J. Ng, V. A. Hong, Y. Yang, C. H. Ahn, C. L. Everhart, and T. W. Kenny. Temperature dependence of the elastic constants of doped silicon. *IEEE Journal of Microelectromechanical Systems*, 24(3):730–741, 2014.

[77] S. H. Nitzan, P. Taheri-Tehrani, M. Defoort, S. Sonmezoglu, and D. A. Horsley. Countering the effects of nonlinearity in rate-integrating gyroscopes. *IEEE Sensors Journal*, 16(10):3556–3563, 2016.

[78] I. V. Novozhilov. *Fractional analysis: Methods of motion decomposition*. Springer Science & Business Media, 1997.

[79] Y. Okada and Y. Tokumaru. Precise determination of lattice parameter and thermal expansion coefficient of silicon between 300 and 1500 K. *Journal of Applied Physics*, 56(2):314–320, 1984.

[80] A. Osipov, S. Aleksandrov, and V. Berezenko. Development of process for fast plasma-chemical through etching of single-crystal quartz in SF6/O2 gas mixture. *Russian Journal of Applied Chemistry*, 91(8):1255–1261, 2018.

[81] C. C. Painter and A. M. Shkel. Active structural error suppression in MEMS vibratory rate integrating gyroscopes. *IEEE Sensors Journal*, 3(5):595–606, 2003.

[82] C. C. Painter and A. M. Shkel. Dynamically amplified micromachined vibratory angle measuring gyroscopes, micromachined inertial sensors and method of operation for the same, Aug. 16 2005. US Patent 6,928,874.

[83] Y.-H. Park and K. Park. High-fidelity modeling of MEMS resonators. Part I. anchor loss mechanisms through substrate. *IEEE Journal of Microelectromechanical Systems*, 13(2):238–247, 2004.

[84] M. Pedersen and M. Huff. Development of process recipes for maximum mask etch selectivity and maximum etch rate having vertical sidewalls for deep, highly-anisotropic Inductively-Coupled Plasma (ICP) etching of fused silica. *ECS Journal of Solid State Science and Technology*, 6(9):644–652, 2017.

[85] M. Pedersen and M. Huff. Plasma etching of deep high-aspect ratio features into fused silica. *IEEE Journal of Microelectromechanical Systems*, 26(2):448–455, 2017.

[86] M. Pedersen and M. Huff. Across substrate lateral dimensional repeatability using a highly-anisotropic deep etch process on fused silica material layers. *IEEE Journal of Microelectromechanical Systems*, 27(1):31–33, 2018.

[87] I. P. Prikhodko, J. A. Gregory, D. I. Bugrov, and M. W. Judy. Overcoming limitations of rate integrating gyroscopes by virtual rotation. In *IEEE International Symposium on Inertial Sensors and Systems (INERTIAL)*, Laguna Beach, CA, USA, February 2016.

[88] I. P. Prikhodko, J. A. Gregory, W. A. Clark, J. A. Geen, M. W. Judy, C. H. Ahn, and T. W. Kenny. Mode-matched MEMS Coriolis vibratory gyroscopes: Myth or reality? In *IEEE/ION Position, Location and Navigation Symposium (PLANS)*, Savannah, GA, USA, April 2016.

[89] I. P. Prikhodko, J. A. Gregory, and M. W. Judy. Virtually rotated MEMS gyroscope with angle output. In *IEEE International Conference on Micro Electro Mechanical Systems (MEMS)*, Las Vegas, NV, USA, January 2017.

[90] I. P. Prikhodko, S. A. Zotov, A. A. Trusov, and A. M. Shkel. Foucault pendulum on a chip: Rate integrating silicon MEMS gyroscope. *Sensors and Actuators A: Physical*, 177:67–78, 2012.

[91] I. P. Prikhodko, S. A. Zotov, A. A. Trusov, and A. M. Shkel. Foucault pendulum on a chip: Rate integrating silicon MEMS gyroscope. *Sensors and Actuators A: Physical*, 177:67–78, 2012.

[92] J. Qi, Z. Wang, J. Xu, Z. Lin, X. Li, W. Chu, and Y. Cheng. Femtosecond laser induced selective etching in fused silica: optimization of the inscription conditions with a high-repetition-rate laser source. *Optics Express*, 26(23):29669–29678, 2018.

[93] J. Roberts and P. Spanos. Stochastic averaging: An approximate method of solving random vibration problems. *International Journal of Non-Linear Mechanics*, 21(2):111–134, 1986.

[94] C. A. Ross, D. G. MacLachlan, D. Choudhury, and R. R. Thomson. Optimisation of ultrafast laser assisted etching in fused silica. *Optics Express*, 26(19):24343–24356, 2018.

[95] R. Roy, D. K. Agrawal, and H. A. McKinstry. Very low thermal expansion coefficient materials. *Annual Review of Materials Science*, 19(1):59–81, 1989.

[96] D. M. Rozelle. The hemispherical resonator gyro: From wineglass to the planets. In *Proceedings AAS/AIAA Space Flight Mechanics Meeting*, volume 134, 2009.

[97] D. Ruixue, Y. Yintang, and H. Ru. Microtrenching effect of SiC ICP etching in SF6/O2 plasma. *Journal of Semiconductors*, 30(1):016001, 2009.

[98] F. Sala, P. Paié, R. Martínez Vázquez, R. Osellame, and F. Bragheri. Effects of thermal annealing on femtosecond laser micromachined glass surfaces. *Micromachines*, 12(2):180, 2021.

[99] A. Sankaran and M. J. Kushner. Etching of porous and solid SiO_2 in Ar/ c-C_4F_8, O_2/ c-C_4F_8 and Ar/ O_2/ c-C_4F_8 plasmas. *Journal of Applied Physics*, 97(2):023307, 2005.

[100] A. Semerok, B. Salle, J.-F. Wagner, and G. Petite. Femtosecond, picosecond, and nanosecond laser microablation: Laser plasma and crater investigation. *Laser and Particle Beams*, 20(1):67–72, 2002.

[101] D. Senkal, S. Askari, M. Ahamed, E. Ng, V. Hong, Y. Yang, C. H. Ahn, T. Kenny, and A. Shkel. 100k Q-factor toroidal ring gyroscope implemented in wafer-level epitaxial silicon encapsulation process. In *IEEE International Conference on Micro Electro Mechanical Systems (MEMS)*, San Francisco, CA, USA, January 2014.

[102] D. Senkal, A. Efimovskaya, and A. M. Shkel. Minimal realization of dynamically balanced lumped mass WA gyroscope: dual Foucault pendulum. In *IEEE International Symposium on Inertial Sensors and Systems (ISISS)*, Hapuna Beach, HI, USA, March 2015.

[103] D. Senkal, E. Ng, V. Hong, Y. Yang, C. Ahn, T. Kenny, and A. Shkel. Parametric drive of a toroidal MEMS rate integrating gyroscope demonstrating¡ 20 ppm scale factor stability. In *IEEE International Conference on Micro Electro Mechanical Systems (MEMS)*, Estoril, Portugal, January 2015.

[104] D. Senkal and A. M. Shkel. Axi-symmetric small-footprint gyroscope with interchangeable whole-angle and rate operation, Jan. 15 2019. US Patent 10,180,323.

[105] D. Senkal, S. A. Zotov, and A. M. Shkel. Fully balanced micro-machined inertial sensor, Apr. 2 2019. US Patent 10,247,554.

[106] L. Shah, J. Tawney, M. Richardson, and K. Richardson. Femtosecond laser deep hole drilling of silicate glasses in air. *Applied Surface Science*, 183(3-4):151–164, 2001.

[107] A. Sharma, M. F. Zaman, M. Zucher, and F. Ayazi. A 0.1/hr bias drift electronically matched tuning fork microgyroscope. In *IEEE International Conference on Micro Electro Mechanical Systems (MEMS)*, Tucson, AZ, USA, January 2008.

[108] N. Shen, M. J. Matthews, J. E. Fair, J. A. Britten, H. T. Nguyen, J. D. Cooke, S. Elhadj, W. D. Henshaw, G. M. Guss, I. L. Bass, et al. Study of CO2 laser smoothing of surface roughness in fused silica. In *Laser-Induced Damage in Optical Materials: 2009*, volume 7504. SPIE, 2009.

[109] D. D. Shin, C. H. Ahn, Y. Chen, V. A. Hong, E. J. Ng, Y. Yang, and T. W. Kenny. Electrostatic tuning of temperature coefficient of frequency of anisotropic disk-shaped resonators. In *IEEE International Symposium on Inertial Sensors and Systems (INERTIAL)*, Kauai, HI, USA, March 2017.

[110] A. M. Shkel. Type I and type II micromachined vibratory gyroscopes. In *Proceedings of IEEE/ION Position, Location, And Navigation Symposium (PLANS)*, Coronado, CA, USA, April 2006.

[111] E.-S. Song, S. Kang, H. Kim, Y.-K. Kim, J.-E. An, and C.-W. Baek. Wafer-level fabrication of a fused-quartz double-ended tuning fork resonator oscillator using quartz-on-quartz direct bonding. *IEEE Electron Device Letters*, 34(5):692–694, 2013.

[112] V. Stankevič and G. Račiukaitis. Formation of rectangular channels in fused silica by laser-induced chemical etching. *Lithuanian Journal of Physics*, 54(3):136–141, 2014.

[113] B. Stuart, M. Feit, S. Herman, A. Rubenchik, B. Shore, and M. Perry. Nanosecond-to-femtosecond laser-induced breakdown in dielectrics. *Physical review B*, 53(4):1749, 1996.

[114] J. Sui, S. Zhang, Z. Liu, J. Yan, and Z. Dai. A multi-scale study on silicon-oxide etching processes in C4F8/Ar plasmas. *Plasma Science and Technology*, 18(6):666–673, 2016.

[115] P. Taheri-Tehrani, A. D. Challoner, and D. A. Horsley. Micromechanical rate integrating gyroscope with angle-dependent bias compensation using a self-precession method. *IEEE Sensors Journal*, 18(9):3533–3543, 2018.

[116] M. Taimoor, A. Alatawi, S. Reuter, H. Hillmer, and T. Kusserow. Single-step inductively coupled plasma etching of sputtered Nb2O5/SiO2 multilayer stacks using chromium etch mask. *Journal of Vacuum Science & Technology A: Vacuum, Surfaces, and Films*, 35(4):041302, 2017.

[117] R. Taylor, C. Hnatovsky, and E. Simova. Applications of femtosecond laser induced self-organized planar nanocracks inside fused silica glass. *Laser & Photonics Reviews*, 2(1-2):26–46, 2008.

[118] W. T. Thomson. *Theory of vibration with applications*. CrC Press, 2018.

[119] D. Titterton, J. L. Weston, and J. Weston. *Strapdown inertial navigation technology*, volume 17. IET, 2004.

[120] A. Trusov, M. Phillips, A. Bettadapura, G. Atikyan, G. McCammon, J. Pavell, Y. Choi, D. Sakaida, D. Rozelle, and A. Meyer. mHRG: Miniature CVG with beyond navigation grade performance and real time self-calibration. In *IEEE International Symposium on Inertial Sensors and Systems (INERTIAL)*, Laguna Beach, CA, USA, February 2016.

[121] A. Trusov, D. Rozelle, G. Atikyan, S. Zotov, B. Simon, A. Shkel, and A. Meyer. Non-axisymmetric coriolis vibratory gyroscope with whole angle, force rebalance, and self-calibration. In *A Solid-State Sensors, Actuators and Microsystems Workshop (Hilton Head)*, Hilton Head Island, SC, USA, June 2014.

[122] A. Trusov, D. M. Rozelle, and D. D. Lynch. Hemispherical resonator gyroscope, Mar. 10 2020. US Patent 10,584,967.

[123] A. A. Trusov, G. Atikyan, D. Rozelle, A. Meyer, S. A. Zotov, B. Simon, and A. M. Shkel. Force rebalance, whole angle, and self-calibration mechanization of silicon MEMS quad mass gyro. In *International Symposium on Inertial Sensors and Systems (ISISS)*, Laguna Beach, CA, USA, February 2014.

[124] A. A. Trusov, A. R. Schofield, and A. M. Shkel. Micromachined tuning fork gyroscopes with ultra-high sensitivity and shock rejection, Dec. 4 2012. US Patent 8,322,213.

[125] D. Vatanparvar, M. H. Asadian, S. Askari, and A. M. Shkel. Characterization of scale factor nonlinearities in Coriolis vibratory gyroscopes. In *IEEE International Symposium on Inertial Sensors and Systems (INERTIAL)*, Naples, FL, USA, April 2019.

[126] D. Vatanparvar and A. Shkel. Effect of electrostatic nonlinearity on force-to-rebalance mode of operation in CVG. In *DGON Inertial Sensors and Systems (ISS)*, Braunschweig, Germany, September 2020.

[127] D. Vatanparvar and A. M. Shkel. Effect of fabrication imperfections on energy loss through mechanical mode coupling in MEMS. In *IEEE International Symposium on Inertial Sensors and Systems (INERTIAL)*, Lake Como, Italy, March 2018.

[128] D. Vatanparvar and A. M. Shkel. Instabilities due to electrostatic tuning of frequency-split in coriolis vibratory gyroscopes. In *IEEE Sensors Conference (SENSORS)*, Rotterdam, Netherlands, October 2020.

[129] D. Vatanparvar and A. M. Shkel. Identification of gain mismatches in control electronics of rate integrating CVGs. In *IEEE International Symposium on Inertial Sensors and Systems (INERTIAL)*, Kailua-Kona, HI, USA, March 2021.

[130] D. Vatanparvar and A. M. Shkel. On correlation of anisoelasticity, angular gain, and temperature in whole-angle CVGs. *IEEE Sensors Journal*, 2021.

[131] D. Wang, M. H. Asadian, A. Efimovskaya, and A. M. Shkel. A comparative study of conventional single-mass and amplitude amplified dual-mass MEMS vibratory gyroscopes. In *IEEE International Symposium on Inertial Sensors and Systems (INERTIAL)*, Kauai, HI, USA, March 2017.

[132] D. Wang, A. Efimovskaya, and A. M. Shkel. Amplitude amplified dual-mass gyroscope: design architecture and noise mitigation strategies. In *IEEE International Symposium on Inertial Sensors and Systems (INERTIAL)*, Naples, FL, USA, April 2019.

[133] S. Wang, C. Zhou, H. Ru, and Y. Zhang. Optimized condition for etching fused-silica phase gratings with inductively coupled plasma technology. *Applied Optics*, 44(21):4429–4434, 2005.

[134] Z. Wang, L. Jiang, X. Li, A. Wang, Z. Yao, K. Zhang, and Y. Lu. High-throughput microchannel fabrication in fused silica by temporally shaped femtosecond laser Bessel-beam-assisted chemical etching. *Optics Letters*, 43(1):98–101, 2018.

[135] P. Ward and A. Duwel. Oscillator phase noise: Systematic construction of an analytical model encompassing nonlinearity. *IEEE Transactions on Ultrasonics, Ferroelectrics, and Frequency Control*, 58(1):195–205, 2011.

[136] M. Weinberg, R. Candler, S. Chandorkar, J. Varsanik, T. Kenny, and A. Duwel. Energy loss in MEMS resonators and the impact on inertial and RF devices. In *International Solid-State Sensors, Actuators and Microsystems Conference (TRANSDUCERS)*, Denver, CO, USA, June 2009.

[137] M. S. Weinberg and A. Petrovich. Quartz resonant gyroscope or quartz resonant tuning fork gyroscope, Feb. 14 1995. US Patent 5,388,458.

[138] C. Weingarten, S. Steenhusen, M. Hermans, E. Willenborg, and J. H. Schleifenbaum. Laser polishing and 2PP structuring of inside microfluidic channels in fused silica. *Microfluidics and Nanofluidics*, 21(11):1–9, 2017.

[139] J.-K. Woo, J. Y. Cho, C. Boyd, and K. Najafi. Whole-angle-mode micromachined fused-silica Birdbath Resonator Gyroscope (WA-BRG). In *IEEE International Conference on Micro Electro Mechanical Systems (MEMS)*, San Francisco, CA, USA, January 2014.

[140] D. Zhang, M. J. Kushner, and C. Cui. Reaction mechanisms and SiO2 profile evolution in fluorocarbon plasmas. In *AVS International Symposium*, pittsburgh, PA, USA, October 2000.

[141] F. Zhang, E. Keikha, B. Shahsavari, and R. Horowitz. Adaptive mismatch compensation for vibratory gyroscopes. In *International Symposium on Inertial Sensors and Systems (ISISS)*, Laguna Beach, CA, USA, February 2014.

[142] Y. K. Zhbanov. Amplitude control contour in a hemispherical resonator gyro with automatic compensation for difference in Q-factors. *Mechanics of Solids*, 43(3):328–332, 2008.

[143] V. Zhuravlev. Oscillation shape control in resonant systems. *Journal of Applied Mathematics and Mechanics*, 56(5):725–735, 1992.

Appendix A

WA Numerical Simulation

In this appendix, we derive differential equations which can be integrated to simulate gyroscope response in the WA mode of operation. As compared to the reduced-order model reported by Lynch [70], the presented model accounts for both the mechanical imperfections and imperfections in the control electronics, and it can be extended to capture non-linear mechanisms and noise effects.

A.1 Averaged Equations of Motion

A lumped mass-spring-damper representation of a Coriolis Vibratory Gyroscope (CVG) is shown in Fig. A.1. The following differential equation governs the dynamics of a CVG

$$\begin{bmatrix} \ddot{q_1} \\ \ddot{q_2} \end{bmatrix} + Z \begin{bmatrix} \dot{q_1} \\ \dot{q_2} \end{bmatrix} + K \begin{bmatrix} q_1 \\ q_2 \end{bmatrix} = \begin{bmatrix} F_1 \\ F_2 \end{bmatrix}, \tag{A.1}$$

where the variables q_1, q_2, F_1, and F_2 denote the displacement and control forces along the reference X and Y axes. The Z and K matrices include the coefficients of damping, elasticity,

and the Coriolis forces

$$Z = \begin{bmatrix} \frac{2}{\tau} + \Delta(\frac{1}{\tau})\cos 2\theta_\tau & \Delta(\frac{1}{\tau})\sin 2\theta_\tau - 2k\Omega \\ \Delta(\frac{1}{\tau})\sin 2\theta_\tau + 2k\Omega & \frac{2}{\tau} - \Delta(\frac{1}{\tau})\cos 2\theta_\tau \end{bmatrix} \tag{A.2}$$

$$K = \begin{bmatrix} \omega^2 - \omega\Delta\omega\cos 2\theta_\omega & -\omega\Delta\omega\sin 2\theta_\omega \\ -\omega\Delta\omega\sin 2\theta_\omega & \omega^2 + \omega\Delta\omega\cos 2\theta_\omega \end{bmatrix},$$

where k and Ω denote the mechanical angular gain (Bryan's coefficient [14]) and the input angular rate. Definitions of the average resonant frequency ω, frequency split $\Delta\omega$, average damping coefficient $1/\tau$, damping difference $\Delta(1/\tau)$, and misalignment angles (θ_ω and θ_τ) can be found in Fig. A.1.

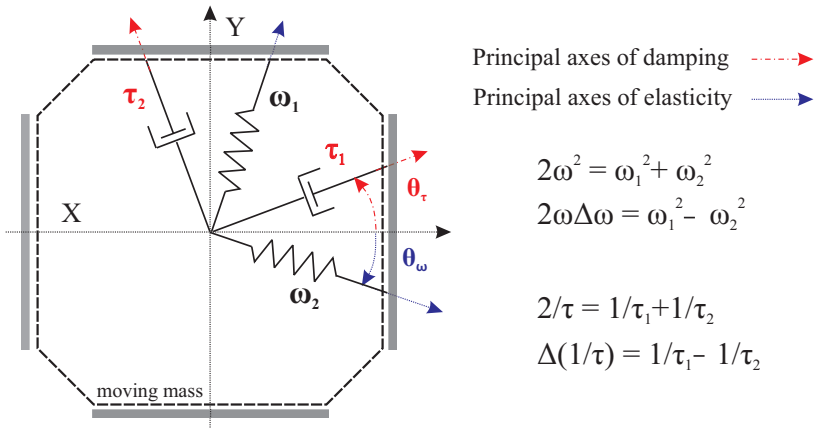

Figure A.1: A lumped mass-spring-damper representation of a Coriolis vibratory gyroscope. The XY axes denote the non-inertial reference frame attached to the sensing element aligned with the direction of actuation and detection. Principal axes of damping, principal axes of elasticity, and their orientation with respect to the reference axes are illustrated.

The mechanical imperfections such as energy loss, anisodamping, and anisoelasticity affect the evolution of the semi-elliptical oscillation pattern studied by Friedland [31] and later by Lynch [70]. As discussed in Chapter 4, the mechanical asymmetries result in systematic errors in the WA output, such as angle-dependent biases (ADB), reduced angular gain, and

the locking effect. These errors are captured in the following equation.

$$\theta = -k_e \int \Omega \, dt + \theta_b, \qquad (\Omega > \Omega_{th}), \tag{A.3}$$

where θ represents the orientation of the oscillation pattern, and k_e, Ω, Ω_{th}, and θ_b denote the effective angular gain, input angular rate, angular rate threshold, and angle bias, respectively. We used the following variables as the states of the system to better represent the actual inputs (readout voltages) and outputs (control voltages) in the WA control architecture.

$$\begin{bmatrix} x \\ y \end{bmatrix} = G_D \begin{bmatrix} q_1 \\ q_2 \end{bmatrix}, \qquad \begin{bmatrix} v_x \\ v_y \end{bmatrix} = G_A^{-1} \begin{bmatrix} F_1 \\ F_2 \end{bmatrix}, \tag{A.4}$$

where G_D and G_A denote the nominal conversion gains in displacement-to-voltage and voltage-to-force-per-mass, respectively. In this representation, parameters x and y express the mass position along X and Y axes in voltages, and v_x and v_y represent the harmonic voltages for generating the electrostatic control forces. The equation of motion governing these variables are

$$\begin{bmatrix} \ddot{x} \\ \ddot{y} \end{bmatrix} + Z \begin{bmatrix} \dot{x} \\ \dot{y} \end{bmatrix} + K \begin{bmatrix} x \\ y \end{bmatrix} = G_A G_D \begin{bmatrix} v_x \\ v_y \end{bmatrix} \tag{A.5}$$

Numerical simulation of gyroscope response in the WA operation can be performed using the second-order differential equations described in (A.5). In theory, an explicit or implicit numerical solver can solve these equations directly. However, since we are dealing with a stiff non-linear system with two very different time scales at which parameters are changing, the simulation would be computationally expensive. Therefore, we reduce the dimension of the system and study the envelope of system parameters.

The state variables and input forces can be represented through the following coordinate

transformation, which decouples the two time scales at which variables change.

$$\begin{aligned} x(t) &= x_c(t)cos(\omega t + \phi(t)) + x_s(t)\sin(\omega t + \phi(t)) \\ y(t) &= y_c(t)\cos(\omega t + \phi(t)) + y_s(t)\sin(\omega t + \phi(t)) \\ v_x(t) &= v_{xc}(t)\cos(\omega t + \phi(t)) + v_{xs}(t)\sin(\omega t + \phi(t)) \\ v_y(t) &= v_{yc}(t)\cos(\omega t + \phi(t)) + v_{ys}(t)\sin(\omega t + \phi(t)) \end{aligned} \tag{A.6}$$

where $\omega t + \phi$ is used as the reference phase in the coordinate transformation. It should be noted that numerical solving for variables x_c, x_s, y_c, y_s, and $\dot{\phi}$ would be enough to recover the complete oscillatory response of a Micro-Rate-Integrating Gyroscope (MRIG) in the WA mode of operation.

Due to a large time constant (τ) in Micro-Electro-Mechanical (MEM) resonators, as compared to the oscillation period ($1/\omega$), it is reasonable to assume that the energy in the system has a narrow bandwidth centered around the resonant frequency. This is equivalent to the assumption that variables x_c, x_s, y_c, y_s, and $\dot{\phi}$ are slow-varying parameters, therefore, the method of averaging can be used to derive equations to study the variation of these variables, [93]

The differential equations governing the slow-varying parameters are derived by substituting Eq. (A.6) in the equation of motion (A.5). The equations were separated using the harmonic balanced method. In a reduced-order approximation of the averaging method, the terms with a higher power, second-time derivatives, and terms not multiplied by the average resonant frequency (ω) were neglected. After following these steps, we would reach the four differential

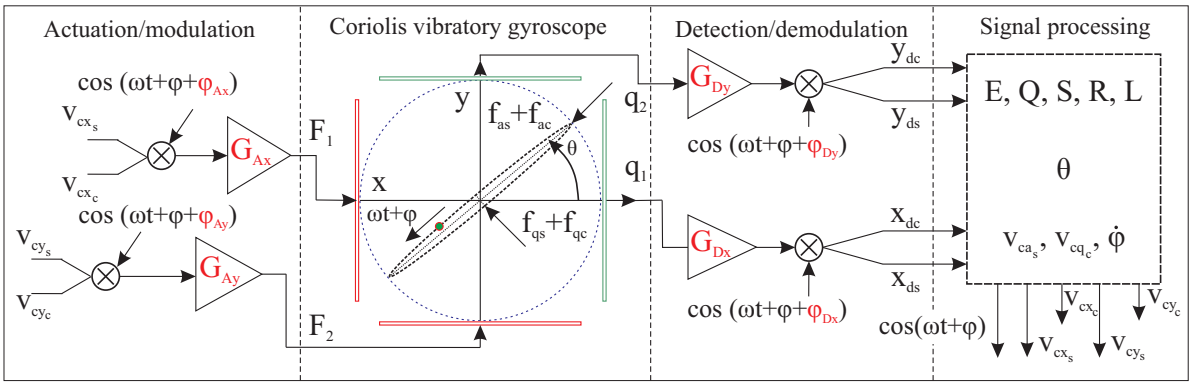

Figure A.2: Block diagram of the WA control, which is divided into four parts. In the actuation/modulation, the command signals from the signal processing unit are modulated using the Numerically Controlled Oscillator (NCO) phase output. The harmonic signals are converted to the electrostatic forces along the X and Y axes using the actuation gains G_{Ax} and G_{Ay}, respectively. The electrostatic control forces would affect the CVG and the evolution of the oscillation pattern. In the detection/demodulation part, the position of the poof-mass along X and Y axes are converted to voltages using detection gains G_{Dx} and G_{Dy}. Then, demodulation is performed using the reference signal for estimating the in-phase and in-quadrature-phase components. In the signal processing unit, the demodulated signals are used to estimate pendulum variables and used to generate the control signals and the reference signal for modulation and demodulation. Parameters in red denote the errors in control electronics categorized as phase errors, detection gain mismatches, and actuation gain mismatches.

equations (A.7) describing the variations in the slow-varying states of the gyroscope.

$$
\begin{aligned}
\dot{x_s} &= +x_c\dot{\phi} + k\Omega y_s - x_s(\frac{2}{\tau} + \frac{1}{2}\Delta(\frac{1}{\tau})\cos 2\theta_\tau) - \frac{1}{2}y_s\Delta(\frac{1}{\tau})\sin 2\theta_\tau + x_c\frac{\Delta\omega}{2}\cos 2\theta_\omega + y_c\frac{\Delta\omega}{2}\sin 2\theta_\omega + \frac{v_{x_c}}{2\omega}G_AG_D \\
\dot{x_c} &= -x_s\dot{\phi} + k\Omega y_c - x_c(\frac{2}{\tau} + \frac{1}{2}\Delta(\frac{1}{\tau})\cos 2\theta_\tau) - \frac{1}{2}y_c\Delta(\frac{1}{\tau})\sin 2\theta_\tau - x_s\frac{\Delta\omega}{2}\cos 2\theta_\omega - y_s\frac{\Delta\omega}{2}\sin 2\theta_\omega - \frac{v_{x_s}}{2\omega}G_AG_D \\
\dot{y_s} &= +y_c\dot{\phi} - k\Omega x_s - y_s(\frac{2}{\tau} + \frac{1}{2}\Delta(\frac{1}{\tau})\cos 2\theta_\tau) - \frac{1}{2}x_s\Delta(\frac{1}{\tau})\sin 2\theta_\tau - y_c\frac{\Delta\omega}{2}\cos 2\theta_\omega + x_c\frac{\Delta\omega}{2}\sin 2\theta_\omega + \frac{v_{y_c}}{2\omega}G_AG_D \\
\dot{y_c} &= -y_s\dot{\phi} - k\Omega x_c - y_c(\frac{2}{\tau} + \frac{1}{2}\Delta(\frac{1}{\tau})\cos 2\theta_\tau) - \frac{1}{2}x_c\Delta(\frac{1}{\tau})\sin 2\theta_\tau + y_s\frac{\Delta\omega}{2}\cos 2\theta_\omega - x_s\frac{\Delta\omega}{2}\sin 2\theta_\omega - \frac{v_{y_s}}{2\omega}G_AG_D
\end{aligned}
\tag{A.7}
$$

These equations are generic and can be used to simulate gyroscope response in the open-loop angular rate, closed-loop angular rate, or the WA mode of operation. The control forces and the variations in the actuation frequency ($\dot{\phi}$) are chosen based on the mode of operation,

As illustrated in Fig. A.2, through the synchronous demodulation process, we have measurements of the slow-varying parameters. We defined the following variables as detection

variables (equivalent to the demodulated signals) to capture phase errors and gain mismatch in the detection electronics.

$$\begin{aligned}\begin{bmatrix} x_{dc} \\ x_{ds} \end{bmatrix} &= R(-\phi_{Dx}) \begin{bmatrix} x_c \\ x_s \end{bmatrix} \\ \begin{bmatrix} y_{dc} \\ y_{ds} \end{bmatrix} &= G_{Dy/x} R(-\phi_{Dy}) \begin{bmatrix} y_c \\ y_s \end{bmatrix},\end{aligned} \tag{A.8}$$

where we assumed that the previously defined nominal detection gain is equal to the detection gain along the X-axis ($G_D = G_{Dx}$) and the ratio of the detection gain along the Y-axis to the nominal value is denoted by $G_{Dy/x}$. The matrix R represents a 2-dimensional rotation matrix and phases ϕ_{Dx} and ϕ_{Dx} denote the phase errors in demodulation along the X and Y axes, respectively.

Based on the detection variables defined in Eq. (A.8), the pendulum variables are estimated as

$$\begin{aligned} E_d &= x_{dc}^2 + x_{ds}^2 + y_{dc}^2 + y_{ds}^2 \\ Q_d &= 2(x_{dc} y_{ds} - y_{dc} x_{ds}) \\ R_d &= x_{dc}^2 + x_{ds}^2 - y_{dc}^2 - y_{ds}^2 \\ S_d &= 2(x_{dc} y_{dc} + y_{ds} x_{ds}) \\ \Im(L_d) &= 2(x_{dc} x_{ds} + y_{dc} y_{ds}) \end{aligned} \tag{A.9}$$

As part of the control algorithm, the estimated pendulum variables are utilized as inputs of three feedback loops to (a) control energy and maintain the amplitude along the semi-major axis of the orbital trajectory, (b) control quadrature and suppress quadrature growth due to anisoelasticity during precession, and (c) to track the oscillation phase through a Phase-Locked Loop (PLL). The mathematical representation of these Proportional-Integral (PI)

feedback loops have been discussed in [70] and are summarized as follows

$$
\begin{aligned}
v_{ca_s} &= K_E[E_d - E_0 + \frac{1}{2\tau_E}\int (E_d - E_0)\,dt] \\
v_{cq_c} &= -K_Q[Q_d - Q_0 + \frac{1}{2\tau_Q}\int (Q_d - Q_0)\,dt] \\
\dot{\phi} &= -K_{L_i}[\Im(L_d) - L_{i0} + \frac{1}{2\tau_L}\int (\Im(L_d) - L_{i0})\,dt]
\end{aligned}
\tag{A.10}
$$

where K_E, K_Q, and K_{L_i} are the proportional coefficients of the PI controllers and τ_E, τ_Q, and τ_L are the integration time constants.

Different architectures have been reported in the literature for applying the control forces in the WA mode of operation. Generally, the intended control forces defined in Eq. (A.10) are projected on to two set of electrodes with orthogonal forcing directions along X and Y. In this approach, the vector summation of the forces along X and Y would have the appropriate direction and phase relative to the orientation of the orbital trajectory and phase of oscillation. The control forces/voltages along the semi-major and minor axes of the orbital trajectory are projected along X and Y axes based on the estimated orientation of the oscillation pattern θ_d as

$$
\begin{aligned}
v_{cx_c} &= -v_{cq_c}\sin(\theta_d) \\
v_{cx_s} &= +v_{ca_s}\cos(\theta_d) \\
v_{cy_c} &= +v_{cq_c}\cos(\theta_d) \\
v_{cy_s} &= +v_{ca_s}\sin(\theta_d)
\end{aligned}
\tag{A.11}
$$

The orientation of the oscillation pattern is estimated through the following

$$
\theta_d = \frac{1}{2}atan(S_d/R_d), \tag{A.12}
$$

where the subscript "d" denotes that these values are estimated based on measurements and

they would be different from the actual pendulum variables in a case of having errors in the detection electronics.

The control signals defined in Eq. (A.11) would go through a similar transformation as the detection signals to capture phase errors in modulation and actuation gain mismatch, illustrated in Fig. A.2.

$$\begin{aligned} \begin{bmatrix} v_{x_c} \\ v_{x_s} \end{bmatrix} &= R(\phi_{Ax}) \begin{bmatrix} v_{cx_c} \\ v_{cx_s} \end{bmatrix} \\ \begin{bmatrix} v_{y_c} \\ v_{y_s} \end{bmatrix} &= G_{Ay/x} R(\phi_{Ay}) \begin{bmatrix} v_{cy_c} \\ f_{cy_s} \end{bmatrix}, \end{aligned} \tag{A.13}$$

where the previously defined nominal actuation gain was assumed to be equal to the actuation gain along the X-axis ($G_A = G_{Ax}$) and the actuation gain ratio is denoted using $G_{Ay/x}$.

Differential equations (A.7) and (A.10) can be numerically integrated along with the defined detection and actuation variables in equations (A.8) and (A.9-A.13) to simulate the response in the WA mode accounting for imperfections in control and detection electronics. The model can be adjusted to have time-based switches to independently turn on/turn off the controllers or have time-variant system parameters for input angular rate, anisodamping, and anisoelasticity in the gyroscope. It should be noted that since all these equations are written in the most generic form, they can be adjusted to simulate other non-idealities, including but not limited to the effect of pick-off noise, stability of angle output, effect of electrostatic/geometrical nonlinearity, capacitive actuation and detection nonlienarity, etc.

A.2 Demonstration

For demonstration purposes, we used system parameters which were experimentally extracted based on characterization of a Dual Foucault Pendulum (DFP) MRIG gyroscope [4], presented in Table A.1, to simulate the gyroscope response in the WA mode of operation.

Table A.1: The gyroscope parameters used for numerical simulation.

Parameter	Value	Parameter	Value
ω	15016.219 Hz	K_E	2.5e3
$\Delta\omega$	0.0354 Hz	τ_E	5e-3
θ_ω	-58.82^o	K_Q	2.5e+3
τ	22.43 s	τ_Q	5e-3
$\Delta\tau$	1.169 s	K_L	2e+4
θ_τ	-1.465^o	τ_L	2.5e-5
E_0	2.5e-3 V^2	$G_A G_D$	1.01e5
Q_0 and L_{i0}	0	Mechanical angular gain	0.76307

The state variables were numerically solved using an explicit fourth-order Runge-Kutta solver with a constant time step of 1E-4 seconds. Based on the closed-loop bandwidth of the PI controller, input rotation rate, and frequency split between the two modes, smaller time steps can be used to reduce simulation time and avoid memory usage for long-duration simulation. In an example, shown in Fig. A.3, we simulated the response of a RIG to an angular rate input ($\mathbf{\Omega}$) increasing from 0 to 100 Degree-Per-Second (DPS) with 25 DPS increments assuming an ideal control and detection electronics (i.e, $G_{Ay/x}, G_{Ay/x} = 1$ and $\phi_{Ax}, \phi_{Ay}, \phi_{Dx}, \phi_{Dy} = 0$).

We characterized the effective angular gain and angle bias error in the WA mode of operation, as defined in Eq. (A.3). A linear line (first-order polynomial) was fitted to the unwrapped angle output in this characterization. The slope was used as an estimate of the effective angular gain; the residual angle error as a function of the pattern angle was estimated, which represents the Angle-Dependent Bias (ADB), illustrated in Fig. A.4.

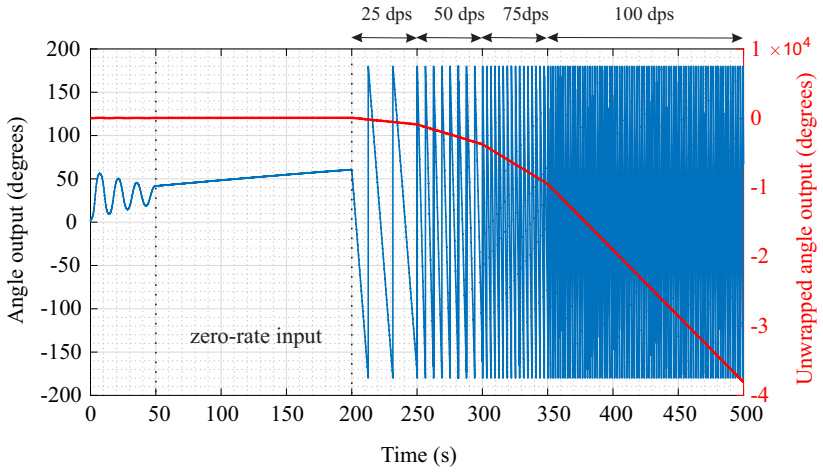

Figure A.3: A numerically simulated gyroscope output in the WA mode of operation is illustrated along with the unwrapped angle output. The energy, PLL, and quadrature controllers were engaged at 0, 10, and 50 seconds simulation time. From 50 to 200 seconds, no input rotation was applied; we observed that the angle was converging to the equilibrium angle (the orientation of the principal axis of damping with the lowest dissipation). From 200 seconds simulation time, the input rotation was increased from 25 DPS to 100 DPS with 25 DPS increments.

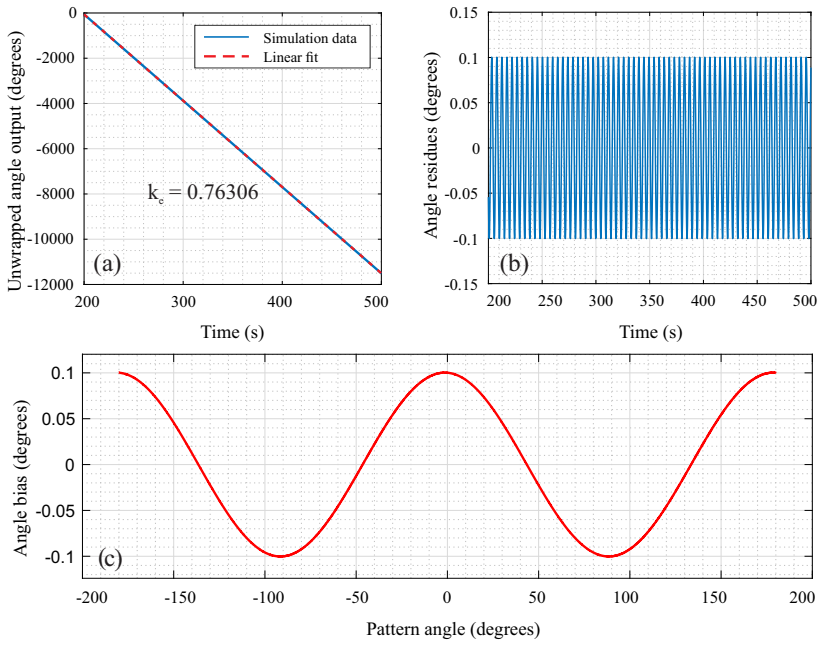

Figure A.4: Characterization of the effective angular gain and the ADB in WA mode of operation. In (a), a linear fit to the unwrapped angle output as a function of time was used to estimate the effective angular gain with the residual error in angle shown in (b). In (c), the residual error as a function of the pattern angle (i.e., the ADB) is shown.

Appendix B

Implementation of WA Control

This appendix discusses a flexible implementation of the Whole-Angle (WA) control based on the slow-varying pendulum variables, as proposed by Lynch [70]. Through this implementation, the WA control can be applied to any nearly mode-matched Coriolis Vibratory Gyroscope (CVG) to perform direct angle measurement.

B.1 Analog Circuits

We utilized a custom-designed Printed Circuit Board (PCB) to implement the analog circuits required for electrostatic actuation and detection. A simplified schematic of the circuits for actuation and detection along the X-axis of a CVG is illustrated in Fig. B.1.

B.1.1 Drive Circuits

The drive circuitry of a capacitive CVG is shown with blue traces in Fig. B.1. For gyroscope control, an AC voltage is applied to the input port of the PCB (V_{ACx}). The AC signal is

generated using a Zurich HF2Li lock-in amplifier, and the amplitude and phase of the AC signal are controlled through the implemented algorithms. The AC signal passes through a 2-channel unity gain amplifier (Analog Devices ADA4898) to create two AC voltages with the same amplitude and 180 ° phase difference. The anti-phase signals are used for differential actuation of the gyroscope (i.e., the push-pull architecture).

A DC voltage (V_{DCx}) is then added to the differential AC signals using a passive RC filter and applied to the differential drive electrodes (D_{x+} and D_{x-}) to generate an electrostatic force with the same phase and frequency as the control signal. In the case of using parallel plate electrodes and a vibration amplitude less than 5% of the capacitive gap size, the control signal and the control force can be represented as

$$V_{ACx}(t) = V_{cx}\cos(\omega t + \phi_{ax}), \quad F_{x+}(t) = V_{DCx}\frac{C_{D0}}{g}V_{cx}\cos(\omega t + \phi_{ax}), \tag{B.1}$$

where V_{cx}, ϕ_{ax}, ω, g, and C_{D0} denote the amplitude and phase of the control signal, the drive frequency, the capacitive gap size, and the nominal drive capacitance, respectively.

The DC voltage is generated using an ultra-stable external DC power supply or the auxiliary outputs of HF2Li. The DC voltage can be regulated to change the voltage-to-force conversion gain, Eq. (B.1), or to regulate the resonant frequencies for mode-matching.

B.1.2 Sense Circuits

The analog circuit for capacitive motion detection is shown in Fig. B.1 with red traces. Through capacitive detection with a differential electrode configuration (S_{x+} and S_{x-}), motional currents are generated due to variation of the capacitive gap size. For the case of using a DC biasing voltage on the proof-mass and a vibration amplitude less than 5% of the

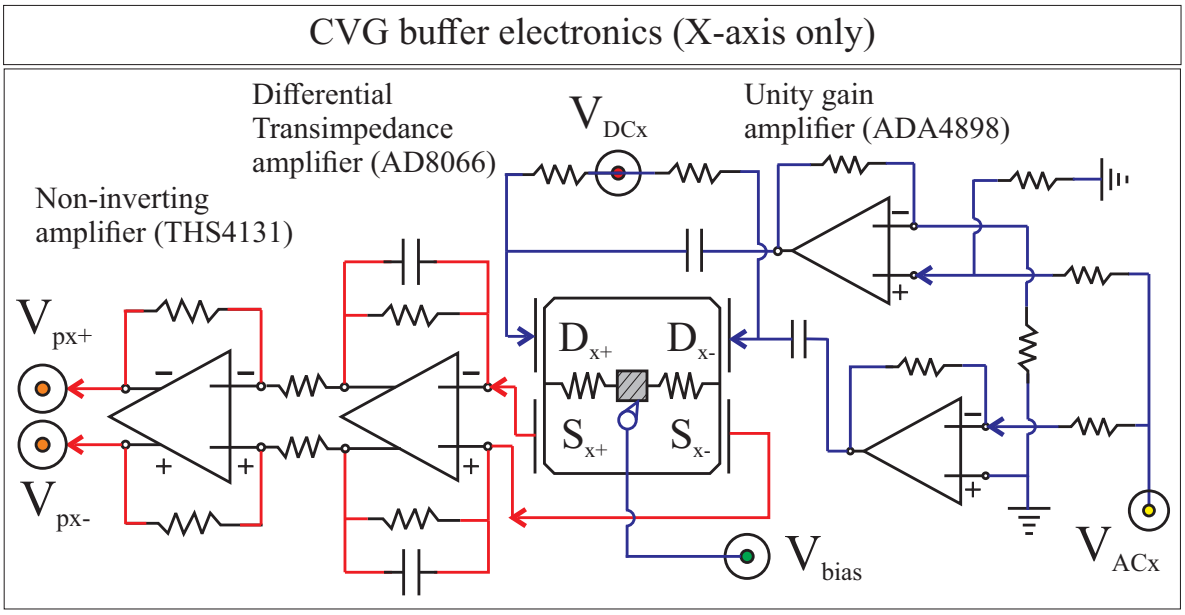

Figure B.1: A simplified schematic of actuation and detection analog circuits along the X-axis of a capacitive Coriolis vibratory gyroscope.

capacitive gap size, the motional current can be calculated as

$$x(t) = X_a cos(\omega t + \phi_{dx}), \quad I_{x+}(t) = V_{bias}\frac{C_{S0}}{g}X_a\omega\cos(\omega t + \phi_{dx} + 90), \tag{B.2}$$

where X_a, ϕ_{dx}, and C_{S0} denote the amplitude and phase of vibration along the X-axis and the nominal sense capacitance, respectively. We used a differential transimpedance amplifier (Analog Devices AD8066) to amplify and convert the motional current in the nA-range to mV-level voltages through the feedback impedance in a differential configuration.

In the case of the DFP gyroscope with a detection capacitance on the order of 1.2 pF, we used a feedback resistor of 500kΩ (gain of 500k). The capacitor in the feedback impedance was selected to avoid instabilities (a 1.5 pF capacitor was used). In the second stage of the sense circuit, we used non-inverting amplifiers (Texas Instrument THS4131) to scale the detection voltages (V_{px+} and V_{px-}) and match them with the input voltage range of the controller. For the HF2Li lock-in amplifier, the input voltage range is 1.5 V peak-to-peak.

Based on the transfer function of the transimpedance amplifier and the non-inverting amplifier, the phase of the detection voltages will be different from the phase of oscillation (ϕ_{dx}). Similarly, a phase error between the control voltage and the control force is inevitable. We compensated for these phase shifts in the signal modulation and demodulation process.

We used symmetric tracing and symmetric component positioning along the X and Y channels to achieve near-to-identical electrical characteristics in the PCB design. However, due to imperfections in PCB fabrication and the electrical components, asymmetries were observed between the input-output phase response of the X and Y channels. The phase errors were identified and compensated for through a calibration procedure. Similarly, we developed and applied a method to identify and compensate for detection and actuation gain mismatches along the X and Y axes, discussed in Chapter 6.

Electro-mechanical Amplitude Modulation (EAM)

To prevent signal feed-through between the input and output channels, we used a carrier signal for biasing the proof-mass. In this case, the motional currents will appear as sidebands centered around the carrier frequency. We employed amplitude demodulation (2-stage demodulation) to recover the motional current/voltage. More detail on the EAM method can be found in [17].

The EAM can be employed through a second HF2Li lock-in amplifier to generate the carrier signal and perform the first stage demodulation. Alternatively, an external wave generator can be use to provide the carrier signal and a single HF2Li can be used to track the carrier frequency (ω_{car}), using a Phase-Locked Loop (PLL), and to perform sideband demodulation through the Amplitude and Frequency Modulation (AM and FM) option of HF2Li. The results reported in this thesis are based on using two HF2Li lock-in amplifiers; the first HF2Li was used for sideband demodulation, and the second HF2Li was used for signal

processing and gyroscope control.

B.2 FPGA and Signal Processing Unit

As discussed in the previous section, through the analog buffer board, control voltages can be applied to exert control forces to the CVG. The readout voltages are used to measure the displacement. The HF2Li lock-in amplifier was utilized to output the control voltages (i.e., control channel) and process the readout signals (i.e., information channel).

The HF2Li includes two differential analog voltage to digital signal converters (ADC), two digital signal to analog voltage converters (DAC), a Field Programmable Gate Array (FPGA), and a Reduced Instruction Set Computer (RISC). The differential readout voltages (V_{px+} and V_{px-}) are converted to digital signals through the ADCs. Subsequently, in the FPGA, the digital signals are downsampled and demodulated based on a reference phase (ϕ). The demodulation process provides in-phase and in-quadrature components of the X-axis and Y-axis detection signals (x_c, x_s, y_c, and x_s). It should be noted that the demodulated quantities are equivalent to the slow-varying parameters governed by the reduced-order averaged model of CVG, [70]. Therefore, they can be used to estimate the pendulum variables (E, Q, S, R, and L), illustrated in Fig. B.2.

Expressions for calculating the pendulum variables and the control algorithms are coded on the RISC of HF2Li through the Real-Time Kit (RTK). As part of the control algorithm, the pendulum variables are used in three Proportional Integral (PI) feedback loops for energy control, quadrature control, and oscillation phase tracking. The output of the controllers are the energy control, quadrature control, and reference phase signals denoted by v_{as}, v_{qc} and ϕ, respectively.

The S and R pendulum variables are used to estimate the orientation of the orbital trajectory

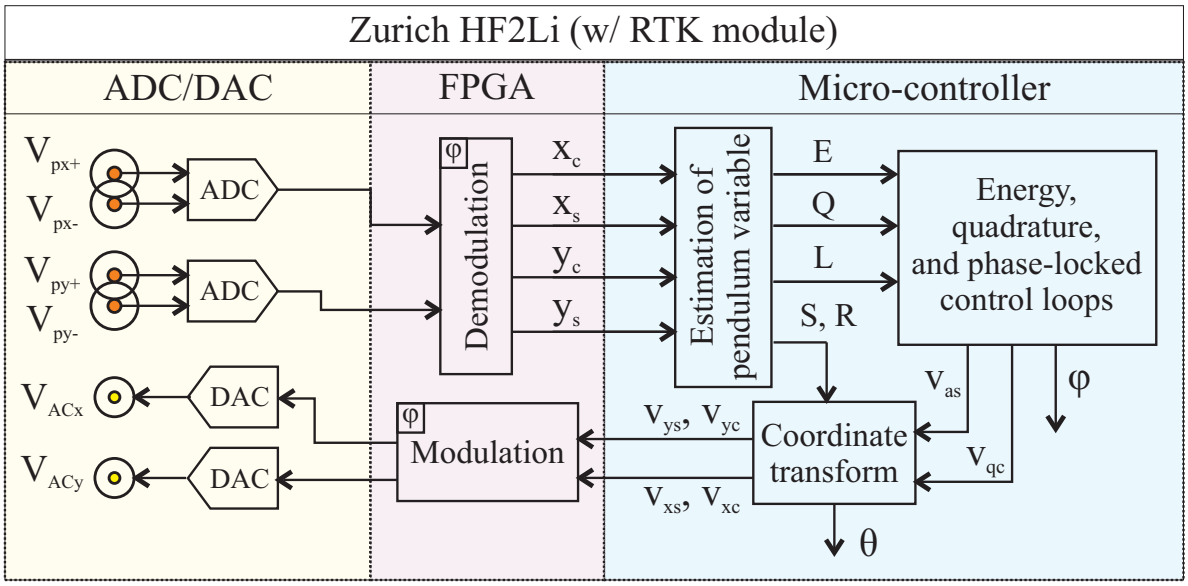

Figure B.2: Schematics of the HF2Li lock-in amplifier, which was used as the Digital Signal Processing (DSP) unit and the control unit.

(θ); the pattern angle measures the input angle of rotation, and it is also used as part of a coordinate transformation to project the control forces along the X and Y axes. The control signals, including in-phase and in-quadrature phase components of the control forces, are modulated at the reference phase. The digital control signals are then converted to analog signals and applied to the input ports of the analog buffer board (V_{ACx} and V_{ACy}). Details of the WA control loops can be found in [70] and Appendix A.

B.2.1 LabOne Interface

In our implementation, the Zurich HF2Li LabOne interface was used to adjust phase offsets in signal modulation and demodulation, sampling rates, low-pass filter characteristics, etc.

When the WA firmware is running on the HF2Li, the amplitude of control voltages in-phase and in-quadrature to the reference phase along the X and Y axes (v_{xc}, v_{xs}, v_{yc}, and v_{ys}) will be showing in boxes 1-4 shown in Fig. B.3. The PLL in the WA control adjusts the frequency of the second numerical oscillator annotated as 5. This frequency is used for modulation and

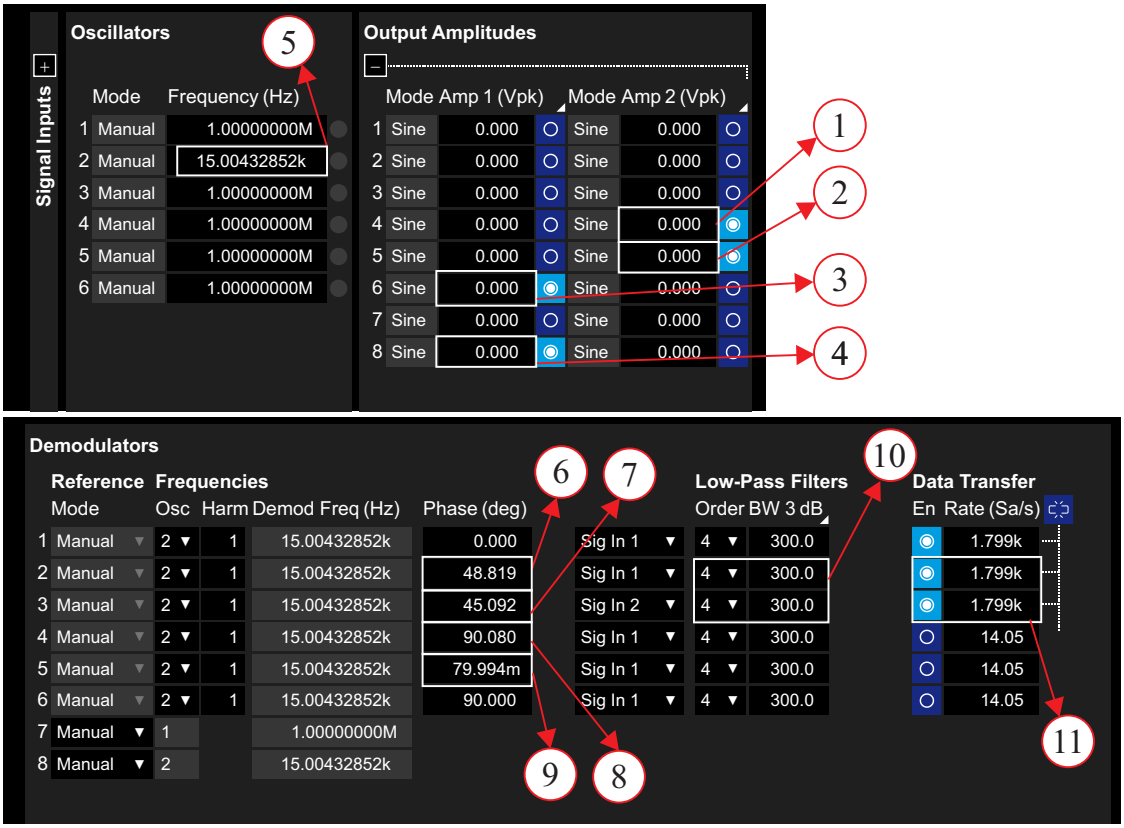

Figure B.3: Lock-in tab in the LabOne interface. One can change demodulation and modulation phases, sampling rates, low-pass filter characteristics, etc. in this tab.

demodulation of control and readout signals. The demodulation phase offsets along the X and Y axes are adjusted in boxes 6 and 7, respectively.

The phase offsets/errors are identified based on the frequency-phase response, which is measured by applying an in-phase control force along the X-axis (v_{xc}) or the Y-axis (v_{yc}). The modulation phase offset along the Y-axis with respect to the X-axis is corrected through quantities in boxes 8 and 9. Please note that the value in box 9 must be 90 ° lower than the value in box 8.

The bandwidth and order of the low-pass filters used as part of the demodulation process are adjusted based on values in box 10. The low-pass filtering of X-axis readouts is configured based on parameters in the second row, and the low-pass filtering of Y-axis readouts is configured based on parameters in the third row. Similarly, the sampling rate of the data,

which is used for recording and running the control algorithms, is set based on values in box 11.

The LabOne interface can be used to record the demodulation signals (x_s, x_c, y_c, and y_s) and the reference frequency $\dot{\phi}$ with synchronized timestamps for post-processing. This enables the characterization of pendulum variables, angle errors, actuation frequency, angular gain, etc.

B.2.2 LabView Control Interface

Please note that when the WA firmware is uploaded on HF2Li, the original PID controllers implemented in the LabOne interface stop working. Therefore, we used a set of registries to set the WA control parameters, including control setpoints, PID control coefficients, enabling/disabling of feedback loops, control output range, input/output channels, and the calibration parameters. We designed a LabView Virtual Instrument (VI) to connect to the HF2Li server for modifying these registries. When the WA control VI is opened, the WA firmware is automatically compiled on the RISC, and the WA algorithms are executed based on the set parameters.

The WA control tab has six different sections. In the first section, the input/output channels of HF2Li are selected for modulation and demodulation of readout and control signals; leave these values as they are. The second section is used to change the energy control loop parameters. The "En" button in each section is used to engage or disable a specific control loop. The "setpoint" box is used for specifying the energy setpoint (E_0). The range parameters represent the lower bound and higher bound saturation points for energy control output; the proportional gain and time constant (i.e., integral coefficient) are used to change the PI controller's gain, response time, and bandwidth. In the quadrature control section, the setpoint is always set to 0. In the phase-locked loop section, the setpoint should be close

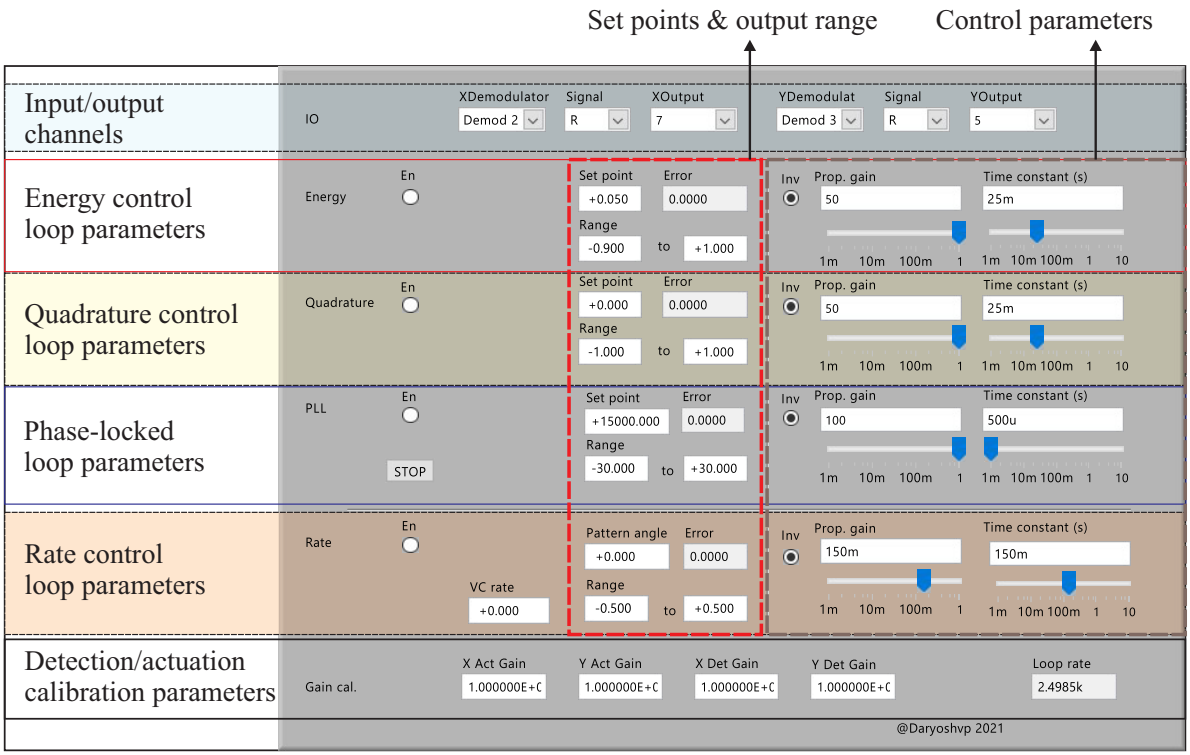

Figure B.4: The LabView VI, which was designed to be used with the WA control firmware.

to the resonant frequency, and the range defines the lower and upper saturation bounds for the actuation frequency.

The rate control loop is not essential for WA operation, but it can control the pattern angle and sustain it at specific orientations. This feature enables the characterization of energy decay time constant at different pattern angles, discussed in Appendix C. On the other hand, by enabling the rate control loop, the CVG can be operated in the Force-to-ReBalance (FRB) mode, [70]. The response time of the rate control loop (i.e., the bandwidth in the FRB mode) can be controlled using the PI coefficients.

The Virtual Carouseling (VC) rate box sets the amplitude of the electrostatic control voltage applied along the minor axis of the elliptical pattern in quadrature to the oscillation phase. The VC force causes a slew rate on the pattern angle (i.e., a linear time-variation). This feature can be employed to overcome the angle locking effect or minimize angular-rate-dependent variations in angular gain, [87]. It can also be used to virtually rotate the pattern

angle for characterization of the asymmetries in damping and elasticity of the gyroscope, discussed in Appendix C.

Parameters in the last section are used to regulate the actuation gains and detection gains along the X and Y axes. In the case of structurally symmetric CVGs, such as the DFP, the values are set to match the detection and actuation gains along the X and Y axes, as discussed in Chapter 6. In the case of asymmetric CVGs, such as the Tuning Fork Gyroscope (TFG), the values are set based on each mode's effective mass (or moment of inertia) and the mismatch in the detection and actuation gains to satisfy pendulum-like equations, [70]. The WA control algorithms are coded to be executed at a fixed rate of 2500 Hz; the actual rate is shown in the "Loop rate" box.

Appendix C

Carouseling and Identification of Mechanical Imperfections

A fast and accurate method for characterization of the mechanical imperfections in Micro-Rate-Integrating Gyroscope (MRIG) is discussed in this appendix. For demonstration, we applied the method to a Dual Foucault Pendulum (DFP) MRIG as a testbed and characterized the mechanical structure's asymmetries in damping and elasticity.

C.1 Anisodamping Characterization

To characterize anisodamping in an MRIG, we utilized the ring-down response in the WA mode and estimated the amplitude decay time constant at different pattern angles, similar to what is illustrated in Fig. C.1. During each ring-down response, the rate control feedback loop applies a force along the minor axis of the elliptical pattern in quadrature with the phase of oscillation to sustain the orientation at a given pattern angle. Assuming for ideal control electronics, the rate control force does not affect the ring-down response [70].

We characterized the time constant values of the Dual Foucault Pendulum (DPF) gyroscope at different pattern angles, shown in Fig. C.2(a). Based on the differential equation for the evolution of energy ($\dot{E}$), [70], due to anisodamping the amplitude decay time constant changes as a function of the pattern angle; the relationship can be represented as

$$\tau'(\theta) = \tau - \frac{1}{2}\Delta\tau \cos 2(\theta - \theta_\tau), \tag{C.1}$$

where $\Delta\tau = \tau_2 - \tau_1$. By fitting the expression Eq. (C.1) to the experimental data in Fig. C.2(a), the averaged energy decay time constant (τ), the mismatch in time constants ($\Delta\tau$), and the misalignment in the principal axes of damping (θ_τ) can be estimated. In the case of the DFP gyroscope with the experimental data shown in Fig. C.2, the extracted parameters are included in Table C.1.

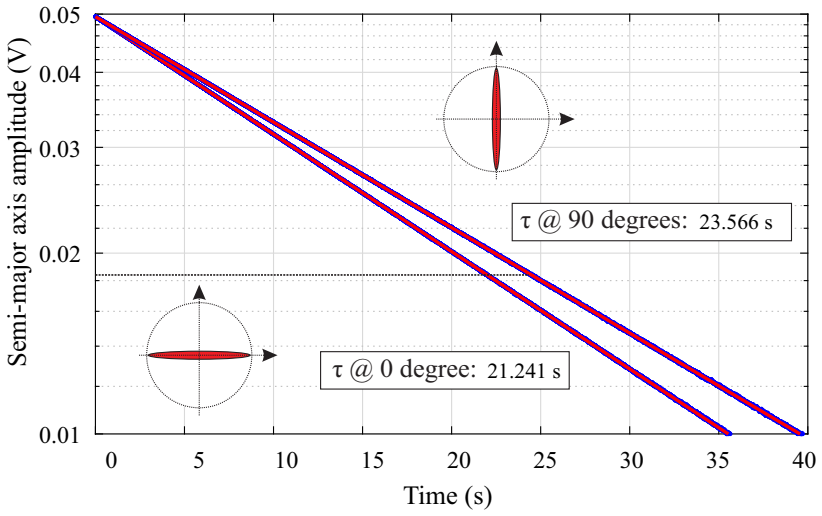

Figure C.1: Experimental characterization of damping along X and Y axes using the amplitude decay rate.

It is an interesting observation that the principal axes of damping were closely aligned with the X and Y axes (θ_τ = -1.465°). We believe that the small misalignment in principal axes of damping resulted from a high DC voltage (8.3 V) applied along the X-axis for electrostatic frequency matching. A DC voltage biasing of electrodes has been reported to reduce the quality factor due to electronics dissipation and a higher anchor loss caused by an

imbalanced electrostatic force exerted on the dual-mass DFP. A DC biasing would increase damping exactly along the X-axis. As a result, the difference between the diagonal terms in the damping matrix increase, and the damping matrix converges to its diagonal Jordan form. This is equivalent to having the principal axes of damping converge to the X and Y axes, $\theta_\tau \approx 0$).

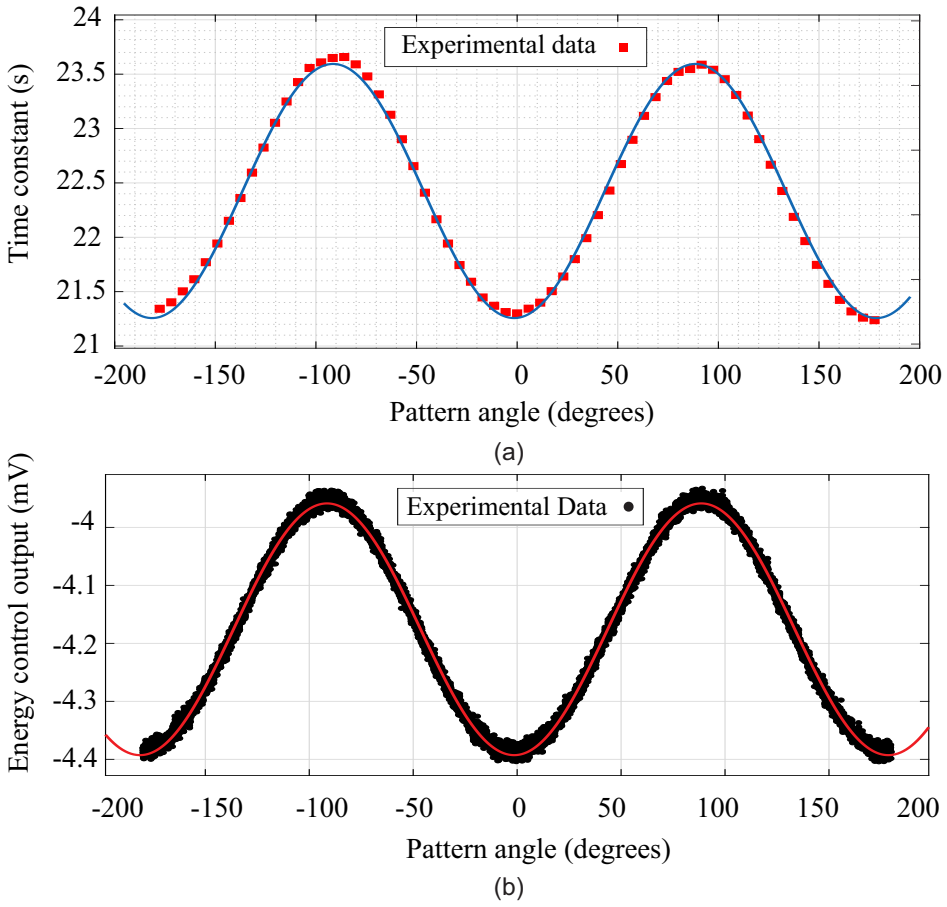

Figure C.2: Experimental results on characterization of anisodamping in the DFP are presented. In (a), estimated amplitude decay time constant values at different pattern angles are shown. In (b), variation in the energy control output is shown as a function of the pattern angle used to estimate the nominal actuation-detection electronics gain ($G_A G_D$).

C.2 Actuation-Detection Gain Characterization

We define the actuation-detection gain as the product of the position-to-voltage and the voltage-to-force conversion gains. To characterize the actuation-detection gain, we applied a 10 DPS physical rotation to the MRIG, and the output of the energy control loop (v_{as}) is measured as a function of the pattern angle, illustrated in Fig. C.2 (b). The variations follow the same trend predicted by the differential equation describing the evolution of the E pendulum variable and can be used to estimate the nominal actuation-detection electronics gain. The nominal value of the actuation-detection gain ($G_A G_D$) can be estimated based on the correlation between the energy decay time constant and the output of the energy control using

$$v_{as}(\theta) G_A G_D = -2\sqrt{E_0}\frac{\omega}{\tau'(\theta)}, \tag{C.2}$$

where the energy control voltage, the energy setpoint, and the average resonant frequency are denoted by v_{as}, E_0, and ω. It is worth mentioning that based on Eq. (C.2), one can utilize the variation in the output of the energy control loop to estimate the damping characteristics, assuming that the electro-mechanical gains are known.

C.3 Anisoelasticity Characterization

In a similar experiment, through physical rotation of MRIG, variations of the actuation frequency (tracked using the PLL) as a function of the pattern angle can be measured, presented in Fig. C.3. The excitation frequency changes with the pattern angle during precession as defined by the following function

$$\omega'(\theta) = \omega - \frac{1}{2}\Delta\omega \cos 2(\theta - \theta_\omega) \tag{C.3}$$

By fitting the expression in Eq. (C.3) to the experimental data in Fig. C.3, we can estimate the average resonant frequency (ω), the frequency split ($\Delta\omega$), and the misalignment in the principal axes of elasticity (θ_ω). In the case of the DFP gyroscope, based on experimental data, we observed that after electrostatic tuning, a frequency split ($\Delta\omega$) on the order of 34 mHz was achieved. Based on the misalignment in the principal axes of elasticity (θ_ω = -58.82°), it was noted that in order to reduce the frequency split below 34 mHz, quadrature electrodes were required to reduce the quadrature coupling between the two modes.

In the case of MRIG with quality factors exceeding 1M, the described method is the most accurate method for fast characterization and monitoring of anisoelasticity during the electrostatic frequency tuning step and during the WA operation. It is worth mentioning that the precession needed for characterization of anisoelasticity can be provided through electrostatic forces (i.e., virtual carouseling), eliminating the need for rate tables.

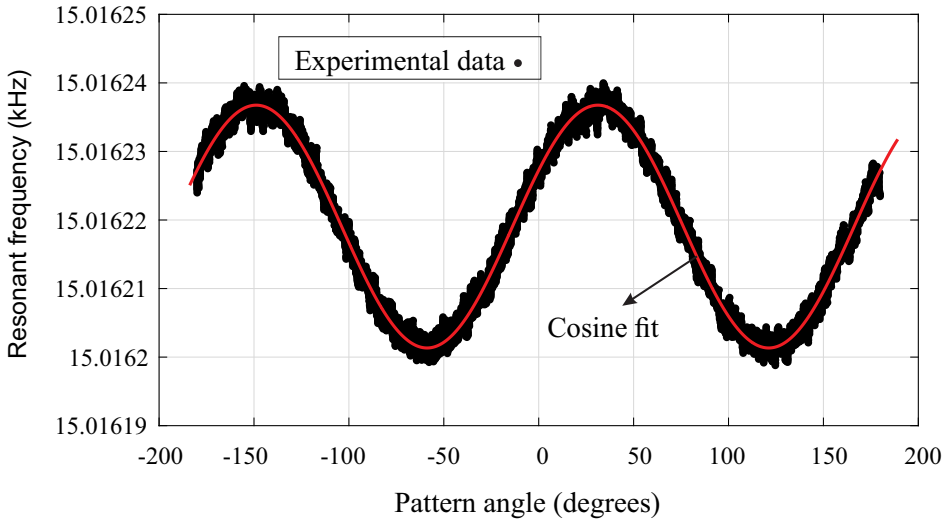

Figure C.3: Variations of the actuation frequency as a function of the pattern angle. In this experiment, a 10 DPS physical rotation was applied to the DFP MRIG, and the vibration amplitude was set to 5 mV.

The gyro parameters extracted from these experiments and the PI values used in the WA control are summarized in Table C.1.

It should be noted that it is imperative to have near-to-ideal electronics to get accurate

Table C.1: Characterized gyroscope parameters of the DFP MRIG.

Parameter	Value	Parameter	Value
ω	15016.219 Hz	K_E	2.5e3
$\Delta\omega$	0.0354 Hz	τ_E	5e-3
θ_ω	-58.82^o	K_Q	2.5e+3
τ	22.43 s	τ_Q	5e-3
$\Delta\tau$	1.169 s	K_L	2e+4
θ_τ	-1.465^o	τ_L	2.5e-5
E_0	2.5e-3 V^2	$G_A G_D$	1.01e5
Q_0 and L_{i0}	0	Mechanical angular gain	0.76307

results through the discussed methods. Phase errors in signal modulation/demodulation and mismatches in the detection and actuation gains can cause coupling between different control loops, and in turn, equations (C.1-C.3) will not hold.